Evaluation of Electronic Structure and Defects in Thick $In_xGa_{1-x}N$ Films Grown by Metalorganic Chemical Vapor Deposition for Application to Photovoltaic Devices

Mickael Lozac'h

March 2013

Evaluation of Electronic Structure and Defects in Thick $In_xGa_{1-x}N$ Films Grown by Metalorganic Chemical Vapor Deposition for Application to Photovoltaic Devices

Mickael Lozac'h
Doctoral Program in Materials Science and Engineering

Submitted to the Graduate School of
Pure and Applied Sciences
in Partial Fulfillment of the Requirements
for the Degree of Doctor of Philosophy in
Engineering

at the
University of Tsukuba

Abstract

It was recently proposed that the bandgap engineering of $In_xGa_{1-x}N$, from 0.7 eV (InN, [1]) to 3.4 eV (GaN), covering most of the solar spectrum, will allow III-V nitride semiconductors to be used in photovoltaic applications [2]. While the technology of light emitting diodes (LEDs) based on III-V nitrides is well established, the operation mechanism of solar cells is quite different from that of LEDs. In photovoltaic devices, the absorption of solar light, the generation of photo carriers and their separation, transportation and collection are all crucial factors. Consequently, high quality InGaN films thicker than 0.3μm are required to maximize absorption. As such, it is necessary to analyze their defects and valence band structures. Since InGaN films of several nm in thickness have been used as quantum-well layers in LEDs, the knowledge and study are needed to provide thicker InGaN films for photovoltaic applications. In the following, I describe the main issues of my study:

- Deposition of InGaN thicker than 0.3μm with smooth surface, especially with InN mole fraction higher than 30 % in order to absorb enough solar light.
- Evaluation of band structure and band alignment depending on the InN mole fraction in order to avoid band offset affecting the carrier transportation at the interfaces between p-GaN/i-InGaN/n-GaN layers.
- Analysis of point defects and deep-level defects in InGaN films in order to form better junctions.
- Control of the p-type doping for GaN and $In_xGa_{1-x}N$ films.
- Realization of solar cell devices to analyze the photovoltaic properties of Schottky, *p-n* homojunction, and *p-i-n* junction using InGaN films.

In this study, I have attempted to improve the $In_xGa_{1-x}N$ films with respect to these issues and have evaluated both their electronic structures and defects for the development of photovoltaic devices.

The thesis is composed of seven chapters. The first chapter will present the history of InGaN films formed by deposition, the purpose of the study, and the features of III-V nitride solar cells. The second chapter will present the fundamental physics for electronic and optical characterizations, and the thin-film analysis techniques performed in this study. The third chapter will present the MOCVD deposition technique and will treat the optimization of $In_xGa_{1-x}N$ growth conditions in order to control its bandgap with high crystallinity. In the fourth chapter, the band structure and band alignment will be evaluated by hard X-ray photoemission spectroscopy. In the fifth chapter, the impurities and defect levels inside InGaN films will be analyzed. In the sixth chapter, the feasibility of n-GaN and n-InGaN films for photovoltaic applications will be underlined by Schottky devices. In the same chapter, the photovoltaic properties of improved Schottky junction, *p-n* homojunction, and *p-i-n* junction for $In_xGa_{1-x}N$ films will be presented. Finally the seventh chapter, the conclusions section, will summarize the achievements and comments on the potential of InGaN films for photovoltaic devices. In the following abstract, I will summarize the main achievements of my study.

1. Optimization of $In_xGa_{1-x}N$ film growth by metalorganic chemical vapor deposition (MOCVD)

To use an $In_xGa_{1-x}N$ film as an active layer, the material requires a controlled bandgap, a high crystal quality to reduce defects and carrier recombination, and high electron mobility to be able to collect the photo-generated carriers.

I fabricated the InGaN semiconductor by a metalorganic chemical vapor deposition (MOCVD) system. The InGaN crystal films display a wurtzite crystalline structure (hexagonal structure) with a c-lattice along the column and an a-lattice along the base. Sapphire or AlN templates are commonly used substrates for the InGaN crystal growth. In this work, I employed sapphire as a substrate. The ammonium (NH_3), two metalorganic sources, trimethylgallium (TMGa) and trimethylindium (TMIn), are the sources for nitrogen (N), gallium (Ga), and indium (In), respectively, deposited under hydrogen (H_2) or nitrogen (N_2) ambient. The Cp_2Mg and $Si(CH_3)_3$ are the common sources for p-type (Mg) and n-type (Si) dopants. The main controllable parameters for MOCVD are the temperature, the choice of carrier gases, and the V/III ratio of the ammonium gas to the metalorganic sources.

Because of the lattice mismatch between the substrate and InGaN, I deposited a thick GaN epi-layer on a low temperature buffer GaN layer (or nucleation layer) in order to reduce the threading dislocations and reduce the lattice mismatch between Sapphire and GaN [3]. However, a high defect density was generated of the order of 10^8 cm^{-2} even with the best GaN buffer layers.

I measured X-ray diffraction (XRD) to estimate the crystal quality, c- and a-lattices, and the growth mode by the full width at half maximum (FWHM) of the GaN and InGaN peaks on the XRD rocking curves. Each peak contains information about the thickness deposited (intensity of the signal) and the flatness between atomic layers (FWHM). The peak position via the 2θ-ω scan for the (002) plane gives information on the c-lattice parameter of the wurtzite structure, which is used to determine the amount of InN mole fraction inside the crystal from Vegard's law [4]. Information about the a-lattice is given by the peak position of the 2θ-ω scan for the (101) plane.

The difficulty of the InGaN growth lies in the fact that the high-temperature growth is necessary for high crystallinity but this high temperature enhances the evaporation of Indium. Thus, by reducing the temperature, higher In content is incorporated inside InGaN films. Due to this lower temperature, the growth rate of InGaN is much lower [about 3.3 nm/min (200 nm/h)] than that of GaN [about 25nm/min (~1.5μm/h)]. I underlined some critical points such as the carrier gases employed. For example, hydrogen used for GaN growth must be changed to nitrogen for InGaN growth in order to prevent the evaporation of Indium. I obtained a good crystal quality with a FWHM between 0.07 and 0.08 degrees for the (002) plane at a growth temperature of 1000ºC for GaN and at 790ºC for InGaN corresponding to an InN mole fraction of 0.10. I demonstrated that a more relaxed growth occurs at InN mole fraction higher than 0.10 underlined by a larger a-lattice, i.e. a larger base of the hexagonal crystal. Thus I deposited $In_xGa_{1-x}N$ with a high crystallinity from x = 0 to 0.10, corresponding to an optical bandgap from 3.4 to 3.0 eV.

I enhanced the electron mobility by optimizing the V/III ratio between the ammonium and the metalorganic sources. With an NH_3 flow of 7L/m (also noted sLm for standard liter per minute), I could achieve InGaN films with lower carrier concentration ($1\text{-}2\times10^{17}cm^{-3}$). This fact could be attributed to an optimal ratio on

surface between each atom and its neighbors which limits the defect generation and thus reduces unintended n-type materials. Due to this lower defect generation, the electron mobility is also affected and enhanced for higher InN mole fraction which is an important result for photovoltaic devices.

The time-resolved photoluminescence (TRPL) was used to estimate the lifetime of photo-generated carriers. The lifetime of 0.28 ns for $In_{0.09}Ga_{0.91}N$ and 0.05 ns for GaN films were measured at room temperature, which are longer than 0.1 ns for similar $In_{0.12}Ga_{0.88}N$ structures from [5]. A particular attention should be paid when using TRPL because the value can be overestimated due to the excitation of defect levels.

Regarding the crystal growth conditions, special care must be taken when the film is grown using Cp_2Mg for p-type doping. A critical thickness of p-InGaN at higher Mg concentration with a phase separation is observed, which is attributed to a bigger covalent radius of Mg atoms (0.130nm) compared with that of Ga atoms (0.126nm) and could increase the compressive strain inside the film [6].

I investigated other solutions to reduce the propagation of threading dislocations from the GaN epi-layer until the $In_xGa_{1-x}N$ on surface, and enhance the InN mole fraction, by fabricating multi-layer (ML) structures. I realized two types of multi-layer structures, AlN-GaN $(2nm/50nm)_{x10}$ and InGaN-GaN $(3nm/50nm)_{x10}$, before the $In_xGa_{1-x}N$ growth. These structures display a slightly enhanced InGaN crystal quality for In content around 10% with a very smooth surface (roughness of 1.44nm for scanned area of 25 μm^2), but do not prevent the formation of threading dislocation at higher In content.

I observed different carrier concentrations inside the $In_xGa_{1-x}N$ layer and the underlayer by capacitance-voltage measurement, with a carrier concentration of 1.5×10^{17} cm^{-3} for $In_{0.9}Ga_{0.91}N$. Therefore, the Hall Effect measurement is not accurate to determine the carrier concentration inside these structures because it can only give an average value for the overall specific carrier concentration.

2. Investigation of electronic structure for III-V nitride thin films by Hard X-ray photoemission spectroscopy

In photovoltaic devices the band offset is one of the crucial issues to design solar cell structures such as p-i-n junctions and to avoid any barrier which could affect the carrier lifetime. I employed Hard X-ray photoemission spectroscopy (HX-PES, measured at SPring-8) to determine the electronic structures of $In_xGa_{1-x}N$, GaN, and InN films. I characterized Ga_{3d}-In_{4d} , N_{1s}, C_{1s}, O_{1s} core levels, and the valence band spectra. Because of the high kinetic energy of electrons excited by hard X-ray (5.95keV), the detection depth is about 20 nm. By changing the angle between the X-ray and the normal of the sample surface (also called take-off angle, or TOA), the detection depth can be adjustable from 20 nm (“bulk” sensitive) to 10 nm (“surface” sensitive).

My analyses reveal a strong hybridization between Ga_{3d} and In_{4d} core levels when InN is alloyed with GaN. Furthermore at higher InN mole fraction, the valence band maximum (VBM) is shifted toward lower binding energy. I proposed a new approach to estimate the valence band maximum. I estimated a VBM of 2.1eV for GaN, which is more consistent with both the Schottky barrier height (SBH) and the build-in potential

evaluated at 1.2eV from C-V measurements. I estimated the band structures for $In_xGa_{1-x}N$ materials depending on the In content compared with the GaN band structure. For $In_{0.09}Ga_{0.91}N$ compared with GaN, a band offset of 0.2 eV between the valence band maxima is present which can reduce the mobility of photogenerated carriers, especially for holes. To avoid any band offset for photo-generated carriers, a homojunction *pn* InGaN is thus more suitable.

Because of the larger observation depth of HX-PES, the spectra contain both surface and bulk information reflecting the band bending on the surface. By modifying the detection depth, the core level N_{1s} was shifted toward lower binding energy, underlining an upward band bending near the surface for GaN films [7]. I confirmed a shift of the core level N_{1s} toward higher binding energy for InN films with a carrier concentration lower than $\sim 1.0\times10^{18}cm^{-3}$ for the first time, which underlines a downward band bending [8]. This downward band bending for the InN film can explain the difficulty in obtaining a Schottky junction by using this material. These results confirmed the importance of the band structure study for the interface and junction properties realized by using $In_xGa_{1-x}N$ films.

3. Fabrication of Schottky junction and investigation of defect levels inside GaN and InGaN films

a. By using transparent conductive polymers

To demonstrate the photovoltaic effect of n-GaN and n-$In_xGa_{1-x}N$ semiconductors, I fabricated a Schottky junction device using a transparent conductive polymer (TCP). I employed two TCPs: PEDOT:PSS and polyaniline, because of their high electron affinity (about 5.2eV, which is the same as gold), their good conductivity and their high transmittance for the solar spectrum of about 80% from 300 to 1500 nm. These TCPs are known as p-type organic materials and are electrochemically stable conjugated polymers [9]. I elaborated a new contact structure on GaN or $In_xGa_{1-x}N$ semiconductors, composed of the TCP and a thin Ti/Au front grid (20/20nm) deposited by an e-beam evaporator. With such a structure, I realized the Schottky junction with excellent properties.

For the n-GaN semiconductor, I obtained the best Schottky barrier height (SBH) of 1.15eV with a low ideality factor of 1.3 using PEDOT:PSS and compared it with a Schottky junction that I fabricated using a thin gold layer of 70Å instead. By using the front contact structure, I obtained a larger surface area of about $0.40cm^2$ and good photovoltaic properties with an improved fill factor to about 0.70. For the $In_xGa_{1-x}N$ semiconductors, I could also observe the photovoltaic properties, but they were weak. Nevertheless, I observed an enhancement of the external quantum efficiency for a wider spectral range of 300 to 420nm for $In_{0.11}Ga_{0.89}N$ compared with the GaN material (300 - 375nm), which shows the potential of $In_xGa_{1-x}N$ as an active layer in photovoltaic applications.

Deep level optical spectroscopy (DLOS) analysis was performed on my best Schottky devices using n-GaN. The signal obtained by the DLOS analysis comes from the variation of the electric capacitance of Schottky junctions. The deep level defects are filled with electrons with a certain bias voltage applied and they are then released by monochromatic excitation without a bias applied. This variation of capacitance is an unique signature

of a specific defect inside the material bandgap. I underlined an enhancement of Ga cation vacancies (V_{Ga}) or complexes associated with oxygen impurities (V_{Ga}-O_N) and shallow carbon acceptors (C_N) at the interface of the TCP and n-GaN films [10]. Unfortunately the signal obtained was weak and the specimens could also contain defects inside the polymer itself. To analyze in detail the deep level defects inside n-$In_xGa_{1-x}N$, I fabricated thick metallic contacts using Ti/Au layers (50/100 nm) and ohmic contacts using Ni/Au (50/100nm) deposited by an e-beam evaporator.

b. By using thick metallic contact

Until now there have been few reports concerning deep level defects in thick $In_xGa_{1-x}N$ films. Those defects could reduce the minority-carrier lifetime, increase the reverse saturation current and reduce the build-in potential of the junction in solar cells. In this work, thermal admittance spectroscopy (TAS), deep level transient spectroscopy (DLTS), and deep level optical spectroscopy (DLOS) were carried out for $In_{0.09}Ga_{0.91}N$ films that I deposited.

TAS measurement is a method that can detect defects located just below the conduction band (E_c). For my $In_{0.09}Ga_{0.91}N$ device, TAS revealed two defects at a level of E_c-7meV and E_c-108meV with low capture cross sections. By applying a bias voltage (i.e. changing the depletion layer), the defect level of E_c-7meV appeared to be homogeneously distributed in the InGaN layer, while the defects at E_c-108meV should be localized near the surface. The first defect could be attributed to an indium fluctuation and / or nitride vacancies (V_N), while the second one could reveal the presence of an interface state between electrodes and InGaN layers.

DLTS measurements, which can analyze deeper defects between E_c and E_v, could underline two other defects at E_c-22meV and E_c-0.6eV with a concentration of about $4\times10^{14}cm^{-3}$ for both of these defects. Because either TAS or DLTS technique could not explain the free carrier concentration of about $1.5\times10^{17}cm^{-3}$ present in the InGaN layer, DLOS analysis was also performed. I observed five photoemission states for $In_{0.09}Ga_{0.91}N$ detected at ~1.02 eV, ~1.70 eV, 2.07 eV (noted T3'), 2.70 eV, and ~3.05 eV (noted T5') in addition to the near-band-edge emission of InGaN and GaN at 3.2-3.4 eV. Compared with the five photoemission states already observed for GaN films, which were identified at ~1.4 eV, ~1.7 eV (dislocation-related defect), ~2.1 eV [T3: Ga vacancies (V_{Ga}; the $2^-/3^-$ transition level) and/or the V_{Ga}-O_N complex] ~2.8 eV (V_{Ga}-C_N complex), and ~3.05 eV [T5: shallow acceptor carbon (C_N)], the DLOS signal for the InGaN film was one order of magnitude higher. I found that the defects T3' and T5' were remarkably enhanced when alloying InN with GaN [11]. These defects contribute to enhance the electron concentration (unintended n-doping) up to about $10^{17}cm^{-3}$ for $In_xGa_{1-x}N$ and degrade the Schottky junction.

Therefore, to enhance the carrier lifetime and improve the junction quality, technological processes had to be developed to reduce or electronically passivate these deep level defects.

4. Photovoltaic properties of Schottky and *p-n* junctions of $In_xGa_{1-x}N$

The best photovoltaic conversion efficiency obtained by the *p-i-n* junction structure of InGaN materials is less than 2% [12], mainly because of the low crystal quality and the p-type doping. I successfully realized a homojunction *p-n* $In_{0.10}Ga_{0.90}N$ revealing the following photovoltaic properties: the V_{oc} is about 1.1 V and the J_{sc} about 0.6 mA/cm^2 with a fill factor of 62 %. To enhance the photovoltaic properties, an intrinsic layer i-InGaN was necessary. With a 150 nm-thick i-InGaN layer, the V_{oc} obtained was about 2 V, the J_{sc} about 0.9 mA/cm^2 with a fill factor of 72 %.

To compensate the unintended n-type material behavior, I fabricated Schottky devices using a Mg-compensated InGaN layer on surface. During the rapid thermal annealing (RTA) of the ohmic and Schottky contacts, Mg atoms were activated and they compensated the unintended n-type InGaN. I achieved a Schottky junction with the following good properties: a Schottky barrier height of 1.18 eV, an ideality factor of 1.07, with a low leakage current density of 10^{-8} mA/cm^2 at -4V bias. These enhanced properties clearly showed the ability of Mg to electronically compensate the defects present in the depletion layer of the Schottky junction. This fact may give a good perspective for future works to reach good *p-n* junction properties, because it is essential to know the diffusion profile of dopants inside the material. Indeed, secondary ion mass spectroscopy analysis revealed a high diffusion of Mg elements inside InGaN. A key point will be the precise control of the junction depth where the hole and electron concentrations are compensated for the realization of *p-n* homojunction InGaN.

To conclude, I have shown the capability of InGaN semiconductor for the photovoltaic application in this thesis. I successfully performed the analysis of the band structure and I revealed the presence of a band offset between the valence bands maximum of GaN and $In_{0.09}Ga_{0.91}N$ films. After optimizing the growth condition for InGaN epitaxial layers, I obtained promising photovoltaic properties of $In_{0.11}Ga_{0.89}N$ by using Schottky junction devices. This device had an extended solar-spectrum absorption from 300 to 430 nm. However the photovoltaic properties were limited because of the generation of defects when alloying InN into GaN. The main defects were successfully determined such as the cation vacancies (V_{Ga} and V_N) and their complexes associated with oxygen or carbon impurities. I found that the defects located below the conduction band at E_c-2.07 eV and E_c-3.05 eV were easily introduced by alloying InN with GaN for $In_{0.09}Ga_{0.91}N$ films. I also showed that the Mg-compensated InGaN layer on the intrinsic InGaN film enhanced the Schottky junction properties and reduced the reverse leakage current.

However the photovoltaic conversion efficiency of our devices is still limited under 1%. After the determination of defects presented in this work, further studies still need to be done in order to reduce the concentration of these defects or to passivate them electronically. For instance, the development of a rapid thermal annealing depending on the temperature and the ambient gas used, such as nitrogen or oxygen, related with the junction properties can open a path to post-fabrication processes for defects passivation. It may be another very interesting study to establish the correlation between the luminescent defects observed by cathodoluminescence and the rapid thermal annealing step used to clarify some defect properties depending on the ambient gas.

The present study was successful in understanding the nature of defects generated, and the band structure of InGaN materials. It opens a path to future processes of defects passivation that will enhance the InGaN material quality for photovoltaic applications.

References of Abstract

[1] J. Wu, W. Walukiewicz, K. M. Yu, J. W. Ager, E. E. Haller, H. Lu, W. J. Schaff, Y. Saito, and Y. Nanishi, "Unusual properties of the fundamental band gap of InN," *Applied Physics Letters*, vol. 80, no. 21, p. 3967, 2002.

[2] T. Nakao, T. Fujii, T. Sugiyama, S. Yamamoto, D. Iida, M. Iwaya, T. Takeuchi, S. Kamiyama, I. Akasaki, and H. Amano, "Fabrication of Nonpolar a-Plane Nitride-Based Solar Cell on r-Plane Sapphire Substrate," *Applied Physics Express*, vol. 4, no. 10, p. 101001, Oct. 2011.

[3] H. Amano, N. Sawaki, I. Akasaki, and Y. Toyoda, "Metalorganic vapor phase epitaxial growth of a high quality GaN film using an AlN buffer layer," *Applied Physics Letters*, vol. 48, no. 5, p. 353, 1986.

[4] M. D. McCluskey, C. G. Van de Walle, C. P. Master, L. T. Romano, and N. M. Johnson, "Large band gap bowing of In x Ga 1 x N alloys," *Applied Physics Letters*, vol. 72, no. 21, pp. 2725–2726, 1998.

[5] M. Smith, G. D. Chen, J. Y. Lin, H. X. Jiang, M. Asif Khan, and Q. Chen, "Time-resolved photoluminescence studies of InGaN epilayers," *Applied Physics Letters*, vol. 69, no. 19, p. 2837, 1996.

[6] L. Sang, M. Takeguchi, L. Woong, Y. Nakayama, M. Lozac'h, T. Sekiguchi, and S. Masatomo, "Phase Separation Resulting from Mg Doping in p-InGaN Film Grown on GaN/Sapphire Template," *Applied Physics Express*, vol. 3, p. 111004, 2010.

[7] M. Sumiya, M. Lozac'h, N. Matsuki, N. Ohhashi, K. Sakoda, H. Yoshikawa, S. Ueda, and K. Kobayashi, "Valence band structure of III-V nitride films characterized by hard X-ray photoelectron spectroscopy," *Physica Status Solidi (C)*, vol. 7, no. 7–8, pp. 1903–1905, 2010.

[8] M. Lozac'h, S. Ueda, S. Liu, H. Yoshikawa, S. Liwen, X. Wang, B. Shen, K. Sakoda, K. Kobayashi, and M. Sumiya, "Determination of the surface band bending in In x Ga 1− x N films by hard x-ray photoemission spectroscopy," *Science and Technology of Advanced Materials*, vol. 14, no. 1, p. 015007, Feb. 2013.

[9] N. Matsuki, Y. Irokawa, Y. Nakano, and M. Sumiya, "Pi-Conjugated polymer/GaN Schottky solar cells," *Solar Energy Materials and Solar Cells*, vol. 95, no. 1, pp. 284–287, 2011.

[10] M. Lozac'h, Y. Nakano, L. Sang, K. Sakoda, and M. Sumiya, "Fabrication of transparent conducting polymer/GaN Schottky junction for deep level defect evaluation under light irradiation," *Physica Status Solidi (a)*, vol. 210, no. 3, pp. 470–473, Mar. 2013.

[11] M. Lozac'h, Y. Nakano, L. Sang, K. Sakoda, and M. Sumiya, "Study of Defect Levels in the Band Gap for a Thick InGaN Film," *Japanese Journal of Applied Physics*, vol. 51, p. 121001, Nov. 2012.

[12] Y. Kuwahara, T. Fujii, Y. Fujiyama, T. Sugiyama, M. Iwaya, T. Takeuchi, S. Kamiyama, I. Akasaki, and H. Amano, "Realization of Nitride-Based Solar Cell on Freestanding GaN Substrate," *Applied Physics*, vol. 3, pp. 5–7, 2010.

Acknowledgments

I did my PhD study at National Institute for Materials Science (NIMS) in partnership with the University of Tsukuba thanks to the Doctoral Program in Materials Science and Engineering. I would like to acknowledge my Supervisor, Prof. Kazuaki Sakoda, Professor at the University of Tsukuba and Director of the Photonic Materials Unit at NIMS. I thank Prof. Sakoda who accepted me in his unit for his kind attention and numerous advices all along this work.

I acknowledge the Dr. Masatomo Sumiya who hosted me also in his group in the Environment and Energy Material Research Division inside NIMS, I wanted to thank him for his support, numerous advices and attention during my degree. I enter in contact with the Dr. Sumiya thanks to Prof. Etienne Gheeraert from the University Joseph-Fourier at Grenoble in France, so I wanted to thanks cheerfully Prof. Gheeraert here with Dr. Sumiya and Prof. Sakoda for the wonderful opportunity of doing my PhD study in Japan.

I am grateful for Prof. Takashi Sekiguchi, Prof. Naoki Futaka from NIMS, and Prof. Takeaki Sakurai of University of Tsukuba who accepted to form the graduation jury of my thesis. I thank these Professors very much for the great advices during my pre-defense.

I want to thank cheerfully Mrs. Kamisaka of Photonic Materials Unit and Mrs. Mabuchi of Environment and Energy Material Research Division who guided and helped me a lot through the different administrative procedures for NIMS, University of Tsukuba and my daily life. I also thank the International Student Center from the University of Tsukuba for all the useful information and accommodations.

All along my PhD study, I could meet and collaborate with many researchers in the group of Sumiya Sensei. I will remember all the moments we had together, especially with Fuke Sensei, Matsuki San, Ito San, Imura San, Mieno San, Akizuki San, Sang Liwen, Kubota San, Hanari San, Yamamoto San, Harada San, Ikeda San and Nakano San. I thank them all for the support, the advices along our work meetings and the very good times I had in their company during some dinners and events. I also thank Antoine Roehrich who brought a good ambiance and his “French touch” in our laboratory during his internship belong NIMS and the University of Grenoble (France) from May to August 2010.

From the group of Sakoda Sensei, I would like to thank Noda Sensei, Martin Elborg, and Yuanzhao Yao for their great discussions. It was a pleasure to meet them, and I will remember the good times passed together.

I also want to thank cheerfully all people who contribute and support me during my work at NIMS between Namiki and Sengen site: Benjamin Dierre, Tanaka Sensei, Elias Castel, Yiuri Garino, Ronit Prakash, Amir Pakdel, Martin Hollamby, Noelias Sanchez, Mehdi Estili, Komatsu Katsuyoshi, Julien Vieaud, Wim Van Rossom, Tanya Terentyeva, Marco Fronzi, Sara Romanazzo, Sun Yu, Noni Creasy, Lucie Szabova, Arnaud Le

Febvrier and Gaulthier Rydzek. They gave me many supports in different ways, and it was a great pleasure to share time and discuss together!

I acknowledge the professors from JST-ALCA project for supports and advices during this work: Nakano Sensei, Uedono Sensei, Honda Sensei and Hasegawa Sensei. More particularly, I am grateful to Nakano Sensei from Chubu University for the measurements and numerous discussions about defect levels.

I could make some measurements at AIST in collaboration with Dr. Koida San. I thank him for his time and support concerning the Hall effect measurement, the ITO deposition technique, the spectral response and the I-V simulator analysis.

Finally I want to thank all my friends I met in Tsukuba who directly or indirectly supported and motivated me during my PhD study. Tsukuba is a pretty small city and I saw a part of family in many of them. I wish all of them an accomplishment in their professional and personal life!

Last but not least, it is concerning my family. I spent a long time very far from my relatives, but I could feel a strong support and warm attention every time that I needed, so I thank them wholeheartedly! I send a special thanks to my brother who lives not so far in Tokyo. My last thoughts and thanks are for Kana the person who supported me the most and gave me the motivation during the hardest time of my thesis.

Table of contents

List of figures

List of tables

Chapter 1

1- Introduction and Purpose of Research

It was recently proposed that the bandgap engineering of $In_xGa_{1-x}N$ from 0.7 eV for InN [1] to 3.4 eV for GaN [2], covering most of the solar spectrum, will allow III-V nitride semiconductors to be used in photovoltaic applications [3]. While the technology of light emitting diodes (LEDs) based on III-V nitrides is well established, the operation mechanism of solar cells is quite different from that of LEDs. In photovoltaic devices, the

absorption of solar light, the generation of photo carriers and their separation, transportation and collection are all crucial factors. High-quality thick InGaN films (0.2~0.3μm) are required to maximize the absorption. It is also necessary to analyze different brakes on the charge transport such as defects and the band structure. While InGaN films of several nm in thickness have been used as quantum-well layers in LEDs, the knowledge and study are needed to provide thicker InGaN films for photovoltaic applications. In the following, I describe the main parts for my study:

- Deposition of thick InGaN films (0.2~0.3μm) with smooth surface, and control of the material bandgap with InN mole fraction in order to absorb enough solar light.
- Analysis of point defects and deep-level defects in InGaN films in order to form better junctions.
- Evaluation of the band structure and band alignment depending on the InN mole fraction in order to avoid a band offset affecting the carrier transportation at the interfaces between p-GaN/i-InGaN/n-GaN layers.
- Realization of devices to analyze the photovoltaic properties of Schottky junction, *p-n* homojunction, and *p-i-n* junction using InGaN films.

In this study, I have improved the $In_xGa_{1-x}N$ films and have evaluated both their electronic structures and defects for the development of photovoltaic devices.

1-1 Growth history of gallium nitride (GaN), indium nitride (InN), and their alloy InGaN

1-1.1 Gallium nitride (GaN)

Gallium nitride was firstly synthesized by Johnson et al. in 1932 [4]. In 1938 Juza and Hahn determined the crystal structure corresponding to the wurtzite structure [5]. In 1969, Maruska and Tietjen succeeded in growing GaN on a sapphire substrate by hybrid vapor phase epitaxy (HVPE) [2], and they clarified that GaN had a direct energy bandgap of 3.39eV.

Amano et al. achieved the first great advance in high-quality GaN growth by employing an AlN buffer layer (or nucleation layer) in 1986 [6]. The same team realized the second large progress in 1989 with the p-type doping control by using the bis-cyclopentadienylmagnesium (Cp_2Mg) and the properties of the GaN *p-n* junction LED were reported for the first time [7]. In this report, the characteristics of p-GaN were hole concentration of $2\times10^{16}cm^{-3}$, hole mobility of 8 cm^2/Vs, and resistivity of about 35 Ωcm.

Thanks to the improvement in the deposition technologies like the Metalorganic Chemical Vapor Deposition technique (MOCVD, also called metalorganic Vapor Phase Epitaxy MOVPE) and the Hybrid Vapor Phase Epitaxy technique (HVPE), three groups succeeded in growing high-quality GaN in a short period. The first group was Amano et al. in 1990 [8] who made the first observation of the room-temperature stimulated emission near UV from a GaN film grown by MOCVD on a (0001) sapphire substrate using an AlN buffer layer. The

second group was Nakamura et al. [9] who realized a new MOCVD system with two different flows. One was an inactive gas perpendicular to the substrate to change the direction of the reactant gas flow. N-type materials had a carrier concentration and Hall mobility of 1×10^{18} cm^{-3} and 200 cm^2/Vs, respectively. And the third group was Khan et al. in 1991 [10] who used low pressure MOCVD. The n-type GaN obtained had a carrier concentration and Hall mobility of about 10^{17} cm^{-3} and 350 cm^2/Vs, respectively, at room temperature. Khan et al. were the first group to publish a report of UV sensors based on as-deposited single crystal insulating GaN films in 1992 [11].

1-1.2 Indium nitride (InN)

The first attempt to synthesize InN was made by Juza and Hahn in 1938 [5]. They obtained InN from $InF_6(NH_4)_3$ and reported the crystal structure of InN to be wurtzite. Hovel and Cuomo had the earliest success in the growth of InN with some good electrical properties in 1972 [12]. They obtained polycrystalline InN films with highly preferred orientation grown on sapphire and silicon substrates at 25-600ºC by reactive RF sputtering.

The previously reported large values of the bandgap, 1.8 – 2.0 eV, were explained by oxygen contamination and the Moss-Burstein shift [13], [14], which will be explained in Chapter 2, because of high electron concentration inherent to this semiconductor. More recently in 2002, J. Wu et al. reevaluated the bandgap of the InN to be about 0.7 eV [1] by growing high crystal-quality wurtzite-InN with an AlN buffer layer on sapphire substrates by molecular beam epitaxy (MBE). Lu et al. grew an high crystal-quality InN on a 200 nm-thick AlN buffer layer by MBE, which had a Hall mobility above 800 cm^2/Vs and a low carrier concentration of 5×10^{18} cm^{-3} at 300 K [15]. Nanishi et al. obtained the same carrier concentration with a higher electron mobility of 1130 cm^2/Vs at room temperature by using RF-molecular beam epitaxy [16].

Thanks to the InN bandgap reevaluation, the spectral range of nitrides covers from the UV with AlN (6.2 eV, corresponding to 200 nm) to the infrared with InN (0.7 eV, 1770 nm), and includes the near UV with GaN (3.4 eV, 364nm) and the visible range with their alloys, InGaN or AlInN. Thus, the research to use InGaN films as active layers for photovoltaic materials was advanced.

High-quality InN films were achieved in 2006 by Wang et al. They studied the polarity of InN films and reported high-quality N-polar InN films [17], and In-polar InN films grown by MBE [18]. For N-polar InN films grown on GaN template, they found that the growth behavior depends strongly on the growth temperature, which greatly influences the surface morphology. Step-flow-like morphologies and spiral growth were observed at temperatures higher than 540ºC with low dislocation density. The N-polar InN films grown at 470-600ºC had a residual electron concentration of $3.5\times10^{18}cm^{-3}$ with a Hall mobility of 1400 $cm^2\ V^{-1}\ s^{-1}$ [17]. They also reported the step-flow mode growth for In-polar InN films on GaN template with a surface rms roughness less than 1nm over a $10\times10\ \mu m^2$ area. After considering the surface electron accumulation layer on Hall electron concentration of 1.2×10^{18} cm^{-3}, they estimated the residual electron concentration of bulk InN at about $5\text{-}6\times10^{17}cm^{-3}$. The Hall mobility was reported 1400 $cm^2\ V^{-1}\ s^{-1}$. For these In-polar InN films, the FWHM of the (002) ω-scan was as small as 350 arcsec, which was close to that of the GaN template [18].

1-1.3 Indium gallium nitride (InGaN)

The InGaN films were deposited for the first time in 1972 by Osamura et al. with the technique of a plasma generated by electron beam on two different substrates, sapphire and quartz [19]. The layers were polycrystalline and the bandgap of InN was estimated at 1.95 eV, which means that the quality of the material fabricated was not so high.

In 1991, Yoshimoto et al. observed the first photoluminescence of $In_{0.23}Ga_{0.77}N$ films grown on a (0001) sapphire substrate at 800ºC by MOVPE [20]. Yoshimoto et al. studied the effect of growth conditions on the carrier concentration and transport properties of $In_xGa_{1-x}N$ for an In composition $0.19 \leq x \leq 0.23$. They observed that if the deposition temperature was increased from 500 to 900ºC, InGaN films grown on (0001) sapphire had a reduction in the carrier concentration from 10^{20} to 10^{18} cm^{-3}, but the carrier mobility was increased from less than 10 to 100 $cm^2V^{-1}s^{-1}$ [20]. Yoshimoto et al. also observed that the indium mole fraction varied linearly with the group-III flow-rate ratio [TMI/(TMI+TEG)] ,where TMI stands for the flow-rate of trimethylindium and TEG for that of triethylgallium.

A major improvement of the InGaN film quality was obtained by Nakamura and Mukai in 1992 [21]. They discovered that the InGaN film quality could be significantly improved if a thick GaN epilayer (~2μm) is grown by MOCVD before the InGaN film on (0001) sapphire substrate. For the InGaN film deposition, Nakamura and Mukai used a temperature range between 830ºC to 780ºC with a high indium flow rate of 24μmol/min compared with the gallium flow rate of 2μmol/min. The indium content was 14 % at 830ºC and 24 % at 780 ºC.

Then, the InGaN films were developed for light emitting diodes (LEDs) with blue / green emission because of its bandgap variation depending on the indium mole fraction in an impressively fast way between 1990 and 2000 [22]. First high-brightness blue InGaN/AlGaN-double-heterostructure LEDs with a 500-Å-thick active layer of Zn-doped $In_{0.06}Ga_{0.94}N$ were developed in 1993 [23] and then, blue/green InGaN single-quantum-well (SQW) structure LEDs with a 30-Å-thick active layer of undoped $In_{0.45}Ga_{0.65}N$ were developed in 1995 [24].

Other optical devices were also achieved such as the UV InGaN/AlGaN-double-heterostructure LEDs using a 400-Å-thick active layer of undoped InGaN with an In composition of nearly zero [25]. An amber InGaN single-quantum-well structure LEDs were achieved with a 25-Å-thick active layer of undoped InGaN [26]. The peak of the emission spectra was 594 nm, but the exact In composition was not determined due to weak signal intensity in X-ray diffraction and photoluminescence measurements. The first violet laser light emission at room temperature was achieved with an InGaN-based multi-quantum-well (MQW) structure [27]. The InGaN MQW structure consisted of 26 periods of 25-Å-thick $In_{0.2}Ga_{0.8}N$ well layers and 50- Å-thick $In_{0.05}Ga_{0.95}N$ barrier layers. We should note that all these InGaN-based optical devices used very thin $In_xGa_{1-x}N$ layers.

These InGaN-based LEDs were fabricated by MOCVD on (0001) sapphire substrate at atmospheric pressure using a GaN buffer layer (300~400 Å) and a GaN epilayer (3~4 μm) before the growth of InGaN-based structure or InGaN/AlGaN-based heterostructures. These growths used trimethylgallium (TMG), trimethylaluminium (TMA), trimethylindium (TMI), monosilane (SiH_4), bis-cyclopentadienyl magnesium (Cp_2Mg) and ammonia (NH_3) as Ga, Al, In, Si (n-type doping), Mg (p-type doping), and N sources, respectively.

The emission wavelength of $In_xGa_{1-x}N$-based devices is tuned by adjusting the indium content *x* in the active layer. Despite such technological developments, the InGaN semiconductor alloy inside these light emitters is a poorly understood material from a fundamental point of view. Most of their properties were simply estimated from the two binary compounds, GaN and InN. In particular, the InGaN bandgap was expected to vary between 3.42 eV and 1.95 eV at room temperature.

Concerning the quality of the $In_xGa_{1-x}N$ films, S. Nakamura reported InGaN single-quantum-well (SQW) blue LEDs grown on sapphire substrates and on ELOG substrates [22]. "Epitaxially laterally overgrown GaN" on sapphire, denoted by ELOG, was developed to reduce the number of threading dislocations (TDs) in the GaN epilayers [28], [29]. The ELOG technique uses the lateral growth and coalescence of GaN homoepitaxial stripes over a SiO_2 mask. By using ELOG substrates, the thick GaN epilayer (26 to 80 µm for [28] and ~5 µm for [29]) had a low dislocation density of $\sim 6\times10^7 cm^{-2}$ compared to 10^9 to 10^{10} cm^{-2} range obtained for GaN epilayer grown on sapphire substrates. S. Nakamura reported that the InGaN (SQW) blue LEDs grown on sapphire substrates had a considerable amount of leakage current compared with the LEDs grown on ELOG substrates. S. Nakamura also clarified that the In composition fluctuation is not caused by threading dislocations.

Chichibu et al. [30], [31] and Narukawa et al. [32], [33] already reported the spatial inhomogeneities of In composition in InGaN, which may act as a quantum dot. In 1997, Singh et al. found a phase separation in thick InGaN films (> 0.3 µm) for In content higher than 30%, and realized InGaN films with In content up to 81 % using InGaN/GaN double heterostructures [34]. In 1999 Parker et al. determined the critical layer thickness in the InGaN/GaN heterostructures, which was 100 nm (65 nm) for InN mole fraction of 8 % (15%) [35].

In 2002, Wu et al. realized InN films with a high crystal-quality by molecular-beam epitaxy on (0001) sapphire substrates with an AlN buffer layer, and estimated the InN bandgap at between 0.7 and 0.8 eV [1], which was significantly smaller than values previously reported. Wu et al. also obtained high-quality In-rich $In_xGa_{1-x}N$ films ($0 \le x \le 0.5$) by molecular-beam epitaxy on (0001) sapphire substrates with an AlN buffer layer (~200nm) [36]. The growth temperature for $In_xGa_{1-x}N$ films was in the range of 470 to 570ºC. Wu et al. found that the bowing parameter of the $In_xGa_{1-x}N$ films ($0 \le x \le 0.5$) was about 1.43 eV [36].

Due to the reevaluated bandgap, InGaN films became also an interesting material for photovoltaic applications. But the growth technique for InGaN films established for LEDs is not sufficient for thicker InGaN films. The passive devices such as solar cells need higher crystal-quality. The knowledge on the nature and concentration of defects and the band structure is also missing.

1-2 Actual status of high efficiency solar cells

The highest conversion efficiency, about 38 %, is obtained for three-junction solar cells under one sun (i.e. without concentrator system) as presented by the National Renewable Energy Laboratory (NREL) [37]. These three-junctions are composed of different semiconductor materials (heterojunction) with higher bandgap on the

front surface and lower bandgap at the bottom of the solar structure in order to optimize the solar spectrum absorption. Because the three different semiconductors are stacked together, it is important that the photogenerated current match each other to avoid current losses, which is limited by the lowest current density among the three junctions. *Figure 1-1* presents the current density matched to 20 mA/cm^2 for each sub-cell. Thus, the material chosen must be close to 1.8 eV for the top surface, 1.2 eV for the middle layer, and 0.7 eV for the bottom layer. For example, Spectrolab Inc. from the Boeing company uses the germanium (Ge, 0.67 eV) for the bottom cell, gallium indium arsenide (GaInAs, 1.3-1.4 eV) for the middle cell, and the gallium indium phosphide ($GaInP_2$, 1.8-1.9 eV) for the top cell [38].

To improve these devices, finding materials with the required bandgap becomes a major challenge. The InGaN films would allow fine tuning in optimization of the performance of possible four-junction or higher solar cells by offering flexibility in the choice of the bandgap [39]. Theoretical simulations for a six-junction InGaN solar cells could reach a conversion efficiency of about 40.3 % under one sun using the following bandgaps from the top to the bottom layers: 2.25, 1.79, 1.47, 1.19, 0.95 and 0.7 eV [39].

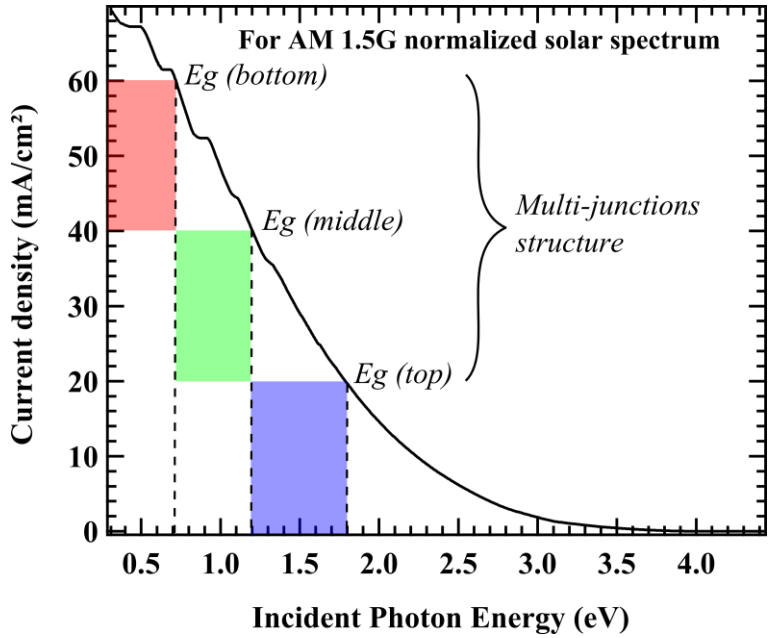

Fig. 1-1: Current density engineering for each sub-cell to match the solar spectrum for a three-junction solar cell.

1-3 Use of $In_xGa_{1-x}N$ films as active layers for solar cell devices

InGaN materials for solar cell devices are still in an early stage. The material quality needs to be firstly enhanced in order to control the junction quality. In the following part, I will describe the advantages of InGaN films for active layers in solar cell devices, the necessary conditions to be reached, a concrete application of $In_xGa_{1-x}N$, and a overview of the present solar cell structures using InGaN films.

1-3.1 Advantages of InGaN films

The greatest advantage of InGaN films concerns its tunable bandgap from 0.7 (InN) [1] to 3.4 eV (GaN). The wide bandgap range of $In_xGa_{1-x}N$ with indium mole fraction range $0 < x < 1$ covers almost the full solar spectrum as presented in *Fig. 1-2*. Compared with other semiconductor materials with a fixed bandgap value [except CuInGa(Se,S)], InGaN covers the largest spectrum range. The InGaN films can be used in the thin-film solar cell technology because $In_xGa_{1-x}N$ displays a direct bandgap for all the InN mole fraction range, which allows the absorption of the solar spectrum within a thin film. This material also shows a high resistivity to radiation, which makes a good choice for concentrator systems or for photovoltaic energy supply in space applications.

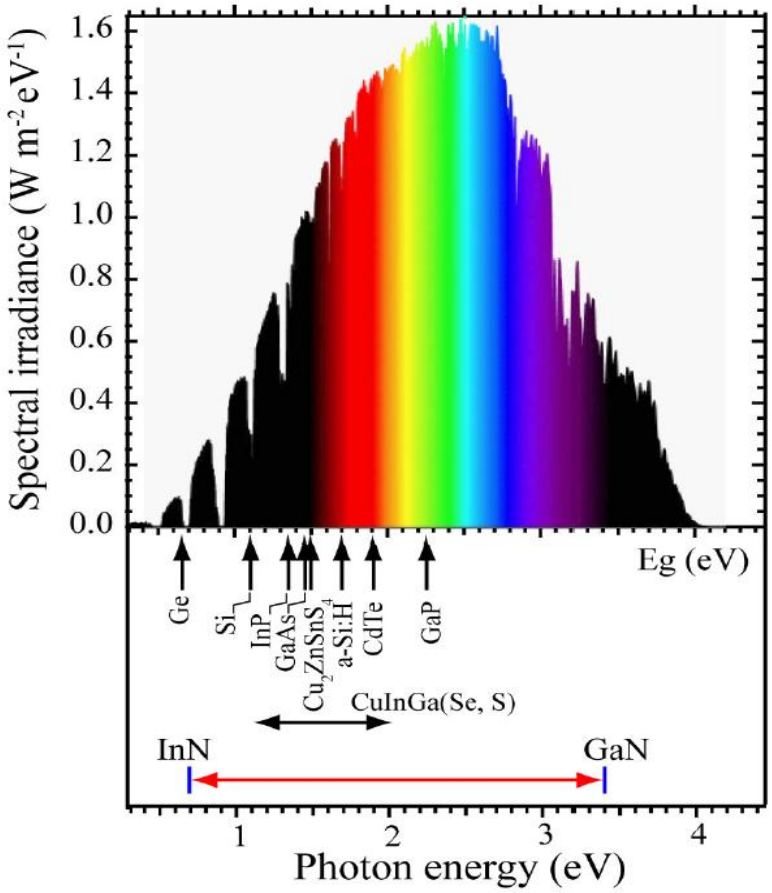

Fig. 1-2: Spectral irradiance of the normalized solar spectrum AM1.5G, and the bandgap of different semiconductors.

1-3.2 Necessary conditions

a) Crystal quality of III-V nitride films

The conditions necessary to use InGaN films as an active layer for photovoltaic devices can be just summarized by a good material quality free from dislocations. This is quite hard to realize in reality. Indeed the III-V nitride films show an unintended n-type material with a high electron concentration in the range of 10^{17} to 10^{18} cm^{-3}. This high carrier concentration is attributed to a high density of defects inside the grown films. These defects mainly come from a large lattice mismatch with the sapphire substrate, which is the principle substrate used for the growth of III-V nitride films. The c- and a-lattice constants correspond to the column lattice and the hexagonal base lattice of the wurtzite crystal. These lattice constants are presented in *Table 1-1* for AlN, GaN, InN, and compared with sapphire's lattice constants at 300 K.

Table 1-1: Lattice constants of III-V nitride crystal compared with sapphire at 300 K.

	AlN	GaN	InN [40]	Sapphire (Al_2O_3)
a-lattice (Å)	3.11	3.189	3.54	4.758
c-lattice(Å)	4.98	5.185	5.70	12.991
Band gap (eV)	6.2	3.4	0.7	9.9

The defects can also be generated because of the large difference in the thermal expansion coefficient between the grown film and the substrate, which is presented in *Table 1-2*.

Table 1-2: Thermal expansion coefficients for a- and c-lattice direction of III-V nitride crystal compared with sapphire.

Thermal expansion coef. for	AlN [41]	GaN [41]	InN [41]	Sapphire (Al_2O_3) [42]
a-lattice, α_a ($\times 10^{-6}$ K^{-1})	from 3.0 (273 K) to 7.1 (1800 K)	from 4.2 (273 K) to 5.3 (1100 K)	from 3.0 (273 K) to 3.8 (600 K)	~ 5.0 (from 20 to 1000 K)
c- lattice, α_c ($\times 10^{-6}$ K^{-1})	from 2.2 (273 K) to 6.1 (1800 K)	from 3.8 (273 K) to 4.6 (1100 K)	from 4.0 (273 K) to 5.8 (600 K)	from 6.7 (20 K) to 9.0 (1000 K)

Both the large lattice mismatch and the large difference of the thermal expansion coefficient between the sapphire substrate and the grown III-V nitride films generate a high density of defects. The necessary condition concerning the InGaN quality is to reach an unintended n-type doping level of about 10^{16} cm^{-3} by realizing the low defect density.

b) Critical thickness of InGaN films

The light emitting diode (LED) technology was the first to find an application of the III-V nitride films. $In_xGa_{1-x}N$ films as active layer were developed because of their bandgap modulation with the InN mole fraction *x*. As active devices, in which an external current is necessary, a thin film of a few angstroms or nanometers is sufficient to produce a light emission. For example, T. Egawa et al. used an active layer composed of an InGaN MQW structure [43], [44] with 3 nm-thick $In_xGa_{1-x}N$ wells and 5 nm-thick $In_yGa_{y-1}N$ barrier layers. The typical indium content (In content) of the wells was 17% and 23 % for the blue and green LED, respectively [43].

For the application to solar cell devices, the InGaN film must be 200 to 300 nm thick in order to absorb the solar spectrum efficiently. The critical thickness of an epitaxial layer is defined by the thickness where a transition from the strained growth to the partially relaxed growth occurs. The difference of mechanical properties between GaN and InN materials is also responsible to the critical thickness of InGaN films. There is s difference of Young's modulus between GaN layer estimated at 210±23 GPa [45] and InN layer estimated at 149±5 GPa along *a*-axis [45]. The stiffness matrix elements C_{ij} (ij = 11, 12, 13, 33, 44) are also quite different between GaN and InN materials as *Table 1-3* presents [46].

Table 1-3: Statistical values from literature data which provides complete experimental or theoretical sets of the stiffness matrix elements C_{ij}.

Wurtzite crystal	C_{11} (GPa)	C_{12} (GPa)	C_{13} (GPa)	C_{33} (GPa)	C_{44} (GPa)
GaN	374±4	138±4	101±4	395±5	98±3
InN	237±7	106±4	85±3	236±6	53±3

Below the critical thickness, the epitaxial layer has the same a-lattice constant as the substrate, these layers are called pseudomorphic. The critical thickness depends strongly on the discrepancy of a-lattices between the grown layer and the substrate, on the growth technique, and on properties of the deposited materials.

Figure 1-3 describes the critical thickness of the $In_xGa_{1-x}N$ on GaN layer as a function of the In content x obtained by experiments [35] and by theoretical calculation [47]. The critical thickness of InGaN decreases when the indium content increases. From experimental values [35], the critical thickness of $In_{0.1}Ga_{0.9}N$ is about 100 nm, whereas it is about 60nm for $In_{0.2}Ga_{0.8}N$. This critical thickness value is much smaller than the one necessary to absorb the solar spectrum, that is, 200 or 300 nm. This means that thicker $In_xGa_{1-x}N$ films generate more dislocations, and especially at higher InN mole fraction. Thus, the challenge to use $In_xGa_{1-x}N$ films for photovoltaic devices is to find a good compromise between the crystal quality and its thickness in order to absorb the solar spectrum efficiently.

In this study, I developed multi-layer structure InGaN/GaN to bypass the problem of the critical thickness and to avoid the propagation of threading dislocations to the upper $In_xGa_{1-x}N$ layer while optimizing the $In_xGa_{1-x}N$ film growth.

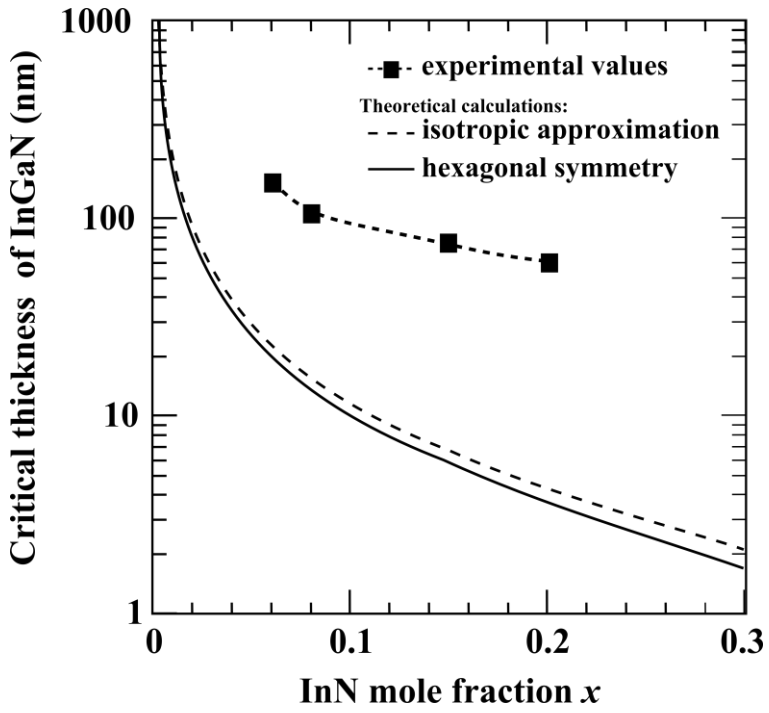

Fig. 1-3: Experimental values [35] and theoretical calculations [47] of the critical thickness of $In_xGa_{1-x}N$ films as a function of the InN mole fraction x for InGaN/GaN single-layer system. Experimental results used (0001) sapphire substrate to grow a GaN epilayer (1μm) followed by $In_xGa_{1-x}N$ growth.

1-3.3 Application of $In_xGa_{1-x}N$ films in solar cell structures

Even if it is still difficult to have a high crystal quality for InGaN with a high In content, $In_xGa_{1-x}N$ material can be used to enhance the global conversion efficiency of a multi-junction solar cell structure. Indeed, a sub-cell with $In_xGa_{1-x}N$ as active layer can be inserted on the top of three-junction solar cells to absorb the solar spectrum at shorter wavelengths. The global conversion efficiency will be higher than a high-efficiency three-junction solar cell, which had reached a conversion efficiency of 40.8% by using GaInP for the top cell and InGaAs for the middle and bottom cells [48]. Of course the photocurrent generated by the InGaN film will produce a current density lower than 20 mA/cm^2, so the InGaN film must be electrically isolated by using a four-terminal solar cell structure as represented in *Fig. 1-4*. The $In_xGa_{1-x}N$ film is optically coupled to the three-junction solar cell at the bottom. By increasing the InN mole fraction, the $In_xGa_{1-x}N$ film will absorb the solar spectrum at longer wavelengths. This will generate a shadow to the three-junction solar cell. However, by using high crystallinity InGaN, the global conversion efficiency of such structure will be enhanced [49]. The global conversion efficiency is enhanced by using an InGaN film on the top of the structure (*Fig. 1-5* of Ref. [49]). The conversion efficiency of the three-junction solar cell decreases due to the shadow of the InGaN film (absorbed photons).

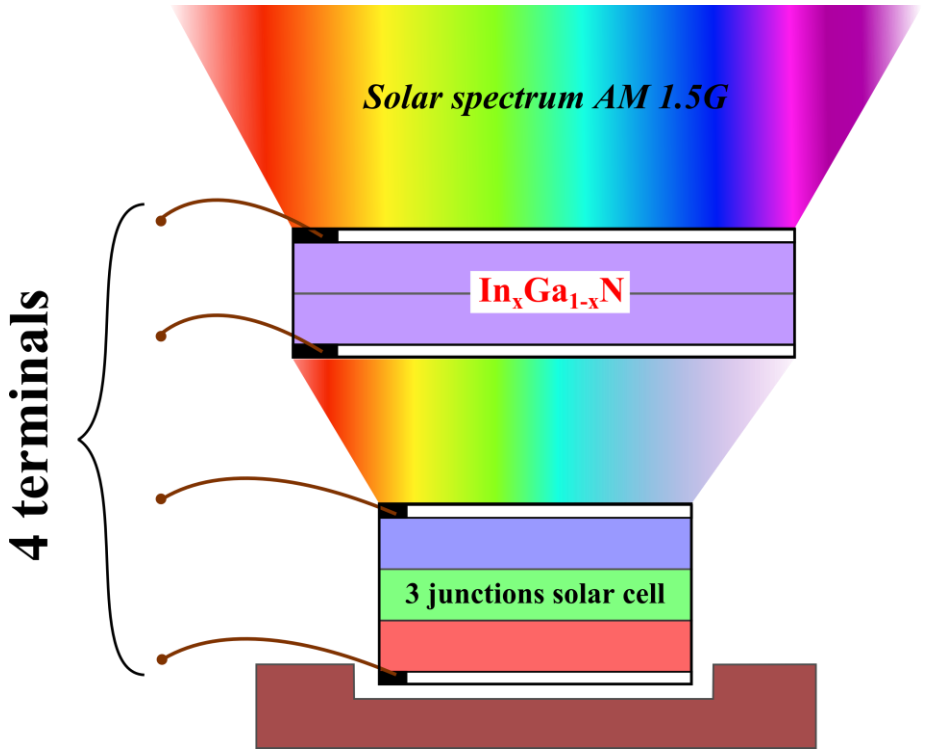

Fig. 1-4: Structure of a four-terminal solar cell using an $In_xGa_{1-x}N$ film on the top to absorb the short wavelengths of the solar spectrum.

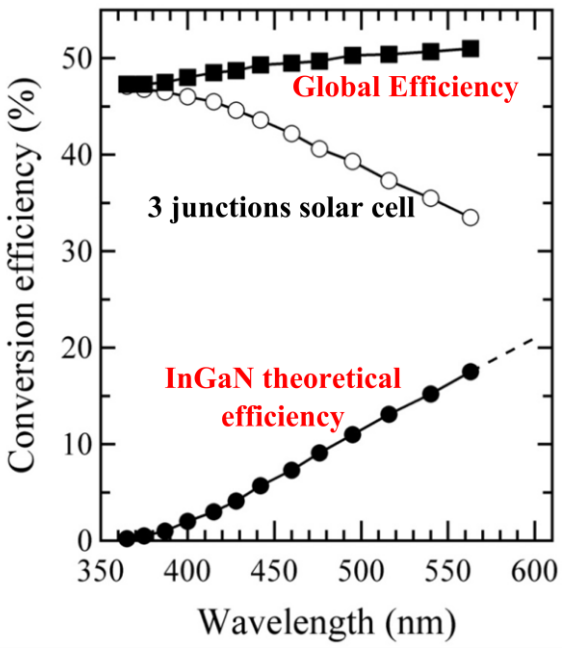

Fig. 1-5: Theoretical conversion efficiency of a four-terminal solar cell structure using an InGaN film on the top [49].

1-3.4 Present solar cell structures using InGaN as an active layer

I summarized in *Table 1-4* the actual structures of solar cells using InGaN films as an active layer. There are mainly two kinds of structures used: the multi quantum-wells (MWQs) InGaN and the *p-i-n* structure using an intrinsic InGaN layer (i-InGaN) between n- and p-type GaN layers.

Table 1-4: Actual situation of solar cell structures using InGaN film as active layer. The photovoltaic properties are presented with the open-circuit voltage (V_{oc}), the short-circuit current (J_{sc}), the fill factor (FF) and the conversion efficiency (η).

Structure	V_{oc} (V)	J_{sc} (mA/cm^2)	FF (%)	η (%)	Light	Reference
p-GaN (300nm)/ i-$In_{0.12}Ga_{0.88}N$ (60nm)/ n-GaN	1.89	1.06	78.6	1.57	AM 1.5G	[50] (2011)
p-GaN (100nm)/ i-$In_{0.11}Ga_{0.89}N$ (200nm)/ n-GaN	2.0	0.83	75.2	1.20	AM 1.5G	[51] (2011)
p-GaN (15nm)/ p-InGaN (90nm)/ i-$In_{0.15}Ga_{0.85}N$ (240nm)/ n-InGaN (150nm)	1.50	1.25	56	1.05	AM 1.5G	[52] (2011)
p-GaN (100nm)/ 50 MQWs $In_{0.17}Ga_{0.83}N$ (3nm)/ $In_{0.07}Ga_{0.93}N$ (0.6nm)/ 10 MQWs $In_{0.1}Ga_{0.9}N$ (3nm)/n-GaN (3nm)	1.78	3.08	70.8	2.5	AM 1.5G	[53] (2011)
p-$In_{0.14}Ga_{0.86}N$ (100nm)/ i(n)-$In_{0.14}Ga_{0.86}N$ (300nm)	1.79	0.99	52	0.71	AM0	[54] (2010)
p-GaN (200nm)/ 30 MQWs $In_{0.13}Ga_{0.87}N$ (2nm)/ GaN (5nm) /n-GaN	2.18	0.54	63	0.73	AM 1.5G	[55] (2010)
p-GaN (200nm)/ 9 MQWs $In_{0.3}Ga_{0.7}N$ (3nm)/ GaN (17nm) /n-GaN	1.95	0.83	30	0.48	AM 1.5G	[56] (2009)
p-GaN (20nm)/ i-$In_{0.02}Ga_{0.98}N$ (50nm)/ i-$In_{0.12}Ga_{0.88}N$ (150nm)/ n-$In_{0.02}Ga_{0.98}N$ (200nm)/n-GaN	1.34	1.66	64	1.42	UV	[57] (2009)
p-$In_{0.19}Ga_{0.81}N$ (60nm)/ 28 MQWs $In_{0.25}Ga_{0.85}N$ (30Å)/ GaN (40Å) /n-GaN	1.38	0.8	55	0.61	AM 1.5G	[58] (2009)
p-GaN (80nm)/ 5 MQWs i-$In_{0.4}Ga_{0.6}N$ (1nm)/ GaN (14nm) /n-GaN	0.5	0.11	51	0.03	UV	[59] (2005)

a) Multi quantum-well (MQW) structures

The MQW structure is a technology already well established by the Light Emitting Diode (LED) technology. This structure consists of an assembly of very thin layers of two materials with different bandgaps, and the active region which absorbs the solar spectrum is enhanced by increasing the number of layers (*Fig. 1-6*). For the MQW structure using InGaN layers, GaN layers or InGaN layers with low indium content are generally used for the layer with a larger bandgap. Due to the small thickness of each InGaN layers (1~3nm), it is possible to grow high crystal quality even with higher InN mole fraction [53].

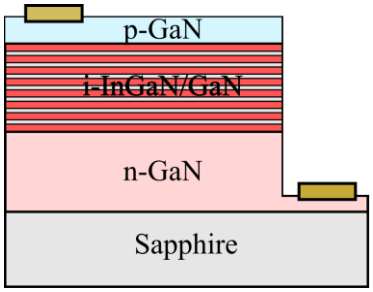

Fig. 1-6: Example of a MQW structure using i-InGaN as active layers separated by a GaN layer.

MQW structures can absorb low-energy photons that the material bandgap cannot utilize due to intraband transitions inside the quantum wells [60]. The width and depth of the quantum wells determine the absorption edge and the spectral response of the MQW solar cells [61].

Kuwahara et al. obtained the highest efficiency of 2.5 % under one normalized solar spectrum (AM 1.5G) using InGaN film and MQWs structure on GaN substrate to reduce the lattice mismatch [53] to the sapphire substrate. This conversion efficiency for $In_{0.17}Ga_{0.83}N$, corresponding to a bandgap of 2.8 eV and a wavelength of 440 nm, is still much lower than the theoretical efficiency estimated at 6% from *Fig. 1-5*.

The MQWs structure has many interfaces, and each interface can also have a bad effect on the transportation of the photogenerated carriers. Thus it is also important to develop and enhance the quality of InGaN film to use it for thick active layers.

b) *p-i-n* junction structure

In *p-i-n* junction structure, the intrinsic i-InGaN layer has a typical thickness between 200 and 300 nm (*Fig. 1-7*). This intrinsic layer is necessary to absorb the solar spectrum and to enlarge the depletion layer between p-GaN and n-GaN. Since the i-InGaN layer is still a strongly unintended n-type-doped material due to the presence of defects, p-GaN and n-GaN layers with higher crystal quality are used to reach a good ohmic contact with the deposited metals.

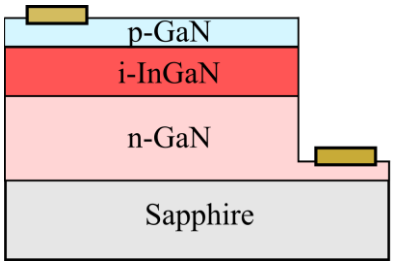

Fig. 1-7: Example of p-i-n junction structure using InGaN as active layer.

Recent *p-i-n* junction solar cells show good photovoltaic properties. For example, Shim et al. obtained a conversion efficiency of 1.2 % under one normalized solar spectrum (AM 1.5G) using an 200-nm-thick intrinsic $In_{0.11}Ga_{0.89}N$ active layer [51]. This conversion efficiency is lower than the theoretical conversion efficiency expected, about 4%, thus other studies to understand the current losses are necessary.

c) *p-n* homojunction structure

The photovoltaic properties of *p-n* InGaN homojunction (*Fig. 1-8*) can be analyzed if a high crystal quality is obtained. However, this structure required a large depletion layer and the InGaN film is a strongly unintended n-type doped material with a carrier concentration of 10^{17} to 10^{18} cm^{-3}. Therefore, it is first necessary to reduce by one or two orders of magnitude this carrier concentration to have a better control of the n-type and p-type doping. This control is necessary to optimize the doping concentration profile, which will enhance the *p-n* homojunction property.

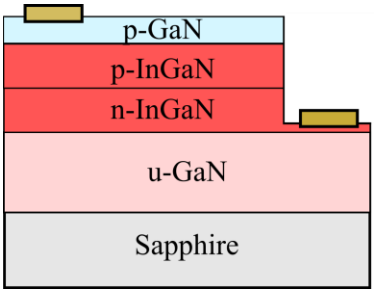

Fig. 1-8: Example of p-n homojunction structure using InGaN as active layer.

The photovoltaic properties of the p-n junction are still poor because of recombination centers inside InGaN films and also because of the difficulty of p-type doping with a high hole concentration. Even if a 0.9-µm-thick GaN epilayer were deposited on (0001) sapphire substrate before InGaN layers, the *p-n* homojunction fabricated in [62] shows poor photovoltaic properties under 360 nm illumination: V_{oc} = 0.43 V, J_{sc} = 3.4×10^{-2} mA/cm^2, and a fill factor, FF = 0.57. To form the p-InGaN layer, nitrogen-ambient thermal annealing at 800ºC was performed for 4min, the p-type $In_{0.18}Ga_{0.82}N$ has a hole concentration of about $4\times10^{18}cm^{-3}$ with a hole mobility below 10 cm^2 V^{-1} s^{-1}. The electron concentration of n-type $In_{0.15}Ga_{0.85}N$ layer was above 10^{19} cm^{-3} with a

mobility above 100 $cm^2\ V^{-1}\ s^{-1}$. This underlines a low J_{sc} due to poor quality of the n-InGaN film with high electron concentration, which is also a brake to the p-type doping.

B. Jampana et al. fabricated a *p-n* InGaN homojunction by MOCVD on (0001) sapphire substrate [63]. After a 350-nm-thick n-GaN epilayer, the carrier concentration of the 45-nm-thick n-$In_{0.16}Ga_{0.84}N$ layers is estimated at $1.03\times10^{18}cm^{-3}$ with a mobility of 342 $cm^2\ V^{-1}s^{-1}$. The p-type dopant was activated at 650ºC for 20min under N_2 ambient. The hole concentration of the 45-nm-thick p- $In_{0.17}Ga_{0.93}N$ is estimated at $1.16\times10^{18}\ cm^{-3}$ with a mobility of 1208 $cm^2\ V^{-1}s^{-1}$. A concentrated AM 1.5 illumination is used to observe the photovoltaic properties: V_{oc} = 1.47 V, J_{sc} = 0.26 mA/cm^2, and a FF = 57%. The V_{oc} value is quite high due to the utilization of a concentrator system. I noticed that even if the hole mobility was quite high in this structure due to a longer annealing time probably, the photovoltaic properties were largely lower than the *p-i-n* InGaN junction solar cell. Thus it is necessary to analyze the defect generation inside thick InGaN in order to understand the possible recombination centers present which limit the conversion efficiency.

1-3.5 Issues of InGaN films for photovoltaic application

As I presented previously, there is still a large discrepancy between the theoretical conversion efficiency of the InGaN films depending on the In content (*Fig. 1-5*) and the actual efficiency obtained with different solar cell structures (*Table 1-4*). In this section, I will present the issues of InGaN films which is necessary to study in order to use those films for photovoltaic application. First, I will present the challenge to grow thick InGaN at high InN mole fraction. The defects present inside InGaN films can contribute to recombination centers for photogenerated carriers. I will describe the defects observed for GaN material because few studies have been performed for InGaN films. A barrier potential inside the band structures of heterostructure can also be the source of carrier recombination or low mobility. I will describe the X-ray spectroscopy analysis realized on GaN, InN and their alloy InGaN films. A junction generating a depletion layer is necessary to analyze the photovoltaic properties but also the defect-levels present inside the material. A Schottky junction can be used to generate this depletion layer, without p-type doping, which simplifies the devices. A presentation of the Schottky junction properties obtained on InGaN films will also be described.

a) Growth of thicker films

The growth of InGaN films by MOCVD is realized on GaN thick epilayer between 1.5 and 2 µm grown on sapphire substrates. As the cross sectional SEM image in *Fig. 1-9* shows, a 0.5-µm-thick InGaN presents two different growth modes with a phase separation [64]. The InGaN (1) layer is strained with the GaN epilayer and the InGaN (2) is relaxed and more crystallographic defects are generated. The Indium content inside InGaN (1) is about 6.9 %. Because of the relaxed growth mode, a higher indium content around 11.2 % is present in the InGaN (2) layer.

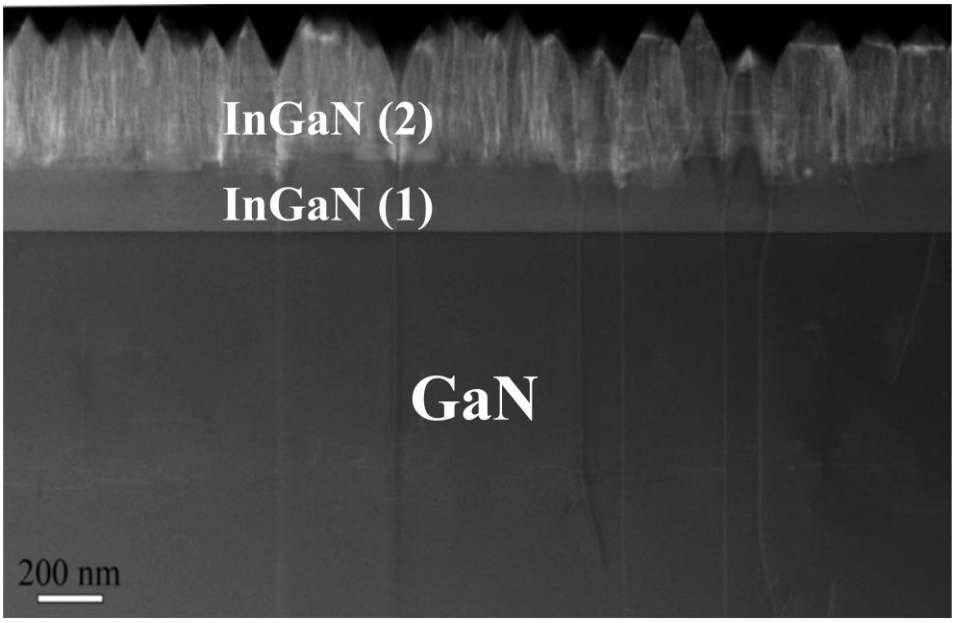

Fig. 1-9: Cross sectional SEM image of InGaN/GaN film grown on sapphire substrate (scale 200 nm) [64].

El-Masry et al. also reported a phase separation in 0.5-µm-thick InGaN films with an InN mole fraction up to 0.5 grown by MOCVD at 690 to 780ºC [65]. Single phase InGaN was obtained for the as-grown films with an InN mole fraction lower than 0.28.

The dislocations inside the GaN are propagated through the InGaN layer where more dislocations are generated resulting in a rough surface. It will be thus important to control the InGaN thickness and find a compromise in order to absorb the solar spectra and to keep higher crystallinity with a smooth surface.

b) GaN films and deep-level defects associated

There is still not enough information about the defects and deep levels generated when alloying InN with GaN. Meneghini et al. reported the deep levels involved inside InGaN-based laser diode emitting at 405 nm [66]. Defect levels, located at 0.35-0.45 eV below the conduction band, were reported by deep-level transient spectroscopy (DLTS). These defects are related to thin layers of InGaN inside the multi-quantum-well structure of the LED, but no information is found about the deep-level defects inside a thick InGaN film.

However the defects and deep levels associated inside the GaN layer have already been investigated. Two Main defects were observed for the GaN layer, located at 0.20 meV, or 0.20-0.35 eV below the conduction band. Although their nature is still controversial, these defects could be related to nitride vacancies (V_N) [67], [68]. The other defect located at 0.5-0.62 eV below the conduction band is the deepest defects for GaN and was already often reported with different descriptions such as a point defect nature [69] or an isolated defect probably related to the gallium vacancies (V_{Ga}) [70]. However, the nature of defects is also difficult to determine precisely because of the generation of complex impurities of V_{Ga} or V_N associated with oxygen or carbon. I will summarize the main

parameters (localization, concentration, capture cross section) of deep-level defects reported by previous studies in Chapter 5 *Table 5-3*.

The gallium vacancies (V_{Ga}) and nitride vacancies (V_N) are known to contribute to unintended n-type GaN materials. It is important to study these deep levels in order to know about their concentration and their nature. In this way, new techniques can be developed to reduce their concentration or to passivate these defects electronically. Furthermore, for photovoltaic application, the junction quality is a crucial point to improve the properties. If some defects are present, the depletion layer will be reduced (*Fig. 1-10*), which will decrease the open-circuit voltage (V_{oc}), the shunt resistance and the conversion efficiency.

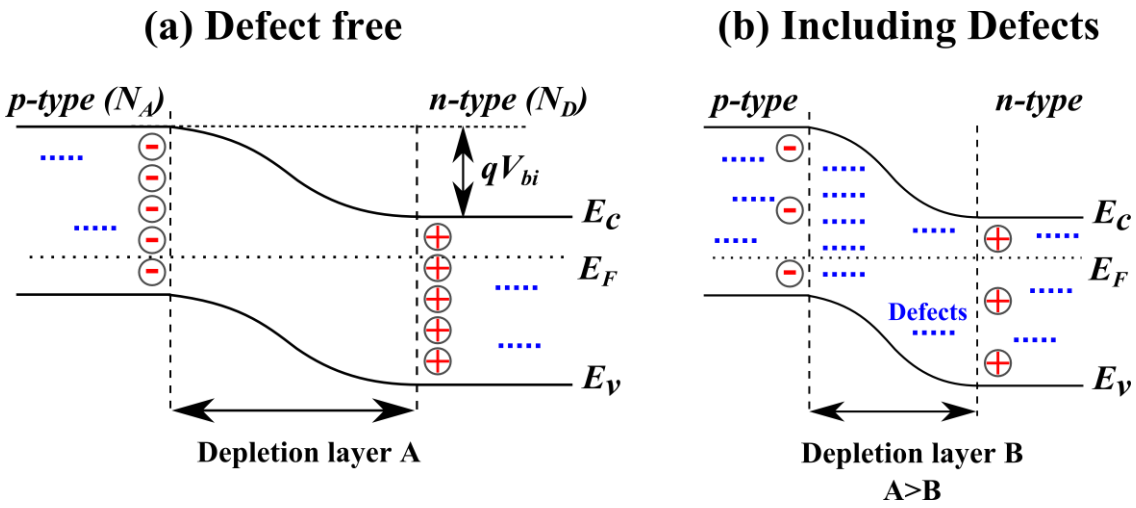

Fig. 1-10: Illustration of the depletion layer width with and without the presence of defects inside.

c) X-ray photoemission spectroscopy for band offsets and band alignments

Another crucial issue is the carrier transportation when considering a heterojunction material. As *Fig. 1-11* presents, the band alignment between p-GaN and i-InGaN needs to be investigated because of the presence of a barrier. This barrier can be a brake for photogenerated carrier, and especially for the hole transportation with a lower mobility than electron. Therefore, the determination of the valence band maximum (VBM) depending on the InN mole fraction needs to be evaluated.

Veal et al. already reported the InN mole fraction *x* dependence of the Fermi-level pinning at the oxidized (0001) surfaces of n-type $In_xGa_{1-x}N$ films with an InN mole fraction range of $0 \leq x \leq 1$ [71], and $0.39 \leq x \leq 1$ [72], by using high resolution X-ray photoemission spectroscopy (XPS). They observed a shift of the valence band maximum (VBM) to lower binding energy when the InN mole fraction increases. For InN films, they reported a VBM at 1.34±0.20 eV below the Fermi level (E_F) with a bandgap estimated at 0.7 eV for InN films. This VBM position means that the conduction band minimum (CBM) is located at 0.76 eV also below the E_F. Veal et al. reported that the E_F is located above the CBM for $In_xGa_{1-x}N$ films with an InN mole fraction range $0 \leq x \leq 0.3$.

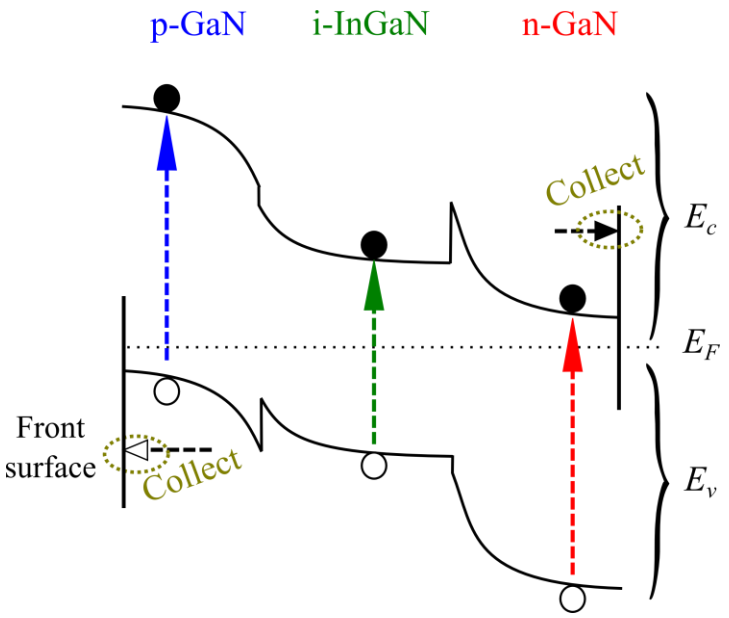

Fig. 1-11: Schema of the depletion layer width with and without the presence of defects inside.

The free electron densities reported have a range from 3×10^{19} cm^{-3} to $1\times10^{18}cm^{-3}$, with an electron mobility range from 20 to 950 cm^2 V^{-1} s^{-1}. These free electron densities are quite high with poor mobility at high concentration which could indicate a high defect concentration. Furthermore, a tail on the valence spectrum could indicate a possible wrong evaluation of the VBM.

In this study, I measured the valence band spectra of $In_xGa_{1-x}N$ at various InN mole fractions and I estimated the VBM by using a hard x-ray photoemission spectroscopy to clarify the effective position of the E_F depending on the InN mole fraction.

d) Schottky junction on InGaN films

Schottky junction devices are employed to fabricate a depletion layer. The main advantage of such devices is that the formation of a p-type doped layer is not necessary. I described previously the difficulty to control the p-type doping for InGaN films due to their high unintended n-type material.

Previously Schottky solar cell devices using the PANI (polyaniline) as transparent conductive polymers on n-GaN were fabricated [73]. These devices revealed high Schottky properties with a Schottky barrier height of 1.28 eV and an ideality factor of 1.22. These devices also revealed a high V_{oc} of 0.70 V, a J_{sc} of 6.7×10^{-1} mA/cm^2, with a poor fill factor of 0.57 under AM 1.5 illumination. The poor fill factor obtained was the result of a high series resistance of the devices.

Another TCP, the PEDOT:PSS, was also reported to fabricate Schottky solar cell devices on n-GaN [74]. The Schottky properties of the PEDOT:PSS/n-GaN devices revealed a low reverse leakage current less than $10^{-8}A/cm^2$ compared with the PANI/n-GaN devices of about 10^{-7} A/cm^2 at -3 V. Thus the V_{oc} of the

PEDOT:PSS/n-GaN could reach 0.7 – 0.8 V under AM 1.5 illumination. For both devices presented in [73], [74] the n-GaN had a high crystal quality with a low carrier concentration of about $6.3\times10^{17}cm^{-3}$.

Transparent conductive polymers as Schottky junction for n-GaN are promising with a high work function of 5.2 eV [74], same as gold, to realize high Schottky contact properties on n-GaN or n-InGaN. However, the active area of those devices is very small (1 to 7 mm^2), and no photovoltaic properties were reported yet using high quality InGaN films. Furthermore, the time stability of the Schottky and photovoltaic properties needs to be clarified. Further device improvements are still necessary to observe the photovoltaic effect from n-InGaN films.

I developed new Schottky solar cell devices using TCP on n-GaN and n-$In_xGa_{1-x}N$ films to increase the fill factor, the conversion efficiency and the time stability of Schottky solar cell devices. The photovoltaic properties of n-GaN and n-$In_xGa_{1-x}N$ films using these devices will be reported and compared in term of solar spectrum absorption.

1-4 Composition of the thesis

Corresponding to the actual issues of InGaN film, my thesis is composed of seven chapters. The history of the growth of GaN, InN and their alloy InGaN films, the purpose of the study, and the features of InGaN solar cells were presented in this first chapter.

The second chapter will present the fundamental physics for *p-n* junctions, Schottky junctions with their theoretical limits. The thin-film analysis techniques performed in this study, the optical and electronic characterization will also be described.

The third chapter will present the MOCVD deposition technique used to grow the InGaN films on (0001) sapphire substrate. I will describe a detailed optimization of the crystal growth to reach a high crystal quality with a bandgap modulation depending on the InN mole fraction. The optimized conditions for the crystal growth enhance the electronic properties, decrease the free carrier concentration of the unintended n-type InGaN. This optimization will be favorable for the fabrication of InGaN-based Schottky and p-n junctions with enhanced photovoltaic properties.

In the fourth chapter, the band structure will be evaluated by hard X-ray photoemission spectroscopy (HX-PES, Spring 8 facility). I will present the valence band spectra for $In_xGa_{1-x}N$ with an InN mole fraction range of $0 < x < 0.21$. I will describe a new method to estimate the valence band maximum of GaN which corresponds well to the build-in potential estimated by capacitance-voltage measurement. This method will also be used to estimate the VBM of high quality InN films deposited by MBE with a low carrier concentration range from 5×10^{17} to 5×10^{18} cm^{-3}. Our analysis shows that for lower carrier concentration the Fermi level of the InN semiconductors is located inside its bandgap, below the conduction band, contrary to previous studies.

In the fifth chapter, the impurities and deep-level defects inside a 200-nm-thick unintended n-type $In_{0.09}Ga_{0.91}N$ films will be analyzed by three different techniques, the deep-level transient spectroscopy (DLTS), the thermal admittance spectroscopy (TAS) and the deep-level optical spectroscopy (DLOS). Due to these three different characterizations, the shallow- and deep-level defects will be presented for the first time. I will also describe a detailed fabrication process of Schottky junction devices using $In_{0.09}Ga_{0.91}N$ with its electronic characterization.

In the sixth chapter, I will present the feasibility of n-GaN and n-InGaN films for photovoltaic applications. GaN and InGaN Schottky solar cells using two different transparent conductive polymers (TCP), the PANI (polyaniline) and the PEDOT:PSS, will be described. I will present a new Schottky solar cell device using a thin metallic layer deposited on the n-GaN or n-InGaN in order to enhance the active area of the solar cell and the ohmic contact on the TCP. By using this new device, the Schottky and photovoltaic properties showed good stability over time. From the optimization of InGaN growth, the *n-p* homojunction InGaN could be realized and compared with a *p-i-n* junction InGaN.

Finally the seventh chapter, the conclusions section, will summarize the achievements and comment on the potential of InGaN films for photovoltaic devices.

References chapter 1

[1] J. Wu, W. Walukiewicz, K. M. Yu, J. W. Ager, E. E. Haller, H. Lu, W. J. Schaff, Y. Saito, and Y. Nanishi, "Unusual properties of the fundamental band gap of InN," *Applied Physics Letters*, vol. 80, no. 21, p. 3967, 2002.

[2] H. P. Maruska and J. J. Tietjen, "The preparation and properties of vapor-deposited single-crystal-line GaN," *Applied Physics Letters*, vol. 15, no. 10, pp. 327–329, 1969.

[3] T. Nakao, T. Fujii, T. Sugiyama, S. Yamamoto, D. Iida, M. Iwaya, T. Takeuchi, S. Kamiyama, I. Akasaki, and H. Amano, "Fabrication of Nonpolar a-Plane Nitride-Based Solar Cell on r-Plane Sapphire Substrate," *Applied Physics Express*, vol. 4, no. 10, p. 101001, Oct. 2011.

[4] W. C. Johnson, J. B. Parsons, and M. C. Crew, "Nitrogen compounds of Gallium," *The Journal of Physical Chemistry*, vol. 36, p. 2651, 1932.

[5] V. R. Juza and H. Hahn, "Uber die Kristallstrukturen von Cu3N, GaN und InN Metallamide und Metallnitride," *Zeitschrift für anorganische und allgemeine Chemie*, vol. 239, pp. 282–287, 1938.

[6] H. Amano, N. Sawaki, I. Akasaki, and Y. Toyoda, "Metalorganic vapor phase epitaxial growth of a high quality GaN film using an AlN buffer layer," *Applied Physics Letters*, vol. 48, no. 5, p. 353, 1986.

[7] H. Amano, M. Kito, K. Hiramatsu, and I. Akasaki, "P-type conduction in Mg-doped GaN treated with low energy electron beam irradiation (LEEBI)," *Japanese Journal of Applied Physics*, vol. 28, no. 12, pp. L2112–L2114, 1989.

[8] H. Amano, T. Asahi, and I. Akasaki, "Stimulated emission near ultraviolet at room temperature from a GaN film grown on sapphire by MOVPE using an AlN buffer layer," *Japanese Journal of Applied Physics*, vol. 29, no. 2, pp. L205–L206, 1990.

[9] S. Nakamura, Y. Harada, and M. Seno, "Novel metalorganic chemical vapor deposition system for GaN growth," *Applied Physics Letters*, vol. 58, no. May, pp. 2021–2023, 1991.

[10] M. Asif Khan, J. N. Kuznia, J. M. Van Hove, D. T. Olson, S. Krishnankutty, and R. M. Kolbas, "Growth of high optical and electrical quality GaN layers using low-pressure metalorganic chemical vapor deposition," *Applied Physics Letters*, vol. 58, no. 5, p. 526, 1991.

[11] M. A. Khan, J. N. Kuznia, D. T. Olson, J. M. Van Hove, M. Blasingame, and L. F. Reitz, "High-responsivity photoconductive ultraviolet sensors based on insulating single-crystal GaN epilayers," *Applied Physics Letters*, vol. 60, no. June, pp. 2917–2919, 1992.

[12] H. J. Hovel and J. J. Cuomo, "Electrical and Optical Properties of rf-Sputtered GaN and InN," *Applied Physics Letters*, vol. 20, no. 2, p. 71, 1972.

[13] J. Wu, W. Walukiewicz, S. X. Li, R. Armitage, J. C. Ho, E. R. Weber, E. E. Haller, H. Lu, W. J. Schaff, A. Barcz, and R. Jakiela, "Effects of electron concentration on the optical absorption edge of InN," *Applied Physics Letters*, vol. 84, no. 15, p. 2805, 2004.

[14] J. Wu and W. Walukiewicz, "Band gaps of InN and group III nitride alloys," *Superlattices and Microstructures*, vol. 34, no. 1–2, pp. 63–75, Jul. 2003.

[15] H. Lu, W. J. Schaff, J. Hwang, H. Wu, G. Koley, and L. F. Eastman, "Effect of an AlN buffer layer on the epitaxial growth of InN by molecular-beam epitaxy," *Applied Physics Letters*, vol. 79, no. 10, p. 1489, 2001.

[16] Y. Nanishi, Y. Saito, and T. Yamaguchi, "RF-Molecular Beam Epitaxy Growth and Properties of InN and Related Alloys," *Japanese Journal of Applied Physics*, vol. 42, no. 5, pp. 2549–2559, 2003.

[17] X. Wang, S.-B. Che, Y. Ishitani, and A. Yoshikawa, "Effect of epitaxial temperature on N-polar InN films grown by molecular beam epitaxy," *Journal of Applied Physics*, vol. 99, no. 7, p. 073512, 2006.

[18] X. Wang, S.-B. Che, Y. Ishitani, and A. Yoshikawa, "Step-Flow Growth of In-Polar InN by Molecular Beam Epitaxy," *Japanese Journal of Applied Physics*, vol. 45, no. No. 28, pp. L730–L733, Jul. 2006.

[19] K. Osamura, K. Nakajima, Y. Murakami, P. H. Shingu, and A. Ohtsuki, "Fundamental absorption edge in GaN, InN and their alloys," *Solid State Communications*, vol. 11, no. 5, pp. 617–621, 1972.

[20] N. Yoshimoto, T. Matsuoka, T. Sasaki, and A. Katsui, "Photoluminescence of lnGaN films grown at high temperature by metalorganic vapor phase epitaxy," *Applied Physics Letters*, vol. 59, no. 18, pp. 2251–2253, 1991.

[21] S. Nakamura and T. Mukai, "High-Quality InGaN Films Grown on GaN Films," *Japanese Journal of Applied Physics*, vol. 31, p. L1457, 1992.

[22] S. Nakamura, "InGaN-based blue light-emitting diodes and laser diodes," *Journal of Crystal Growth*, vol. 201–202, pp. 290–295, May 1999.

[23] S. Nakamura, T. Mukai, and M. Senoh, "Candela-class high-brightness InGaN/AlGaN double-heterostructure blue-light-emitting diodes," *Applied Physics Letters*, vol. 64, no. 13, p. 1687, 1994.

[24] S. Nakamura, M. Senoh, N. Iwasa, S. Nagahama, T. Yamada, and T. Mukai, "Superbrigth Green InGaN Single-Quantum-Well-Structure Light-Emitting Diodes," *Japanese Journal of Applied Physics*, vol. 34, p. L1332, 1995.

[25] T. Mukai, D. Morita, and S. Nakamura, "High-power UV InGaN/AlGaN double-heterostructure LEDs," *Journal of Crystal Growth*, vol. 189–190, pp. 778–781, Jun. 1998.

[26] T. Mukai, H. Narimatsu, and S. Nakamura, "Amber InGaN-Based Light-Emitting Diodes Operable at High Ambient Temperatures," *Japanese Journal of Applied Physics*, vol. 37, p. L479, 1998.

[27] S. Nakamura, M. Senoh, S. Nagahama, N. Iwasa, T. Yamada, T. Matsushita, H. Kiyoku, and Y. Sugimoto, "InGaN-Base Multi-Quantum-Well-Structure Laser Diodes," *Japanese Journal of Applied Physics*, vol. 35, p. L74, 1996.

[28] A. Usui, H. Sunakawa, A. Sakai, and A. Yamaguchi, "Thick GaN Epitaxial Growth with Low Dislocation Density by Hybride Vapor Phase Epitaxy," *Japanese Journal of Applied Physics*, vol. 36, p. L899, 1997.

[29] O.-H. Nam, M. D. Bremser, T. S. Zheleva, and R. F. Davis, "Lateral epitaxy of low defect density GaN layers via organometallic vapor phase epitaxy," *Applied Physics Letters*, vol. 71, no. 18, p. 2638, 1997.

[30] S. Chichibu, T. Azuhata, T. Sota, and S. Nakamura, "Spontaneous emission of localized excitons in InGaN single and multiquantum well structures," *Applied Physics Letters*, vol. 69, no. 27, p. 4188, 1996.

[31] S. Chichibu, K. Wada, and S. Nakamura, "Spatially resolved cathodoluminescence spectra of InGaN quantum wells," *Applied Physics Letters*, vol. 71, no. 16, p. 2346, 1997.

[32] Y. Narukawa, Y. Kawakami, S. Fujita, and S. Nakamura, "Recombination dynamics of localized excitons in In0.20Ga0.80N-In0.05Ga0.95N multiple quantum wells," *Physical Review B*, vol. 55, no. 4, pp. 1938–1941, 1997.

[33] Y. Narukawa, Y. Kawakami, M. Funato, S. Fujita, S. Fujita, and S. Nakamura, "Role of self-formed InGaN quantum dots for exciton localization in the purple laser diode emitting at 420 nm," *Applied Physics Letters*, vol. 70, no. 8, p. 981, 1997.

[34] R. Singh, D. Doppalapudi, T. D. Moustakas, and L. T. Romano, "Phase separation in InGaN thick films and formation of InGaN / GaN double heterostructures in the entire alloy composition," *Applied Physics Letters*, vol. 70, no. 9, pp. 1089–1091, 1997.

[35] C. A. Parker, J. C. Roberts, S. M. Bedair, M. J. Reed, S. X. Liu, and N. A. El-Masry, "Determination of the critical layer thickness in the InGaN/GaN heterostructures," *Applied Physics Letters*, vol. 75, no. 18, pp. 2776–2778, 1999.

[36] J. Wu, W. Walukiewicz, K. M. Yu, J. W. Ager III, E. E. Haller, H. Lu, and W. J. Schaff, "Small band gap bowing in In 1−xGaxN alloys," *Applied Physics Letters*, vol. 80, no. 25, p. 4741, 2002.

[37] "Research Cell Efficiency Records," *NERL - National Center for Photovoltaic*, no. March, 2013.

[38] R. R. King, D. C. Law, K. M. Edmondson, C. M. Fetzer, G. S. Kinsey, H. Yoon, R. a. Sherif, and N. H. Karam, "40% efficient metamorphic GaInP/GaInAs/Ge multijunction solar cells," *Applied Physics Letters*, vol. 90, no. 18, p. 183516, 2007.

[39] H. Hamzaoui, A. S. Bouazzi, and B. Rezig, "Theoretical possibilities of InxGa1-xN tandem PV structures," *Solar Energy Materials and Solar Cells*, vol. 87, pp. 595–603, 2005.

[40] V. Y. Davydov, A. a. Klochikhin, V. V. Emtsev, D. a. Kurdyukov, S. V. Ivanov, V. a. Vekshin, F. Bechstedt, J. Furthmuller, J. Aderhold, J. Graul, A. V. Mudryi, H. Harima, A. Hashimoto, A. Yamamoto, and E. E. Haller, "Band Gap of Hexagonal InN and InGaN Alloys," *Physica Status Solidi (B)*, vol. 234, no. 3, pp. 787–795, Dec. 2002.

[41] O. Ambacher, "Growth and applications of Group III-nitrides," *Journal of Physics D: Applied Physics*, vol. 31, pp. 2653–2710, 1998.

[42] F. A. Ponce, "Defects and interfaces in GaN epitaxy," *MRS Bulletin*, vol. 22, no. 2, pp. 51–57, 1997.

[43] T. Egawa, B. Zhang, and H. Ishikawa, "High performance of InGaN LEDs on (111) silicon substrates grown by MOCVD," *IEEE Electron Device Letters*, vol. 26, no. 3, pp. 169–171, Mar. 2005.

[44] T. Egawa and B. A. B. A. Shuhaimi, "High performance InGaN LEDs on Si (1 1 1) substrates grown by MOCVD," *Journal of Physics D: Applied Physics*, vol. 43, no. 35, p. 354008, Sep. 2010.

[45] S. O. Kucheyev, J. E. Bradby, J. S. Williams, C. Jagadish, M. Toth, M. R. Phillips, and M. V. Swain, "Nanoindentation of epitaxial GaN films," *Applied Physics Letters*, vol. 77, no. 21, p. 3373, 2000.

[46] F. M. Morales, D. Gonzales, J. G. Lozano, R. Garcıa, S. Hauguth-Frank, V. Lebedev, V. Cimalla, and O. Ambacher, "Determination of the composition of In x Ga 1-x N from strain measurements," *Acta Materialia*, vol. 57, pp. 5681–5692, 2009.

[47] D. Holec, P. M. F. J. Costa, M. J. Kappers, and C. J. Humphreys, "Critical thickness calculations for InGaN/GaN," *Journal of Crystal Growth*, vol. 303, pp. 314–317, 2007.

[48] J. F. Geisz, D. J. Friedman, J. S. Ward, a. Duda, W. J. Olavarria, T. E. Moriarty, J. T. Kiehl, M. J. Romero, a. G. Norman, and K. M. Jones, "40.8% Efficient Inverted Triple-Junction Solar Cell With Two Independently Metamorphic Junctions," *Applied Physics Letters*, vol. 93, no. 12, p. 123505, 2008.

[49] N. G. Toledo, D. J. Friedman, R. M. Farrell, E. E. Perl, C.-T. (Tony) Lin, J. E. Bowers, J. S. Speck, and U. K. Mishra, "Design of integrated III-nitride/non-III-nitride tandem photovoltaic devices," *Journal of Applied Physics*, vol. 111, no. 5, p. 054503, 2012.

[50] E. Matioli, C. Neufeld, M. Iza, S. C. Cruz, A. A. Al-heji, X. Chen, R. M. Farrell, S. Keller, S. Denbaars, U. Mishra, S. Nakamura, J. Speck, and C. Weisbuch, "High internal and external quantum efficiency InGaN / GaN solar cells," *Applied Physics Letters*, vol. 98, p. 021102, 2011.

[51] J.-P. Shim, M. Choe, S.-R. Jeon, D. Seo, T. Lee, and D.-S. Lee, "InGaN-Based p–i–n Solar Cells with Graphene Electrodes," *Applied Physics Express*, vol. 4, no. 5, p. 052302, May 2011.

[52] L. Sang, M. Liao, N. Ikeda, Y. Koide, and M. Sumiya, "Enhanced performance of InGaN solar cell by using a super-thin AlN interlayer," *Applied Physics Letters*, vol. 99, no. 16, p. 161109, 2011.

[53] Y. Kuwahara, T. Fujii, T. Sugiyama, D. Iida, Y. Isobe, Y. Fujiyama, Y. Morita, M. Iwaya, T. Takeuchi, S. Kamiyama, I. Akasaki, and H. Amano, "GaInN-Based Solar Cells Using Strained-Layer GaInN/GaInN Superlattice Active Layer on a Freestanding GaN Substrate," *Applied Physics Express*, vol. 4, no. 2, p. 021001, Jan. 2011.

[54] C. Boney, I. Hernandez, R. Pillai, D. Starikov, A. Bensaoula, M. Henini, M. Syperek, and J. Misiewicz, "Growth and characterization of InGaN for photovoltaic devices," *Photovoltaic Specialists Conference (PVSC), 2010 35th IEEE*, p. 003316, 2010.

[55] M.-J. Jeng, T.-W. Su, Y.-L. Lee, Y.-H. Chang, L.-B. Chang, R.-M. Lin, J.-H. Jiang, and Y.-C. Lu, "Effect of Silicon Doping on Performance of 30-Pair In x Ga 1- x N/GaN Quantum Well Solar Cells," *Japanese Journal of Applied Physics*, vol. 49, no. 5, p. 052302, May 2010.

[56] K. Y. Lai, G. J. Lin, Y.-L. Lai, Y. F. Chen, and J. H. He, "Effect of indium fluctuation on the photovoltaic characteristics of InGaN/GaN multiple quantum well solar cells," *Applied Physics Letters*, vol. 96, no. 8, p. 081103, 2010.

[57] X. Cai, S. Zeng, and B. Zhang, "Fabrication and characterization of InGaN p-i-n homojunction solar cell," *Applied Physics Letters*, vol. 95, no. 17, p. 173504, 2009.

[58] J. Sheu, C. Yang, S. Tu, K. Chang, M. Lee, W. Lai, and L. Peng, "Demonstration of GaN-Based Solar Cells With GaN/InGaN Superlattice Absorption Layers," *IEEE Electron Device Letters*, vol. 30, no. 3, p. 225, 2009.

[59] O. Jani, C. Honsberg, A. Asghar, D. Nicol, I. Ferguson, A. Doolittle, and S. Kurtz, "Characterization and Analysis of InGaN photovoltaic devices," *31st IEEE Photovoltaic Specialists Conference, January 3-7 2005*, pp. 2–7, 2005.

[60] S. J. Lade and a. Zahedi, "A revised ideal model for AlGaAs/GaAs quantum well solar cells," *Microelectronics Journal*, vol. 35, no. 5, pp. 401–410, May 2004.

[61] J. C. Rimada and L. Hernandez, "Modelling of ideal AlGaAs quantum well solar cells," *Microelectronics Journal*, vol. 32, no. 9, p. 719, 2001.

[62] C. Yang, X. Wang, H. Xiao, J. Ran, C. Wang, G. Hu, X. Wang, X. Zhang, J. Li, and J. Li, "Photovoltaic effects in InGaN structures with p – n junctions," *Physica Status Solidi (a)*, vol. 204, no. 12, pp. 4288–4291, 2007.

[63] B. R. Jampana, A. G. Melton, M. Jamil, N. N. Faleev, R. L. Opila, I. T. Ferguson, and C. B. Honsberg, "Design and Realization of Wide-Band-Gap (~2.67 eV) InGaN p-n Junction Solar Cell," *IEEE Electron Device Letters*, vol. 31, no. 1, pp. 32–34, 2010.

[64] L. Sang, M. Takeguchi, L. Woong, Y. Nakayama, M. Lozac'h, T. Sekiguchi, and S. Masatomo, "Phase Separation Resulting from Mg Doping in p-InGaN Film Grown on GaN/Sapphire Template," *Applied Physics Express*, vol. 3, p. 111004, 2010.

[65] E. L. Piner, S. X. Liu, and S. M. Bedair, "Phase separation in InGaN grown by metalorganic chemical vapor deposition," *Growth (Lakeland)*, vol. 72, no. January, pp. 40–42, 1998.

[66] M. Meneghini, C. de Santi, N. Trivellin, K. Orita, S. Takigawa, T. Tanaka, D. Ueda, G. Meneghesso, and E. Zanoni, "Investigation of the deep level involved in InGaN laser degradation by deep level transient spectroscopy," *Applied Physics Letters*, vol. 99, no. 9, p. 093506, 2011.

[67] H. K. Cho, F. A. Khan, I. Adesida, Z. Fang, and D. C. Look, "Deep level characteristics in n-GaN with inductively coupled plasma damage," *Journal of Physics D: Applied Physics*, vol. 41, p. 155314, 2008.

[68] D. C. Look, Z.-Q. Fang, and B. Claflin, "Identification of donors, acceptors, and traps in bulk-like HVPE GaN," *Journal of Crystal Growth*, vol. 281, no. 1, pp. 143–150, Jul. 2005.

[69] H. K. Cho, C. S. Kim, and C. Hong, "Electron capture behaviors of deep level traps in unintentionally doped and intentionally doped n-type GaN," *Journal of Applied Physics*, vol. 94, p. 1485, 2003.

[70] Z. H. Mahmood, A. P. Shah, A. Kadir, M. R. Gokhale, A. Bhattacharya, and B. M. Arora, "Charge deep level transient spectroscopy of electron traps in MOVPE grown n-GaN on sapphire," *Physica Status Solidi (B)*, vol. 245, no. 11, pp. 2567–2571, 2008.

[71] T. D. Veal, P. H. Jefferson, L. F. J. Piper, C. F. McConville, T. B. Joyce, P. R. Chalker, L. Considine, H. Lu, and W. J. Schaff, "Transition from electron accumulation to depletion at InGaN surfaces," *Applied Physics Letters*, vol. 89, no. 20, p. 202110, 2006.

[72] L. R. Bailey, T. D. Veal, P. D. C. King, C. F. McConville, J. Pereiro, J. Grandal, M. a. Sánchez-García, E. Muñoz, and E. Calleja, "Band bending at the surfaces of In-rich InGaN alloys," *Journal of Applied Physics*, vol. 104, no. 11, p. 113716, 2008.

[73] N. Matsuki, Y. Irokawa, T. Matsui, M. Kondo, and M. Sumiya, "Photovoltaic Action in Polyaniline/n-GaN Schottky Diodes," *Applied Physics Express*, vol. 2, p. 092201, 2009.

[74] N. Matsuki, Y. Irokawa, Y. Nakano, and M. Sumiya, "Pi-Conjugated polymer/GaN Schottky solar cells," *Solar Energy Materials and Solar Cells*, vol. 95, no. 1, pp. 284–287, 2011.

Chapter 2

2- Fundamental physics for electronic and optical characterizations and thin film analysis techniques

This chapter presents the principle of photovoltaic cells and their critical parameters are presented for the *p-n* junction and the Schottky junction, then the theoretical limits of these parameters are described. This is followed by a presentation of the different characterization techniques in order to estimate the crystal quality, the optical and electronic properties.

2-1 Principle of photovoltaic cells and presentation of critical parameters

The following section will present the principle of photovoltaic cells with the interaction between radiation and materials. The theory of the *p-n* junction with the introduction of critical parameters, electrical characteristics, and the different losses in the structure will be approached.

2-1.1 Structure of solar cells and interaction between radiation and matter

The principle of photovoltaic cells is to generate an electrical current by absorption of the radiation energy of the solar spectrum. A photovoltaic system is composed of an absorbent material in the range of the solar spectrum and a structure for collecting charges. The most employed material is silicon for its semi-conductor properties, which allow the absorption of light and the generation of electron-hole pairs. To be usable, these pairs must be generated and separated inside the bulk of the material. The separation of these pairs is possible thanks to the presence of an internal electric field created by the fabrication of a *p-n* junction (*Fig. 2-1*).

A photon of wavelength λ is associated with energy equal to

$$E(eV) = h\upsilon = \frac{hc}{\lambda} \approx \frac{1{,}24}{\lambda(\mu m)}, \tag{2-1}$$

with h the Planck constant (4.14×10^{-15} eV s), c the velocity of light in vacuum (2.99×10^{8} m s^{-1}), υ the photon frequency (s^{-1}) and λ the wavelength (m).

The incident photons are absorbed by the material. The Lambert law describes this phenomenon:

$$I = I_0 \exp(-\alpha \cdot z), \tag{2-2}$$

with:
$$\alpha = \alpha(\lambda) = \frac{4\pi k}{\lambda}, \tag{2-3}$$

where I_0 and I are the incident and transmitted light intensity, respectively, z (µm) the absorption depth, α the absorption coefficient (cm^{-1}) depending on wavelength λ, and k the extinction coefficient of the material.

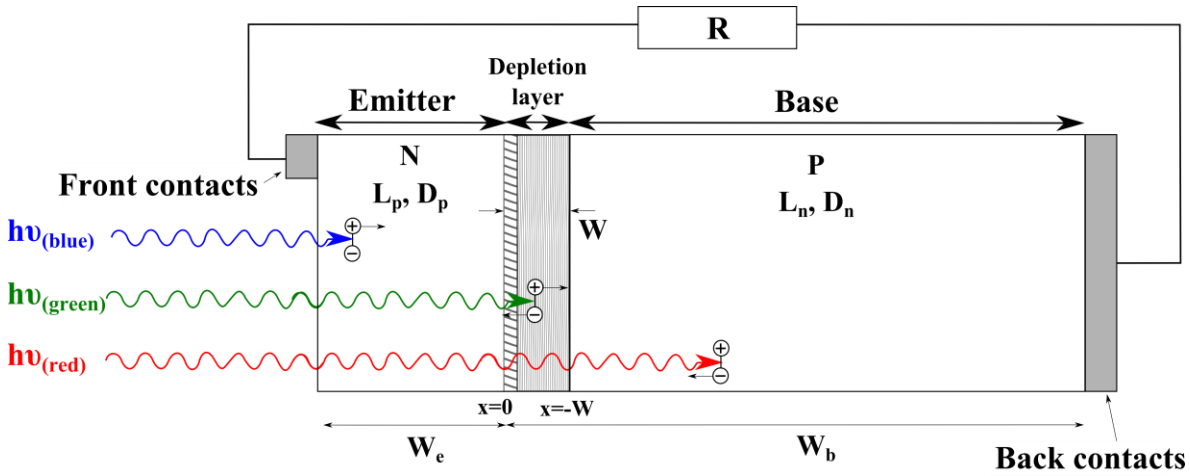

Fig. 2-1: Illustration of the operating principle of a solar cell.

The choice of material is crucial for the absorption of the radiation. The material employed must be a semiconductor, defined with a specific energy gap (E_g) between the valence band and the conduction band. Contrary to a metal with a high conductivity or an insulator, the absorption of energy equivalent to the bandgap of the semiconductor allows an electron to break its binding energy from the valence band and create an electron-hole pair.

An incident photon with radiation energy lower than the bandgap of the semiconductor will not be able to transfer its energy and the semiconductor will be transparent for the corresponding wavelength. Photon with higher energy will be absorbed and will generate electron-hole pairs inside the semiconductor. A part of its energy will be used to break the binding energy of a valence electron, and the excess energy will be transformed into thermal energy and will create a collective excitation in the lattice material, so called phonons. The free carriers generated will be able to participate in the photoelectric current.

The interaction between radiation and the matter modifies the thermodynamic equilibrium. An excess of carriers is generated between the photo-generation rate (G) and the recombination rate (R). The minority carriers, electrons for a p-type material and holes for an n-type material, move (diffuse) to the depletion layer due to a concentration gradient. Indeed, electrons and holes tend to diffuse from region of high concentration to regions of low concentration. Then the carriers are accelerated by the electric field (*E*) near the depletion layer, and reach the other area where they are majority to participate in the photogenerated current. In the following part, the principle of *p-n* junctions will be introduced.

2-1.2 The *p-n* junction

The *p-n* junction, realized by doping, is the main element in solar cells. For the same voltage, a large current can flow in one direction through the diode and a very small current in the other direction. This property is due to the existence of a depletion layer (or space charge region) at the *p-n* interface.

a) Equations for the physics of semiconductors

Three equations describe the transport of charges inside a semiconductor, which were given by W. Shockley:

- Poisson's equation
- The equations of drift current under the effect of an electric field
- The equations of continuity concerning the phenomenon of generation and recombination of charges

The Poisson equation links the divergence of the electric field (E) with the density of volume charges (ρ). The charges in a semiconductor are the electrons (n) in the conduction band (negative charges), the holes (p) in the valence band (positive charges) and the doping impurities. The donor impurities have a net positive charge because they give an electron (N_D^+). And the acceptor impurities have a net negative charge because they catch an electron (N_A^-). We can write the following expression [1]:

For the axis x: $$div\vec{E} = \frac{\partial E}{\partial x} = \frac{\rho}{\varepsilon} \text{ with } \rho = q(p - n + N_D^+ - N_A^-), \quad (2\text{-}4)$$

where ε is the electrical permittivity of the material (for silicon ε = 1×10^{-12}F/cm, and for GaN ε_s = 9.5×8.8×10^{-14} F/cm = 8.4×10^{-13} F/cm [2–4]), and q the elementary charge (q = 1.6×10^{-19} C). Furthermore, the majority of donors and acceptors are ionized, so we can write: $N_D^+ \approx N_D$, $N_A^- \approx N_A$ with N_D and N_A the total density of donors and acceptors.

The electrons and holes contribute to the current density J (A/cm^2) by two phenomenons: the drift current and the diffusion current. The drift current is due to the electric field generated by the *p-n* junction. The diffusion current arises from the concentration gradient of the existing charges between the depletion layer (or space charge region) and the quasi-neutral areas. The following equations of the current density are the sum of the two phenomenons for each carrier, the first term describes the drift current and the second term the diffusion current:

For electron: $$\overrightarrow{J_n} = \overrightarrow{J_n^{drift}} + \overrightarrow{J_n^{diff.}} = q\mu_n n\vec{E} + qD_n \nabla n = -q\mu_n n\nabla\phi + qD_n\nabla n . \quad (2\text{-}5)$$

For hole: $$\overrightarrow{J_p} = \overrightarrow{J_p^{drift}} + \overrightarrow{J_p^{diff.}} = q\mu_p p\vec{E} - qD_p \nabla p = -q\mu_p p\nabla\phi - qD_p\nabla p , \quad (2\text{-}6)$$

with $\mu_{n,p}$: the electron or hole mobility (cm^2 V^{-1} s^{-1})

$D_{n,p}$: the diffusion coefficient for each carrier type (cm^2 s^{-1})

n, p : the concentration of free electrons and free holes respectively (cm^{-3})

ϕ: the electrostatic potential ($\vec{E} = -\nabla\phi$)

The continuity equations provide information about the carrier concentration. These equations are obtained by writing the charge conservation in a volume element during time "*dt*". When there are charge injection and / or recombination in this volume, the continuity equations are also functions of the generation rate (G) and recombination rate (R). The net generation rate (G), created by external processes such as illumination by

light, and the net recombination rate (R) contribute to the current density. Under steady-state conditions the net rate of increasing carriers must be zero so that [1]:

$$\text{for electron:} \quad \frac{dn}{dt} = 0 = G - R_n + \frac{1}{q}\frac{dJ_n}{dx} \quad , \tag{2-7}$$

$$\text{for hole:} \quad \frac{dp}{dt} = 0 = G - R_p - \frac{1}{q}\frac{dJ_p}{dx} \quad , \tag{2-8}$$

with G : the optical generation rate of electron-hole pairs.

R_n, R_p : the global recombination rate of these carriers, which is a sum of the radiative recombination, the Auger recombination and the Shockley-read-hall recombination presented on page 47.

b) The *p-n* junction in thermodynamic equilibrium

A *p-n* junction is composed of two areas inside a semiconductor. In the p-type area, the semiconductor is doped with acceptors due to their deficit of valence electrons. In the n-type area, the semiconductor is doped with donors due to their excess of valence electrons.

The balance of carrier density is presented in *Table 2-1* [1]. The majority carriers are denoted by n_{n0} and p_{p0} in the n-type and p-type part, respectively, the subscript *0* indicates the case of the thermodynamic equilibrium.

Table 2-1: Carrier density in the n-type and p-type parts of doped semiconductor

Carriers	Carrier density in **n-type** (cm^{-3})	Carrier density in **p-type** (cm^{-3})
Majority carriers	Electrons: $n_{n0} = N_D$	Holes: $p_{p0} = N_A$
Minority carriers $(n_{n0} \times p_{p0} = n_i^2)$	Holes: $p_{n0} = \frac{n_i^2}{N_D}$	Electrons: $n_{p0} = \frac{n_i^2}{N_A}$

I assume a perfect contact between the n-type and p-type parts with an abrupt junction. At the interface, the majority electrons in the n-type will diffuse and recombine in the p-type part (*Fig. 2-2(a)*). In the same way, the majority holes in p-type will recombine in the n-type part. Thus, the atoms of acceptors and donors will be ionized near the *p-n* interface. These ions create an electric field (E) from n-type to p-type. An area without free carriers will be generated, which is called the depletion layer or space charge region (*Fig. 2-2(b)*).

Because of the electric field, the flow of minority carriers is promoted: the electrons from the p-type are accelerated in the n-type, and the holes from the n-type are accelerated in the p-type. This flow of minority carriers is opposite to the diffusion flow of majority carriers. A thermodynamic equilibrium will be generated between the drift and diffusion flows.

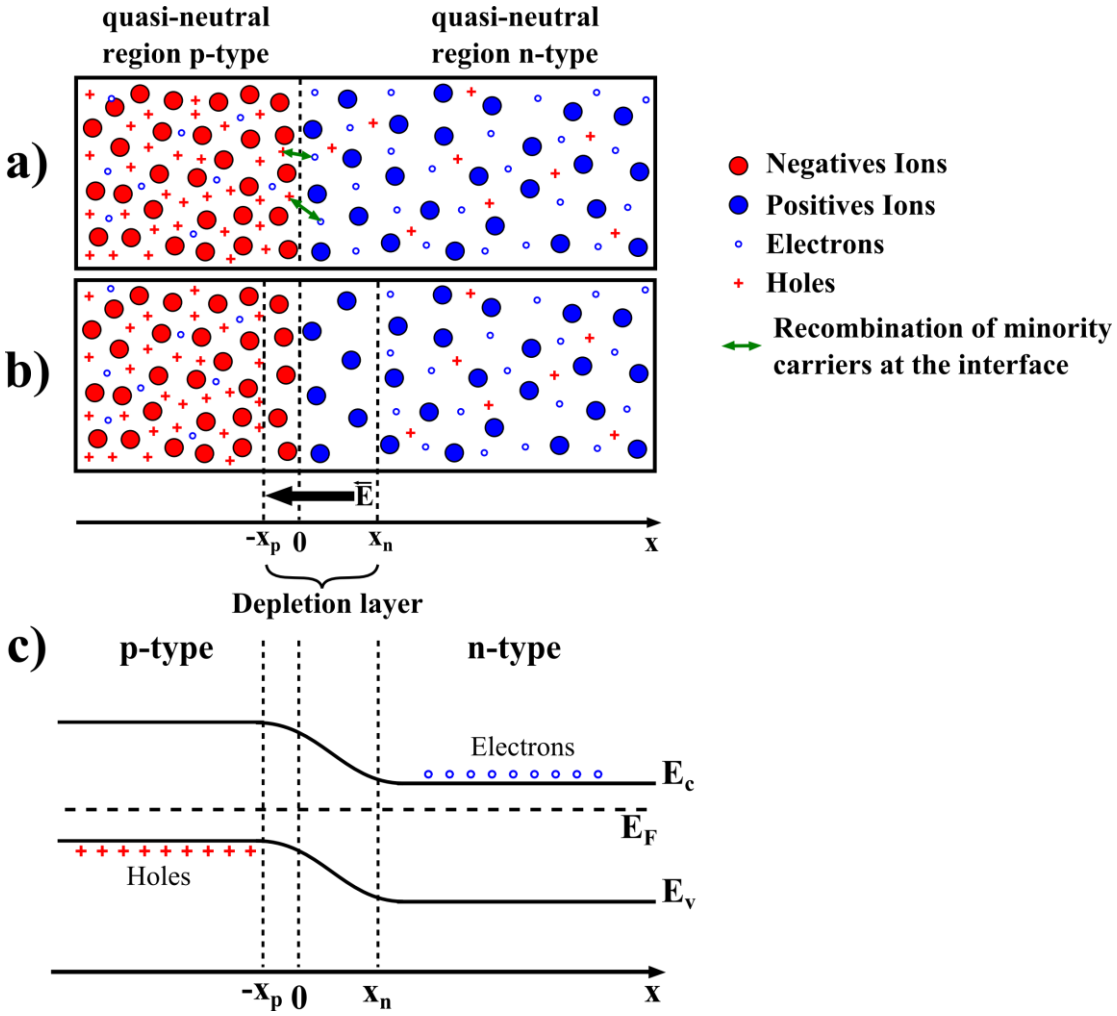

Fig. 2-2: Representation of p-n homojunction at thermal equilibrium: (a) and (b) inside the material with the formation of the depletion layer, and (c) the electronic band structure.

Figure 2-2(a) illustrates the recombination of minority carriers at the interface. *Figure 2-2(b)* presents the *p-n* junction composed of three areas: two areas of n-type and p-type (quasi-neutral regions at the thermodynamic equilibrium) and the depletion layer.

Inside the depletion layer, the Fermi levels of the n-type and p-type areas balance, which induces a band bending (*Fig. 2-2(c)*). A potential difference (V_D) appears which explains the generation of the electric field. This potential between both areas forms a barrier potential (height: qV_D) balancing the diffusion of carriers. This barrier potential blocks the electrons to diffuse in the p-type region, and the holes to diffuse in the n-type region.

2-1.3 Electrostatic Characteristics

In the following, the electrostatic characteristics of *p-n* junctions will be described. These characteristics include the diffusion potential (V_D), the expression of the electric field inside the depletion layer and the depletion layer thickness as functions of the dopant concentration.

a) Diffusion potential (V_D)

The electrostatic characteristics can be deduced from the charge flows by considering the electron and hole flows equal to zero in the thermodynamic equilibrium:

$$J_n = J_p = 0 .$$

The expression of the diffusion potential V_D can be deduced from the equation of the current density *(2-5)* :

$$\overrightarrow{J_n} = q\mu_n n\vec{E} + qD_n \nabla n = 0 . \tag{2-9}$$

From Einstein relation:

$$\frac{D_n}{\mu_n} = \frac{D_p}{\mu_p} = \frac{kT}{q} = 26mV \text{ at 300 K,} \tag{2-10}$$

with: k = 1.38×10^{-23} J K^{-1}, the Boltzmann constant

T : the temperature (K)

q =1.60×10^{-19} C, the elementary charge

By integrating *Eq. (2-9)* at bounds of the depletion layer:

$$V_D = -\int_{-x_p}^{x_n} E \cdot dx = \frac{kT}{q}\int_{-x_p}^{x_n} \frac{dn}{n} = \frac{kT}{q}\ln\left(\frac{n(x_n)}{n(-x_p)}\right)$$

From *Table 2-1*,

$$n(x_n) \approx N_D \text{ and } n(-x_p) \approx \frac{n_i^2}{N_A}$$

The diffusion potential can be written in the following form:

$$V_D = \frac{kT}{q}\ln\left(\frac{N_D N_A}{n_i^2}\right) \tag{2-11}$$

Thus we can write the variation of carriers as a function of the diffusion potential at equilibrium [1]:

$$p_{n0} = p_{p0}\exp\left(-\frac{qV_D}{kT}\right) \approx \frac{n_i^2}{N_D} \tag{2-12}$$

$$n_{p0} = n_{n0}\exp\left(-\frac{qV_D}{kT}\right) \approx \frac{n_i^2}{N_A} \tag{2-13}$$

b) Expression of the electric field

The calculation of the electric field is realized by integration of Poisson's equation for the two regions inside the depletion layer. I made the hypothesis that there is no free carrier in the depletion layer.

Table 2-2: Expression of the electric field E inside the depletion layer. $-x_p$ and x_n are defined as the borders of the depletion layer: $-x_p$ in the p-type area, and x_n in the n-type area (Fig. 2-2)

	p-type area ($-x_p < x < 0$)	**n-type area ($0 < x < x_n$)**
Charge density	N_A	N_D
Charges	$-q\times N_A$	$+q\times N_D$
Poisson's equation from *Eq. (2-4)*	$\frac{dE}{dx}=\frac{-qN_A}{\varepsilon}$	$\frac{dE}{dx}=\frac{qN_D}{\varepsilon}$
Expression of *E*	$E(x)=\left(\frac{-qN_A}{\varepsilon}\right)x+A$	$E(x)=\left(\frac{qN_D}{\varepsilon}\right)x+B$
Bounds condition (to determine the constants)	$E(-x_p)=0$	$E(x_n)=0$
Final expression of *E*	$E(x)=\frac{-qN_A}{\varepsilon}(x+x_p)$	$E(x)=\frac{qN_D}{\varepsilon}(x-x_n)$

The condition of continuity for the electric field at x=0 require the following relation:

$$x_p N_A = x_n N_D \ . \tag{2-14}$$

Thus, to conserve the electric neutrality, the depletion layer enlarges upon the lightly doped region.

c) Thickness of the depletion layer

The following expression appears after writing the potential difference between $-x_p$ and x_n:

$$V_D = V(x_n) - V(-x_p) = -\int_{-x_p}^{x_n} E(x)dx \ ,$$

$$V_D = \frac{q}{2\varepsilon}\left(N_A x_p^2 + N_D x_n^2\right). \tag{2-15}$$

Combining *Eq. (2-15)* with the relation *(2-14)*, I can have an expression of x_p and x_n as functions of the diffusion potential V_D [1]:

$$x_n = \frac{1}{N_D}\sqrt{\frac{2\varepsilon}{q}\frac{N_A N_D}{N_A + N_D}\times V_D} \qquad x_p = \frac{1}{N_A}\sqrt{\frac{2\varepsilon}{q}\frac{N_A N_D}{N_A + N_D}\times V_D}$$

The thickness of the depletion layer is $W = x_n + x_p$:

$$W = \sqrt{\frac{2\varepsilon}{q}\frac{N_A + N_D}{N_A N_D} \times V_D} \tag{2-16}$$

We can perform the following calculation to make an estimation of the thickness of the depletion layer:

For the case of a typical *p-n* junction inside silicon:

T=300 K	kT/q = 2.6×10^{-2} V
$N_D = 10^{20}$ cm^{-3}	$n_i = 10^{10}$ cm^{-3} (for Si)
$N_A = 10^{16}$ cm^{-3}	$\varepsilon_{Si} = 10^{-12}$ F/cm

For a typical *p-n* junction inside silicon the diffusion potential is about $V_D \approx 0.95$V, and the thickness of the depletion layer is about $W \approx 0.35$μm.

For the case of a *p-n* junction inside GaN, at the same temperature:

$N_D = 10^{16}$ cm^{-3}	n_i : calculated below for GaN
$N_A = 10^{18}$ cm^{-3}	$\varepsilon_{GaN} = 9.5\times8.85\times10^{-12} = 0.84\times10^{-12}$ F/cm

Calculation of the intrinsic carrier concentration n_i inside GaN:

$$n_i = \sqrt{N_C N_V}\exp\left(\frac{-E_g}{2kT}\right) \tag{2-17}$$

With N_c and N_v the effective density of state at the conduction band and valence band edges

$$N_C = 2\left(\frac{2\pi m_e^* kT}{h^2}\right)^{3/2} M_C \propto T^{3/2}, \tag{2-18}$$

$$N_V = 2\left(\frac{2\pi m_h^* kT}{h^2}\right)^{3/2} \propto T^{3/2}, \tag{2-19}$$

where m_e^* and m_n^* are the density-of-state effective mass for electrons and holes, respectively, M_C is the number of equivalent minima in the conduction band [5]. For wurtzite GaN material, N_C and N_V are estimated at $N_C \sim 4.3\times10^{14}\times T^{3/2}$ cm^{-3} and $N_V \sim 8.9\times10^{15}\times T^{3/2}$ cm^{-3}, thus at 300 K the intrinsic carrier concentration inside GaN is $n_i \sim 1.4\times10^{-8}$cm^{-3}, which is in the same order as $10^{-8} \sim 10^{-9}$ cm^{-3} from [6].

The estimated thickness of the depletion layer for GaN material is estimated at $W \approx 0.56$ μm by using *Eq. (2-16)* with a diffusion potential of 2.96 V [*Eq. (2-11)*]. This estimated thickness is pretty wide because I chose a donor concentration of about 10^{16} cm^{-3}, which can correspond to a very high crystal quality. If the donor

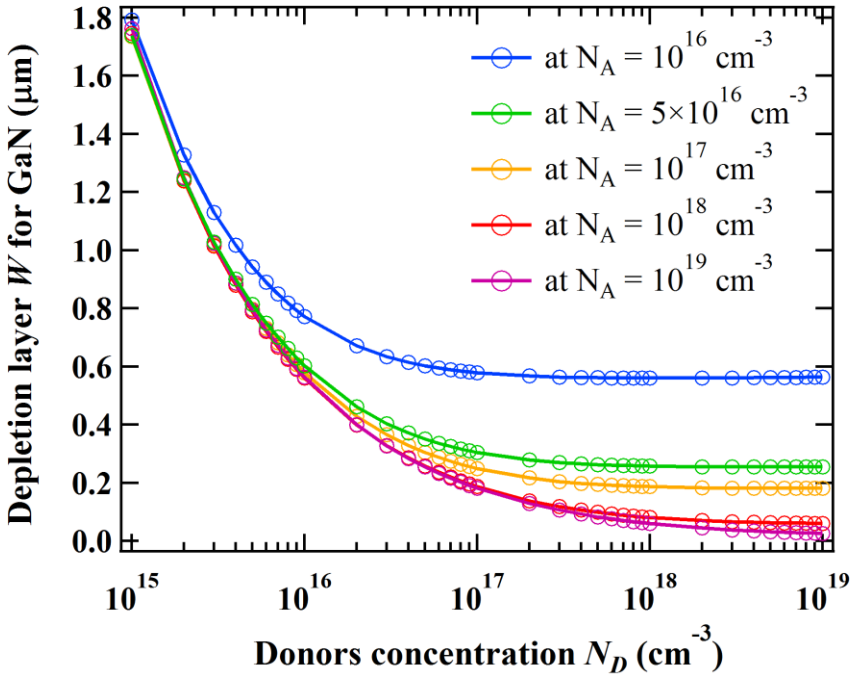

Fig. 2-3: Theoretical calculation of the depletion layer width W for GaN in function of the donors concentration N_D, the acceptor concentration N_A is fixed at 10^{16}, 10^{17}, 10^{18} and 10^{19} cm^{-3}and the temperature at 300 K.

concentration is about 5×10^{17} cm^{-3}, the depletion layer thickness becomes $W \approx 0.10$ µm. I plotted the depletion layer width W of GaN material as a function of the donor concentration N_D at 300 K depending on the acceptor concentration N_A in *Fig. 2-3*. In my example, the donor concentration N_D corresponds to the unintended n-type doping observed in GaN films, and the acceptor concentration N_A corresponds to the p-type doping. As *Fig. 2-3* shows, the depletion width decreases exponentially when the donor concentration increases.

To fabricate a solar cell device using GaN or InGaN, it is thus very important to decrease the unintended donor concentration to enhance the thickness of the depletion layer.

2-1.4 Junction under polarization

A potential difference modifies the diffusion potential V_D existing at equilibrium when a voltage "V" is applied at the bounds of *n* and *p* areas. An energy gap "$-qV$" is generated between the Fermi levels of the quasi-neutral regions n and p, and the total potential difference becomes "V_D-V".

The polarization is direct for V positive: the potential difference and the electric field across the depletion layer decrease. There will consequently be a lower drift current and a higher diffusion current. This global diffusion current from p to n regions is important because it is formed by extraction of majority carriers.

The polarization is indirect for V negative: it is the case of a solar cell under illumination. The potential difference is enhanced and the electric field increase. There is an enhancement of the drift current and a lower

diffusion current. This global conduction current from *n* to *p* regions is low because it is formed by the minority carriers. If the voltage applied between *n* and *p* is strong, there will be no more minority carriers inside the quasi-neutral regions and a saturation of the current will appear.

The new expression of the minority carrier concentration is [1]:

for hole (*n* region)
$$p_n = p_{n0} \exp\left(-\frac{qV}{kT}\right) = \frac{n_i^2}{N_D} \exp\left(-\frac{qV}{kT}\right), \tag{2-20}$$

for electron (*p* region)
$$n_p = n_{p0} \exp\left(-\frac{qV}{kT}\right) = \frac{n_i^2}{N_A} \exp\left(-\frac{qV}{kT}\right). \tag{2-21}$$

The concentration of minority carriers at the boundary of the depletion layer changes exponentially with the applied voltage *V*.

a) Calculation of the diffusion current in the quasi-neutral regions under dark condition

Electrons generated thermally in the *p* region are diffused to the depletion layer by a concentration gradient, and then they are accelerated in the *n* region due to the electric field. The same process occurs for holes generated in the *n* region, which are diffused then accelerated to the *p* region. Thus, a diffusion of electrons and holes far away from the depletion layer exists.

To estimate the diffusion current inside the quasi-neutral region, I consider the electric field far away so that the perturbation due to the electric field becomes negligible. In this case, only diffusion current is present, *Eq. (2-5)* and *Eq. (2-6)* become:

for electron
$$J_n = qD_n \frac{\partial n}{\partial x}, \tag{2-22}$$

for hole
$$J_p = -qD_p \frac{\partial p}{\partial x}. \tag{2-23}$$

Under low-level injection ($\Delta p = \Delta n << N_D, N_A$), the recombination rate (for the case of hole here) can be written in the following form:

$$R_p = \frac{\Delta p}{\tau_p} = \frac{p_{(t)} - p_{(t=0)}}{\tau_p}, \tag{2-24}$$

with τ_p the lifetime of hole (from ns to µs).

Considering these results substituted inside the continuity equation, *Eq. (2-7),* we obtain for a steady-state $\left(\frac{dp}{dt} = 0\right)$ and under dark condition (so $G_p=0$, there is no generation rate):

$$\frac{1}{q}\frac{dJ_p}{dx} = -\frac{\Delta p}{\tau_p},$$

with J_p given by *Eq. (2-23)*:

$$D_p \frac{\partial^2 p}{\partial x^2} = \frac{\Delta p}{\tau_p},$$

furthermore $\frac{\partial p}{\partial x} = \frac{\partial \Delta p}{\partial x}$:

$$\frac{\partial^2 \Delta p}{\partial x^2} = \frac{\Delta p}{L_p^2}. \qquad (2\text{-}25)$$

L_p characterizes the diffusion length for the hole, which can be written in the following form:

$$L_{n,p} = \sqrt{D_{n,p}\tau_{n,p}} = \sqrt{\frac{kT}{q}\mu_{n,p}\tau}\,. \qquad (2\text{-}26)$$

The diffusion length is a very important parameter for the photovoltaic cells. If this value is high, it means that less recombination occurs in the bulk and on surface of the semiconductor, and a better efficiency to collect the photogenerated carriers is possible.

A general solution of *Eq (2-25)* is:

$$\Delta p = A e^{\frac{x}{L_p}} + B e^{-\frac{x}{L_p}}.$$

We use the boundary conditions to find the constants A and B: if x tends to the infinity Δp must stay at a finite value, which means that A must be equal to zero. For $x = -x_n$, $p(-x_n) = B = p_{n0} e^{\frac{qV}{kT}}$, thus, a particular solution of the differential equation is written:

$$p_{n0} + p_{n0}\left(e^{\frac{qV}{kT}} - 1\right)e^{-\frac{x-x_p}{L_p}}. \qquad (2\text{-}27)$$

Now that we know the concentration of minority carriers inside the quasi-neutral regions, the diffusion current can be deduced by substituting the expression of $p_n(x)$ in *Eq. (2-23)*:

for hole

$$J_p(x) = \frac{qD_p p_{n0}}{L_p}\left(e^{\frac{qV}{kT}} - 1\right)e^{-\frac{x-x_n}{L_p}}, \qquad (2\text{-}28)$$

In the same way, for electron

$$J_n(x) = \frac{qD_n n_{p0}}{L_n}\left(e^{\frac{qV}{kT}} - 1\right)e^{-\frac{x+x_p}{L_n}}. \qquad (2\text{-}29)$$

The carrier density is low in the depletion layer so we made the hypothesis that there is no recombination inside. The electron and hole density at the boundary of the depletion layer is thus constant. We have at the boundary of the depletion layer $x = x_n$ for the n side and $x = x_p$ for the p side, so we can write:

$$J_p(x) = \frac{qD_p p_{n0}}{L_p}\left(e^{\frac{qV}{kT}} - 1\right) \text{ and } J_n(x) = \frac{qD_n n_{p0}}{L_n}\left(e^{\frac{qV}{kT}} - 1\right). \quad (2\text{-}30)$$

The global current density under dark condition can be written by the sum of the current densities of charges [1]:

$$J_{dark} = J_n + J_p,$$

$$J_{dark} = J_0 \cdot \left(e^{\frac{qV}{kT}} - 1\right) \text{ with } J_0 = \left(\frac{qD_p p_{n0}}{L_p} + \frac{qD_n n_{p0}}{L_n}\right), \quad (2\text{-}31)$$

by using *Table 2-1* :

$$J_0 = \left(\frac{qD_p n_i^2}{L_p N_D} + \frac{qD_n n_i^2}{L_n N_A}\right). \quad (2\text{-}32)$$

J_0 is the saturation current density for an ideal *p-n* junction. The saturation current density is a very important parameter affecting the open circuit voltage (V_{oc}). In the part of the electrical characterization, I underlined that the lowest saturation current is necessary to optimize V_{oc}.

b) Influence under illumination

To observe the influence under illumination, we must take the previous case with a generation rate *($G \neq 0$)*. In this case, *Eq. (2-25)* is written for holes:

$$\frac{\partial^2 \Delta p}{\partial x^2} = \frac{\Delta p}{L_p^2} - \frac{G_p}{D_p}. \quad (2\text{-}33)$$

If we suppose that the ratio G/D is a constant, a general solution is:

$$\Delta p = G\tau_p + Ce^{\frac{x}{L_p}} + De^{-\frac{x}{L_p}}.$$

Because the boundary conditions do not change, the following solution is obtained:

$$p_n(x) = p_{n0} + G\tau_p + \left[p_{n0}\left(e^{\frac{qV}{kT}} - 1\right) - G\tau_p\right]e^{-\frac{x-x_p}{L_p}}. \quad (2\text{-}34)$$

As before, the recombination inside the depletion layer is negligible, however we must take into account the generation of the electron-hole pairs. From *Eq. (2-34)*, only the term inside the bracket is not constant and is a function of the current density because of the voltage *V*. In a general way, the contribution of the electron-hole pair generation reduces the current density to a value denoted by J_{ph} [1]:

$$J_{ill} = J_0\left(e^{\frac{qV}{kT}} - 1\right) - J_{ph}. \quad (2\text{-}35)$$

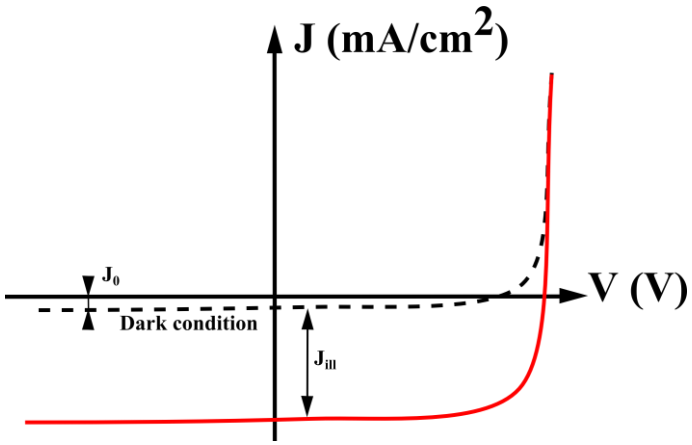

Fig. 2-4: Characteristic current-voltage under dark condition (dotted black) and under illumination (red).

This equation is the characteristic current-voltage of an ideal *p-n* diode. In the following section, we will study this property under illumination and under dark condition. I represented in *Fig. 2-4* the I(V) curves characteristic under dark condition and under illumination.

2-1.5 Electrical characteristics

As I previously demonstrated, the characteristic I (V) of a *p-n* diode under illumination can be written [1]:

$$I = I_0\left(e^{\frac{qV}{nkT}} - 1\right) - I_L\,, \tag{2-36}$$

with *n*, the ideality factor of the diode. For an ideal case $n = 1$.

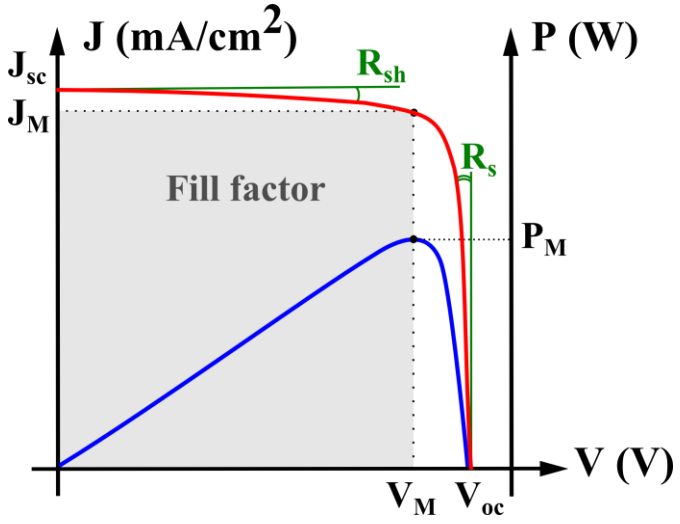

Fig. 2-5: Characteristics current-voltage (red) and power-voltage (blue) for a solar cell under illumination.

As presented in *Fig. 2-5*, the characteristic I(V) is necessary to extract the most important parameters of photovoltaic cells.

- The short-circuit current I_{sc} (A):

This current is defined for a voltage equal to zero. The short-circuit current corresponds to the photogenerated current under illumination. It is usual to speak about the short-circuit current per centimeter square (current density) denoted by J_{sc} (mA/cm^2) to compare solar cells of different sizes.

- The open-circuit voltage V_{oc} (V):

This voltage is defined for a current equal to zero. In this case from *Eq. (2-36)*, the voltage can be written as follows [1]:

$$V_{oc} = \frac{nkT}{q} \ln\left(\frac{I_L}{I_0} + 1\right). \tag{2-37}$$

- The maximal power P (W):

The maximal power of a solar cell is defined for a voltage V_{MP} and a current I_{MP}.

- The fill factor FF (without unit):

The fill factor refers to the structure quality and is defined as follows [1]:

$$FF = \frac{P_M}{V_{oc} \cdot I_{cc}} = \frac{V_{MP} \cdot I_{MP}}{V_{oc} \cdot I_{cc}}. \tag{2-38}$$

It corresponds graphically to the ratio between the areas $V_{MP} \times I_{MP}$ and $V_{oc} \times I_{sc}$.

- The conversion efficiency η (without unit):

The conversion efficiency is the main parameter to evaluate solar cells, the process quality, and the material quality. The conversion efficiency is defined by the ratio between the electric power generated and the incident light power (P_{ill}). The conversion efficiency is written [1]:

$$\eta = \frac{P_M}{P_{ill}} = \frac{FF \cdot V_{oc} \cdot I_{cc}}{P_{ill}}. \tag{2-39}$$

- The series resistance (R_s):

The influence of the series resistance in the I(V) characteristic is located at open-circuit voltage (high voltage), in ideal case the series resistance is null and the I(V) curve follows a vertical line from V_{oc}. The larger the series resistance is the more seriously the fill factor will be reduced. The sources of the series resistance are found in all the resistive losses of the solar cell device. Firstly in the resistivity of the quasi-neutral regions, in the

lateral ohmic losses, in the contact resistance of the front and rear metallic contacts and finally the resistivity of the metallic contacts themselves. The value of the series resistance must be as small as possible.

- The shunt resistance (R_{sh}):

The shunt resistance influences the I(V) characteristic at low voltage at the short-circuit condition, for ideal case, the shunt resistance is infinite and the I(V) curve follows a horizontal line from J_{sc}. The smaller the shunt resistance is, the more seriously the fill factor will be reduced. The shunt resistance considers all the short-circuit phenomena of the *p-n* junction. The value of the shunt resistance must be as high as possible.

2-1.6 Equivalent electric circuit of solar cells

Equation (2-36) of a diode under illumination concerns an ideal case, in fact it is necessary to take into account other parameters to represent the I-V characteristic under dark and light conditions. For this, the model with one or two diodes can be used as *Fig. 2-6* presents.

The equation of the photogenerated current, including these parameters, can be rewritten as follows [1]:

$$I = I_{01}\left(\exp\left(\frac{q(V-IR_s)}{n_1 kT}\right)-1\right)+I_{02}\left(\exp\left(\frac{q(V-IR_s)}{n_2 kT}\right)-1\right)+\frac{V-IR_s}{R_p}-I_{ph}, \quad (2\text{-}40)$$

with: I_{01}, the saturation current of the first diode. This saturation current corresponds to that inside the emitter and the base.

I_{02}, the saturation current of the second diode. This saturation current corresponds to that inside the depletion layer.

n_1 and n_2, the ideality factors of the first and second diodes, respectively. For ideal case the value of n_1=1

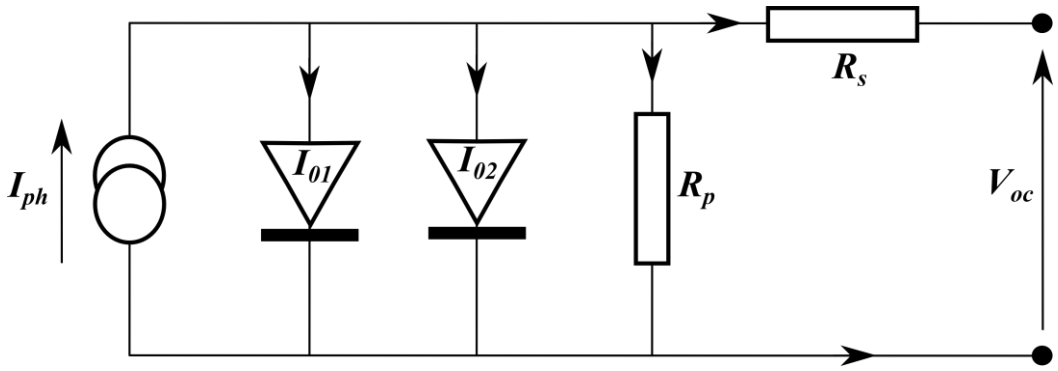

Fig. 2-6: Equivalent electric circuit of solar cells represented by a two-diode model.

and the value of n_2=2.

R_s, the series resistance.

R_p, the parallel resistance also denoted shunt resistance (R_{sh}).

In the case of one diode model, the diode I_{02} is simply removed from the equivalent electric circuit and the term I_{02} is equal to zero in *Eq. (2-40)*.

I displayed in *Fig. 2-7* the I(V) characteristics for one and two-diode model. *Equation (2-40)* can fit the I-V curve only for the forward positive voltage. The leakage current represented for the negative bias voltage can not be fitted by using the same equation.

For silicon solar cells, it is usual to describe the saturation current I_{01} by the one of the quasi-neutral areas and the saturation current I_{02} by the one of the depletion layer. However, the III-V nitride solar cells are a thin-film technology, which means that it is quite difficult to separate the front surface from the depletion layer and the "bulk" of the thin film. During the fabrication of Schottky solar cell devices using n-GaN or n-InGaN as an active layer, I could mainly observe the "one-diode model behavior" for the I-V characteristic under dark condition as shown on the left graph in *Fig. 2-7*. Nevertheless, sometimes the I-V characteristic under dark condition had the "two-diode model behavior" as shown on the right graph in *Fig. 2-7*. I think it is due to the interface between the metallic contact and the III-V nitride thin film where a complex diffusion of the metallic component could occur during the annealing step of the ohmic and Schottky contacts.

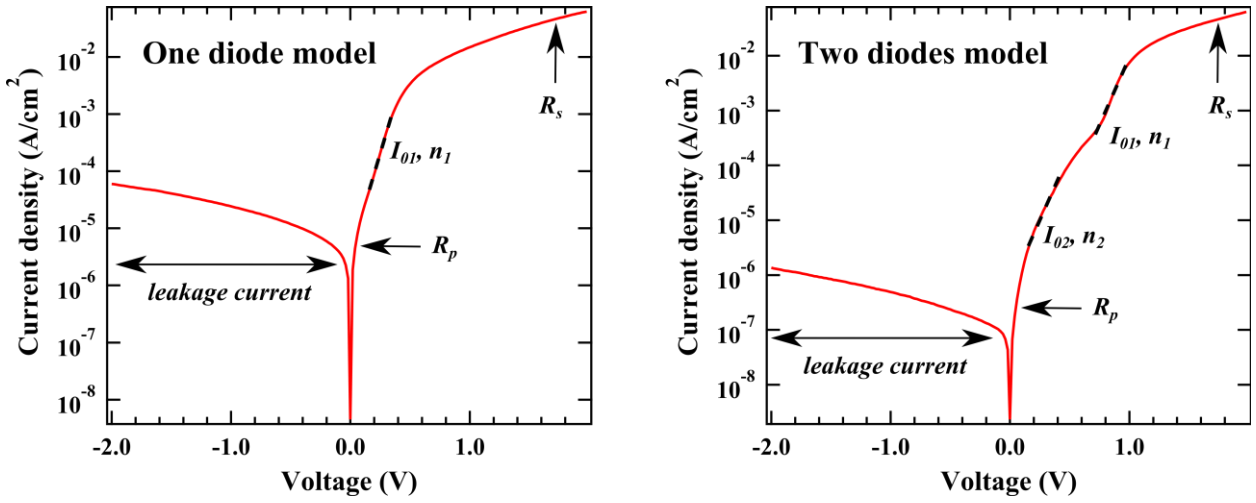

Fig. 2-7: Current-voltage characteristic for one diode model (left) and two diodes model (right).

2-1.7 Theoretical limit

Each of the electrical characteristics previously introduced has a theoretical limit. To understand the possible enhancement of the solar cell performance, I firstly introduce the different concepts behind the theoretical limit of these electrical characteristics.

a) The short-circuit current limit and solar spectrum

The short-circuit current of a solar cell is limited theoretically by the maximum amount of incident light. Of course in the nature, the power of incident light fluctuates a lot depending on the day time, the weather, and the temperature. Because each country has a different solar intensity depending on the latitude, a normalized spectrum (constant) was adopted internationally to compare the performance of solar cells fabricated around the world. The normalized solar spectrum is called AM 1.5G (AM for Air-mass) at the Earth ground level, some parts of the spectra are absorbed by the atmosphere (*Fig. 2-8*). The letter G of AM1.5 G stands for "Global tilt", which means that the spectral radiation from the sun plus the sky diffusion and the diffusion reflected from the ground are taken into account on a south facing surface tilted at 37 deg. from horizontal plane.

The AM1.5 D stands for "Direct", which means that the direct normal radiation on a surface tracking the

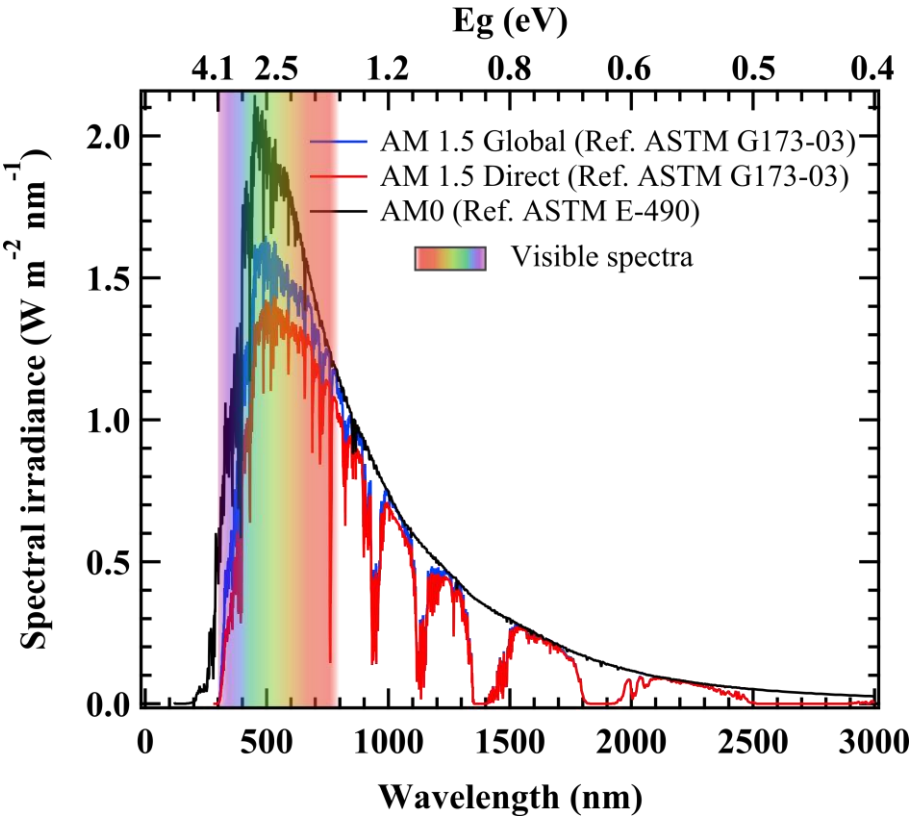

Fig. 2-8: The different normalized solar spectra are presented. AM0 spectrum corresponds to the solar spectrum before the atmosphere, AM1.5G the spectrum used to characterize the solar cell on the ground level with some absorbed regions due to elements constituting the atmosphere.

sun position, excluding scattered sky and reflected ground radiation. For space solar cells, the normalized solar spectrum AM 0 is used.

The theoretical limit of the short circuit current density (J_{sc}) can be estimated from the standard AM1.5 G solar spectrum, which is used for the terrestrial solar cells. The standard AM1.5 G corresponds to a power of 1000W/m^2.

To estimate the theoretical limit of the short circuit current density, we take into account the bandgap of the semiconductor that determines the limit of absorption wavelength and we assume that the entire spectrum below this limit is absorbed. The J_{sc} theoretical limit is calculated by the integral (area under curve) of the standard AM1.5 G from 4.41 eV (280nm) to the material bandgap E_g (eV). The J_{sc} theoretical limit is plotted as a function of the material band gap in *Fig. 2-9*.

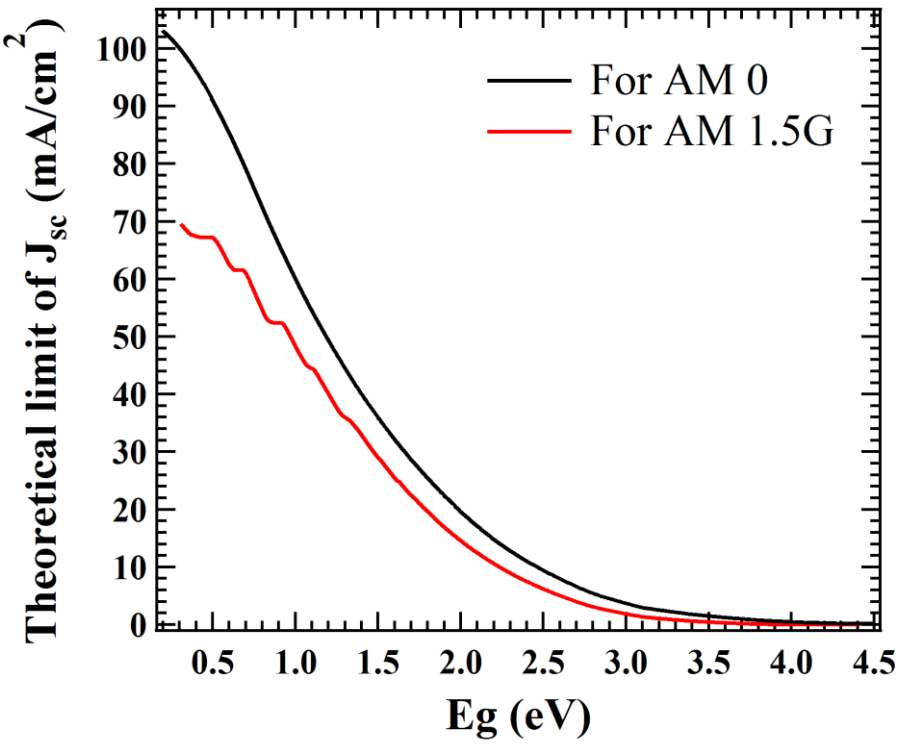

Fig. 2-9: Theoretical limit of the current density depending on the material bandgap (supposing a full absorption) under normalized AM0 and AM1.5G solar spectra.

For silicon with a bandgap of 1.1 eV, the theoretical limit of the J_{sc} is 44.5 mA/cm^2 under AM 1.5G illumination. For GaN with a bandgap of 3.4 eV, the theoretical limit becomes 0.6 mA/cm^2.

b) The open-circuit voltage limit

For the theoretical limit of V_{oc}, *Eq. (2-37)* is used where V_{oc} limit depends on the saturation current density J_0. The saturation current depends on the material bandgap according to the following expression [7]:

$$J_0 = J_{00} \times \exp\left(\frac{-E_g}{kT}\right). \tag{2-41}$$

M.A. Green gave a lower limit for the J_0 in *p-n* junctions, which is $J_{00}=1.5\times10^5$ mA/cm^2 [1]. I could estimate the theoretical limit of V_{oc} as a function of the material bandgap presented in *Fig. 2-10*. For silicon (1.12 eV), V_{oc} limit is about 0.8 V, whereas for GaN, it is about 2.8 V.

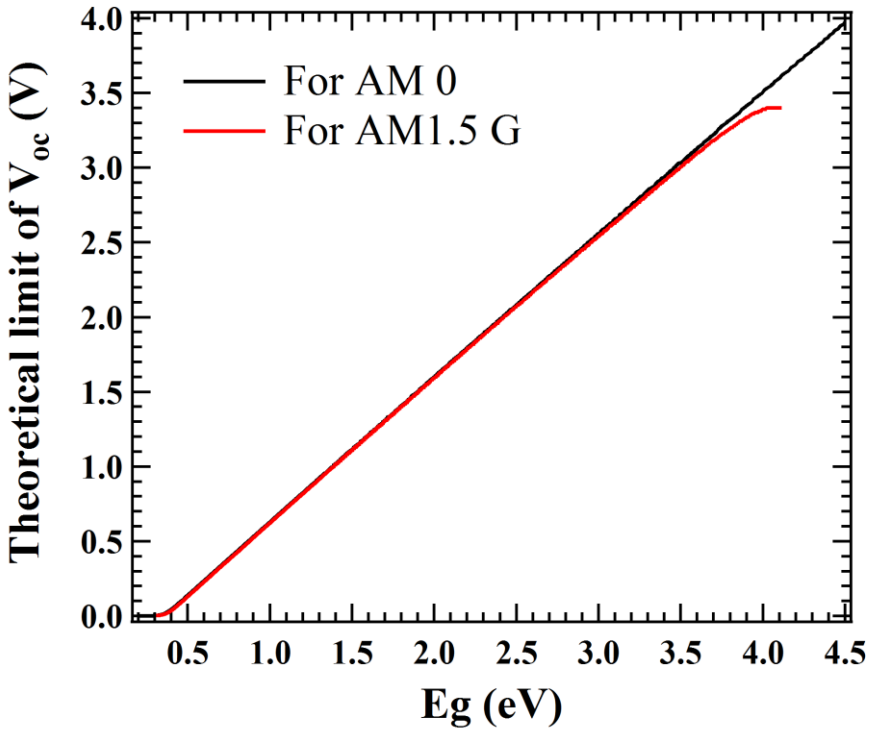

Fig. 2-10: Theoretical limit of the current density depending on the material bandgap (supposing a full absorption) under normalized AM0 and AM1.5G solar spectra.

c) The conversion efficiency limit

Knowing the theoretical limits of both V_{oc} and J_{sc}, we can determine the theoretical conversion efficiency limit depending on the material bandgap. *Figure 2-11* provides the information about the highest conversion efficiency. For the silicon case (1.12 eV), assuming a fill factor of 0.85, the conversion efficiency limit is about 27 % for single *p-n* junctions. The records of conversion efficiency are close to this ideal value, that is, 25 % (cf. Chapter 1). If I consider an InGaN material with an indium content of 10% (E_g = 3.0 eV), the conversion efficiency limit is much smaller than silicon and it is about 5 %. The InGaN material is still an excellent challenger if good material quality with higher In content can be obtained to absorb most of the solar spectrum by stacking different InGaN layers with modulable bandgaps.

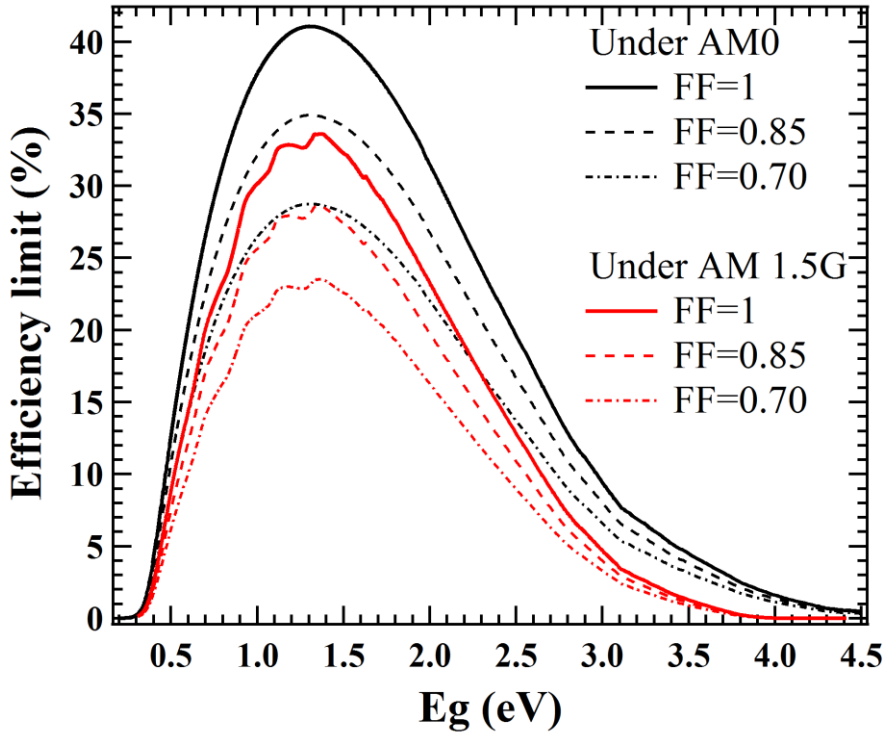

Fig. 2-11: Theoretical limit of the conversion efficiency calculated for a fill factor of 1 (ideal case), 0.85 and (highest fill factor possible) and 0.75 under normalized AM 0 and AM1.5 G solar spectra.

Because of the assumption of a perfect material free from defects and recombination, there is a difference between the theoretical limit calculated for the short-circuit current (Jsc), the open-circuit voltage (Voc) and the conversion efficiency, and the ones measured. In the following part, I described the different recombination possible in semiconductor material.

2-1.8 Recombination inside the material

Several phenomena of recombination exist in semi-conductor materials, which influence the effective lifetime of the photogenerated carriers. The effective lifetime is an important parameter to describe the quality of the material. The processes of recombination are often complex and coexist. The recombination in the bulk of the material is separate from the recombination on the surface.

Three types of recombination inside the volume affect the diffusion length (L_d) of the carriers and consequently their effective lifetimes: the radiative recombination, the Auger recombination and the Shockley-Read-Hall (SRH) recombination [8].

- Radiative recombination (τ_{rad}):

A radiative recombination is a recombination band to band, the inverse phenomenon of the generation of electron-hole pairs after the absorption of a photon. An electron located in the conduction band recombines with a hole located in the valence band with the emission of a photon. The energy of this photon is equal to the material bandgap. This process mainly appears for direct band gap semiconductors but is relatively rare in indirect bandgap semiconductors.

- Auger recombination (τ_{Auger}):

This non-radiative recombination appears when the density of free carrier is higher than 10^{17} cm^{-3} [9]. Because of this high carrier concentration, the probability of hits between free carriers is high. Some carriers release their energy (kinetic energy) to another carrier, which has a higher energetic state (equivalent to the band-to-band transition). The second carrier with higher energetic state comes back to the normal state by thermalization emitting a phonon.

Zhang et al. reported Auger recombination is largely responsible for limiting $In_{0.1}Ga_{0.9}N/GaN$ quantum well LED efficiencies at high injection current density $J \geq 40$ A/cm^2, which corresponds to a free carrier concentration of about 2.75×10^{18} cm^{-3} [10].

- The Shockley-Read-Hall recombination (τ_{SRH}):

This type of recombination, considered as extrinsic, is due to the crystal defects and metallic impurities present inside the material. The crystal defects create some deep levels inside the bandgap of the material, which reduce the effective lifetime of the free carriers.

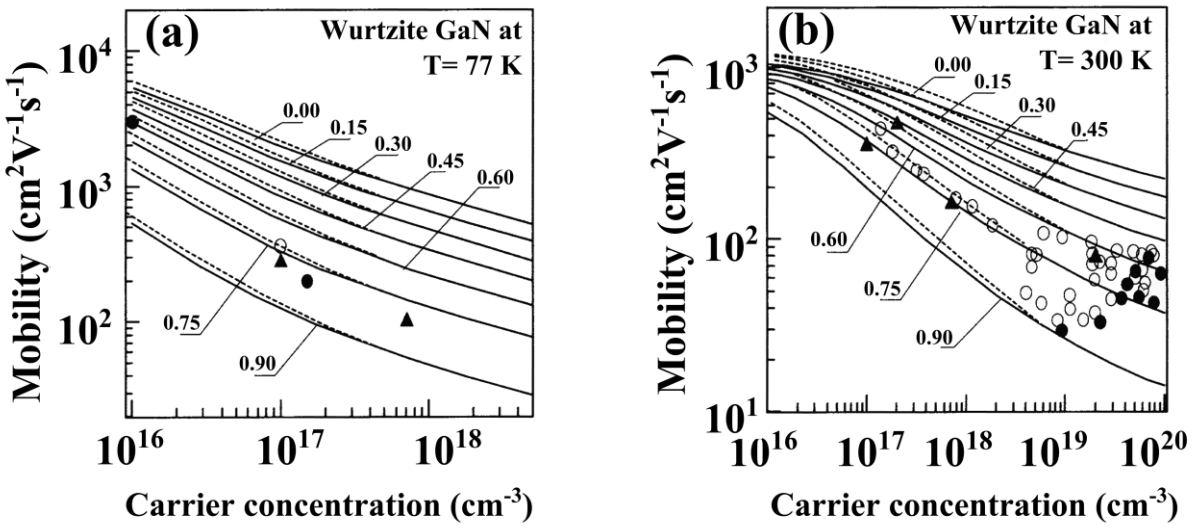

Fig. 2-12: Electron mobility of GaN at 77 K (a) and 300 K (b) as a function of carrier concentration with compensation ratios, denoted N_A/N_D, of 0, 0.15, 0.30, 0.45, 0.60, 0.75, and 0.90 [11].

The III-V nitride materials such as GaN and InGaN have a high concentration of free electrons resulting in an unintended n-type material. This high carrier concentration is not favorable to enhance the mobility of the photogenerated carriers. This is presented in *Fig. 2-12* for the wurtzite GaN at 77 and 300 K [11]. It is consequently important to develop growth techniques for this material to decrease the free electron concentration and thus enhance the mobility of the free carriers. This problem will be dealt with in Chapter 3. Furthermore, the deep level defects generated in the InGaN will be examined in Chapter 5.

InN films also have a high carrier concentration about 10^{18} - 10^{20} cm^{-3} [12], which is related to a poor crystal quality. This high carrier concentration was also responsible to a large difference between the bandgap measured by photoluminescence and the effective bandgap of InN films. This effect can be explained by the Moss-Burstein shift, which is presented in the following section.

2-1.9 Moss-Burstein shift

The Moss-Burstein shift can explain the difference between the InN bandgap values previously measured at 1.9 eV and more recently estimated at 0.7 eV. For the semiconductor with a small bandgap like InSb and InAs [13], it is known that the bottom of the conduction band has a non-parabolic dispersion because of the $\boldsymbol{k \cdot p}$ repulsion through the small energy gap between the valence and conduction bands. The dispersion of the conduction band as a function of the wave vector can be written as follows:

$$E_C(k) = E_g + \frac{\hbar^2 k^2}{2m_0} + \frac{1}{2}\left(\sqrt{E_g^2 + 4E_p \frac{\hbar^2 k^2}{2m_0}} - E_g\right), \tag{2-42}$$

where $\hbar$ is the reduced Planck constant (6.582×10^{-16} eV s), k is the wave vector (cm^{-1}), E_p the interaction energy $\boldsymbol{k}\cdot\boldsymbol{p}$ equal to $E_p = \left(\frac{2m_0}{\hbar^2}\right)\times\left|P_Z\right|^2$, where P_Z is the matrix element of the z component of the momentum operator.

From *Eq. (2-42)*, a large interaction energy $\boldsymbol{k}\cdot\boldsymbol{p}$ (E_p) increases the non-parabolic behavior of the conduction band. *Figure 2-13* shows the dispersion of the valence band and conduction band of InN material, calculated from *Eq. (2-42)* [14]. The Fermi level corresponds to an electron concentration of about 10^{20} cm^{-3}. For a small value of k, it is possible to approximate the dispersion of the conduction band by a parabola:

$$E_C(k) \approx E_g + \frac{\hbar^2 k^2}{2m_e^*(0)}. \tag{2-43}$$

$m_e^*(0)$ is the effective mass of an electron located at the minimum of the conduction band at the Γ point [unit: $MeV\times c^{-2}$].

The parabolic form of the conduction band is also found in *Fig. 2-13*. We can notice that for wave vectors $k > 0.05$ $Å^{-1}$, the parabolic and non-parabolic dispersions differ considerably.

Figures 2-14 shows the absorption threshold of InN materials as a function of the free electron concentration and also the bandgap calculation for the parabolic and non-parabolic cases [12]. For free electron concentration above 10^{19} cm^{-3} the bandgap follows a non-parabolic behavior. It means that for an electron concentration of 10^{19} cm^{-3} and above inside InN materials, the Fermi level is located inside the conduction band. The optical absorption is thus forbidden for transitions under the Fermi level. The optical absorption starts from energies above the Fermi level, which overestimates the intrinsic bandgap of the material. This is the Moss-Burstein effect. The optical emission under the Fermi level is still possible, like photoluminescence, but with a weak intensity and a wider energy peak compared to the emission of the intrinsic band edge.

Because of the high carrier concentration inside GaN, InN and their alloys InGaN, these semiconductors are unintended n-type doping material. The fabrication of a *p-n* InGaN junction is quite challenging due to the p-type doping that must compensate the n-type doping. A possible way to bypass the p-type doping is the fabrication of a Schottky junction. In the following I presented the principle of the Schottky junction, the current transport processes, and the theoretical limit of the open-circuit voltage compared to the *p-n* junction.

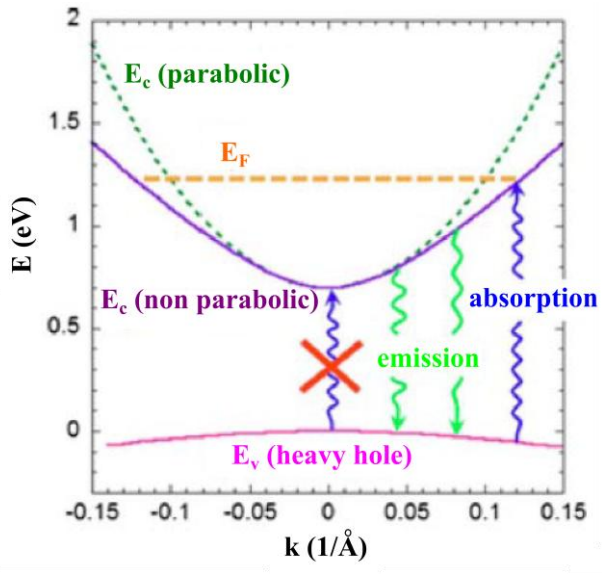

Fig. 2-13: Theoretical dispersion curve of valence and conduction band of InN by using the k·p model. The Fermi level for n = 10^{20} cm^{-3} is represented in orange [14].

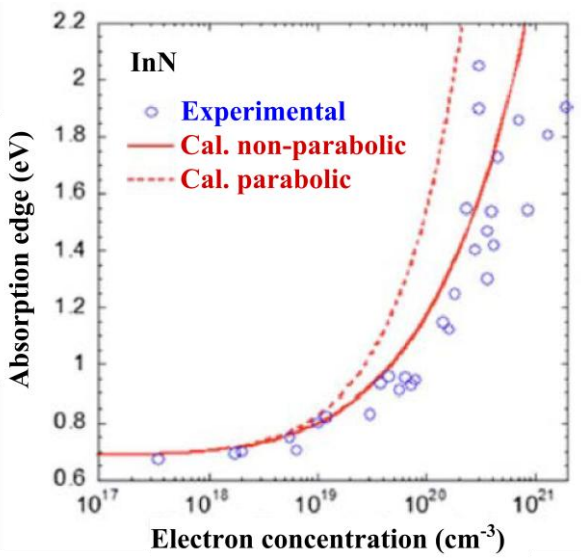

Fig. 2-14: Absorption threshold (optical bandgap) in function of electron concentration. InN bandgap calculated by a dispersion curve of the parabolic conduction band and non-parabolic is also represented [12].

2-2 Schottky junction

In Chapter 1, I presented the issues relevant to InGaN films, one of them was the poor properties of *p-n* homojunction InGaN because of high unintended n-type doping material due to the presence of defects. A simple way to fabricate a junction can also be realized by Schottky contact. In this section, I will present the Schottky junction with a short history, the principle and an overview of Schottky junction properties using GaN and InGaN films.

2-2.1 First discovery and introduction to Schottky diodes

Charles Fritts fabricated one of the world's first solar cell in 1883. This solar cell consisted of coated selenium semiconductor with a thin layer of gold to form the junction, which was a Schottky junction.

The Schottky junction is a junction between metal and semiconductor. This name comes from German physicist, Walter Hermann Schottky, who founded the basis of semiconductor physics and electronics. He is famous after his research based on the theory of thermionic emission and field electron emission, the Schottky junction and Schottky anomaly (punctual defects). The barrier existing at the junction between metal and

semiconductor due to the difference of their work functions, now widely known as Schottky barrier, was suggested in the context of semiconductor devices in 1930s.

Because of differences in the availability of charged carriers in metal and semiconductor, essentially all the potential drop occurs on the semiconductor side of the junction. At the interface, a depletion region is formed as in *p-n* junctions. The metal acts similarly to a very heavily doped semiconductor from a point of view of its effect on the electrostatic properties of the depletion layer.

The height of the Schottky barrier varies with applied voltage, which gives rise to a thermionic emission component of the current, which is given by:

$$J_{oe} = A^* T^2 \exp\left(\frac{-q\phi_B}{kT}\right)\exp\left(\frac{-qV}{kT}-1\right), \tag{2-44}$$

where A^* is the effective Richardson constant (in A cm^{-2} K^{-2}), which is specific to each semiconductor. The magnitude of this constant depends primarily on the height of the barrier at interface, ϕ_B. The majority-carrier component is much larger than the minority-carrier. This extra component of current is undesirable from the point of view of photovoltaic energy conversion because it increases the dark saturation current of the diode, and hence, decreases V_{oc}. Therefore, a larger barrier ϕ_B enhances the photovoltaic performance.

We may choose a metal with the highest work function. However, it was found experimentally that, for many semiconductors, the size of the induced barrier was independent of the metal work function. This was attributed to a very large number of interface states at the metal-semiconductor interface due to lattice mismatch and to possible contaminants on the semiconductor surface. These clamp the potential in the surface region.

Even though Schottky diodes can be made in a simple way without the *p-n* junction formation, their performance is limited by an additional parasitic current component compared with *p-n* junctions [1].

2-2.2 Early researches and theory about Schottky diodes (silicon case)

To study the properties of Schottky diodes, the most common semiconductor material was silicon. In 1968, M.J. Turner and E.H. Rhoderick recognized the effect of an interfacial film on the height of Schottky barriers obtained by evaporating metal films (Au, Ag, Cu, Ni, Pb and Al) on n-type silicon [15]. They observed that the height of the barrier initially depended on the particular method of surface preparation, and subsequently showed a slow change with time, reaching a steady value over a period of days or even weeks. This final value was independent of the method of surface preparation, but depended on the choice of metal. For junctions made by evaporation on to silicon cleaved in an ultra-high vacuum, the barrier height shows no ageing and is substantially independent of the metal. These observations can be explained in terms of the existence of a thin oxide layer on the chemically prepared surfaces, together with the assumption that the density of surface states is about two orders of magnitude lower on the chemically prepared surfaces than on the cleaved surfaces.

In 1971, H.C. Card and E.H. Rhoderick were the first to attempt to relate the properties of the interfacial region to Schottky diode characteristics in a quantitative manner [16]. They realized a MIS silicon Schottky diode, gold/silicon, oxide/silicon, and studied its properties depending on the oxide thickness from 8 to 26 Å. A theory was developed which allowed the saturation current obtained from a semi logarithmic I-V plot to be corrected for the parameters of the interfacial film. This theory has a limitation imposed by the assumption that the tunneling transmission probability of the film is independent of the bias voltage applied to the diode.

The interest for the MIS silicon Schottky diode is the capability to reach very high V_{oc}, higher than *p-n* junctions. This was theoretically demonstrated by M.A. Green in 1974 [17] and silicon MIS solar cells were fabricated by R.B. Godfrey and M.A. Green in 1979 with V_{oc} of 655mV and conversion efficiency of 17.6% [18].

Electron transport at metal-semiconductor interface was explained in a general theory by R.T. Tung in 1992. It explains many anomalies such as ideal factors greater than 1 in the experimental results by the presence of inhomogeneities in the Schottky barrier height [19].

2-2.3 Schottky contact on III-V nitride films

After the success of high quality GaN growth by Amano et al. in 1990 [20], Nakamura et al. [21], and Khan et al. in 1991 [22], the research of both ohmic and Schottky contacts on GaN was of a primary interest. S. C. Binari et al. measured the Schottky barrier height (SBH) of Ti on n-type GaN as 0.58 eV [23]. P. Hacke et al. estimated the SBH between Au and n-type GaN at 0.84 eV and 0.94 by current-voltage (I-V) and capacitance-voltage (C-V) measurements, respectively [24]. Lin et al. achieved low resistance ohmic contacts to n-type GaN using Ti/Al bilayer metallization after annealing the contact at 900ºC for 30 sec. The lowest specific contact obtained was $8\times10^{6}\ \Omega\ cm^{2}$ [25].

From these advancements, many research activities focused on obtaining a good Schottky junction on GaN, *Table 2-3* summarizes the SBH and ideality factor *n* at 300 K for various metals used [26].

Table 2-3: Schottky barrier obtained on n-GaN grown on sapphire substrate using different metal deposited.

Metal	Work function (eV)	Ideality factor	SBH from I-V (eV)	SBH from C-V (eV)
Pt	5.65	1.21	1.03	1.04
Pd	5.12	1.14	0.91	0.94
Au	5.1	1.03	0.84 (0.87)	0.94
Ti	4.33	1.28	0.59	0.58
Ni	5.15	1.15	0.66	0.56
Ni +200ºC	-	1.14	1.0	0.8

After annealing Ni above 200ºC, the formation of Ni_3N and Ni_4N at the Ni/GaN interface increases SBH.

The Schottky properties at 300 K obtained for n-GaN grown on SiC substrates for various metals are given in *Table 2-4* [27].

Table 2-4: Schottky barrier obtained on n-GaN grown on SiC substrate using different metal deposited.

Metal	From I-V		From C-V	
	SBH (eV)	Ideality factor	SBH (eV)	Carrier concentration (cm^{-3})
Cr	0.53	1.05	0.58	6×10^{17}
Au	1.03	1.15	1.03	6×10^{17}
Ni	1.15	1.17	1.11	1×10^{18}

Due to the depletion layer generated by the Schottky junction, researches about deep-level defects were reported. Y. Nakano et al. reported about the acceptor levels in Pt/Mg-doped GaN Schottky junction by deep-level transient spectroscopy [28].

Concerning the Schottky contact on InGaN films, limited works on Schottky barriers of metal/n-InGaN are reported because of the presence of many defects. J. S. Jang et al. reported Schottky characteristics of Pt contacts to Si-doped n-$In_{0.1}Ga_{0.9}N$ [29]. Pt with a thickness of 50 nm was deposited to form the Schottky junction. They reported Schottky barrier height of 0.62 eV with an ideality factor of 2.90 by thermionic emission fit, and 1.39 eV with an ideality factor of 2.31 by thermionic field emission fit [29]. D. J. Chen et al. reported a high quality Schottky contact on n-$In_{0.2}Ga_{0.8}N$ alloys prepared for photovoltaic devices [30]. They deposited Au/Pt (5/5nm) by e-beam evaporator to form the Schottky contacts. They observed a variation of the Schottky barrier depending on the carrier concentration of n-$In_{0.2}Ga_{0.8}N$. For carrier concentration of about 7.7×10^{16}, 5.0×10^{17}, and 2.0×10^{18} cm^{-3}, the Schottky barrier height was measured at 1.04, 0.52 and 0.49, respectively [30].

In the following part, I describe the current transport inside a Schottky junction and the theoretical limit of the open-circuit voltage.

2-2.4 Fundamental differences between Schottky and *p-n* junctions

The fundamental difference between these two components is that the Schottky diode uses majority carriers while the *p-n* diode uses minority carriers. As *Fig. 2-15* shows, we can notice the following differences between their characteristic I-V:

- The inverse current is weaker for the *p-n* diode.

- The forward current starts to increase at a higher voltage for the *p-n* diode (for example, 0.3 V for Al-n:Si and 0.6 V for the *p-n* diode).
- The fluctuation of the forward voltage as a function of temperature is smaller for the barrier metal/semiconductor than for the *p-n* diode.
- The inverse current is more sensible to the inverse tension for the barrier metal/semiconductor.

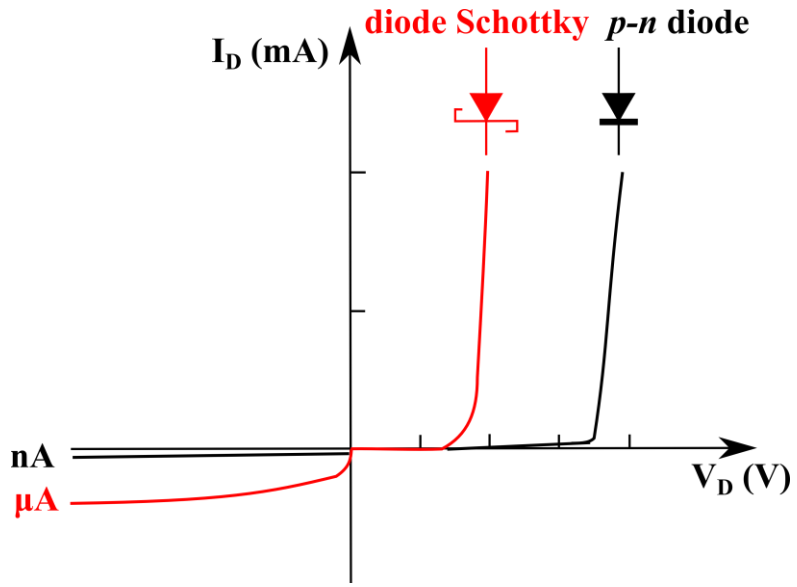

Fig. 2-15: Current-voltage characteristics comparison between Schottky and p-n diodes.

2-2.5 Current transport process inside Schottky junction

We can categorize the current transport processes inside Schottky junction into three types: the thermionic emission (TE) over the barrier, the field emission (FE) near the Fermi level, and the thermionic-field emission (TFE) at energy between TE and FE (*Fig. 2-16*). While FE is a pure tunneling process, TFE is tunneling of thermally excited carriers which see a thinner barrier than FE. The relative contribution of these components depends on both temperature and doping level. A rough criterion can be set by comparing the thermal energy kT to E_{00} that is defined by:

$$E_{00} \equiv \frac{qh}{4\pi}\sqrt{\frac{N_D}{m^* \varepsilon_s}}, \tag{2-45}$$

where N_D is the donor impurity concentration, m^* is the electron effective mass, ε_S is the electric permittivity of the semiconductor, and h is the Planck constant. The rough criterion is given as following:

thermionic emission (TE) $$\frac{kT}{E_{00}} >> 1, \tag{2-46}$$

thermionic field emission (TFE)
$$\frac{kT}{E_{00}} \approx 1, \tag{2-47}$$

field emission (FE)
$$\frac{kT}{E_{00}} << 1, \tag{2-48}$$

In *Fig. 2-16*, ϕ_m represents the metal work function, χ is the electron affinity of the semiconductor, SBH is the Schottky barrier height and ϕ_{bi} is the build-in potential. The quantitative examination will be done in Chapter 5.

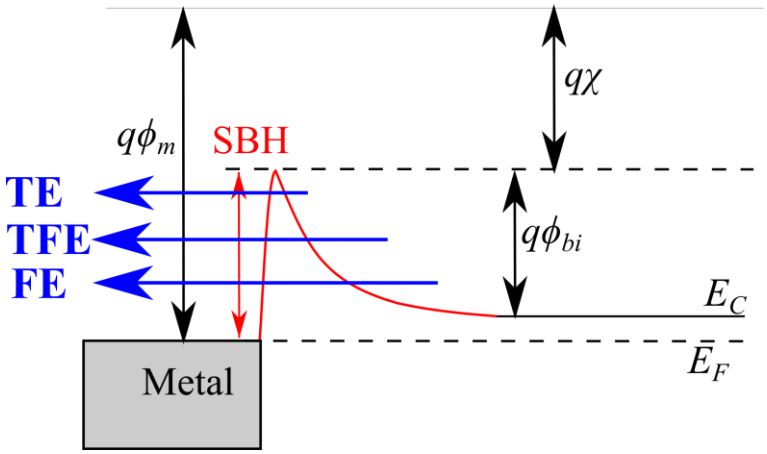

Fig. 2-16: Diagram of a Schottky junction on n-type semiconductor representing the different regimes of current transport.

The following estimation of the ideality factor *n* can also be used to describe the current transport process:

$$n = \frac{E_{00}}{kT} \coth\left(\frac{E_{00}}{kT}\right). \tag{2-49}$$

The current conduction can be explained by the thermionic emission (TE) model if *n*~1. But if *n*~2 or higher, the current conduction must be considered by the thermionic field emission (TFE) model [31].

2-2.6 Theoretical limit of the open-circuit voltage (V_{oc}) for Schottky junction compared to *p-n* junction

Under illumination, Schottky solar cells display a current-voltage characteristic with a similar shape as *p-n* junctions. The main different is that the limitation in V_{oc} for the Schottky junction is due to the limit in short-circuit current (J_{sc}) and also the Schottky barrier height, which is the difference between the work function of the metal and the electron affinity (3.3±0.2 eV for GaN [32]). V_{oc} can be written as follows:

$$V_{OC} = \frac{nkT}{q}\left[\ln\left(\frac{J_{SC}}{A^{*}T^{2}}\right) + \frac{q\phi_B}{kT}\right], \tag{2-50}$$

where n is the ideality factor of the diode, A^{*} is the Richardson constant, which equal to 26.4 A.cm^{-2}.K^{-2} for GaN (a detailed calculation will be presented in Chapter 5), ϕ_B is the Schottky barrier height, and T the temperature. At 300 K for n-GaN, if we assume that all the photon above the bandgap energy are absorbed and converted to photogenerated carriers for a normalized solar spectrum AM1.5G (from 300 to 365 nm), the theoretical limit of J_{sc} is J_{sc}= 0.61 mA/cm^2. To estimate the V_{oc} limit, we assume the ideality factor equal to 1 and the Schottky barrier height to 1.9 eV which is the difference between the electron affinity of GaN (3.3 eV) and the gold work function (5.2 eV). In this case the V_{oc} limit is calculated to be 1.34 V for the Schottky junction formed by a gold layer on n-GaN. This V_{oc} limit is much smaller than the case of a *p-n* junction using the same semiconductor material calculated at 2.8 V previously in this chapter.

Thus the Schottky device is very useful to fabricate a depletion layer, which is necessary to study the deep level defects inside the material as I will present in Chapter 5, but as far as the photovoltaic performance is concerned the *p-n* junction has a higher potential. In my thesis, I focused first on realizing good Schottky junctions on n-GaN and n-InGaN in order to study the deep level defects of these materials and also on clarifying their potential for photovoltaic application.

2-3 Equipments for characterization

In this section I will describe succinctly the different equipments for electric and optical characterizations. The equipments used to analyze the crystal quality of thin film epitaxial layer and the surface roughness will also be described.

2-3.1 Structural characterization

a) X-ray diffraction (XRD)

I used a PANalytical X'Pert PRO diffractometer for X-ray diffraction analysis in order to estimate the c- and a-lattice parameters of the III-V nitride films grown on (0001) sapphire substrates by MOCVD. This measurement is also useful to determine the indium composition (or InN mole fraction) of the deposited $In_xGa_{1-x}N$ layer by using the Vegard law. The wurtzite crystal structure is illustrated in *Fig. 2-17*, and the diffraction geometry is represented in *Fig. 2-18*. The reflected X-ray analysis gives information for all the deposited layers and the substrate at the same time. The c-lattice and a-lattice constants of the $In_xGa_{1-x}N$ layer and the GaN epilayer are necessary to estimate the crystal quality and the growth condition. The c-lattice constant is determined

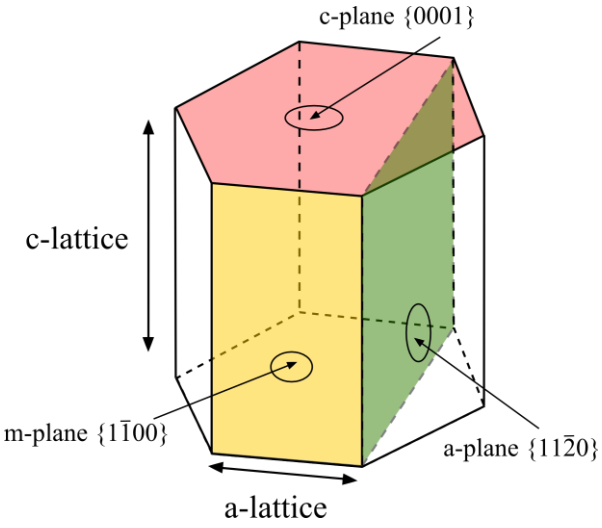

Fig. 2-17: Illustration of the wurtzite crystal structure with the c- and a-lattice constants, and the c-,a- and m-planes.

by the scan of the parallel plane (0002), normal to the surface, and the a-lattice constant is then determined by the scan of the anti-parallel plane (10$\bar{1}$1).

For each peaks of GaN and $In_xGa_{1-x}N$, the position in degree (horizontal axis), the intensity in counts per second (vertical axis), and the full width at half maximum (FWHM) are important parameters. For each peak, the distance between atomic layers (d) is directly calculated by the software depending on the crystal orientation, and can be estimated by using the relation of the Bragg diffraction $n\lambda=2d\times sin\theta$ where n is an integer, λ the wavelength of the X-rays source, and θ estimated with the peak position.

The distance between atomic layers (d) is necessary to estimate the c- and a-lattices constants by using

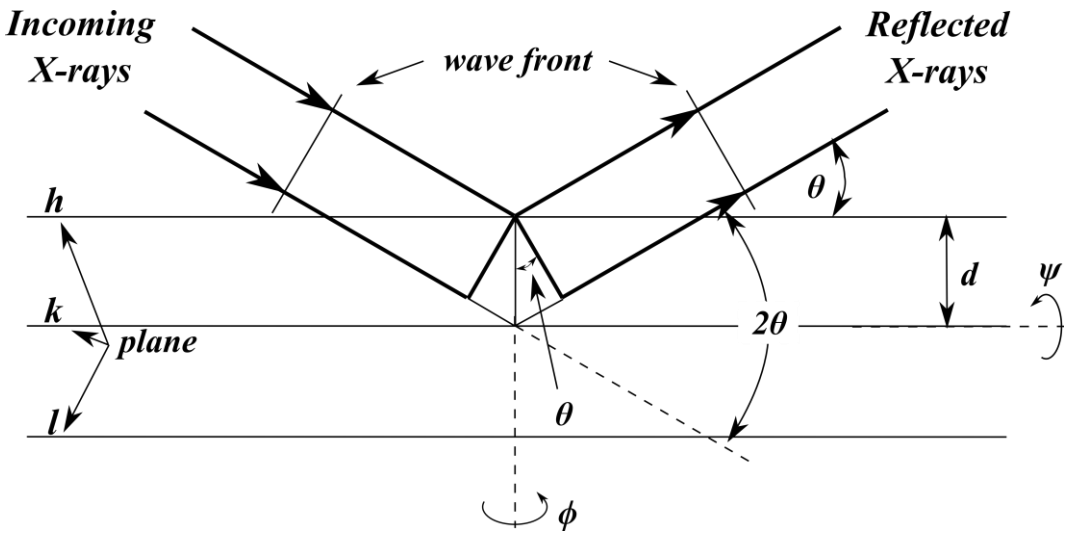

Fig. 2-18: Illustration of the diffraction geometry with the different crystalline planes of the sample and the angles of the diffractometer used.

the general formula for the wurtzite crystal structure:

$$\frac{1}{d^2} = \frac{4}{3a^2}\left(h^2 + hk + k^2\right) + \frac{1}{c^2}l^2 , \tag{2-51}$$

where a is the a-lattice constant, c is the c-lattice constant, and $h\ k\ l$ the Miller indices of parallel planes depending on the crystal orientation. *Equation (2-51)* is written as follows depending on the $(h\ k\ l)$ plane analyzed:

for (0002) plane $$c = 2d , \tag{2-52}$$

for $(10\bar{1}1)$ plane $$a = \sqrt{\frac{4}{3}\left(\frac{c^2 d^2}{c^2 - d^2}\right)} . \tag{2-53}$$

The intensity of a specific peak observed has the information about the thickness of the specific layer studied. For two layers with identical thickness, the peak with the lowest FWHM value has a better crystal quality. Indeed, the reflected signal is a sum of the diffracted X-rays intensity from a specific crystal orientation. The layer with homogeneous c- and a- lattice constants has a unique angle 2θ of diffraction instead of a poor crystal quality with non-homogeneous lattice constants that has a larger 2θ distribution of diffracted X-rays.

The Vegard law used the bandgap of the GaN and the $In_xGa_{1-x}N$ films to estimate the InN mole fraction by using the following equation:

$$E_{g(In_xGa_{1-x}N)} = x \times E_{g(InN)} + (1-x) \times E_{g(GaN)} - bx(1-x) , \tag{2-54}$$

where $E_{g(InxGa1-xN)}$, $E_{g(InN)}$ and $E_{g(GaN)}$ are the bandgap of the $In_xGa_{1-x}N$, InN and GaN films, respectively. The parameter b is called the bowing parameter. Many different values of bowing parameter are found in literature: such as a large bandgap bowing of 3.8 eV in 1998 [33] before the reevaluation of the InN bandgap to 0.7 eV. For my $In_xGa_{1-x}N$ films, I found that a bowing parameter of 1.43 eV fits well our experimental values, which corresponds to another value found in literature [34] using 0.7 eV for the InN bandgap.

The growth mode of the crystal is determined by a mapping of the $(10\bar{1}4)$ plane. If the atoms of the GaN layers and the atoms of the $In_xGa_{1-x}N$ layers are vertically aligned, it means that the a-lattice constants are equivalent. This growth mode of the $In_xGa_{1-x}N$ is strained to the GaN layer as represented on *Fig. 2-19 (a)*. The corresponding mapping in reciprocal space of a strained growth is presented in *Fig. 2-20*, where the centers of GaN and InGaN peaks are vertically aligned. If the peak of $In_xGa_{1-x}N$ layer becomes closer to the axis at 45° (*Fig. 2-21*) the growth mode is more relaxed and the a-lattice is enlarged compared with the one of the GaN epilayer as presented in *Fig. 2-19 (b)*. A strained growth is preferable to decrease the formation of defects inside the crystal structure, which affects the electrical and optical properties of the material.

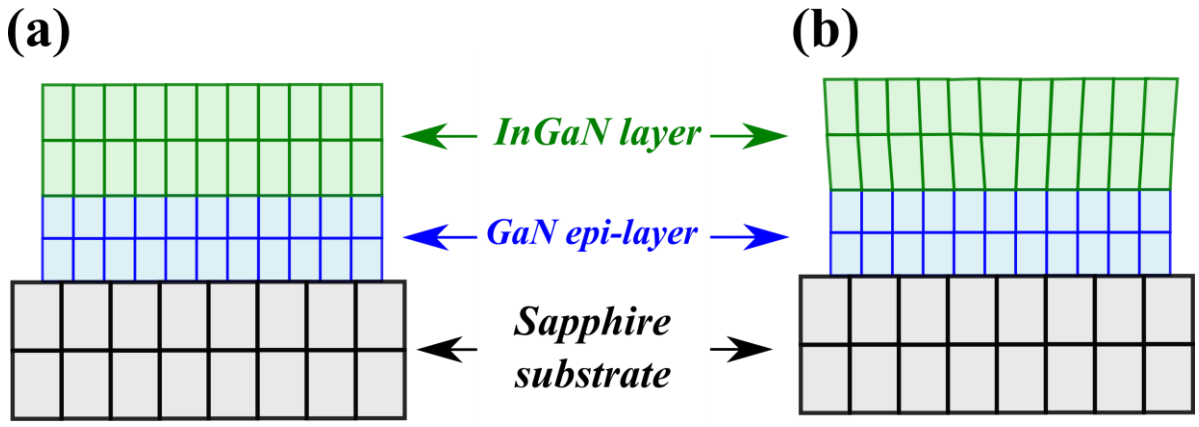

Fig. 2-19: Illustration of the crystal structure for a strained growth mode (a) and a more relaxed growth mode (b).

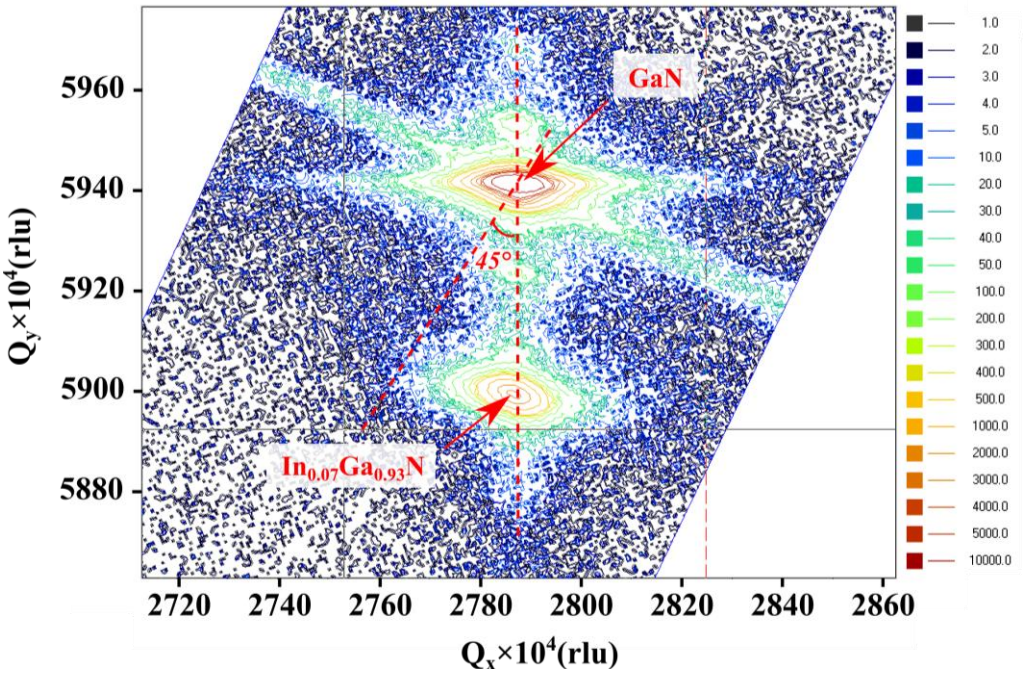

Fig. 2-20: Mapping of the ($\mathbf{10\bar{1}4}$) plane for $In_{0.07}Ga_{0.93}N$ / epi-GaN structure represented in reciprocal lattices Q_x, Q_y to illustrate a strained growth mode of InGaN on GaN.

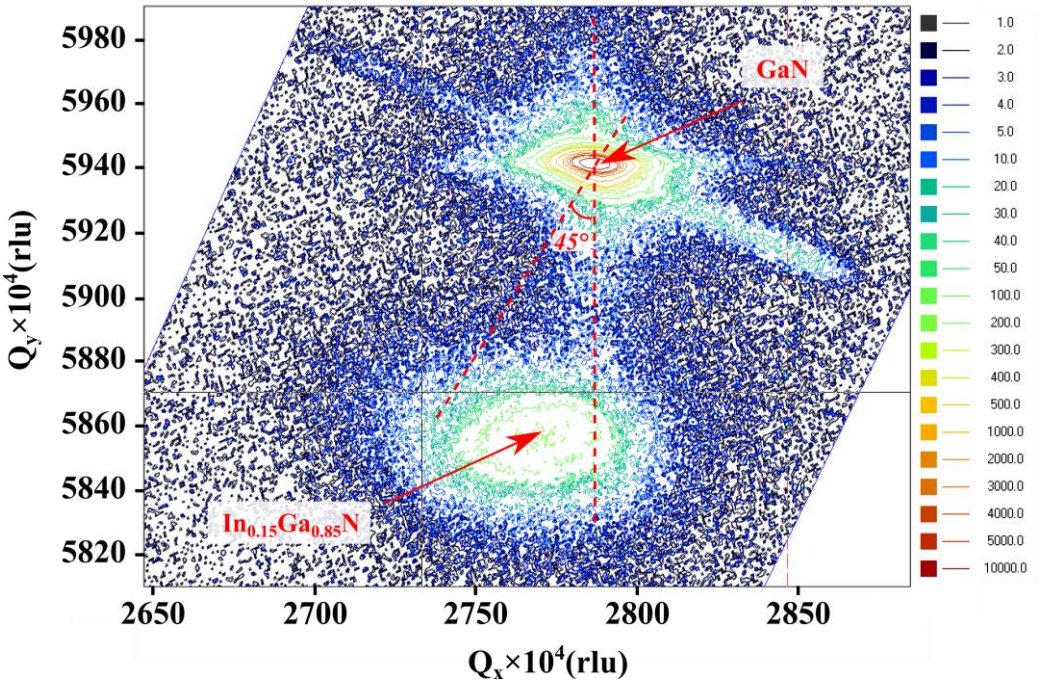

Fig. 2-21: Mapping of the ($10\bar{1}4$) plane for $In_{0.15}Ga_{0.85}N$ / epi-GaN structure represented in reciprocal lattices Q_x, Q_y to illustrate a more relaxed growth mode.

b) The Atomic Force Microscope (AFM)

Another important parameter is the surface roughness to evaluate the surface quality of the crystal grown. If the growth condition is not optimized the distance between each atomic plane can fluctuate, which generates dislocations inside the layer grown. This will result in a rough surface on the top of the crystal structure. In opposite way, if the conditions are well optimized the density of dislocations decreases considerably, which will result in a smooth surface. In the following the AFM will be described briefly.

I illustrated the schematic principle of the AFM in *Fig. 2-22*. The measurement of the roughness used the reflection of a laser beam on the surface of the cantilever. The tip is mounted on a reflecting cantilever. If the laser beam is deviated, it means that the cantilever is inflected (could be in both ways up or down), which means the presence of inter-atomic forces between the atoms of the tip and the atoms of the surface sample. The measurement of the pit deviation is realized by the deviation of the laser on the photodiodes detector. The voltage detected, coming from the light intensity, is compared between each of the 4 photodiodes to calculate the deviation and thus the topography of the sample surface.

The lateral resolution is on the order of few nanometers, but the vertical resolution of an AFM is on the order of few angstroms, atomic steps are easily visualized for samples with clean and smooth surface.

AFM images will be presented in Chapter 3 concerning the optimization of the growth condition of $In_xGa_{1-x}N$ films.

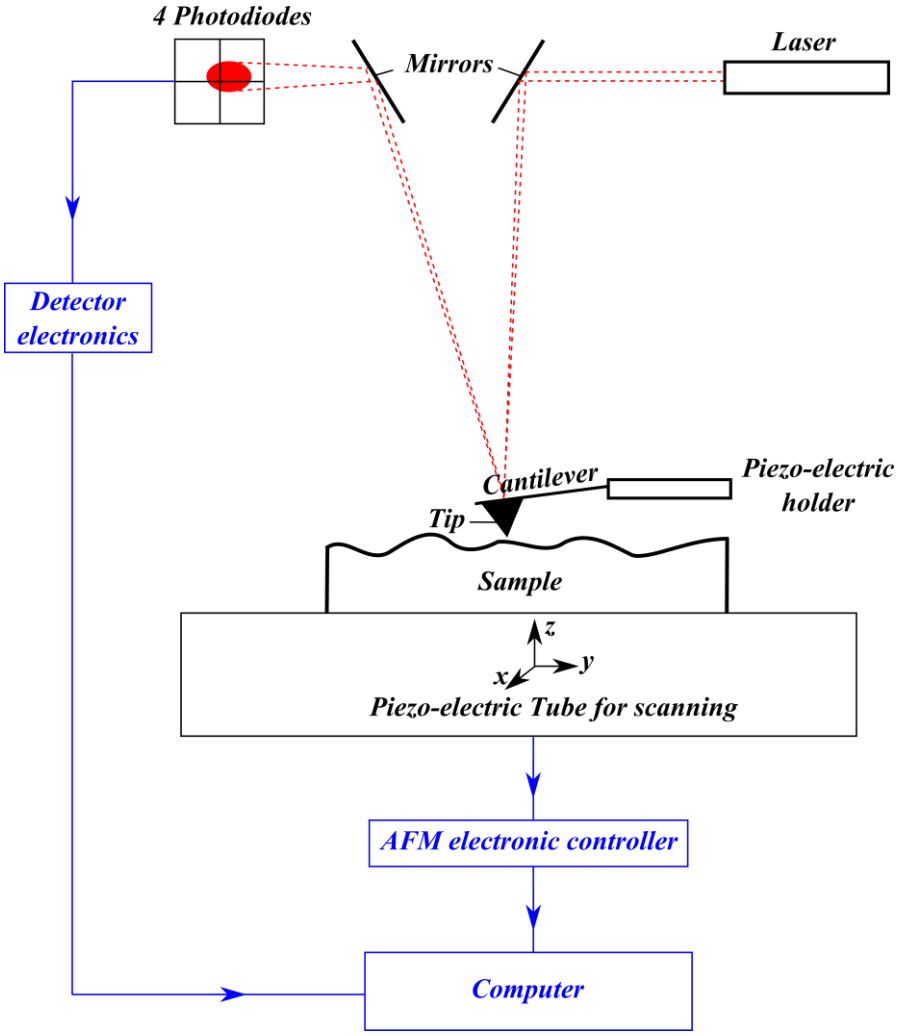

Fig. 2-22: Schematic principle of an Atomic Force Microscope (AFM).

2-3.2 Optical characterizations

a) Transmittance and reflectivity

I used the transmittance equipment to describe the optical bandgap of the $In_xGa_{1-x}N$ films deposited. The transmittance spectrum was realized by a ultra-violet and visible sources coupled to a monochromator. A sapphire without a deposited layer is also used as reference. At each wavelength, the transmittance of our sample is compared with the reference.

By using *Eq. (2-2)*, the absorption coefficient can be calculated for each wavelength. I obtained the optical bandgap by plotting $(\alpha h\upsilon)^2$ as a function of $h\upsilon$ (eV), where α is the absorption coefficient (cm^{-1}), h the Planck constant, and υ the frequency of the wavelength related by *Eq. (2-1)*.

b) X-ray photoemission spectroscopy

The X-ray photoemission spectroscopy (XPS) is used to analyze the chemical composition by the binding energy of the electrons coming from atomic orbitals of different atoms constituting the sample. X-rays at a particular wavelength hit the sample surface. The electrons from different atomic orbitals of different atoms that absorb this high energy are expulsed with a high kinetic energy and collected in an electron energy analyzer. A magnetic field inside the electron energy analyzer curves the path of electrons depending on their particular kinetic energy. A electron detector counts the number of electrons at a specific kinetic energy. This measurement is realized under ultra high vacuum between 10^{-7}-10^{-8} torr. The detection depth of conventional XPS is about a few nanometers. The relation to convert the kinetic energy to the binding energy is given by the following equation:

$$E_{Binding} = E_{photon} - (E_{kinetic} + \phi), \tag{2-55}$$

where $E_{Binding}$ is the binding energy (BE) of an electron, E_{photon} is the energy of the x-ray photons being used, $E_{kinetic}$ is the equivalent kinetic energy of the same analyzed electron, and ϕ is the work function of the spectrometer.

For my study, I could use the hard x-ray photoemission spectroscopy at SPring 8 facility, which delivers the most powerful synchrotron radiation currently available. Because of the high kinetic energy of the electron excited by hard x-rays (5.95 KeV), the detection depth is about ~20nm. The total energy resolution is as fine as 240 meV, which is considerably higher than conventional XPS of ~600meV. Thus, the electrons from the valence spectra with a very low binding energy are analyzed with a much higher sensitivity than conventional XPS. A detailed characteristic is given in Chapter 4.

2-3.3 Electrics characterizations

a) The Current-voltage (I-V), current- frequency (C-f) and current-capacitance (C-V) analysis

During the description of the solar cell principle, I introduced the current-voltage characteristic which gives the most important characterization parameters such as the open-circuit voltage (V_{oc}), the short-circuit current (J_{sc}), the series resistance (R_s), the shunt resistance (R_{sh}), the fill factor (FF) and the conversion efficiency (η) under normalized AM1.5G light. The I-V characteristic under dark condition is also important to determine the Schottky barrier height and the ideality factor of the diode.

The current-voltage characteristics for Schottky solar cell under dark condition will be examined in Chapter 5 together with the current-frequency and the current-capacitance characteristics, which are important characterization to determine the carrier concentration, the build-in potential (V_{bi}) and the width of the depletion layer (W).

The characterization of the small solar cell devices using GaN and InGaN materials generates a low current, thus it is important to have an accurate I-V probe system with noise reduction. The I-V probe system and the Keithley current-voltage measurement facility used both tri-axial cables for the noise reduction, but an adaptor is necessary to effectively connect these two elements. I fabricated an adaptor to use tri-axial cables and thus to reduce the electrical noise during the measurement with the I-V probe system. I detailed the electrical circuit of this adaptor in *Fig. 2-23*.

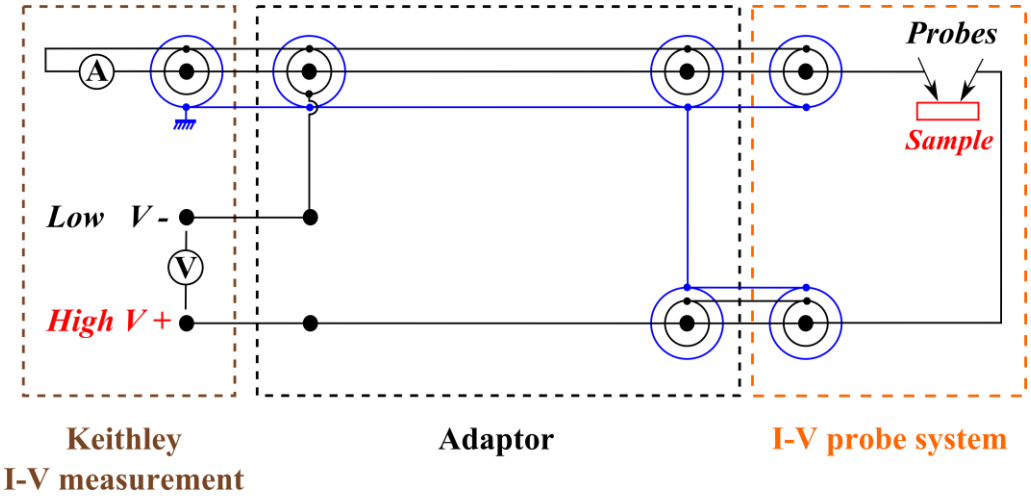

Fig. 2-23: Electrical circuit of the adaptor fabricated between the I-V measurement and the I-V probe system with tri-axial cables connection.

To confirm the noise reduction, two Schottky devices were tested with the previous I-V probe system and the new I-V probe system using the tri-axial cables. The I-V characteristics under dark condition are presented in *Fig. 2-24*. For both high quality device (Device B) and low quality device (Device A), the reverse current was slightly reduced due to the noise reduction from the tri-axial cable, so a more accurate estimation of the reverse leakage current can be performed. The forward current is similar, so the evaluation of the Schottky barrier height and the ideality factor remain equal.

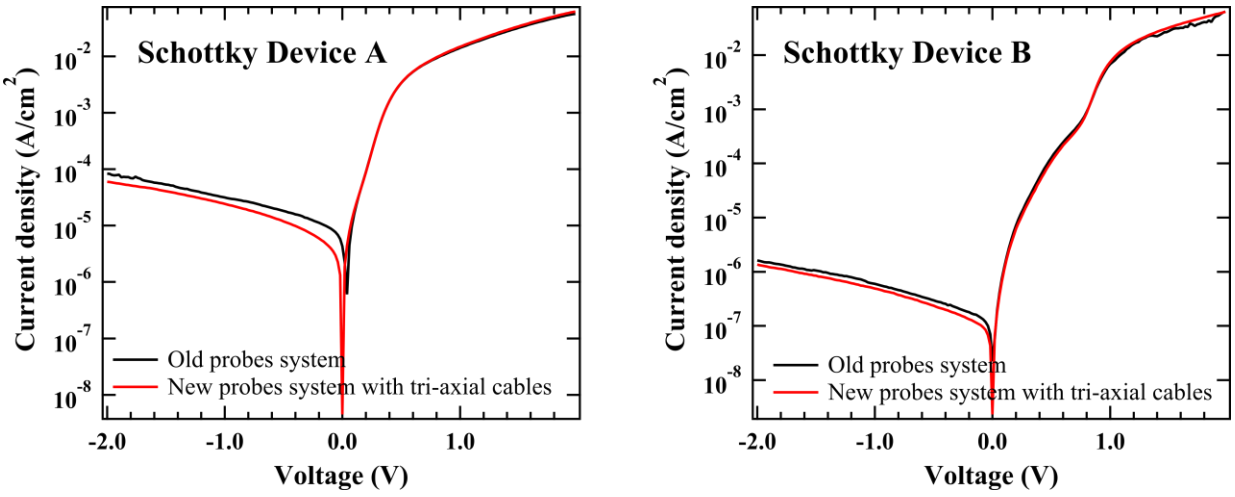

Fig. 2-24: I-V characteristic of two Schottky devices using the previous probes system and the new I-V probes system with the adaptor using tri-axial cables connection.

I measured the I-V characteristic by using a solar simulator of grade AAB. Each solar simulator is classified into A, B or C grades according to three features: the spectral match to the normalized spectra AM1.5G, the spatial uniformity, and the temporal stability. Each of these features is tested and classified with letter A, B or C reflecting the quality of the solar simulator to reproduce the normalized solar spectrum AM1.5G. The best solar simulator has a class AAA representing the spectral match, the irradiance spatial non-uniformity and the temporal stability, respectively.

I could use a solar simulator composed of a xenon lamp and some filters to match the normalized AM1.5G spectrum and also a solar simulator of class AAB. The solar spectrum AM1.5G is represented in *Fig. 2-25* beside the xenon lamp with and without AM1.5G filter. As we can see, a slight difference exists in short wavelengths even for good quality solar simulators due to the xenon lamp used. Two perturbations in the xenon lamp spectra exist around 470 and 770 nm.

A referenced solar cell is used to calibrate the spectral irradiance with an accurate current output under AM1.5G illumination before the characterization of our samples. Because the referenced solar cell is made by amorphous silicon solar cell (a-Si) with a material band gap of 1.7 eV, even if the output current measured is the same for both solar simulators, a large difference for the short circuit-current (J_{sc}) is observed for our devices that are more sensible in the short wavelengths. As a consequence, the photovoltaic characteristic for large bandgap materials can depend strongly on the solar simulator itself. It is important to take this fact into consideration and to compare the photovoltaic properties by using the same solar simulator.

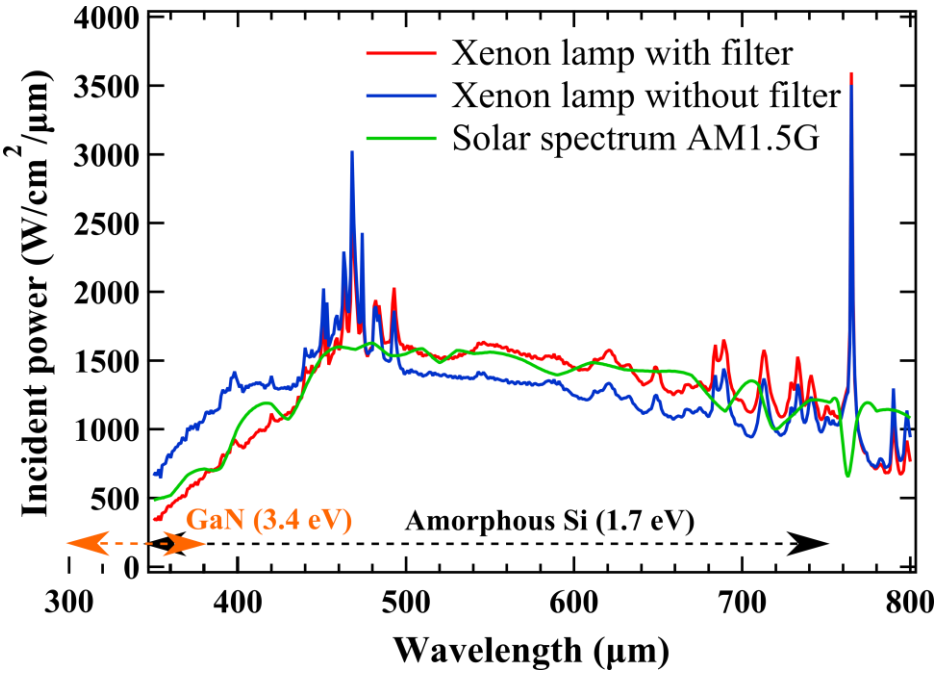

Fig. 2-25: Solar spectrum AM1.5G from 350 to 800nm compared to the Xenon lamp spectrum with and without filter to match the AM1.5G spectrum.

2-4 Conclusion

I described in this chapter the principle of a solar cell and its essential parameters such as the open-circuit voltage (V_{oc}), the short-circuit current (J_{sc}), the series resistance (R_s), the shunt resistance (R_{sh}), the fill factor (FF) and the conversion efficiency (η) under normalized AM1.5G light. The case of p-n junction and the Schottky junction were approached with their theoretical limits concerning the conversion efficiency. The limiting factors were also described, especially the high concentration of the free carriers present unintentionally in the GaN, InN and their alloys $In_xGa_{1-x}N$ films. Finally the different equipments of characterization were also presented. Some characterization such as the current-voltage analysis or the deep-level defect analysis will be fully described in Chapter 5 and 6.

The next chapter will present the deposition technique, the Metal Organic Chemical Vapor Deposition system, and an optimization of the growth of $In_xGa_{1-x}N$ in order to control the bandgap of the material with a good crystal quality.

References chapter 2

[1] M. A. Green, *Solar cells Operating Principles, Technology and System Applications*. Prentice Hall, 1998.

[2] S. Strite and H. Morkoç, "GaN, AlN, and InN: A review," *Journal of Vacuum Science & Technology B*, vol. 10, no. 4, p. 1237, Jul. 1992.

[3] F. Mireles and S. E. Ulloa, "Zeeman splitting of shallow donors in GaN," *Applied Physics Letters*, vol. 74, no. 2, pp. 248–250, 1999.

[4] S. Lin, S. Zeng, X. Cai, J. Zhang, S. Wu, L. Sun, and B. Zhang, "Simulation of doping levels and deep levels in InGaN-based single-junction solar cell," *Journal of Materials Science*, vol. 47, pp. 4595–4603, 2012.

[5] Y. Xi and E. F. Schubert, "Junction-temperature measurement in GaN ultraviolet light-emitting diodes using diode forward voltage method," *Applied Physics Letters*, vol. 85, no. 12, pp. 2163–2165, 2004.

[6] H. Morkoç, *Handbook of Nitride Semiconductors and Devices, volume 2, Electronic and Optical Processes in Nitrides*. © 2008 Wiley-VCH Verlag GmbH & Co. KGaA, 2008.

[7] F. Meillaud, A. Shah, C. Droz, and C. Miazza, "Efficiency limits for single-junction and tandem solar cells," *Solar Energy Materials*, vol. 90, pp. 2952–2959, 2006.

[8] D. H. Macdonald, "Recombination and Trapping in Multicrystalline Silicon Solar Cells," Australian National University, 2001.

[9] M. J. Kerr and A. Cuevas, "General parameterization of Auger recombination in crystalline silicon," *Journal of Applied Physics*, vol. 91, no. 4, p. 2473, 2002.

[10] M. Zhang, P. Bhattacharya, J. Singh, and J. Hinckley, "Direct measurement of auger recombination in In(0.1)Ga(0.9)N/GaN quantum wells and its impact on the efficiency of In(0.1)Ga(0.9)N/GaN multiple quantum well light emitting diodes," *Applied Physics Letters*, vol. 95, no. 20, p. 201108, 2009.

[11] V. W. L. Chin, T. L. Tansley, and T. Osotchan, "Electron mobilities in gallium, indium, and aluminum nitrides," *Journal of Applied Physics*, vol. 75, no. 11, p. 7365, 1994.

[12] J. Wu, W. Walukiewicz, S. X. Li, R. Armitage, J. C. Ho, E. R. Weber, E. E. Haller, H. Lu, W. J. Schaff, A. Barcz, and R. Jakiela, "Effects of electron concentration on the optical absorption edge of InN," *Applied Physics Letters*, vol. 84, no. 15, p. 2805, 2004.

[13] E. O. Kane, "Band Structure of Indium Antimonide," *Journal of Physics and Chemistry of Solids*, vol. 1, pp. 249–261, 1957.

[14] J. Wu, "When group-III nitrides go infrared: New properties and perspectives," *Journal of Applied Physics*, vol. 106, no. 1, p. 011101, 2009.

[15] M. J. Turners and E. H. Rhoderick, "Metal-Silicon schottky barriers," *Solid-State Electronics*, vol. 11, pp. 291–300, 1968.

[16] H. C. Card and E. H. Rhoderick, "Studies of tunnel MOS diodes I . Interface effects in silicon Schottky diodes," *Journal of Physics D: Applied Physics*, vol. 4, p. 1589, 1971.

[17] M. A. Green, F. D. King, and J. Shewchun, "Minority carrier MIS tunnel diodes and their application to electron and photovoltaic energy conversion - I. Theory," *Solid State Electronics*, vol. 17, pp. 551–561, 1974.

[18] R. B. Godfrey and M. a. Green, "655 mV open-circuit voltage, 17.6% efficient silicon MIS solar cells," *Applied Physics Letters*, vol. 34, no. 11, p. 790, 1979.

[19] R. T. Tung, "Electron transport at metal-seiconductor interfaces: General theory," *Physical Review B*, vol. 45, no. 23, p. 13509, 1992.

[20] H. Amano, T. Asahi, and I. Akasaki, "Stimulated emission near ultraviolet at room temperature from a GaN film grown on sapphire by MOVPE using an AlN buffer layer," *Japanese Journal of Applied Physics*, vol. 29, no. 2, pp. L205–L206, 1990.

[21] S. Nakamura, Y. Harada, and M. Seno, "Novel metalorganic chemical vapor deposition system for GaN growth," *Applied Physics Letters*, vol. 58, no. May, pp. 2021–2023, 1991.

[22] M. Asif Khan, J. N. Kuznia, J. M. Van Hove, D. T. Olson, S. Krishnankutty, and R. M. Kolbas, "Growth of high optical and electrical quality GaN layers using low-pressure metalorganic chemical vapor deposition," *Applied Physics Letters*, vol. 58, no. 5, p. 526, 1991.

[23] S. C. Binari, H. B. Dietrich, G. Kelner, L. B. Rowland, K. Doverspike, and D. K. Gaskill, "Electrical characterisation of Ti Schottky barriers can n-type GaN - Electronics Letters," *Electronics Letters*, vol. 30, no. 11, pp. 909–911, 1994.

[24] P. Hacke, T. Detchprohm, K. Hiramatsu, and N. Sawaki, "Schottky barrier on n-type GaN grown by hybride vapor phase epitaxy," *Applied Physics Letters*, vol. 63, no. 19, pp. 2676–2678, 1993.

[25] M. E. Lin, Z. Ma, F. Y. Huang, Z. F. Fan, L. H. Allen, and H. Morkoc, "Low resistance ohmic contacts on wide band-gap GaN," *Applied Physics Letters*, vol. 64, no. February, pp. 1003–1005, 1994.

[26] J. D. Guo, "Schottky contact and the thermal stability of Ni on n -type GaN," vol. 80, no. 3, pp. 1623–1627, 1996.

[27] E. V Kalinina, N. I. Kuznetsov, V. A. Dmitriev, K. G. Irvine, and C. H. Carter, "Schottky Barriers on n-GaN Grown on SiC," *Journal of Electronic Materials*, vol. 25, no. 5, pp. 1–4, 1996.

[28] Y. Nakano and T. Kachi, "Current deep-level transient spectroscopy investigation of acceptor levels in Mg-doped GaN," *Applied Physics Letters*, vol. 79, no. 11, p. 1631, 2001.

[29] J.-S. Jang, D. Kim, and T.-Y. Seong, "Schottky barrier characteristics of Pt contacts to n-type InGaN," *Journal of Applied Physics*, vol. 99, no. 7, p. 073704, 2006.

[30] D. J. Chen, Y. Huang, B. Liu, Z. L. Xie, R. Zhang, Y. D. Zheng, Y. Wei, and V. Narayanamurti, "High-quality Schottky contacts to n-InGaN alloys prepared for photovoltaic devices," *Journal of Applied Physics*, vol. 105, no. 6, p. 063714, 2009.

[31] Y. Park and K. Hyunsoo, "Substantial Pinning of the Fermi Level of Plasma-Treated n-Type GaN Surfaces," *Applied Physics Express*, vol. 4, p. 015702, 2011.

[32] C. I. Wu and a. Kahn, "Electronic states and effective negative electron affinity at cesiated p-GaN surfaces," *Journal of Applied Physics*, vol. 86, no. 6, p. 3209, 1999.

[33] M. D. McCluskey, C. G. Van de Walle, C. P. Master, L. T. Romano, and N. M. Johnson, "Large band gap bowing of In x Ga 1 x N alloys," *Applied Physics Letters*, vol. 72, no. 21, pp. 2725–2726, 1998.

[34] J. Wu, W. Walukiewicz, K. M. Yu, J. W. Ager III, E. E. Haller, H. Lu, and W. J. Schaff, “Small band gap bowing in In 1−xGaxN alloys,” *Applied Physics Letters*, vol. 80, no. 25, p. 4741, 2002.

Chapter 3

3- MOCVD growth technique and optimization of $In_xGa_{1-x}N$ films

In this chapter, I focus on the metalorganic chemical vapor deposition growth (MOCVD) technique used in this work to fabricate InGaN and GaN films. After a short presentation of different existing deposition techniques, I will describe the way for the optimization of the InGaN films and the key factors to enhance the film

quality. The recipe used will be linked with their electronic and optical properties and the bandgap modulation by means of the In content will be explained.

3-1 Nitride growth techniques

Various growth techniques have been employed to grow III-V nitride thin films. These growth techniques are classified into two types: the Vapor Phase Epitaxy (VPE) and the Molecular Beam Epitaxy (MBE). The VPE technique is further classified into the Metalorganic Chemical Vapor Deposition (MOCVD), also called Metalorganic Vapor Phase Epitaxy (MOVPE) or Organometallic Vapor Phase Epitaxy (OMVPE), and the Vapor Phase Epitaxy (VPE) of a narrower sense.

For the VPE techniques, the name of the growth techniques employed depends on the source used. The term HVPE is employed if a hybrid source for the group V element is used, and the term metalorganic is employed if at least one of the sources is an organic compound.

3-1.1 Molecular Beam Epitaxy

In the Molecular Beam Epitaxy technique, films are grown on a heated substrate in vacuum through various reactions between thermal molecular beams of the constituent elements and the surface species on the substrate. The MBE gives actually the highest material quality with a very high vacuum inside the chamber. M. Hori et al. used a RF-MBE at low temperature with an InN buffer layer to grow $In_xGa_{1-x}N$ films over the entire composition range [1], and found that the phase separation with $x > 0.53$ could be completely suppressed.

3-1.2 Vapor Phase Epitaxy

The Vapor Phase Epitaxy was the first method to produce single crystal GaN with quality sufficient to launch the first stages of the GaN technology. The typical deposited thickness is 50 to 150 μm. The advantage of this technique is the thick buffer layer grown at a high growth rate on any available substrates to be used as templates for MOCVD or MBE techniques.

3-1.3 Metalorganic Chemical Vapor Deposition

In contrast to MBE with a crystal growth under vacuum, the growth of crystals takes place from the gas phase at moderate pressures (2 to 100kPa) for MOCVD. As such, this technique is preferred for the formation of devices incorporating thermodynamically metastable alloys, and it has become a major process in the manufacture of optoelectronics. This is the growth technique that I used for $In_xGa_{1-x}N$ and GaN film deposition.

3-2 Different defects present in a crystal

Some random structural defects are generated during the crystal growth. Here, I will present different types of defects present in crystals. These defects are classified into two categories, punctual defects and extended defects.

3-2.1 Punctual defects

The punctual defects are further classified into the following categories:

- Vacancies: an atom is missing inside the lattice structure. For example, in GaN films the gallium vacancies (V_{Ga}) and nitride vacancies (V_N) exist.
- Anti-site: an atom occupies the site of another atom. For example, one of the regular nitride atom occupies a gallium site (N_{Ga}) or the opposite situation (Ga_N).
- Impurities by substitution: a foreign atom occupies atomic sites. For example, carbon occupies a gallium site (C_{Ga}). These impurities come from metalorganic sources, carrier gases that are not completely pure, reactor chamber, or from the surface of the substrate, if it is not clean enough, and the diffusion of atoms from the substrate through the deposited film.
- Interstitial defects: an atom from the host material or an impurity occupies an interstitial site. For example, an nitrogen atom of nitride is located at an interstitial site ($N_{int.}$).

3-2.2 Extended defects

Extended defects or major structural defects are further classified into the following categories:

- Dislocation: dislocations are a discontinuity inside the crystal structure. Misfit dislocations and threading dislocations exist. There are three types of threading dislocations: pure edge, pure screw [2] and mixed dislocations as presented in *Fig. 3-1*.
- Stacking mismatch defect: the stacking sequence of atomic layers is not regular (…ABCABCABABCABC…). This mismatch can take place for one or more atomic layers. The stacking mismatch defects are less likely to occur if proper surface preparation is made and unnecessary chemical reactions are avoided.
- Inclusion defect: it is a precipitate or a different crystalline phase in an area of the crystal matrix.
- Grain boundaries: they are formed between two different crystals with different orientations. This type of defect has a very low probability to exist in the films deposited by epitaxial techniques.

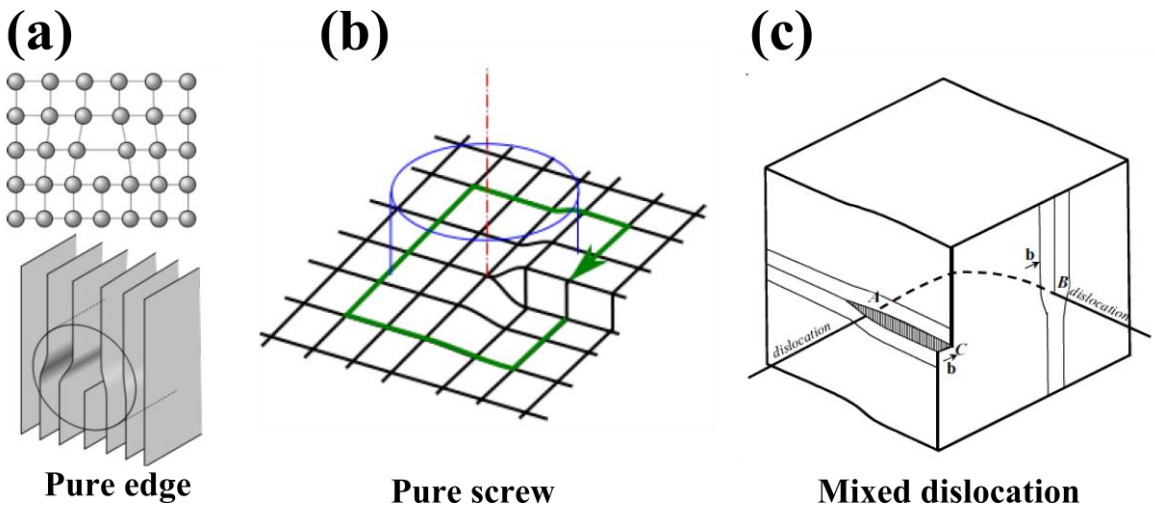

Fig. 3-1: Illustration of different type of threading dislocation: pure edge (a), pure screw (b), and mixed dislocations (c).

The presence of defects influences the electronic properties of the film and can act as recombination centers for photogenerated carriers. Thus, a crucial step is the control of high crystal quality of InGaN layers. I will explain the optimization of InGaN layers grown by MOCVD technique in the following.

3-3 Sapphire substrate

During all this work, I used sapphire substrates to grow GaN or InGaN films. It is the most common substrate for MOCVD because of its reasonable price and even if there is a lattice mismatch between sapphire and GaN, the crystallinity of the GaN films is usually very high. The full width at half maximum (FWHM) of rocking curves for GaN was about 0.07–0.08º for (0002) plane and about 0.14–0.16º for $(10\bar{1}1)$ plane. About $In_xGa_{1-x}N$ films with InN mole fraction $6 \leq x \leq 9$, the FWHM of rocking curves was about 0.06–0.09º for (0002) plane and 0.15–0.18º for $(10\bar{1}1)$ plane.

Figure 3-2 presents the projection of the basal plane of sapphire and GaN cation positions in the epitaxial growth orientation. Open circles mark N-atom positions and solid lines show the GaN basal unit cells.

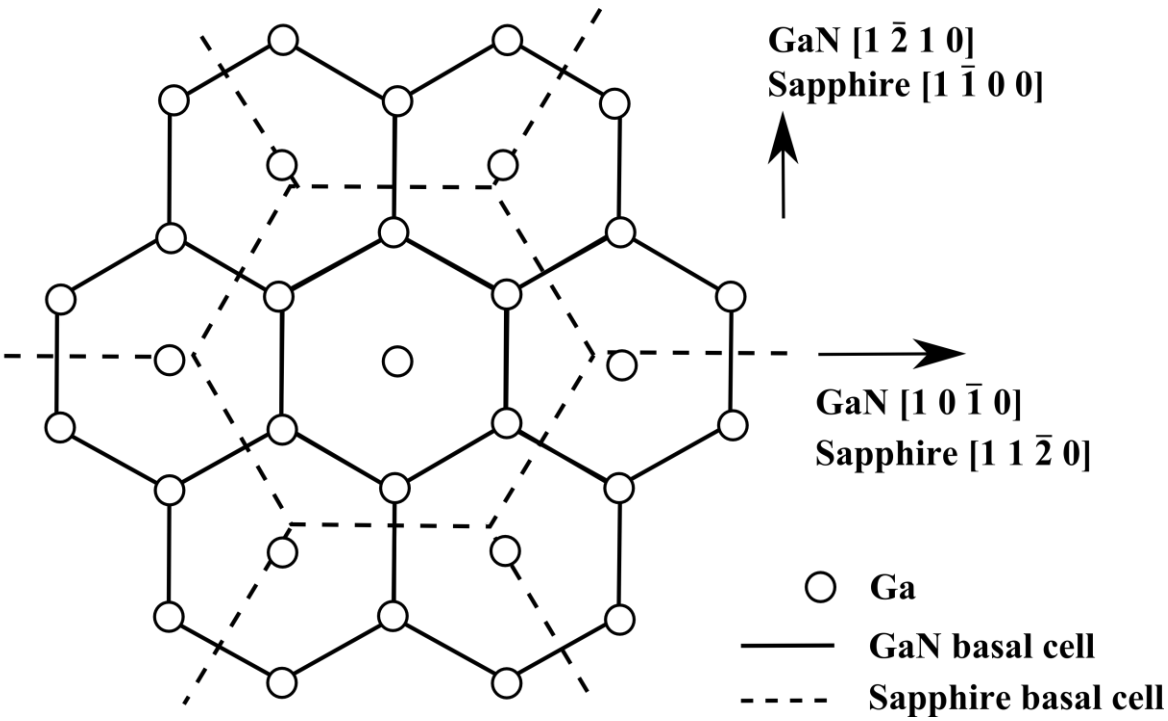

Fig. 3-2: Projection of bulk basal plane sapphire and GaN cations positions for the observed epitaxial growth orientation [7].

3-4 Metalorganic Chemical Vapor Deposition

3-4.1 Recipe for $In_xGa_{1-x}N$ film growth

The recipe used for $In_xGa_{1-x}N$ film deposition is presented in *Fig. 3-3*. This recipe is composed of ten steps where five steps are crucial for the crystal growth. First, a cleaning step must be performed to etch the oxide layer present on the sapphire substrate under a reducing environment such as hydrogen at temperature above 1000ºC. This is followed by the GaN buffer layer or nucleation layer at low temperature around 500ºC. The low temperature buffer layer is the most important step to reach a high crystal quality with a low defect concentration. Amano et al. were the first to obtain the high crystal quality, smooth surface free from cracks by depositing a low-temperature AlN layer before the GaN growth in 1986 [3]. This low-temperature buffer layer was necessary because of the large lattice mismatch between the (0001) sapphire substrate and GaN.

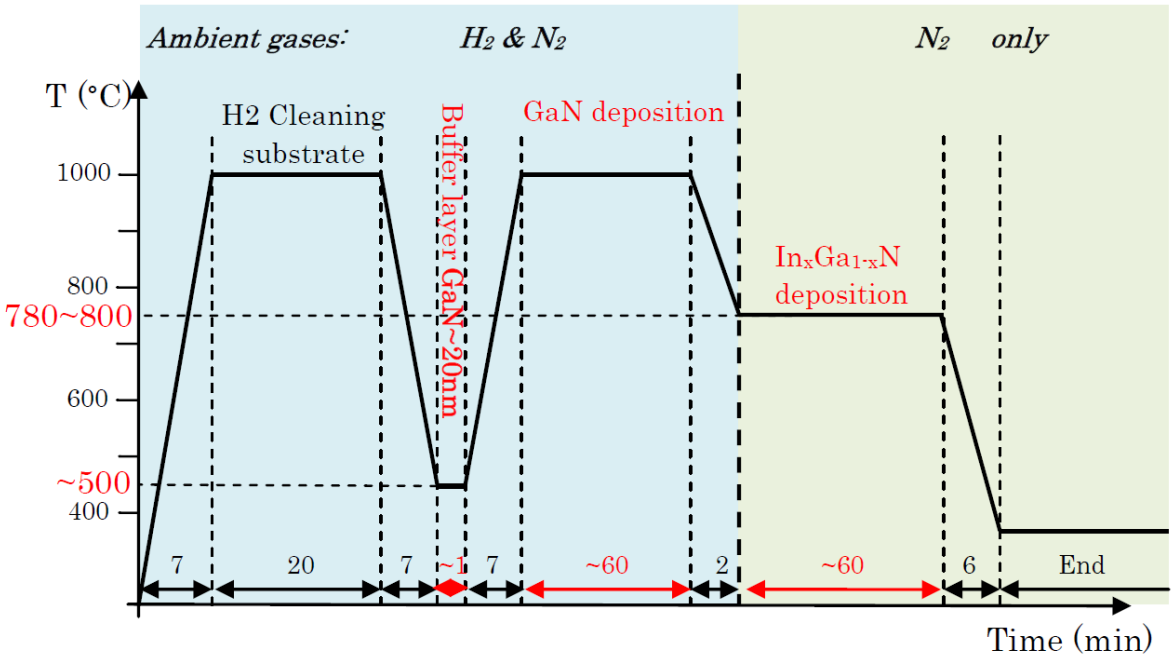

Fig. 3-3: Example of deposition recipe used for $In_xGa_{1-x}N$ grown by MOCVD.

The following parameters are very important for InGaN crystal growth:

- The GaN nucleation layer (or buffer layer) deposited at low temperature.
- The ambient gas must be changed from H_2+N_2 to N_2 for InGaN deposition.
- The balance between adsorption and desorption (Kinetic model) to optimize the growth speed of the deposited layer generates a lower defect density inside the film.

The temperature, the III-V ratio depending on the ammonium flow, and the MO ratio for InGaN characterized by TMIn/(TMIn+TMGa) are all important factors to control the growth speed of the deposited layer and thus to reduce the generation of high defect density.

3-4.2 Role of the low temperature GaN as buffer layer (or nucleation layer)

As I presented previously, the low temperature GaN as buffer layer (or nucleation layer) is one of the key parameters to achieve high crystal quality. Even if this step is very short, on the order of one minute or below, it is crucial to reduce the defect concentration and obtain a smooth surface for the next layer, the GaN thick epilayer.

Figure 3-4 illustrates the buffer layer formation and the crystal growth. Depending on the temperature and the deposition time, the generation of dislocations through the GaN epilayer can be minimized. On (0001) sapphire, the optimized conditions for the GaN buffer layer were 490ºC during 50 seconds with a TMGa flow of 30 sccm and NH_3 flow of 2 sLm under H_2 (4.5 sLm) and N_2 (2 sLm) ambient gases. The thickness of the GaN buffer layer is on the order of dozen nanometers.

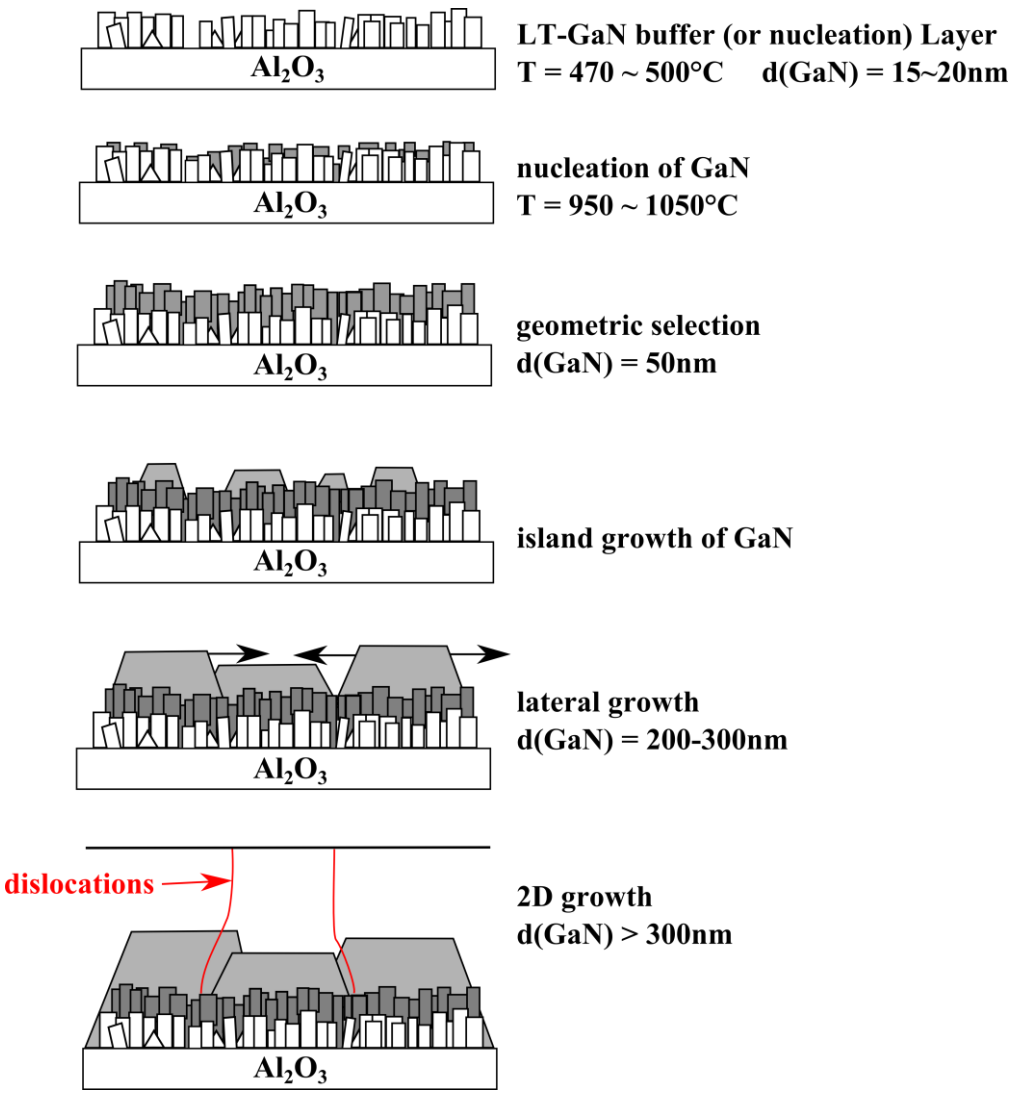

Fig. 3-4: Illustration of the buffer layer formation and the crystal growth.

3-4.3 MOCVD reactor chamber

Figure 3-5 illustrates the MOCVD chamber and *Fig. 3-6* is a picture of the MOCVD technique used in this work. From *Fig. 3-5*, we can see that there are three entrances for the ambient gases H_2 or N_2, one for the ammonium flow, and one for the metalorganic source with the suitable carrier gases (H_2 or N_2) depending on the material grown. During deposition, the pressure controlled inside the reactor was about 730 Torr, just below the atmospheric pressure of 760 Torr. When no deposition is in process, the chamber is kept under vacuum to avoid contamination.

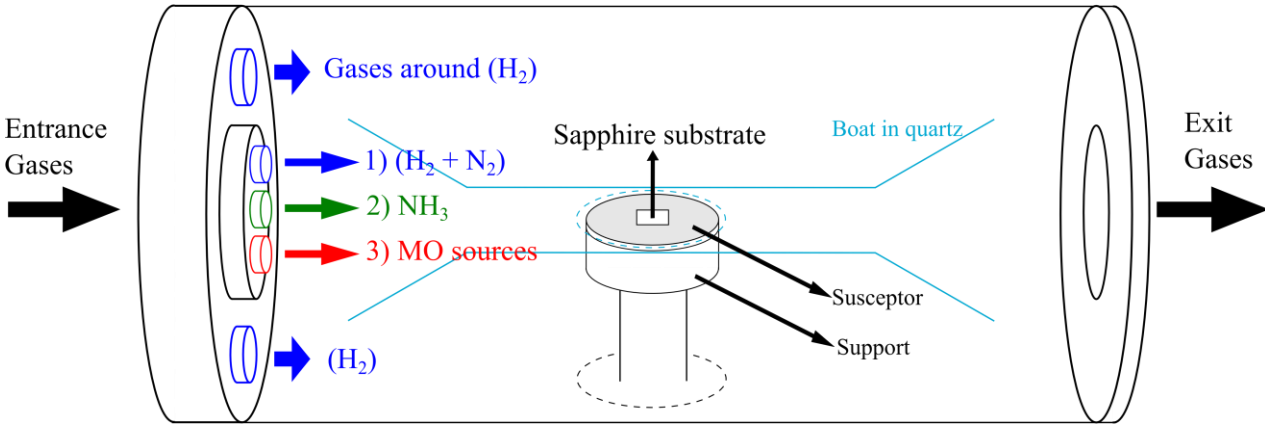

Fig. 3-5: Illustration of the MOCVD chamber used in this work.

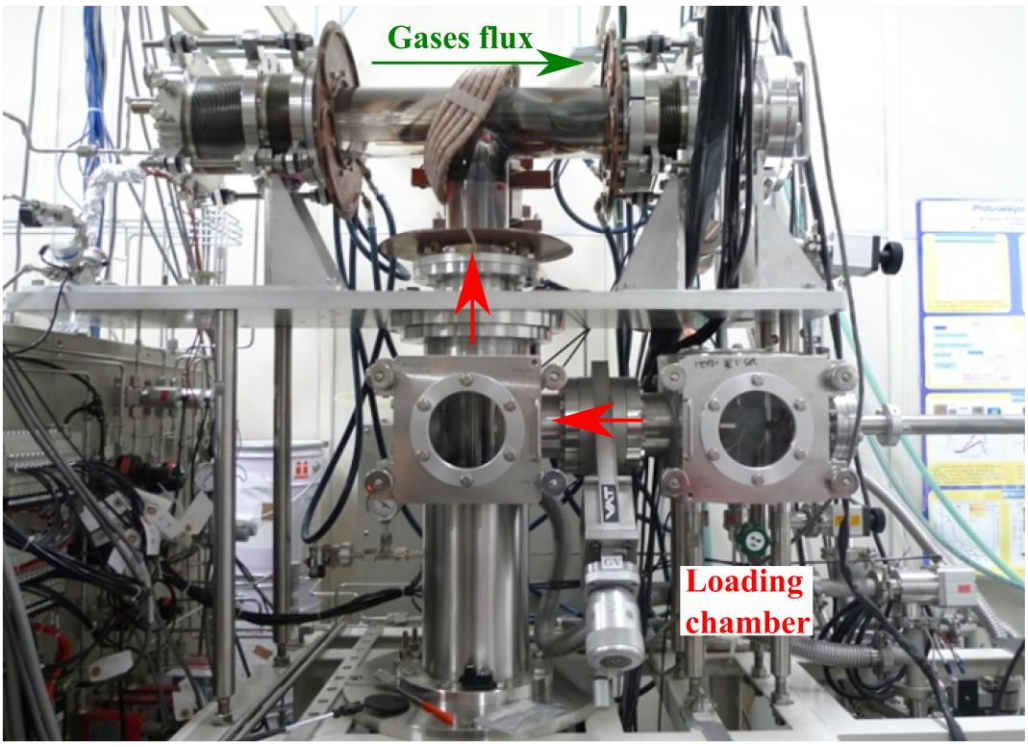

Fig. 3-6: Picture of the MOCVD equipment used to deposit GaN and InGaN films.

3-4.4 Control of the flow of Metalorganic sources

Hydrogen, nitrogen and ammonium flows have a flow rate of several standard liters per minute (sLm). On the other hand, the flow rate of metalorganic (MO) sources is very small and is of the order of several standard cubic centimeters per minute (sccm). Two different flows and an automatic pressure control are necessary to

transport the MO sources to the MOCVD furnace chamber. As *Fig. 3-7* illustrates, one flow is going to the MO source to transport the molecules, called the carrier gas. Because the flow rate of the carrier gas is very small (between 6 to 30 sccm for TMGa), another flow, denoted acceleration flow, is used at the exit of the MO sources. This acceleration flow increases the flow rate up to about 250 to 500 sccm for TMGa. The transport of MO sources through the MOCVD chamber is then governed by a pressure difference. An automatic pressure control regulates the pressure to 790 torr inside the pipeline, which is higher than the pressure inside the MOCVD chamber, that is 730 torr, to force the MO flow through the MOCVD chamber.

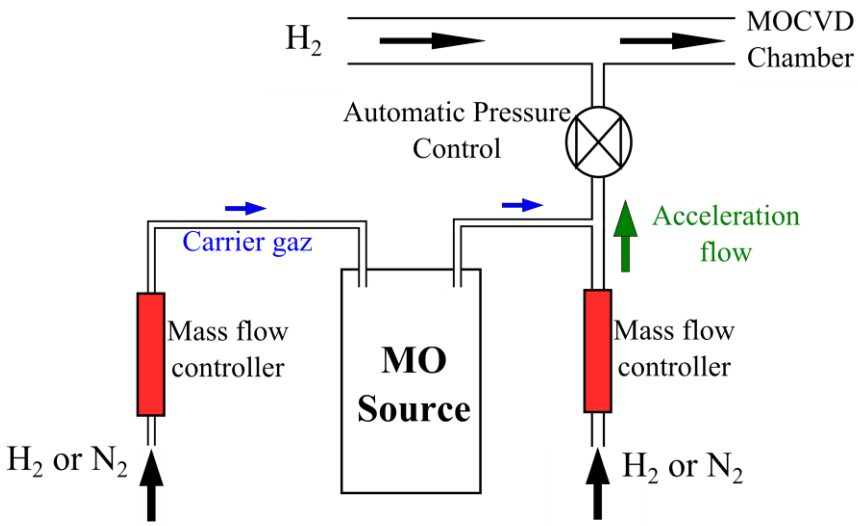

Fig. 3-7: System of the flows for metalorganic sources.

A rough estimation of the indium composition can be obtained by using the flow rates of the metalorganic sources:

$$In(\%) = \frac{P_{In} \cdot F_{In}}{P_{Ga} \cdot F_{Ga}} \times 100 = \frac{2mmHg \times 75}{35mmHg \times 33} \times 100 = 15\%, \tag{3-1}$$

where P_{In} and P_{Ga} are the pressure of indium and gallium, respectively, and F_{In} and F_{Ga} are the respective flow rates. The pressure of the metalorganic sources depends on their temperature. The vapor pressure curves can be calculated as follows for each metalorganic source:

For TMGa source: $$Vp(mmHg) = \exp\left[\left(\frac{8.07 - 1703}{T(K)}\right) \times \ln(10)\right] \tag{3-2}$$

For TMIn source: $$Vp(mmHg) = \exp\left[\left(\frac{10.52 - 3014}{T(K)}\right) \times \ln(10)\right] \tag{3-3}$$

For TMAl source: $$Vp(mmHg) = \exp\left[\left(\frac{8.22 - 2134}{T(K)}\right) \times \ln(10)\right] \tag{3-4}$$

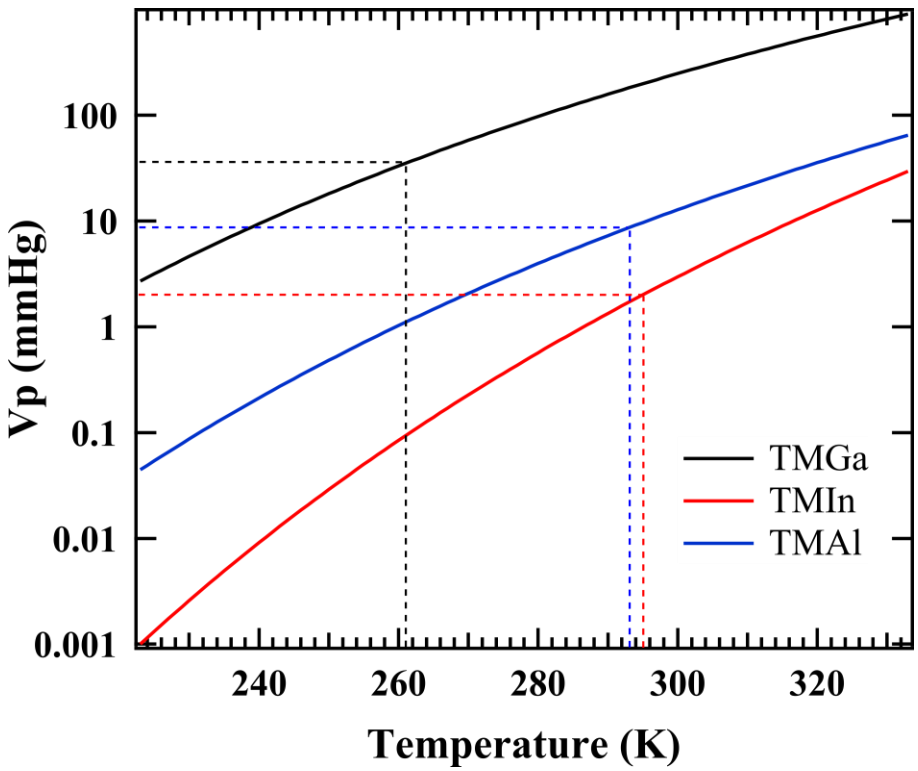

Fig. 3-8: Equilibrium vapor pressure curves for TMGa, TMIn and TMAl metalorganic sources.

I plotted the vapor pressure or equilibrium vapor pressure curve for each metalorganic source in *Fig. 3-8*.

The equilibrium vapor pressure of TMGa is quite higher than that of TMIn, thus TMGa is kept at -12ºC, while the temperature is +22ºC for TMIn and +20ºC for TMAl. At these temperatures, the corresponding vapor pressure is about 35.08, 2.01 and 8.64 mmHg, respectively.

I wanted to obtain an InN mole fraction of about 15% for InGaN films, thus considering the equilibrium vapor pressure at the above-mentioned temperatures, the first deposition using a flow rate of 33 sccm for TMGa and 75 sccm for TMIn was performed. These flow rates correspond to a metalorganic source ratio defined as follows:

$$Ratio = \frac{TMIn}{TMIn + TMGa}. \tag{3-5}$$

The first deposition had a ratio of 0.11. In fact, no InGaN was deposited because of a high evaporation rate of indium on surface, thus a much higher ratio between 0.7 to 0.9 was necessary to increase the indium incorporation inside the InGaN films.

3-4.5 Control of indium composition

To use $In_xGa_{1-x}N$ material as an active layer, its band gap needs to be controlled and its crystal quality should be high. The material requires a controlled bandgap, a high crystal quality to reduce defects and recombination, and high electron mobility to efficiently collect the photo-generated carriers.

Because of the lattice mismatch between the substrate and InGaN films, I deposited a thick GaN epi-layer on a low-temperature buffer GaN layer (or nucleation layer) in order to reduce the threading dislocations and reduce the lattice mismatch between sapphire and GaN [3]. However, a high dislocation density was generated on the order of 10^8 cm^{-2} even for good GaN material.

I measured X-ray diffraction (XRD) to evaluate the crystal quality, c- and a-lattices, and the growth method by the full width at half maximum (FWHM) of the GaN and InGaN peaks on the XRD rocking curves. Each peak contains information about the thickness deposited (intensity of the signal) and the flatness between atomic layers (FWHM). The peak position via 2θ-ω scan for the (0002) plane gives information on the c-lattice parameter of the wurtzite structure, which is used to determine the amount of InN mole fraction inside the crystal from the Vegard law [4]. Information about the a-lattice constant is given by the peak position of the 2θ-ω scan for the $(10\bar{1}1)$ plane.

I plotted the InN mole fraction as a function of the temperature for four different growth conditions in *Fig. 3-9*. The InN mole fraction was enhanced by decreasing the temperature of $In_xGa_{1-x}N$ films deposition. The full width at hall maximum (FWHM) of $In_xGa_{1-x}N$ films depending on the temperature growth for each growth conditions is shown in *Fig. 3-10*. The FWHM of $In_xGa_{1-x}N$ peak for (0002) plane increases considerably when the

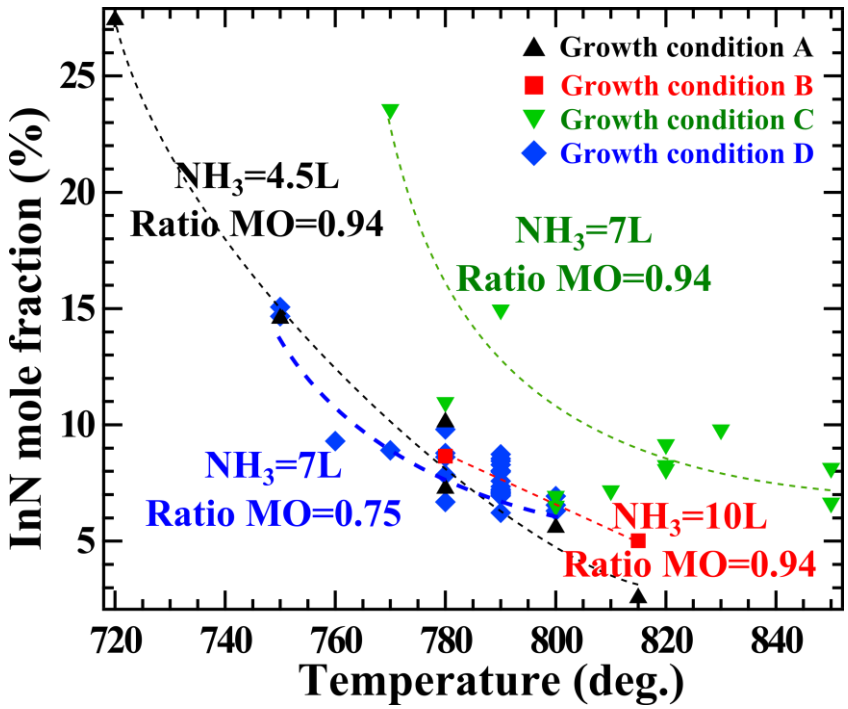

Fig. 3-9: Control of the InN mole fraction depending on the temperature for four different growth conditions A, B, C, and D.

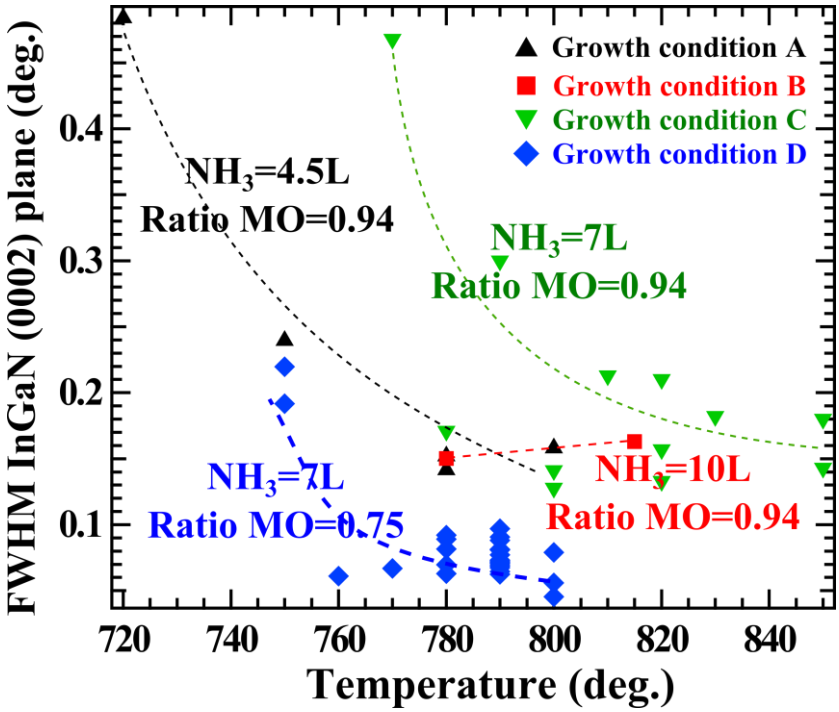

Fig. 3-10: Full with at half maximum (FWHM) of the InGaN peak for (0002) plane depending on the temperature for four different growth conditions A, B, C, and D.

temperature of $In_xGa_{1-x}N$ film deposition decreases. This underlines a degradation of the crystallinity at higher indium composition. By adjusting the growth conditions, I could obtain a FWHM lower than 0.10º for the temperature range between 760 to 800ºC (*Fig. 3-10*), which corresponds to an indium composition from 6 to 10% (*Fig. 3-9*).

I presented a list of $In_xGa_{1-x}N$ films grown by MOCVD classified by the four growth conditions A, B, C, and D. The growth conditions, the InN mole fraction and the FWHM of $In_xGa_{1-x}N$ for (0002) plane are listed for each group A, B, C, and D in the following tables:

Conditions A: NH3 flow = 4.5 sLm and ratio TMI/ (TMI+TMGa)= 0.86~0.96

Table 3-1: List of the growth condition A parameters for InGaN films grown by MOCVD

InN mole fraction (%)	Temperature of InGaN deposition	TMI flow (sccm)	TMGa flow (sccm)	Ratio TMI/(TMI+TMG)	FWHM (0002) plane for InGaN (º)	NH_3 flow (sLm)
5.59	800	150	1.0	0.86	0.1580	4.5
7.27	780	150	1.0	0.86	0.1416	4.5
14.57	750	150	1.0	0.88	0.2396	4.5
27.41	720	150	1.0	0.88	0.4840	4.5
10.12	780	250	1.0	0.91	0.1520	4.5
28.41	780	350	1.0	0.94	-	4.5
2.56	815	350	0.7	0.96	-	4.5

Conditions B: NH3 flow = 10 sLm and ratio TMI/ (TMI+TMGa)= 0.95

Table 3-2: List of the growth condition B parameters for InGaN films grown by MOCVD

InN mole fr action (%)	Temperature of InGaN deposition	TMI flow (sccm)	TMGa flow (sccm)	Ratio TMI/(TMI+ TMG)	FWHM 0002 plane for InGaN (°)	NH_3 flow (sLm)
5.02	815	350	1.0	0.95	0.1630	10
8.65	780	350	1.0	0.95	0.1502	10

Conditions C: NH3 flow = 7 sLm and ratio TMI/ (TMI+TMGa)= 0.88~0.94

Table 3-3: List of the growth condition C parameters for InGaN films grown by MOCVD

InN mole fr action (%)	Temperature of InGaN deposition	TMI flow (sccm)	TMGa flow (sccm)	Ratio TMI/(TMI+ TMG)	FWHM 0002 plane for InGaN (°)	NH_3 flow (sLm)
10.97	780	350	1.0	0.94	0.1710	7
6.93	800	350	1.0	0.94	0.1410	7
8.14	850	350	1.0	0.94	0.1430	7
9.79	830	350	1.0	0.94	0.1820	7
6.64	850	350	2.8	0.89	0.1800	7
8.26	820	350	1.5	0.94	0.2100	7
8.08	820	350	1.5	0.94	0.1570	7
14.94	790	350	1.5	0.94	0.3000	7
7.17	810	350	1.5	0.94	0.2130	7
9.16	820	350	1.5	0.94	0.1330	7
6.51	800	350	1.5	0.94	0.1277	7
23.56	770	350	2.3	0.88	0.4680	7

Conditions D: NH3 flow = 7 sLm and ratio TMI/ (TMI+TMGa)= 0.75

Table 3-4: List of the growth condition D parameters for InGaN films grown by MOCVD

InN mole fr action (%)	Temperature of InGaN deposition	TMI flow (sccm)	TMGa flow (sccm)	Ratio TMI/(TMI+ TMG)	FWHM 0002 plane for InGaN (°)	NH_3 flow (sLm)
8.73	790	350	6.0	0.75	0.07256	7
8.44	790	350	6.0	0.75	0.09076	7
8.55	790	350	6.0	0.75	0.08129	7
7.98	790	350	6.0	0.75	0.08800	7
8.28	790	350	6.0	0.75	0.09703	7
14.67	750	350	6.0	0.75	0.19175	7
15.07	750	350	6.0	0.75	0.21979	7

7.35	790	350	6.0	0.75	0.07704	7
7.12	790	350	6.0	0.75	0.07153	7
7.08	790	350	6.0	0.75	0.07326	7
7.05	790	350	6.0	0.75	0.06852	7
7.18	790	350	6.0	0.75	0.06957	7
7.58	790	350	6.0	0.75	0.06247	7
7.22	790	350	6.0	0.75	0.08083	7
6.95	790	350	6.0	0.75	0.06450	7
7.01	790	350	6.0	0.75	0.07088	7
8.03	790	350	6.0	0.75	0.06738	7
8.62	780	350	6.0	0.75	0.06280	7
8.90	770	350	6.0	0.75	0.06682	7
9.30	760	350	6.0	0.75	0.06101	7
6.22	790	350	6.0	0.75	0.06247	7
6.55	800	350	6.0	0.75	0.07905	7
6.30	800	350	6.0	0.75	0.05595	7
6.93	800	350	6.0	0.75	0.04540	7
8.79	780	350	6.0	0.75	0.06974	7
6.68	780	350	6.0	0.75	0.09217	7
7.85	780	350	6.0	0.75	0.08151	7
9.80	780	350	6.0	0.75	0.08908	7

For clarity, these experimental results were summarized in *Table 3-5* with the different growth conditions A, B, C, and D used for $In_xGa_{1-x}N$ film deposition:

Table 3-5: Summary of the four growth conditions used to deposit $In_xGa_{1-x}N$ with different InN mole fractions.

Growth conditions	**NH_3 flow (sLm)**	**Ratio TMI/(TMI+TMGa)**	**Temperature range of InGaN deposition (ºC)**	**InN mole fraction range (%)**	**FWHM range of InGaN peak for (0002) plane**
A	4.5	0.86 – 0.94	720 – 815	2 – 27	0.15 – 0.48
B	10	0.95	780 – 815	5 – 8	0.15 – 0.17
C	7	0.88 – 094	770 – 850	7 – 23	0.13 – 0.47
D	7	0.75	750 - 850	6 – 15	0.07 – 0.22

The optimized growth conditions, denoted by D in *Table 3-5*, have an ammonium flow of 7 sLm, a ratio between the metalorganic sources of 0.75 and a range temperature from 750 to 850ºC.

3-4.6 Bandgap control and crystallinity

The difficulty of the InGaN growth lies in the fact that high temperature is necessary for a high crystallinity, but this high temperature enhances the evaporation of indium. Thus, by reducing the temperature, higher In content is incorporated inside InGaN. Due to this lower temperature, the growth rate of InGaN is much lower (~3.3 nm/min) than GaN (~25nm/min). I found some critical issues such as the carrier gases employed. For example, hydrogen used for GaN growth must be changed to nitrogen for InGaN growth in order to prevent the evaporation of indium. I obtained a good crystal quality with a FWHM between 0.07 and 0.08 degrees for the (002) plane at a growth temperature of 1000ºC for GaN and at 790ºC for InGaN corresponding to an InN mole fraction of 0.10. I demonstrated that a more relaxed growth occurred at InN mole fraction higher than 0.10, which is characterized by a larger a-lattice, i.e. a larger base of the hexagonal crystal. As *Fig. 3-11* shows, the a-lattice is almost constant until an InN mole fraction of 0.10, and then the a-lattice increases considerably at higher InN mole fraction. Thus I deposited $In_xGa_{1-x}N$ with a high crystallinity from x = 0 to 0.10 corresponding to an optical bandgap of 3.4 to 3.0 eV.

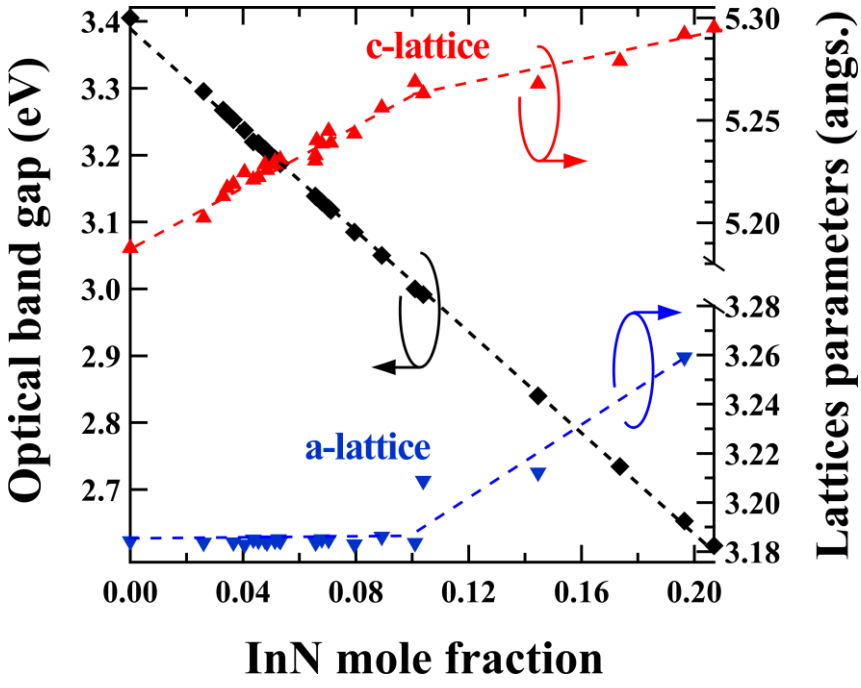

Fig. 3-11: Control of the optical bandgap by the InN mole fraction, c- and a- lattices of the wurtzite crystal are also reported depending on the InN mole fraction.

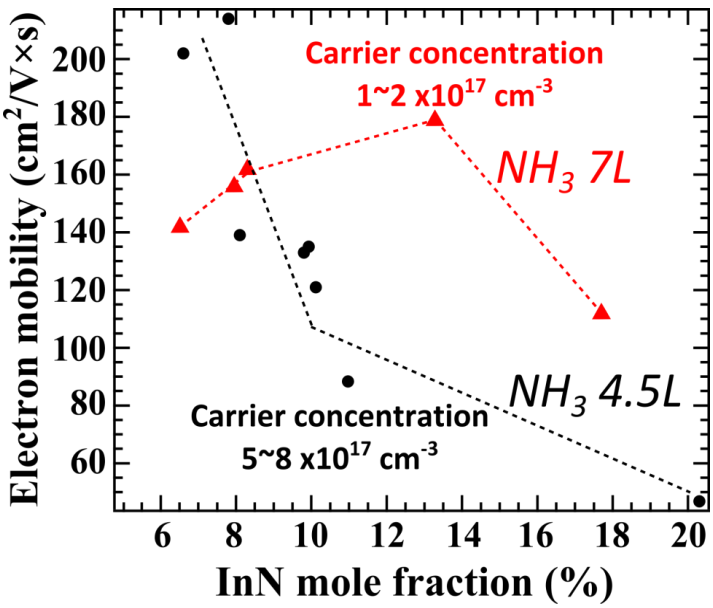

Fig. 3-12: Tendency of the electron mobility of InGaN films at different carrier concentration depending on the InN mole fraction.

3-4.7 Enhancement of electron mobility

a) For InGaN films

I improved the electron mobility by optimizing the V/III ratio between the ammonium and the metalorganic sources. With an NH_3 flow of 7sLm, I could achieve InGaN films with lower carrier concentration ($1\text{-}2\times10^{17}cm^{-3}$). An optimal ratio between the ammonium flow and the metalorganic flows should be found on the sample surface, which limits the defect generation and thus reduces the unintended n-type material. Due to this lower defect generation, the electron mobility was enhanced for higher InN mole fraction (*Fig. 3-12*), which is an important result for photovoltaic devices. We should note that the carrier concentration estimated by Hall effect measurement is an average value of all the structure of the deposited films including the GaN epi-layer and the $In_xGa_{1-x}N$ layer.

b) For GaN films

In the case of only GaN films, the Hall effect measurement gives an accurate estimation of the carrier concentration. I could control the growth speed of the epitaxial layer by controlling the ammonium flow. I observed that the carrier concentration had a minimum at a growth speed of 250 angst./min in *Fig. 3-13 (a)*. For the same sample, the electron mobility measured was the highest value of about 240-260 cm^2/Vs (*Fig. 3-13 (b)*). Thus, for GaN film deposition, an optimized condition was found with a low carrier concentration and a high electron mobility.

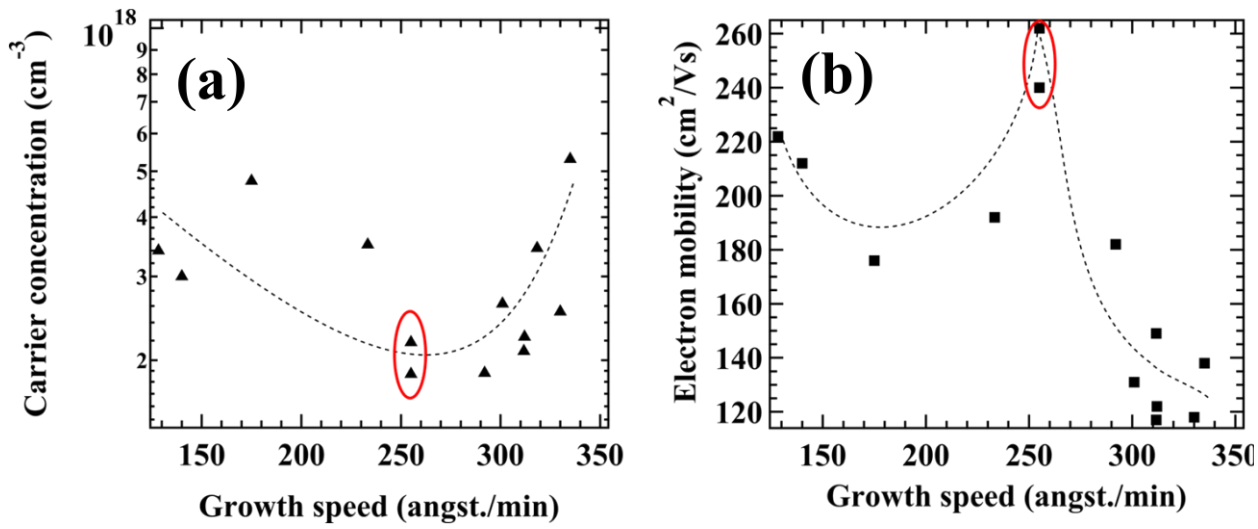

Fig. 3-13: Tendency of the electron mobility of InGaN films at different carrier concentration depending on the InN mole fraction.

The time-resolved photoluminescence (TRPL) was used to estimate the lifetime for photo-generated carriers. TRPL of 0.28 ns for $In_{0.09}Ga_{0.91}N$ and 0.05 ns for GaN films were measured at room temperature (*Fig. 3-14*), which was longer than 0.1 ns for similar $In_{0.12}Ga_{0.88}N$ structures reported in Ref. [5]. A particular attention should be paid when using TRPL because the value can be overestimated due to the excitation of defect levels.

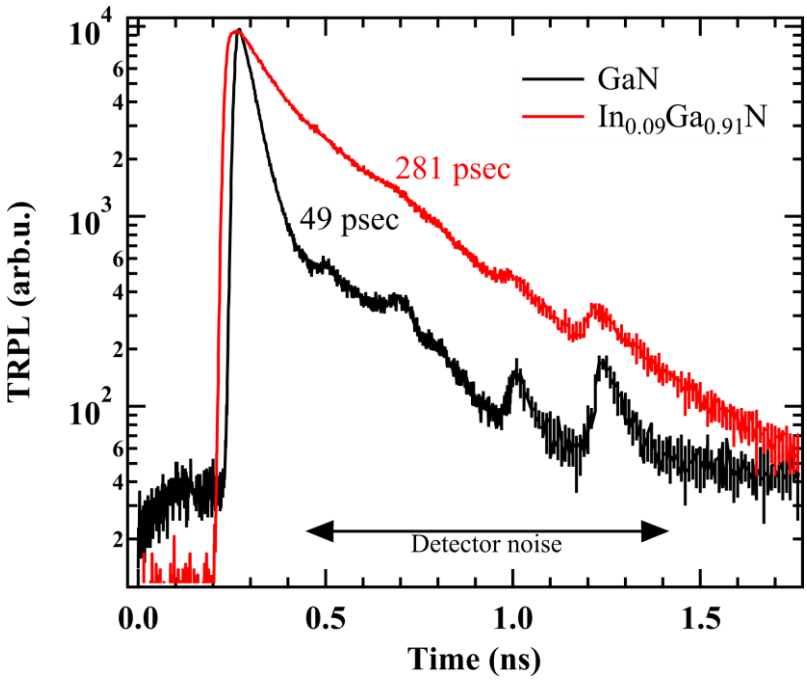

Fig. 3-14: Time-resolved photoluminescence for $In_{0.09}Ga_{0.91}N$ and GaN films.

3-4.8 Magnesium as p-type doping for InGaN films

Concerning the crystal growth conditions, special care must be taken when the film is grown using Cp_2Mg for p-type doping. A critical thickness of p-InGaN with a phase separation was observed at higher Mg concentration, which was attributed to a bigger covalent radius of Mg atoms (0.130nm) compared to that of Ga atoms (0.126nm) and could increase the compressive strain inside the film [6]. So, the generation of defects can be higher in high Mg doped InGaN layer or a thicker p-InGaN layer, which can be a brake for the development of *p-n* junction solar cells. This explains the motivation for the fabrication of Schottky junction solar cells using InGaN films.

3-4.9 Multi-layer (ML) structures

I investigated other solutions to reduce the propagation of threading dislocations from the GaN epi-layer into the $In_xGa_{1-x}N$ on surface, and enhance the InN mole fraction, by fabricating multi-layer (ML) structures. I realized two types of multi-layer structures, AlN-GaN $(2nm/50nm)_{x10}$ and InGaN-GaN $(3nm/50nm)_{x10}$ (*Fig. 3-15*), before the $In_xGa_{1-x}N$ growth. These structures had a slightly improved InGaN crystal quality for In content of about 10% with a very smooth surface (roughness of 1.44nm for scanned area of 25 μm^2), but did not prevent the formation of threading dislocations at higher In content.

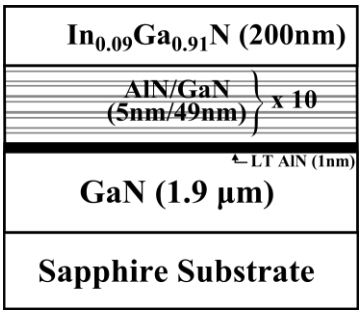

Fig. 3-15: $In_{0.09}Ga_{0.91}N$ thick film structure deposited by MOCVD on c-plane sapphire substrate.

I will present a detailed fabrication of the Schottky contact on $In_xGa_{1-x}N$ deposited on the multi-layer structure AlN-GaN $(2nm/50nm)_{x10}$ in Chapter 5.

3-4.10 Enhancement of the surface morphology

By using the optimized growth condition previously found, I could also improve the surface morphology of the InGaN films. AFM image of an $In_{0.08}Ga_{0.92}N$ film realized in early development showed a roughness of 3.24nm with a dislocation density of $4.9\times10^{8}cm^{-2}$ (*Fig. 3-16(a)*). AFM image of an $In_{0.07}Ga_{0.93}N$ using the optimized growth condition showed a roughness of 0.92nm with a dislocation density of 4.0×10^{7} cm^{-2}(*Fig. 3-16(b)*). The roughness and the dislocation density were decreased considerably.

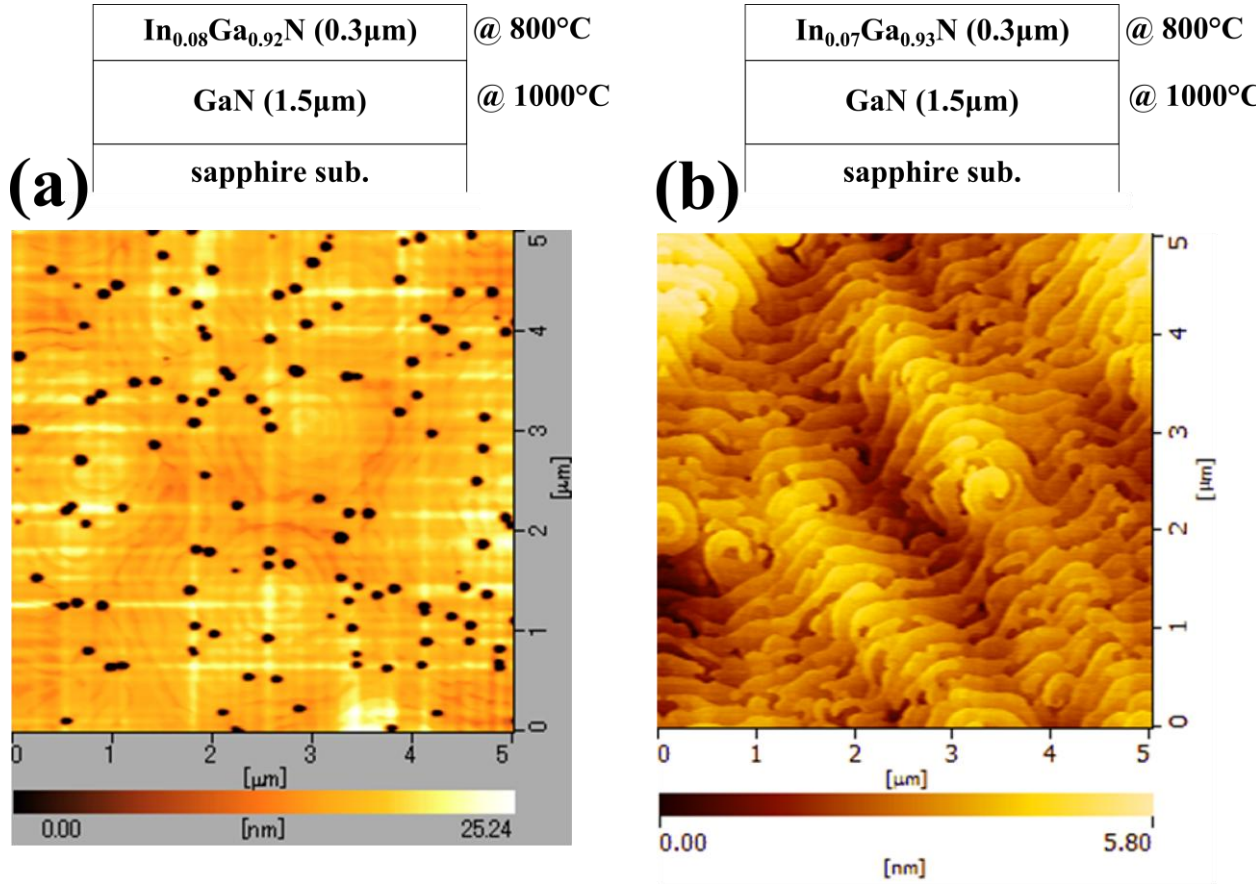

Fig. 3-16: Comparison of AFM image ($5\times5\mu m^2$) between the InGaN surface in early development (a) and the InGaN with an optimized growth condition (b), both structures were also illustrated.

3-5 Cathodoluminescence analysis

The cathodoluminescence (CL) technique were used on $In_xGa_{1-x}N$ films to observe the homogeneity of the InN mole fraction. By secondary electron (SE) image, the surface of $In_{0.09}Ga_{0.91}N$ presented some dark spots, which can be attributed to dislocations on surface in *Fig. 3-17(a)*. The cathodoluminescence of the same area at a specific wavelength 362, 388, 433, and 550 nm is also presented. The signal at 362 and 388 nm corresponded to the GaN and $In_{0.09}Ga_{0.91}N$ films *Fig. 3-17(a)*, *(b)*. At 388 nm some areas started to appear brighter. At 433 nm

some bright areas could be clearly observed, which are related to some radiative recombination centers *Fig. 3-17(d)*. At higher wavelength, no signal were detected *Fig. 3-17(e)*.

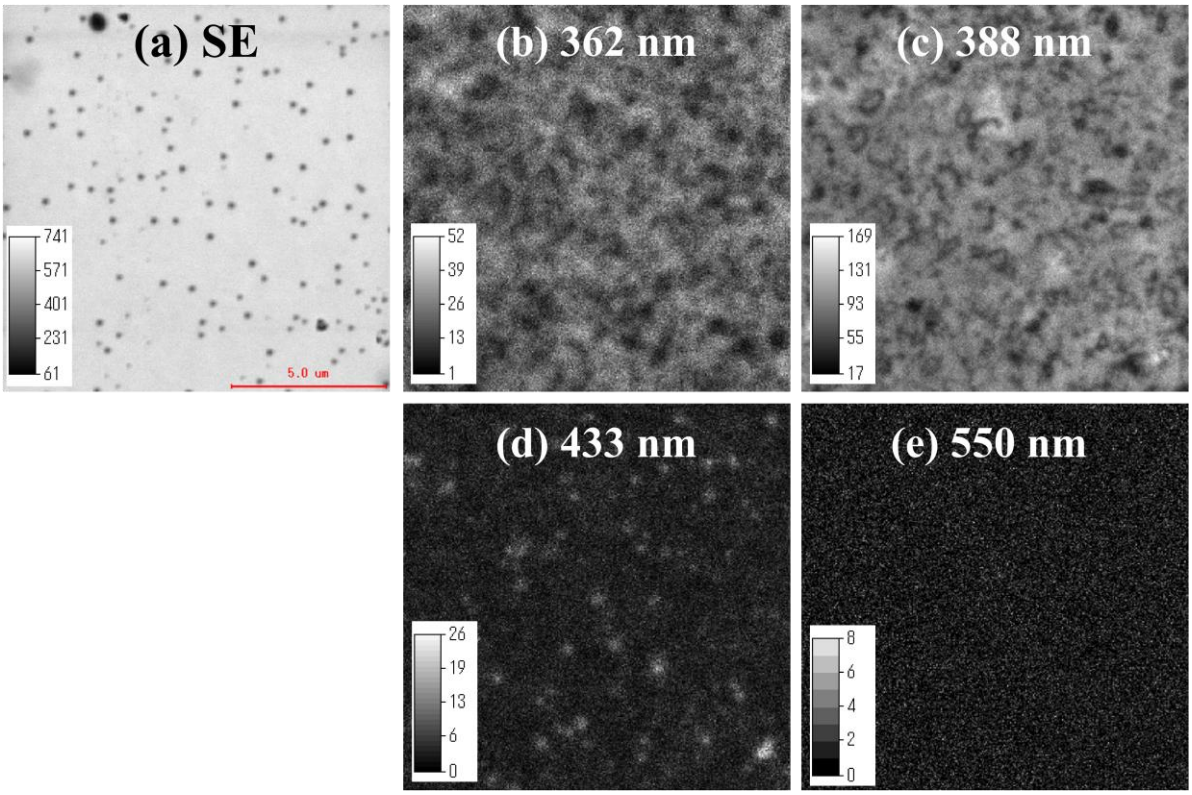

Fig. 3-17: Cathodoluminescence analysis of $In_{0.09}Ga_{0.91}N$ *with an electron beam of 10kV. (a) Secondary electron image at a scale of 5µm. (b) Luminescence observed at 362 nm, (c) at 388 nm, (d) at 433 nm, and (e) at 550 nm.*

Figure 3-18 presents 10 cathodoluminescence spectra according to the 10 points measured. The $In_{0.09}Ga_{0.91}N$ peak appeared at 388nm without fluctuation, which confirm the homogeneity of the InN mole

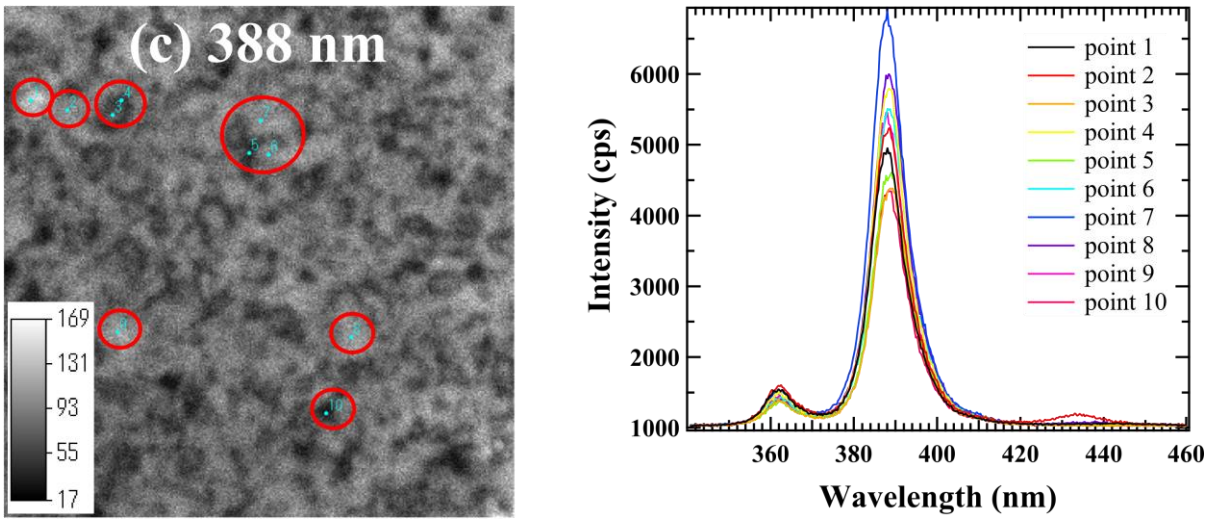

Fig. 3-18: Cathodoluminescence analysis for 10 points of $In_{0.09}Ga_{0.91}N$ *film.*

fraction inside the film. A radiative recombination center located at 433 nm (2.87 eV) could be observed.

Interestingly, a large structural defect could be analyzed by CL as presented in *Fig. 3-19*. This structural defect is probably due to a large particle deposited on surface prior to the crystal growth. In the center, a bright area corresponding to the GaN (362 nm) and the $In_{0.09}Ga_{0.91}N$ (386 nm) is observed in *Fig. 3-19 (a)*, *(b)*. Two other radiative recombination centers could be observed at 430 nm (2.85 eV) and 480 nm (2.57 eV). These cathodoluminescence spectra were clearly observable near the large structural defect *Fig. 3-19 (c)*, *(d)*.

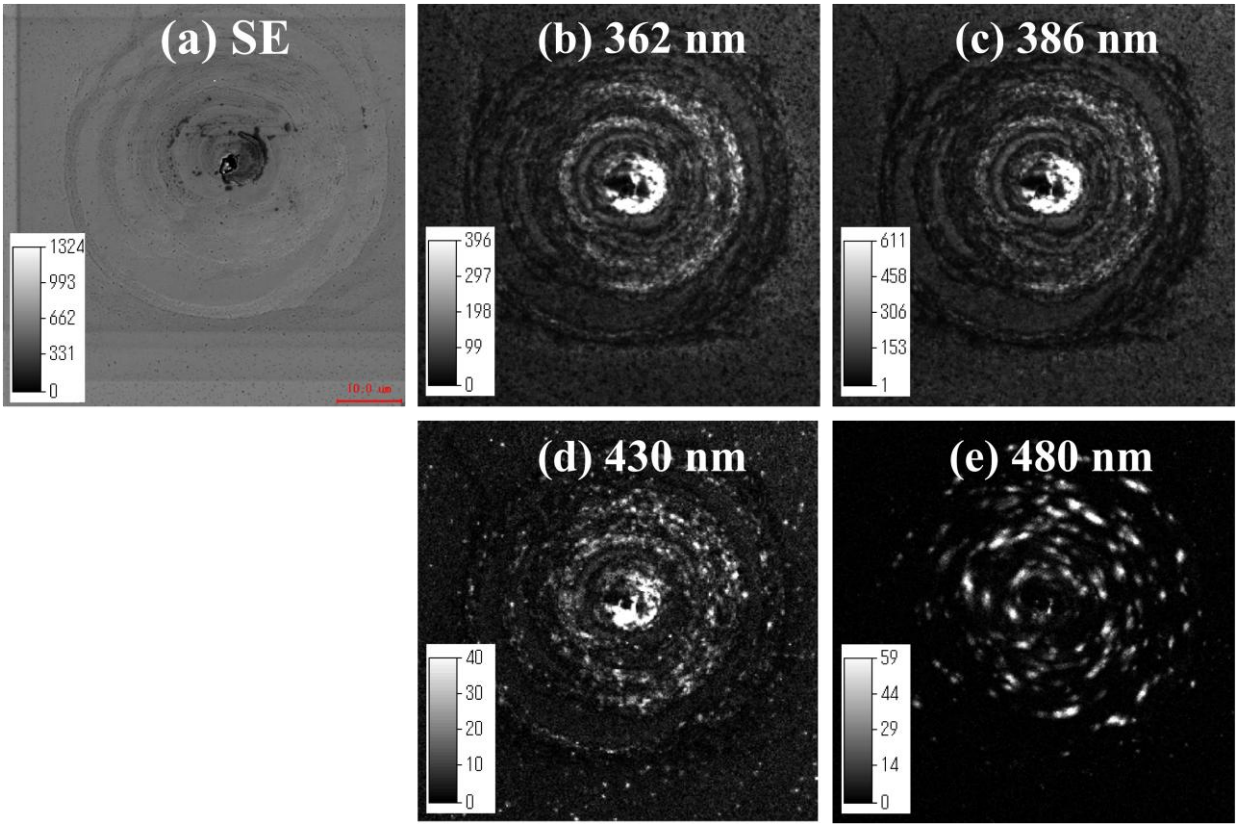

Fig. 3-19: Cathodoluminescence analysis of a structural defect $In_{0.09}Ga_{0.91}N$ *with an electron beam of 10kV. (a) Secondary electron image at a scale of 10µm. (b) Luminescence observed at 362 nm, (c) at 386 nm, (d) at 430 nm, and (e) at 480 nm.*

Figure 3-20 presents 10 cathodoluminescence spectra realized at some bright and dark areas around the structural defect. Beside the recombination centers at 430 and 480 nm observable, a shift of the $In_{0.09}Ga_{0.91}N$ peak position is clearly present, which clarifies the fluctuation of InN mole fraction beside structural defects.

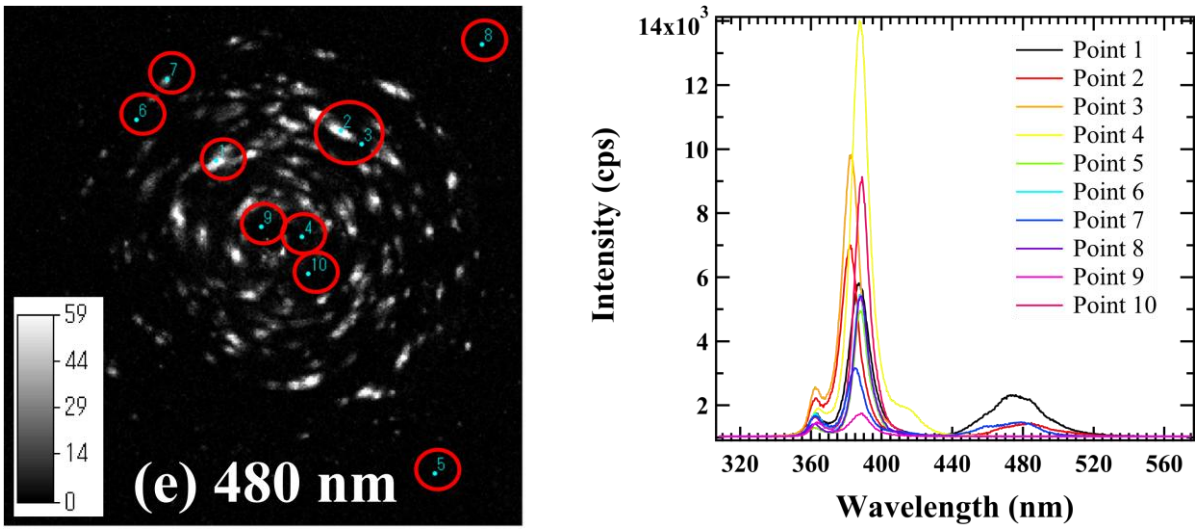

Fig. 3-20: Cathodoluminescence analysis for 10 points near the structural defect on surface of $In_{0.09}Ga_{0.91}N$ *films.*

For $In_{0.07}Ga_{0.93}N$ film at higher quality with a smooth surface (*Fig. 3-21(a)*), the CL analysis revealed mainly the peak at 384 nm (*Fig. 3-22*). Some radiative recombination centers could be observed at 430 nm in *Fig. 3-21(d)*, but the cathodoluminescence are very weak compared to the one of $In_{0.07}Ga_{0.93}N$ films. The intensity of the luminescence $In_{0.07}Ga_{0.93}N$ peak is much higher than the two previous measurements. There is no position

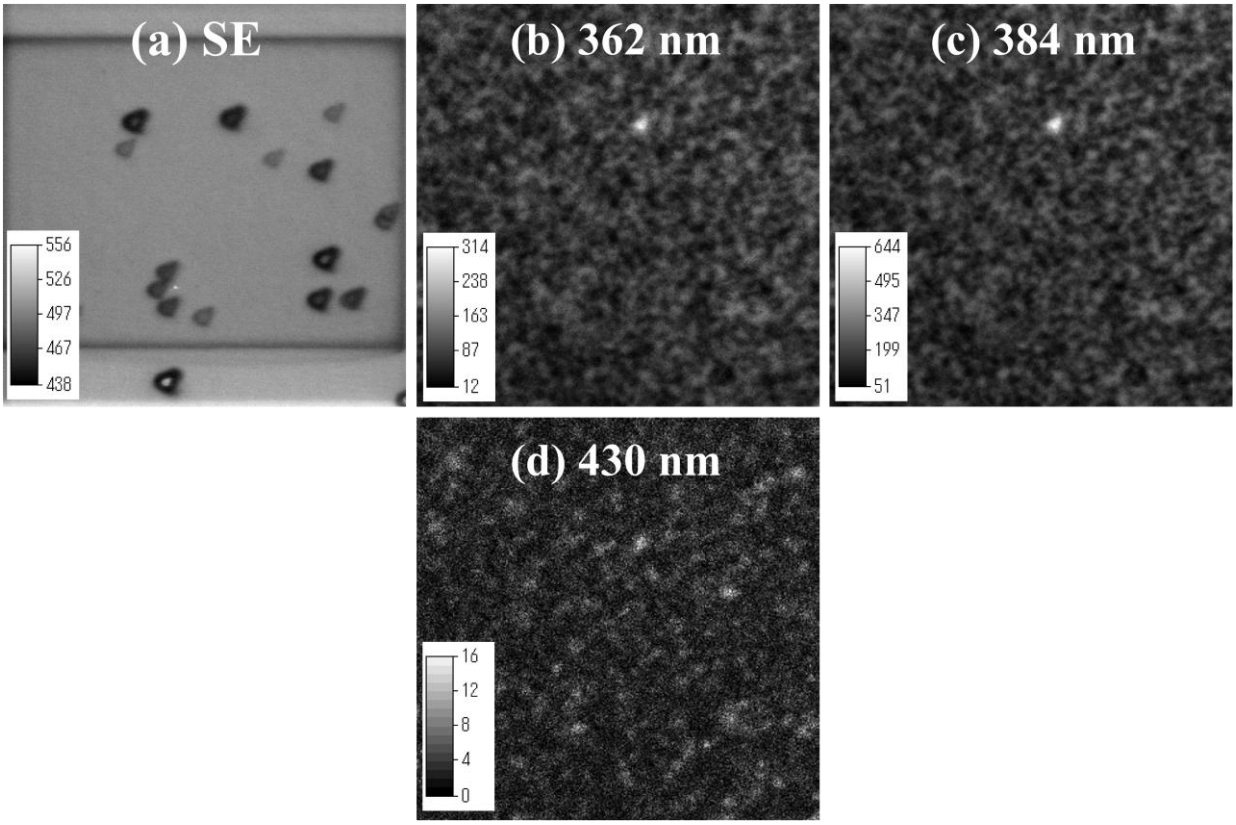

Fig. 3-21: Cathodoluminescence analysis of a structural defect $In_{0.1}Ga_{0.9}N$ *with an electron beam of 10kV. (a) Secondary electron image at a scale of 10µm. (b) Luminescence observed at 362 nm, (c) at 384 nm, and (d) at 430 nm.*

shift, which clarifies a homogeneous InN mole fraction inside the film.

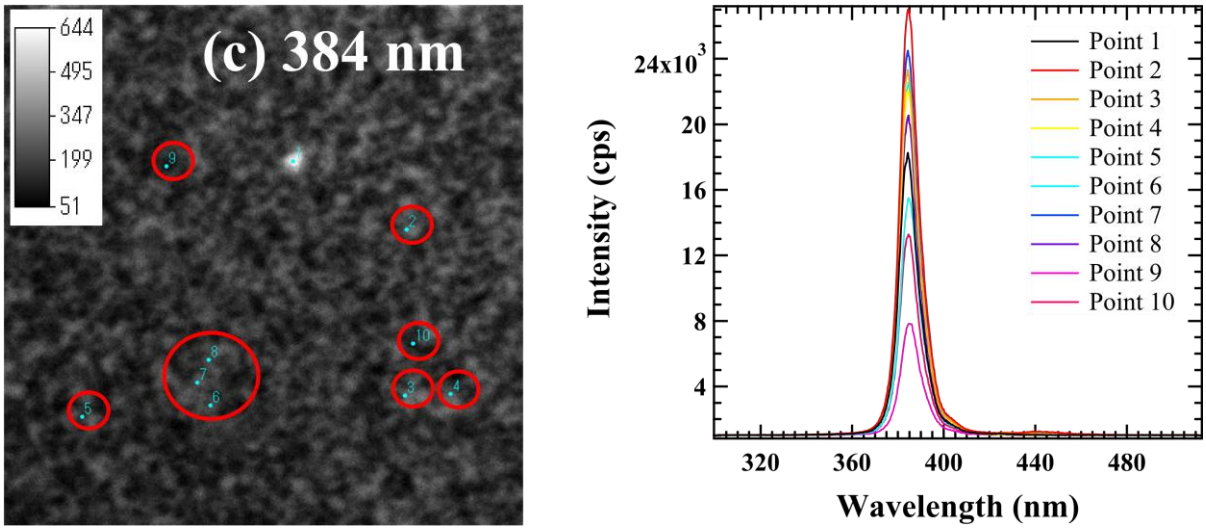

Fig. 3-22: Cathodoluminescence analysis for 10 points near the structural defect on surface of $In_{0.07}Ga_{0.93}N$ films.

The CL analysis is thus a powerful technique to give information about the homogeneity of InN mole fraction inside the film and possible radiative recombination centers. The presence of these recombination centers appears near structural defects.

3-6 Conclusion

In this chapter, I described the MOCVD deposition system and the optimization of $In_xGa_{1-x}N$ growth condition. The temperature is the main parameter to control the InN mole fraction, and thus the material bandgap. Nevertheless, a more relaxed growth mode occurred at InN mole fraction higher than 10%. This constrains the $In_xGa_{1-x}N$ bandgap between 3.0 to 3.4 eV, which is still too large for photovoltaic applications.

The ammonium flow (NH_3) was optimized to 10 sLm for GaN epi-layer and 7 sLm for InGaN deposition. The ammonium flow influences the growth speed of the layer, thus an optimized speed could decrease the free carrier concentration in GaN layers of about 8×10^{17} cm^{-3}, and increase the electron mobility up to about 260 cm^2/Vs. Even if we could not separate the carrier concentration and electron mobility between GaN and InGaN layers, the optimized condition could also enhance the electron mobility for InGaN films. I obtained for InGaN films a smooth surface with a roughness of about 0.92 nm and decreased considerably the dislocation density down to about $4.0\times10^7 cm^{-2}$.

By using the optimized conditions, high quality InGaN films could be achieved. Thanks to this work, Schottky contact could be made, which was a necessary condition to analyze the deep level defects (cf. Chapter 5) and realize photovoltaic devices (cf. Chapter 6).

The cathodoluminescence analysis underlined a fluctuation of InN mole fraction near structural defects, and radiative recombination centers at 430 nm and 480 nm. For $In_{0.07}Ga_{0.93}N$ film with high crystal quality, a homogeneous InN mole fraction was observed.

References chapter 3

[1] M. Hori, K. Kano, T. Yamaguchi, Y. Saito, T. Araki, Y. Nanishi, N. Teraguchi, and A. Suzuki, "Optical Properties of In x Ga 1 – x N with Entire Alloy Composition on InN Buffer Layer Grown by RF-MBE," *Physica Status Solidi (b)*, vol. 234, no. 3, pp. 750–754, 2002.

[2] F. a. Ponce, D. P. Bour, W. Götz, N. M. Johnson, H. I. Helava, I. Grzegory, J. Jun, and S. Porowski, "Homoepitaxy of GaN on polished bulk single crystals by metalorganic chemical vapor deposition," *Applied Physics Letters*, vol. 68, no. 7, p. 917, 1996.

[3] H. Amano, N. Sawaki, I. Akasaki, and Y. Toyoda, "Metalorganic vapor phase epitaxial growth of a high quality GaN film using an AlN buffer layer," *Applied Physics Letters*, vol. 48, no. 5, p. 353, 1986.

[4] M. D. McCluskey, C. G. Van de Walle, C. P. Master, L. T. Romano, and N. M. Johnson, "Large band gap bowing of In x Ga 1 x N alloys," *Applied Physics Letters*, vol. 72, no. 21, pp. 2725–2726, 1998.

[5] M. Smith, G. D. Chen, J. Y. Lin, H. X. Jiang, M. Asif Khan, and Q. Chen, "Time-resolved photoluminescence studies of InGaN epilayers," *Applied Physics Letters*, vol. 69, no. 19, p. 2837, 1996.

[6] L. Sang, M. Takeguchi, L. Woong, Y. Nakayama, M. Lozac'h, T. Sekiguchi, and S. Masatomo, "Phase Separation Resulting from Mg Doping in p-InGaN Film Grown on GaN/Sapphire Template," *Applied Physics Express*, vol. 3, p. 111004, 2010.

[7] T. Lei, K. F. Ludwig, and T. D. Moustakas, "Heteroepitaxy, polymorphism, and faulting in GaN thin films on silicon and sapphire substrates," *Journal of Applied Physics*, vol. 74, no. 7, p. 4430, 1993.

Chapter 4

4- Investigation of electronic structure for III-V nitride thin films by Hard X-ray photoemission spectroscopy

In solar cell hetero-structures, the band alignment is one of the crucial issues to design the device. Hard X-ray photoemission spectroscopy (HX-PES) is used for InGaN material, beside GaN and InN, to determine the valence band, valence band maxima, core levels and band offset. In this chapter, I will show that the valence band maximum is shifted toward lower binding energy at higher InN mole fraction, and estimate the band offset between the valence bands maximum of GaN and $In_xGa_{1-x}N$. A new approach to estimate the valence band maximum is discussed, which clarifies the band bending on surface of GaN, InGaN and InN. This affects the interface and junction properties realized by $In_xGa_{1-x}N$.

4-1 Use of SPring 8 facilities for Hard X-ray photoemission spectroscopy measurement

4-1.1 SPring 8 facilities

The name SPring 8 is the acronym of "Super Photon ring - 8 GeV", the synchrotron radiation facility located in Hyogo Prefecture, Japan, opened in 1997. SPring-8 delivers the most powerful synchrotron radiation currently available. The equipment consists of a storage ring containing a narrow and powerful electron beams accelerated nearly to the speed of light and forced to travel in a curved path by magnetic field that produces the electromagnetic radiation. A schematic view of a beamline is presented in *Fig. 4-1* [1].

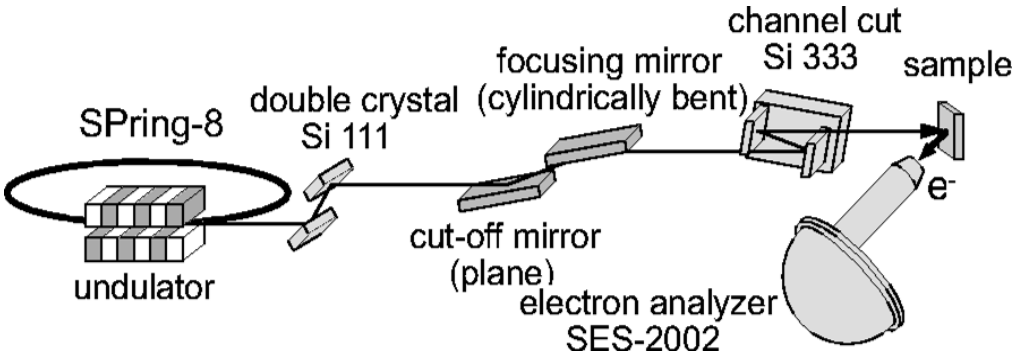

Fig. 4-1: Schematic illustration of a beamline at SPring 8.

4-2 Investigation of electronic structure for III-V nitride thin films by Hard X-ray photoemission spectroscopy

In photovoltaic devices, the band offset is one of the crucial issues in designing solar cell structures such as p-i-n junctions and to avoid any barrier that may affect the carrier lifetime. I employed hard x-ray photoemission spectroscopy (HX-PES), measured at SPring-8 to determine the electronic structures of $In_xGa_{1-x}N$, GaN, and InN films. I characterized Ga 3*d* - In 4*d*, N 1*s*, C 1*s*, O 1*s* core levels, and the valence band spectra. Because of the high kinetic energy of electrons excited by hard X-ray (5.95keV), the detection depth is about ~20 nm. By increasing the angle between the X-ray and the normal of the sample surface (also called take-off angle, or TOA), the detection depth was adjustable from 20 nm ("bulk" sensitive) to 10nm ("surface" sensitive).

My analyses revealed a strong hybridization between Ga 3*d* and In 4*d* core levels when InN was alloyed with GaN. Furthermore at higher InN mole fraction, the valence band maximum was shifted toward lower binding energy (*Fig. 4-2(a)*). The extrapolating *line a* is usually employed to determine the valence band maximum (VBM). *Line a* corresponds to a bulk sensitive approach for GaN films as presented in *Fig. 4-2(b)*. But, valence spectra show a large tail at low binding energy. I proposed a new approach to estimate the VBM taking into account this tail with the extrapolating *line b* (*Fig. 4-2(a)*) to have a surface sensitive approach. By extrapolating

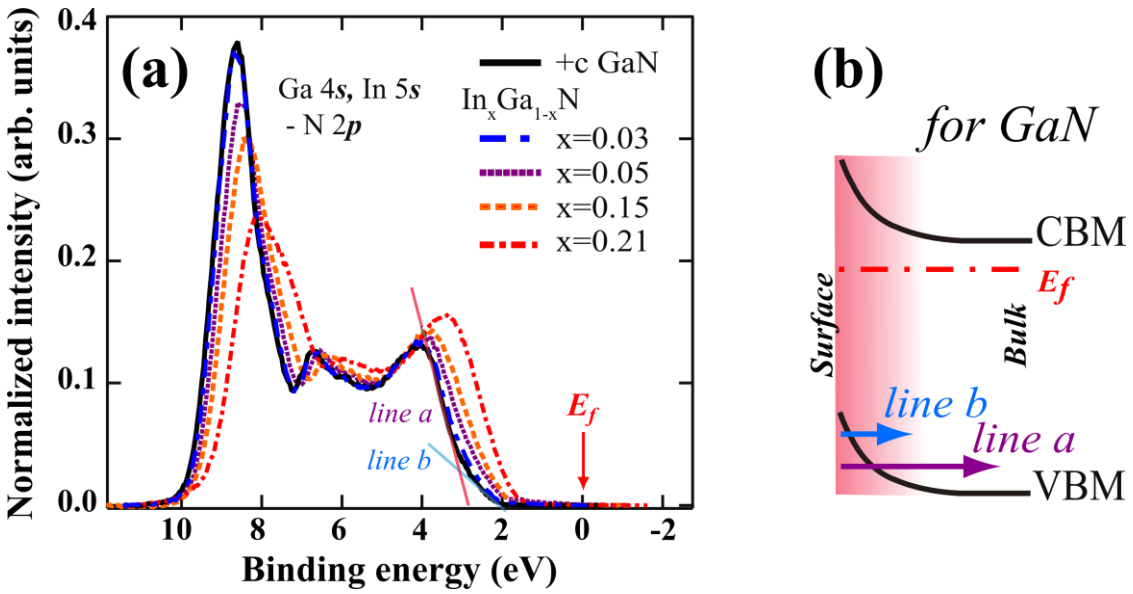

Fig. 4-2: (a) Valence band spectra of GaN and $In_xGa_{1-x}N$ for different InN mole fractions. (b) Illustration of the GaN band structure representing the upward band bending on surface.

line b, I estimated VBM at 2.1eV for GaN, which is more consistent with both the Schottky barrier height (SBH) and the build-in potential evaluated at 1.2eV from C-V measurements. It can be considered that the VBM determined from *line a* originates from the bulk of the film whereas the one calculated from *line b* is related to the surface region (*Fig. 4-2(b)*). I estimated the band structure of $In_xGa_{1-x}N$ material depending on the In content and the doping. In *Fig. 4-3* the valence band maximum (VBM) and conduction band minimum (CBM) are shown. To avoid any band offset for photo-generated carriers, a low In content layer and p-GaN, p-InGaN with Mg doping must be located on the top of the surface of the *p-i-n* junction.

Because of the larger observation depth of HX-PES, the spectra contain both surface and bulk

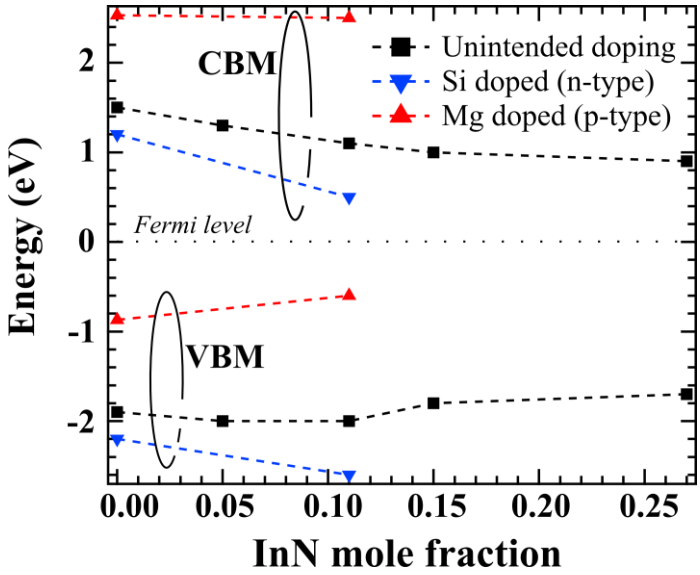

Fig. 4-3: Valence band maximum of GaN, $In_xGa_{1-x}N$ (0<x<0.27), and n-type, p-type doped films.

information reflecting the band bending near the surface. By modifying the detection depth, the core level N 1*s* was shifted toward lower binding energy, which implies an upward band bending near the surface of GaN films [2]. I confirmed a shift of the core level N 1*s* toward higher binding energy for InN films with a carrier concentration lower than ~1.0×10^{18}cm^{-3} for the first time, which implies a downward band bending [3].

This downward band bending of the InN film can explain the difficulty in obtaining a Schottky junction using this material. These results confirmed the importance of the band structure study for the interface and junction properties realized by $In_xGa_{1-x}N$ films.

Core-level and valence band spectra of $In_xGa_{1-x}N$ films were measured using hard x-ray photoemission spectroscopy (HX-PES). Fine structure caused by coupling of the localized Ga 3*d* and In 4*d* with N 2*s* states was experimentally observed in the films. Because of the large detection depth of HX-PES (~20 nm), the spectra contain both surface and bulk information due to the surface band bending. The $In_xGa_{1-x}N$ films (x=0~0.21) exhibited upward surface band bending, and the valence band maximum was shifted to lower binding energy as the mole fraction of InN was increased. On the other hand, downward surface band bending was confirmed for an InN film with low carrier density despite its n-type conduction. Although the Fermi level (E_F) near the surface of the InN film was detected inside the conduction band as reported previously, it was considered that E_F in the bulk of the film must be located in the band gap below the conduction band minimum.

4-2.1 Introduction

Indium nitride (InN) materials are desirable for applications such as high-speed transistors, terahertz emission devices and solar cells because of their low band gap of ~0.7 eV [4]. However, their intrinsic carrier density is higher than 1.0×10^{18}cm^{-3}, which has made it difficult to realize these applications. Recently, the quality of InN films has been improved so that the residual carrier density can be reduced to the order of ~10^{17} cm^{-3} [5]. InN can be doped with Mg as an acceptor, and the formation of *p*-type InN has been confirmed by capacitance voltage (C-V) measurements [6]. However, it is still very difficult to fabricate Schottky or *p*-*n*-junctions using InN films to obtain functional devices. It has been reported that the Fermi level (E_F) must be located in the conduction band for InN with carrier concentrations greater than 1.0×10^{18} cm^{-3} [7]. Also, it has been proposed that electrons are likely to accumulate on the InN surface [8], [9]. However, clear evidence of downward band bending at the InN surface has not been detected directly.

The band offset between GaN and its alloys such as $Al_xGa_{1-x}N$ and $In_xGa_{1-x}N$ affects the performance of electronic devices. Although the band offsets of the InN/GaN system have been studied, there are discrepancies between theoretical (0.3 [10] - 0.6 eV [11], [12]) and experimental values (0.58-1.1 eV [13–18]). Therefore, it is necessary to evaluate the variation of the valence band structure in $In_xGa_{1-x}N$ films as a function of InN mole fraction.

X-ray photoelectron spectroscopy (XPS) has been used as surface-analysis method to detect core-level spectra with respect to chemical bond and shift of materials. Conventional XPS is sensitive to surface

contamination because its detection depth is only a few nanometers. The intensity of photoelectrons from the valence band is generally too weak to precisely determine the surface band bending and offset. To overcome these disadvantages of conventional XPS, $In_xGa_{1-x}N$ films were investigated using hard X-rays from synchrotron radiation at SPring-8 (hard X-ray photoemission spectroscopy (HX-PES) [1]). Because of the high kinetic energy of electrons excited by hard X-rays (5.95 keV), the detection depth of HX-PES is ~20 nm. HX-PES detects photoelectrons sufficiently well to study the valence band structure and band bending of $In_xGa_{1-x}N$ films in a similar manner as previously reported for *p*-$Al_xGa_{1-x}N$ films [19].

Here, I studied the valence band and core-levels of $In_xGa_{1-x}N$ films using HX-PES. Ga 3*d* and In 4*d* core spectra and valence band structures are assessed to determine the effects of alloying GaN with InN. The influence of surface band bending on the determination of the valence band maximum (VBM) from the angular dependence of the N 1*s* core-level and valence band spectra is discussed.

4-2.2 Experimental details

Undoped $In_xGa_{1-x}N$ films (x= 0-0.21) were grown on GaN templates with Ga-face (+c) polarity that were deposited on a c-plane sapphire substrate by metalorganic chemical vapor deposition. Each $In_xGa_{1-x}N$ layer was 0.3-0.4 μm thick. The mole fraction of InN was controlled by the substrate temperature and was determined by X-ray diffraction measurement [20], [21]. From Hall measurement characterization, the carrier concentration was in the range of 1.8-5.0×10^{17} cm^{-3}. For comparison with high indium concentration films, InN films with carrier concentrations of 5.0×10^{17}, 1.5×10^{18} and 5.0×10^{18} cm^{-3} were also prepared by molecular beam epitaxy as reported in Ref. [6].

The samples were introduced into the HX-PES apparatus at the undulator beamline BL15XU [22] of SPring-8. The energy and diameter of the X-ray beam were 5.95 keV and ~ϕ60 μm, respectively. The detection depth was approximately ~20 nm, three times the inelastic mean free path of the photoelectrons, with respect to the sample surface in the normal emission geometry where the E-vector of the X-ray and the detection direction of photoelectrons are parallel [23]. This experimental configuration enabled us to detect bulk-sensitive information with a minimized influence from surface contamination. Another advantage of HX-PES in this configuration is the photoionization cross-section of the *s*-orbital larger than that of conventional XPS (Al *K*α x-ray source: 1486.6 eV) [24]. The total energy resolution was as fine as 240 meV, which is significantly higher than that of conventional XPS of ~600 meV comparable to the band gap of InN. The system was referenced to the E_F of a bulk gold. A gold layer was also deposited over half of the sample surface, and the C 1*s* core-level was measured on both areas. Thus the binding energy of the sample was calibrated by monitoring the shift in the position of the C 1*s* core-level peak detected on the gold layer. The spectra were corrected with a Shirley-type background subtraction [25].

4-2.3 Core-level spectra of Ga 3d and In 4d for $In_xGa_{1-x}N$

Ga 3*d*, N *2s* and In 4*d* core-level spectra normalized by the integrated intensity for the $In_xGa_{1-x}N$ films with x=0~0.21 and InN films with carrier concentration of $5.0\times10^{17}cm^{-3}$ measured at take-off angle (TOA) of 88º (bulk-sensitive, detection depth ~20nm) conditions are presented in *Fig. 4-4*. The small Ga 3*d*-N 2*s* energy separation gives rise to hybridization between Ga 3*d* and N 2*s* in GaN. The hybridization causes splitting of the t_2 level into bonding (t_{2g}) and antibonding (t_{2u}) states, while the nonbonding state e_g remains nearly atomic, showing spin-orbit splitting [26]. The peak~19.8 eV is mainly bonding t_{2g} state of Ga 3*d*-like, whereas the broad peak at ~16 eV is dominantly antibonding t_{2u} of N 2*s*.

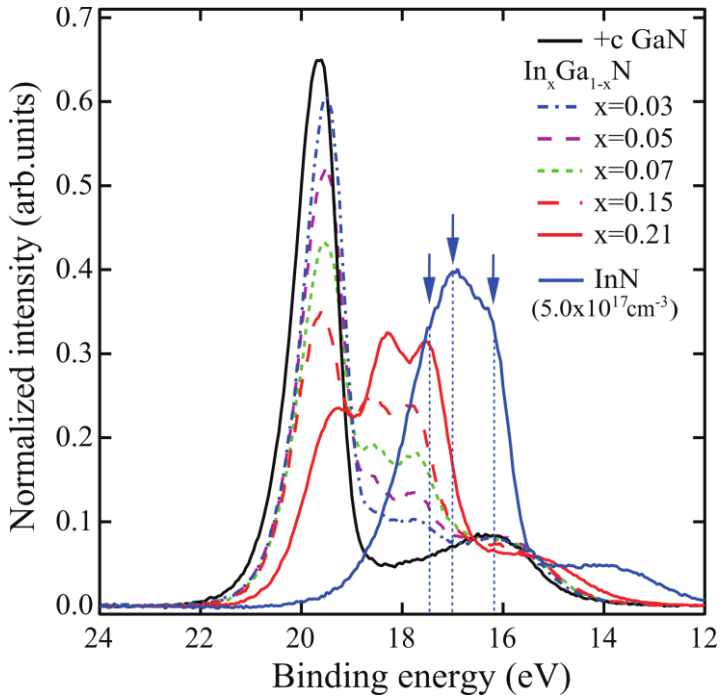

Fig. 4-4: Ga 3d, In 4d, N2s core-level spectra normalized by the integrated intensity of the $In_xGa_{1-x}N$ films at TOA of 88º.

From angular-momentum decomposition of the atom projected densities of states done by F. Litimein et al. [27], the orbital of N 2*s* in InN is attributed to three peaks, which are detected at 14 eV, 16 eV and 17.3 eV in *Fig. 4-4*. In the calculation of Ref. [27], the In 4*d* orbital is predominantly contributed of three densities of states in the range from 16 to 18 eV as indicated with arrows in *Fig. 4-4*. The highest peak at 17 eV originates from In 4*d* as reported previously [28]. Although the peak of In 4*d*- N 2*s* at 17.3 eV should be theoretically smaller [27], the intensity becomes higher experimentally due to a larger cross section of the *s*-orbitals in the HX-PES. With increase of InN mole fraction, the localized Ga 3*d* and In 4*d* states were dispersed through the hybridization with N 2*s* as calculated in the model of $In_{0.5}Ga_{0.5}N$ [29]. This is supported by two peaks emerging predominately around 17.5 and 18.3 eV.

4-2.4 Surface band bending and VBM of GaN film

The valence band structures also change as the mole fraction of InN is increased as shown in *Fig. 4-5*. The intensity of the Ga 4*s*-N 2*p* peak at around 8.5 eV [30] is enhanced because of the larger cross-section of *s*-orbital in HX-PES than that in conventional XPS. The VBM shifted to lower binding energy (towards E_F) when GaN is alloyed with InN.

There are two possible extrapolations, *lines a* and *b* in *Fig. 4-5* (expanded plot in *Fig. 4-6*), which are used to determine the VBM for the intrinsic GaN film at TOA of 88º. The VBM calculated using *line a* is 2.9-3.0 eV. By taking the band gap of GaN (E_g^{GaN}: 3.4 eV) into account, the energy difference between E_F and the conduction band minimum (CBM) near the surface implies a value of 0.5 eV. This value is too small to explain the Schottky barrier height (SBH) on GaN film larger than ~1.0 eV [18], [31]. On the other hand, the VBM determined using *line b* is 2.1 eV which is more consistent with both the SBH and the built-in potential evaluated at 1.2 eV from C-V measurements [2]. It can be considered that the VBM determined from *line a* originates from the bulk of the film whereas the one calculated from *line b* is related to the surface region, as shown in the inset of *Fig. 4-5*.

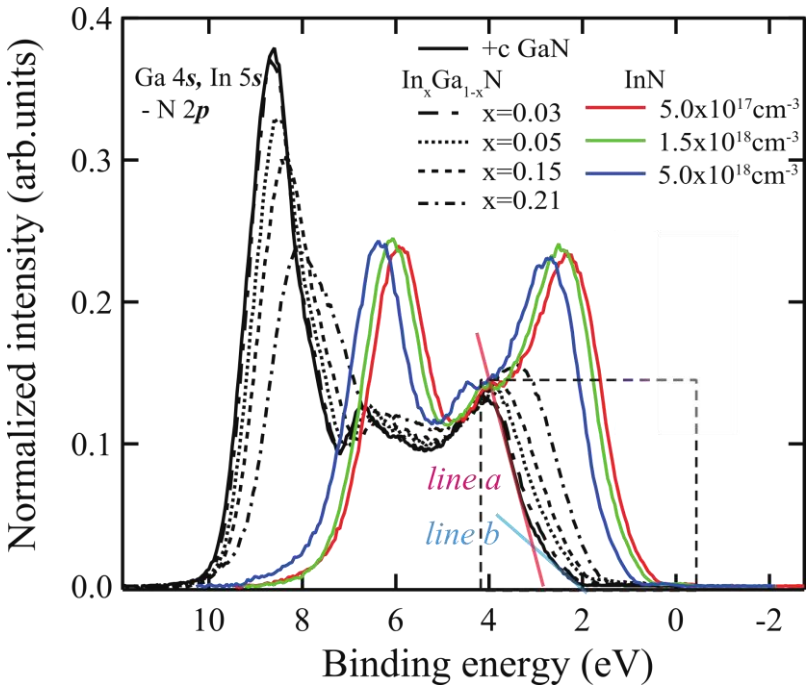

Fig. 4-5: Valence band spectra normalized by the integrated intensity of typical $In_xGa_{1-x}N$ and InN films observed by HX-PES at a TOA of 88º.

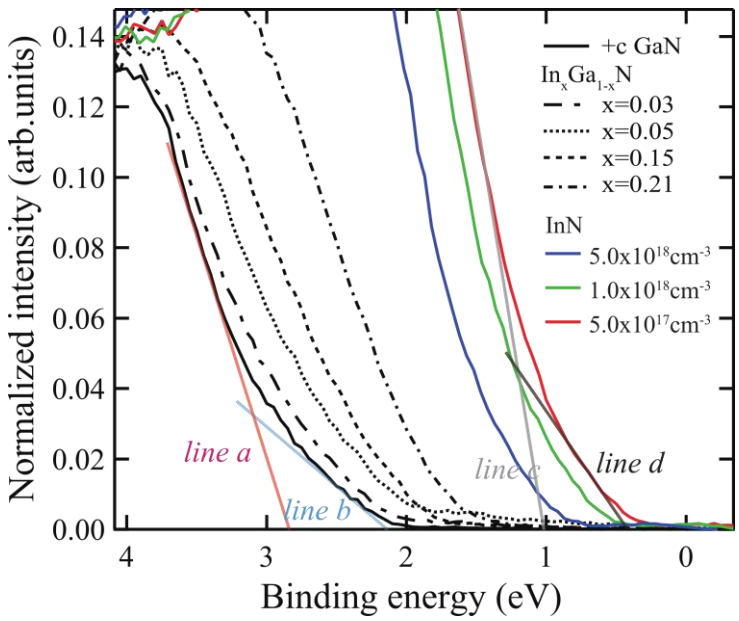

Fig. 4-6: Expansion of Fig. 4-5 at the valence band maximum. The lines are extrapolated to determine the VBM.

4-2.5 N 1s core-level spectra of InN films grown by MBE

At take-off angle (TOA) of 88°, the peak position of N 1*s* core-level spectra was chemically shifted from 397.3 eV for GaN to 395.8 eV for InN when increasing the indium composition. *Figure 4-7* represents N 1*s* core-level spectra of the InN films measured under bulk (TOA of 88°) and surface-sensitive (TOA of 30°, detection depth ~10 nm) conditions. For the sample with a carrier concentration of 5.0×10^{17} cm^{-3}, the spectrum with TOA of 88° exhibits an asymmetrical shape with a tail at higher binding energy (*Fig. 4-7 (a)*). A clear shift to higher binding energy is observed at TOA of 30°, and the spectrum becomes more symmetric with a smaller tail at higher binding energy, compared to the spectrum at TOA of 88°. This implies the presence of a downward band bending near the film surface, as shown in the inset of *Fig. 4-7 (a)*.

The N 1*s* core-level spectra at TOA of 30° are symmetrical and the peak positions are constant at ~396.2 eV in spite of the carrier concentration, which is the same as the value determined by conventional XPS [32]. The asymmetric spectrum shape originates from two dominant components at a lower binding energy of 395.8 eV in the bulk of the film and at 396.2 eV near its surface due to the downward surface band bending. We attempted to determine the value of surface band bending according to the literature analyzing surface band bending of Si [33]. However, the N 1s core spectra were found not to be simulated by simple surface band bending profile. The profiles were not simulated even by introducing flat potential near the surface. This might imply that InN surface must be complex such as In fluctuation.

As the carrier concentration increases, the shift of the N 1*s* core-level spectra is reduced and a more symmetric shape is observed in *Fig. 4-7 (c)*. For the InN film with a carrier concentration of 5.0×10^{18} cm^{-3}, the surface band should be almost flat, implying that the depletion layer should be too shallow to detect the difference between

detection depths of ~10 nm (TOA of 30°) and ~20 nm (TOA of 88°) (inset in *Fig. 4-7 (c)*). The TOA dependence of the N1s core-level spectral shape and its position shift is consistent with the expected thickness variation of the accumulation layer depending on the carrier concentration.

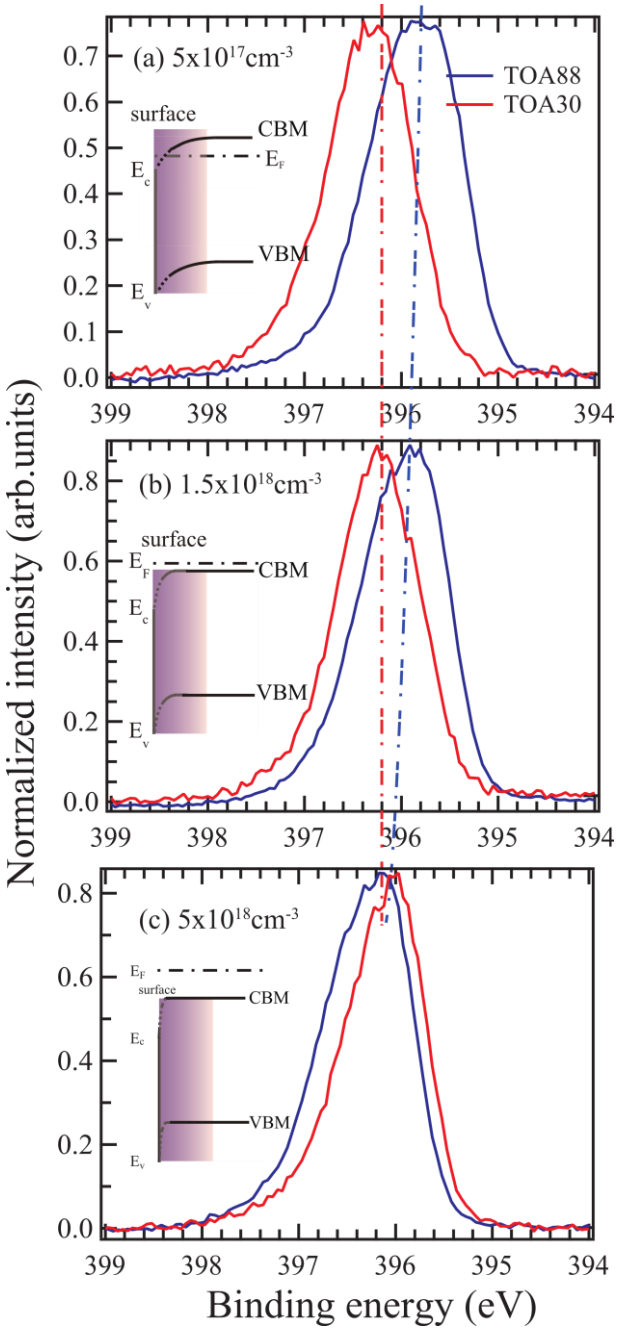

Fig. 4-7: N 1s core-level spectra detected at TOAs of 88° and 30° for InN samples grown by MBE with carrier concentrations of (a) 5.0×10^{17} cm^{-3}, (b) 1.5×10^{18} cm^{-3}, and (c) 5.0×10^{18} cm^{-3}. The dashed lines are a guide to highlight the variation of peak position. The insets show energy band diagrams explaining the relationship between surface band bending and the detection depth of HX-PES, although the profile for the surface of InN remains unclear.

4-2.6 VBM of InN films

Figure 4-6 shows an expanded plot near the VBM of $In_xGa_{1-x}N$ films. The valence band spectra for the InN films with various carrier concentrations are represented by colored lines. At lower carrier concentration, the VBM of the InN films shifted to lower binding energy. Two possible lines, *c* and *d*, were used to determine the VBM of InN. It can be considered that the VBM determined from *line d* originates from the bulk of the film whereas the one calculated from *line c* is related to the surface region, as shown in the inset of *Fig. 4-7*. By extrapolating *line c*, the VBM of InN with a carrier concentration of 5.0×10^{17} cm^{-3} is around 1.0 eV below E_F, which means that E_F is located inside the conduction band. As far as normal carrier conduction occurs, the E_F should not be located inside the conduction band as common understanding for semiconductor materials. It was therefore assumed that surface band bending influences the estimation of VBM as mentioned in the part "Surface band bending and VBM for GaN films" on page 100.

A slight difference of the VBM was observed between the spectra detected at TOAs of 88° and of 30° for the InN film with a carrier concentration of 5.0×10^{18} cm^{-3}. The VBM calculated from both spectra was 1.3 eV (*Fig. 4-8 (a)*), which is the same as the E_F on surface lying above the VBM previously determined using conventional XPS [7]. On the other hand, for InN with a carrier concentration of 5.0×10^{17} cm^{-3}, the valence band spectrum near the surface of the film (TOA of 30°) is clearly shifted towards higher binding energy, as shown in *Fig. 4-8 (b)*. When the conventional method is used (i.e., extrapolation of *line c*), the VBM values from both spectra are the same at 1.0eV, although the valence band spectrum for TOA of 30° is apparently shifted towards higher binding energy. The conventional approach is likely to overestimate the VBM because of the downward band bending at the surface of InN film.

The energy shift between TOAs of 88° and 30° is 0.5 eV (*Fig. 4-8 (b)*). Hence, the VBM determined from the spectrum at TOA of 88° must be located at the binding energy of 0.5 eV, which corresponds to the value determined from *line d* in *Fig. 4-6*. By taking both this estimated VBM and the band gap of 0.7 eV for InN into account, the E_F in the bulk must be located inside its band gap under the condition of a carrier concentration of less than 5.0×10^{17} cm^{-3}.

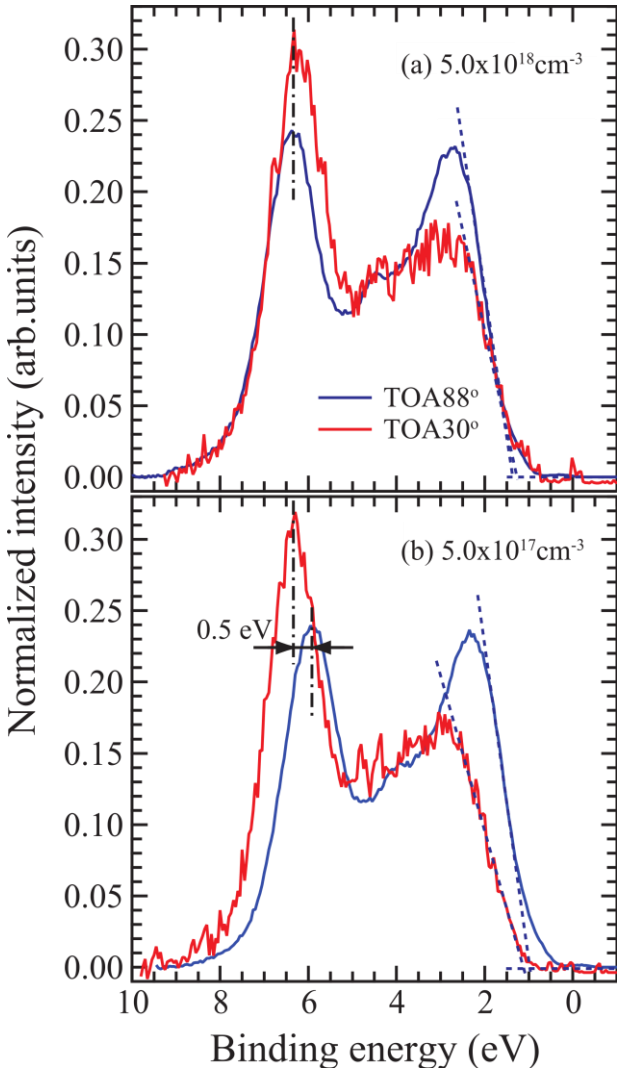

Fig. 4-8: Valence band structures detected at TOAs of 88° and 30° for InN films with carrier concentrations of (a) 5×10^{18} cm^{-3} and (b) 5×10^{17} cm^{-3}.

4-2.7 Conclusion

The electronic structures of $In_xGa_{1-x}N$ films were investigated by HX-PES. Because of the larger observation depth (~20 nm) of HX-PES than conventional XPS, the spectra contain both surface and bulk information reflecting the band bending on surface. A shift to lower binding energy is observed when the InN mole fraction increases inside $In_xGa_{1-x}N$ films, which means that the VBM gets closer to the E_F with higher InN mole fraction.

A new method for the evaluation of the valence band maximum (VBM) was described. With this method, the distance between the VBM and the Fermi level for GaN films (2.1 eV) is more consistent with the Schottky barrier height and the build-in potential of n-GaN films, which is 1.2 eV, estimated from capacitance-voltage measurement.

Downward band bending near the surface was confirmed for InN films with a carrier concentration lower than ~1.0×10^{18} cm^{-3} for the first time. Our measurement describes for the first time that the position of the E_F must be located inside the InN bandgap for high InN film quality with a low free carrier concentration of about $5\times10^{17}cm^{-3}$. This result is in opposition to previous researches, which estimated the E_F above the conduction band of the InN films.

The estimation of the E_F inside the InGaN bandgap for the full range of InN mole fraction is another important result for the development of future heterojunction solar cells using only $In_xGa_{1-x}N$ films.

References chapter 4

[1] K. Kobayashi, "High-resolution hard X-ray photoelectron spectroscopy: Application of valence band and core-level spectroscopy to materials science," *Nuclear Instruments and Methods in Physics Research Section A: Accelerators, Spectrometers, Detectors and Associated Equipment*, vol. 547, no. 1, pp. 98–112, Jul. 2005.

[2] M. Sumiya, M. Lozac'h, N. Matsuki, N. Ohhashi, K. Sakoda, H. Yoshikawa, S. Ueda, and K. Kobayashi, "Valence band structure of III-V nitride films characterized by hard X-ray photoelectron spectroscopy," *Physica Status Solidi (C)*, vol. 7, no. 7–8, pp. 1903–1905, 2010.

[3] M. Lozac'h, S. Ueda, S. Liu, H. Yoshikawa, S. Liwen, X. Wang, B. Shen, K. Sakoda, K. Kobayashi, and M. Sumiya, "Determination of the surface band bending in In x Ga 1− x N films by hard x-ray photoemission spectroscopy," *Science and Technology of Advanced Materials*, vol. 14, no. 1, p. 015007, Feb. 2013.

[4] J. Wu, W. Walukiewicz, K. M. Yu, J. W. Ager, E. E. Haller, H. Lu, W. J. Schaff, Y. Saito, and Y. Nanishi, "Unusual properties of the fundamental band gap of InN," *Applied Physics Letters*, vol. 80, no. 21, p. 3967, 2002.

[5] N. Ma, X. Q. Wang, S. T. Liu, L. Feng, G. Chen, F. J. Xu, N. Tang, L. W. Lu, and B. Shen, "Deep donor state in InN: Temperature-dependent electron transport in the electron accumulation layers and its influence on Hall-effect measurements," *Applied Physics Letters*, vol. 99, no. 18, p. 182107, 2011.

[6] X. Wang, S.-B. Che, Y. Ishitani, and A. Yoshikawa, "Systematic study on p-type doping control of InN with different Mg concentrations in both In and N polarities," *Applied Physics Letters*, vol. 91, no. 24, p. 242111, 2007.

[7] P. King, T. Veal, P. Jefferson, S. Hatfield, L. Piper, C. McConville, F. Fuchs, J. Furthmüller, F. Bechstedt, H. Lu, and W. Schaff, "Determination of the branch-point energy of InN: Chemical trends in common-cation and common-anion semiconductors," *Physical Review B*, vol. 77, no. 4, p. 045316, Jan. 2008.

[8] H. Lu, W. J. Schaff, L. F. Eastman, and C. E. Stutz, "Surface charge accumulation of InN films grown by molecular-beam epitaxy," *Applied Physics Letters*, vol. 82, no. 11, p. 1736, 2003.

[9] I. Mahboob, T. Veal, C. McConville, H. Lu, and W. Schaff, "Intrinsic Electron Accumulation at Clean InN Surfaces," *Physical Review Letters*, vol. 92, no. 3, p. 036804, Jan. 2004.

[10] C. G. Van de Walle and J. Neugebauer, "Small valence-band offsets at GaN/InGaN heterojunctions," *Applied Physics Letters*, vol. 70, no. 19, p. 2577, 1997.

[11] S.-H. Wei and A. Zunger, "Valence band splittings and band offsets of AlN, GaN, and InN," *Applied Physics Letters*, vol. 69, no. 18, p. 2719, 1996.

[12] P. G. Moses and C. Van de Walle, "Band bowing and band alignment in InGaN alloys," *Applied Physics Letters*, vol. 96, no. December 2009, p. 021908, 2010.

[13] C.-F. Shih, N.-C. Chen, P.-H. Chang, and K.-S. Liu, "Band Offsets of InN/GaN Interface," *Japanese Journal of Applied Physics*, vol. 44, no. 11, pp. 7892–7895, Nov. 2005.

[14] P. King, T. Veal, C. Kendrick, L. Bailey, S. Durbin, and C. McConville, "InN/GaN valence band offset: High-resolution x-ray photoemission spectroscopy measurements," *Physical Review B*, vol. 78, no. 3, p. 033308, Jul. 2008.

[15] G. Martin, a. Botchkarev, a. Rockett, and H. Morkoç, "Valence-band discontinuities of wurtzite GaN, AlN, and InN heterojunctions measured by x-ray photoemission spectroscopy," *Applied Physics Letters*, vol. 68, no. 18, p. 2541, 1996.

[16] C.-L. Wu, H.-M. Lee, C.-T. Kuo, S. Gwo, and C.-H. Hsu, "Polarization-induced valence-band alignments at cation- and anion-polar InN/GaN heterojunctions," *Applied Physics Letters*, vol. 91, no. 4, p. 042112, 2007.

[17] T. Ohashi, P. Holmström, A. Kikuchi, and K. Kishino, "High structural quality InN/In0.75Ga0.25N multiple quantum wells grown by molecular beam epitaxy," *Applied Physics Letters*, vol. 89, no. 4, p. 041907, 2006.

[18] K. (Albert) Wang, C. Lian, N. Su, D. Jena, and J. Timler, "Conduction band offset at the InN/GaN heterojunction," *Applied Physics Letters*, vol. 91, no. 23, p. 232117, 2007.

[19] M. Sumiya, Y. Kamo, N. Ohashi, M. Takeguchi, Y.-U. Heo, H. Yoshikawa, S. Ueda, K. Kobayashi, T. Nihashi, M. Hagino, T. Nakano, and S. Fuke, "Fabrication and hard X-ray photoemission analysis of photocathodes with sharp solar-blind sensitivity using AlGaN films grown on Si substrates," *Applied Surface Science*, vol. 256, no. 14, pp. 4442–4446, May 2010.

[20] L. Sang, M. Takeguchi, L. Woong, Y. Nakayama, M. Lozac'h, T. Sekiguchi, and S. Masatomo, "Phase Separation Resulting from Mg Doping in p-InGaN Film Grown on GaN/Sapphire Template," *Applied Physics Express*, vol. 3, p. 111004, 2010.

[21] M. Lozac'h, Y. Nakano, L. Sang, K. Sakoda, and M. Sumiya, "Study of Defect Levels in the Band Gap for a Thick InGaN Film," *Japanese Journal of Applied Physics*, vol. 51, p. 121001, Nov. 2012.

[22] S. Ueda, Y. Katsuya, M. Tanaka, H. Yoshikawa, Y. Yamashita, S. Ishimaru, Y. Matsushita, K. Kobayashi, R. Garrett, I. Gentle, K. Nugent, and S. Wilkins, "Present Status of the NIMS Contract Beamline BL15XU at SPring-8," *10th internation conference on Synchrotron Radiation Instrumentation*, pp. 403–406, 2010.

[23] S. Tanuma, C. J. Powell, and D. R. Penn, "Calculations of Electron Inelastic Mean Free Paths.," *Surface and Interface Analysis*, vol. 21, no. September 1993, pp. 165–176, 1993.

[24] J. J. Yeh and I. Lindau, "Atomic subshell photoionization cross sections and asymmetry parameters: $1 < Z < 103$," *Atomic data and nuclear data tables*, vol. 32, pp. 1–155, 1985.

[25] D. A. Shirley, "High-Resolution X-Ray Photoemission Spectrum of the Valence Bands of Gold," *Physical Review B*, vol. 5, no. 12, pp. 4709–4714, 1972.

[26] K. Kobayashi, Y. Takata, T. Yamamoto, J.-J. Kim, H. Makino, K. Tamasaku, M. Yabashi, D. Miwa, T. Ishikawa, S. Shin, and T. Yao, "Intrinsic Valence Band Study of Molecular-Beam-Epitaxy-Grown GaAs and GaN by High-Resolution Hard X-ray Photoemission Spectroscopy," *Japanese Journal of Applied Physics*, vol. 43, no. No. 8A, pp. L1029–L1031, Jul. 2004.

[27] F. Litimein, B. Bouhafs, G. Nouet, and P. Ruterana, "Meta-GGA calculation of the electronic structure of group III–V nitrides," *Physica Status Solidi (B)*, vol. 243, no. 7, pp. 1577–1582, Jun. 2006.

[28] L. Piper, T. Veal, P. Jefferson, C. McConville, F. Fuchs, J. Furthmüller, F. Bechstedt, H. Lu, and W. Schaff, "Valence-band structure of InN from x-ray photoemission spectroscopy," *Physical Review B*, vol. 72, no. 24, p. 245319, Dec. 2005.

[29] M. Usuda, N. Hamada, K. Shiraishi, and A. Oshiyama, "Band Structures of Wurtzite InN and Ga 1- x In x N by All-Electron G W Calculation," *Japanese Journal of Applied Physics*, vol. 43, no. No. 3B, pp. L407–L410, Mar. 2004.

[30] W. R. L. Lambrecht, B. Segall, S. Strite, G. Martin, A. Agarwal, H. Morkoç, and A. Rockett, "X-ray photoelectron spectroscopy and theory of the valence band and semicore Ga 3d states in GaN," *Physical Review B*, vol. 50, no. 19, pp. 155–160, 1994.

[31] N. Matsuki, Y. Irokawa, T. Matsui, M. Kondo, and M. Sumiya, “Photovoltaic Action in Polyaniline/n-GaN Schottky Diodes,” *Applied Physics Express*, vol. 2, p. 092201, 2009.

[32] T. Veal, P. King, P. Jefferson, L. Piper, C. McConville, H. Lu, W. Schaff, P. Anderson, S. Durbin, D. Muto, H. Naoi, and Y. Nanishi, “In adlayers on c-plane InN surfaces: A polarity-dependent study by x-ray photoemission spectroscopy,” *Physical Review B*, vol. 76, no. 7, p. 075313, Aug. 2007.

[33] K. Kakushima, K. Okamoto, K. Tachi, J. Song, S. Sato, T. Kawanago, K. Tsutsui, N. Sugii, P. Ahmet, T. Hattori, and H. Iwai, “Observation of band bending of metal/high-k Si capacitor with high energy x-ray photoemission spectroscopy and its application to interface dipole measurement,” *Journal of Applied Physics*, vol. 104, no. 10, p. 104908, 2008.

Chapter 5

5- Investigation of defect levels inside GaN and InGaN films

In this chapter, I will describe the fabrication and characterization of Schottky junctions on thick $In_{0.09}Ga_{0.91}N$ films, and then I will present an investigation of defect levels inside the bandgap of $In_{0.09}Ga_{0.91}N$. Up to now there is no report about deep level defects inside thick $In_xGa_{1-x}N$ films. Thermal admittance spectroscopy (TAS), deep level transient spectroscopy (DLTS), and deep level optical spectroscopy (DLOS) were carried out for $In_xGa_{1-x}N$ films with a thickness of 200 nm. This work shows that indium fluctuation, cation vacancies (V_{III}), nitride vacancies (V_N) and complexes associated (V_{III}-O_N, V_{III}-C_N, V_{III}-V_N) are found to be greatly increased when alloying InN with GaN. These defects contribute to enhance the electron concentration (unintended n-doping) of about $10^{17}cm^{-3}$ for $In_xGa_{1-x}N$ and degrade the Schottky junction with a high leakage current under negative bias voltage.

5-1 Schottky junction characterization on $In_{0.09}Ga_{0.091}N$ thick film

In order to determine the deep level defects present inside thick InGaN films, three techniques were employed: the thermal admittance spectroscopy (TAS), the deep level transient spectroscopy (DLTS), and the deep level optical spectroscopy (DLOS). For each technique, the principle of measurement, the extractable parameters, and the results obtained on thick InGaN films are presented. The same Schottky device was used for the three defect level techniques in order to compare and discuss the different results obtained.

5-1.1 Sample preparation

I deposited InGaN films on c-plane sapphire substrate by metalorganic chemical vapor deposition (MOCVD) with a horizontal reactor. After deposition of GaN epilayer of 1.9 µm in thickness at 1000 ºC by using the conventional low-temperature buffer layer technique, a multi-layer (ML) structure consisting of 10 pairs of AlN/GaN (9 nm / 38 nm) layers was fabricated at 1000 ºC on the GaN template to prevent the propagation of dislocations to the upper layer. Subsequently, an InGaN layer of 200 nm in thickness was grown on the ML structure at 790 ºC for 1h under N_2 gas ambient as shown in *Fig. 5-1*.

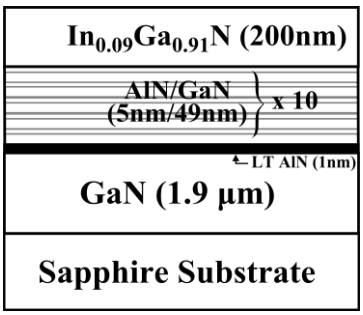

Fig. 5-1: $In_{0.09}Ga_{0.91}N$ thick film structure deposited by MOCVD on c-plane sapphire substrate.

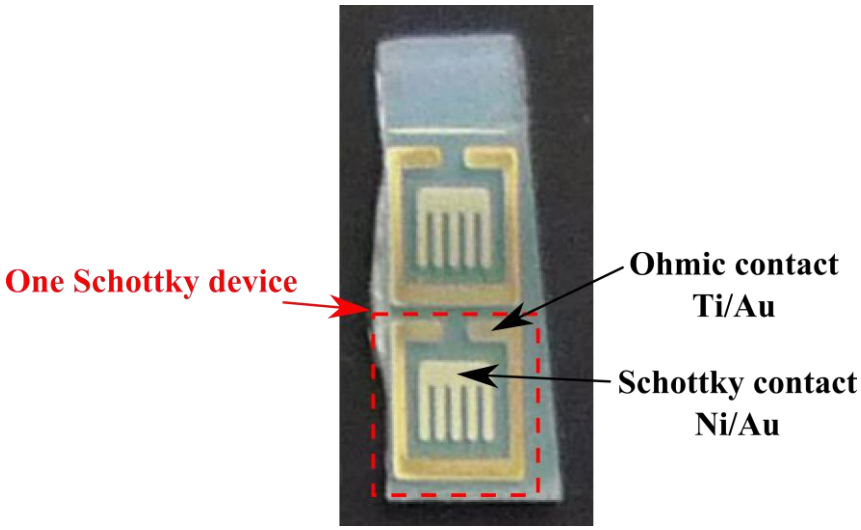

Fig. 5-2: Picture of two Schottky devices deposited by e-beam evaporator on InGaN film itself deposited on GaN epilayer / sapphire substrate.

I cleaned the sample's surface by dipping subsequently in acetone, methanol, and deionized water to remove organic impurities. And then, I treated the sample by HCl (10 %) solution for 10 min to etch the natural oxide layer. I deposited the Ti/Au (50 nm/100 nm) on the InGaN film by e-beam evaporator, followed by a rapid thermal annealing (RTA) process. The device was annealed in vacuum at 750 ºC for 1.5 min to form the ohmic contact. The Schottky contact was realized by using Ni/Au (50 nm/100 nm) after annealing at 550 ºC for 3 min. The area of Schottky contact was 6.2×10^{-3} cm^2. These RTA processes were optimized for the ohmic and Schottky contacts. *Figure 5-2* presents a picture of such Schottky devices fabricated.

The InN mole fraction of the sample in this study was estimated to be 9.0 % from the InGaN peak position of x-ray diffraction (XRD) by Vegard's law. The satellites and interference peaks were observed for the 2θ-ω scan of (0002) plane (*Fig. 5-3*), which indicates both the designed periodicity of the AlN/GaN ML structure, and smooth interface between InGaN and the under-layer. The value of full width at half maximum (FWHM) of ω (0002) for InGaN and GaN diffraction peak was 261 arcsec and 276 arcsec, respectively.

The thickness of AlN and GaN layers inside the ML structure was estimated by simulation with the XRD software using the position of the different orders of satellite peaks. To confirm the accurate thickness of each layer inside the structure presented in *Fig. 5-1*, TEM measurements were preformed (*Fig. 5-4* and *Fig. 5-6*).

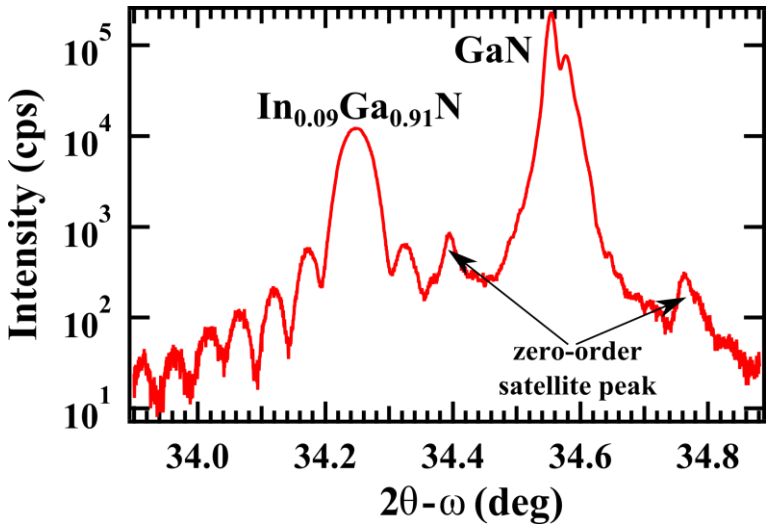

Fig. 5-3: XRD analysis of $In_{0.09}Ga_{0.91}N$ thick film structure for (0002) plane.

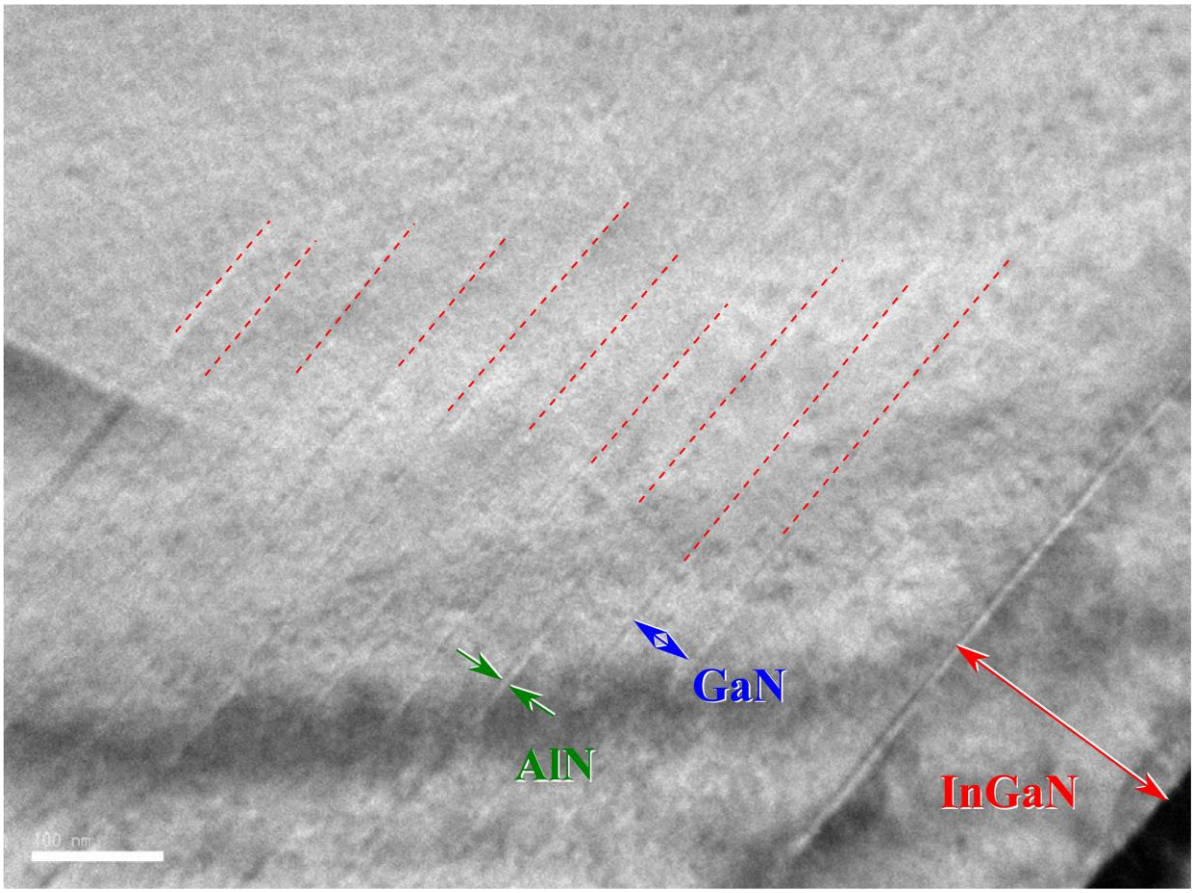

Fig. 5-4: TEM image of the $In_{0.09}Ga_{0.91}N$ on multi-layer structure $(AlN\text{-}GaN)_{\times 10}$ (scale 100nm).

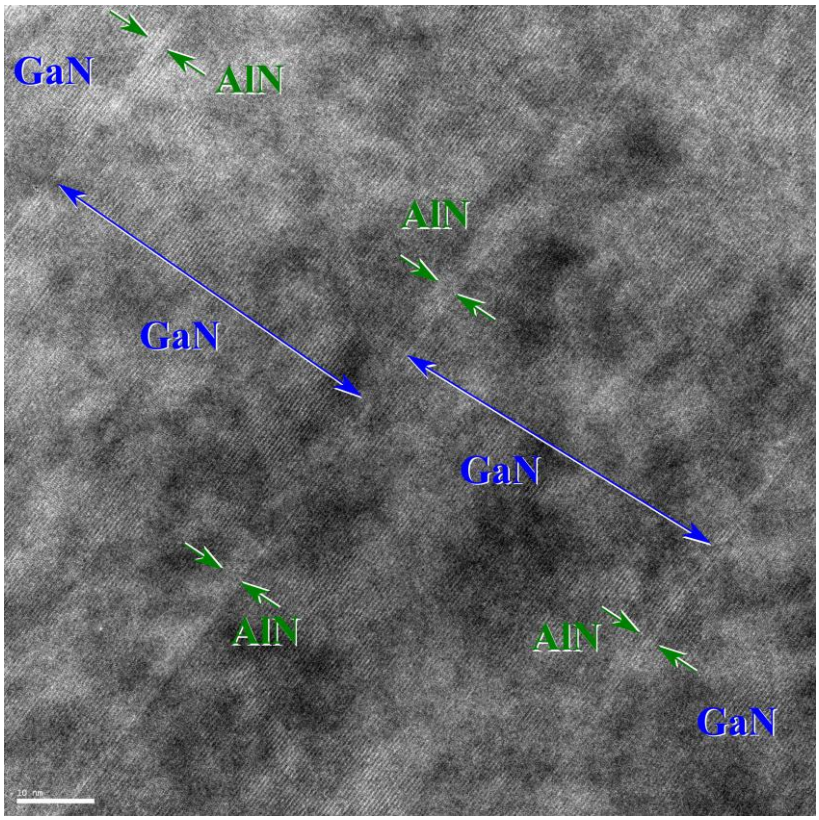

Fig. 5-6: TEM image of the multi-layer structure $(AlN\text{-}GaN)_{\times 10}$ (scale 10nm).

The InGaN film was found to be completely strained on the ML layers from $(10\bar{1}4)$ plane by XRD reciprocal space mapping as shown in *Fig. 5-5*.

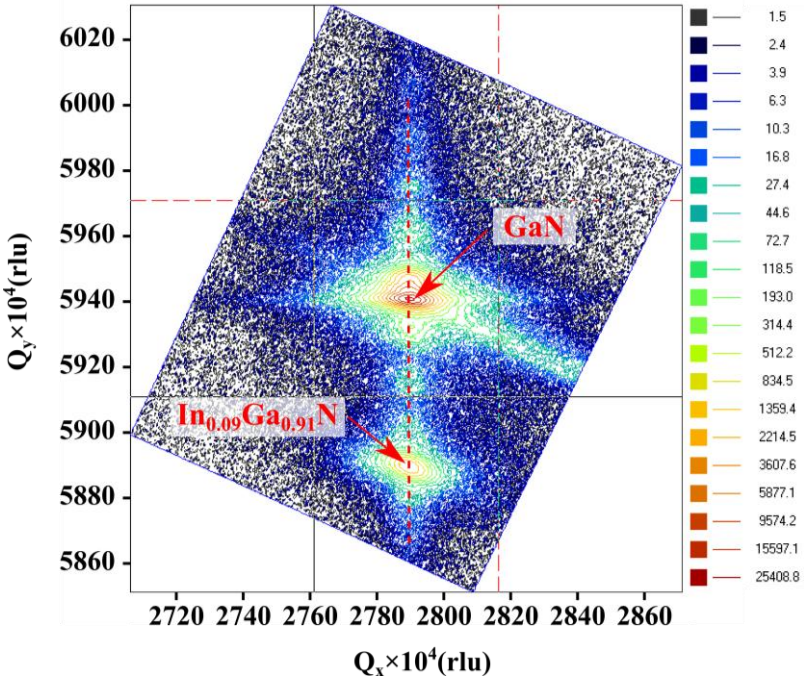

Fig. 5-5: XRD mapping of $In_{0.09}Ga_{0.91}N$ thick film structure for $(10\bar{1}4)$ plane represented in the reciprocal space.

I confirmed the smooth surface of the $In_{0.09}Ga_{0.91}N$ thick film by AFM measurement, the density of pits on the InGaN surface was less than 2×10^{7} cm^{-2} with a root-mean-square (rms) of 1.4 nm for a 5×5 μm^2 scanning area (*Fig. 5-7*). No threading dislocation was observed. For samples directly grown on the GaN layer, a density of pits ($3.2x10^{7}cm^{-2}$), a density of threading dislocation ($5.2x10^{8}cm^{-2}$) and a root mean square (rms) roughness of 3.74nm (for a 5×5 μm^2 scanning area) were obtained. Thus the introduction of ML structure improved the material quality.

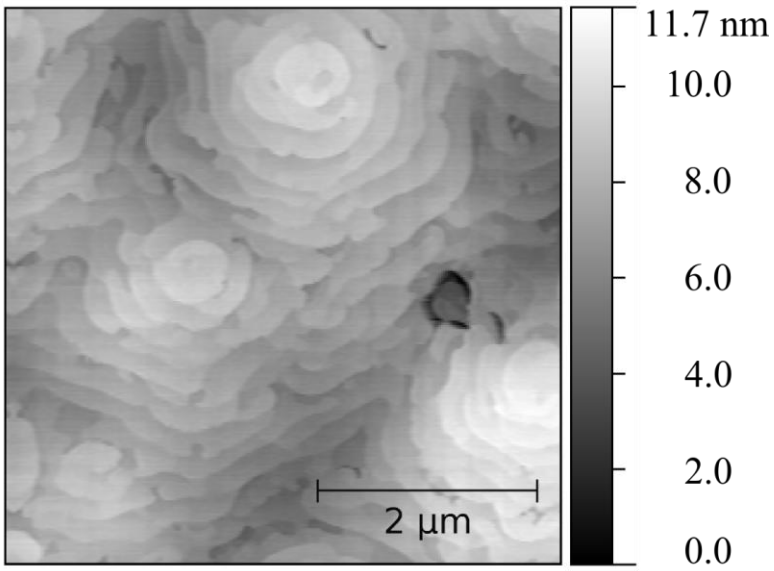

Fig. 5-7: Surface of thick $In_{0.09}Ga_{0.91}N$ film by AFM measurement for a 5×5 µm scanning area.

The Schottky properties of $In_{0.09}Ga_{0.91}N$ thick films were characterized by current-voltage (J-V), capacitance-frequency (C-f) and capacitance - voltage (C-V) measurements.

5-1.2 Current-voltage measurement

According to Padovani and Stratton [1], [2], the different emission regimes should be determined according to the temperature T (293 K), carrier concentration N_d, and energy E_{00}:

$$E_{00} = \left(\frac{qh}{4\pi}\right)\left(\frac{N_d}{\varepsilon_s \varepsilon_0 m_e^*}\right)^{1/2}. \qquad (5\text{-}1)$$

The thermionic emission (TE) is predominant when $kT/E_{00} >> 1$, the thermionic-field emission (TFE) when $kT/E_{00} \approx 1$, and the field emission when $kT/E_{00} << 1$, where q is the electron charge, h the Planck constant, and k the Boltzmann constant.

For wurtzite-GaN, I used the dielectric constant ε_s = 9.5 [3–5] with ε_0 the permittivity of free space ε_0=8.854×10^{-14} F/cm, and the electron effective mass is chosen at m_e^* = 0.22 m_0 [6], [7] with N_d at 6.3×10^{17} cm^{-3}.

In these conditions kT/E_{00} is estimated at 2.49, which is in the regime of TE. Furthermore, the ideality factor n was estimated by the following relation:

$$n = \frac{E_{00}}{kT}\coth\left(\frac{E_{00}}{kT}\right). \tag{5-2}$$

n has a value of 1.06, which indicates that the current conduction in our samples can be explained by the TE model.

For InN case, the value of electron effective mass in wurtzite-InN at 295 K is $m_0^*{}_{InN} = 0.045m_0$, based on the empirical relationship $m_0^* \sim 0.07\ E_g$ for III-V materials [8]. The dielectric constant of w-InN was previously estimated at $\varepsilon_s = 15.3$ [9], or 6.7 [10] and more recently at $\varepsilon_s = 9.3$ [5], [11].

For the $In_xGa_{1-x}N$ case, the dielectric constant and the electron effective mass can be estimated by a linear variation depending on the In content [5], [12]. The effective mass for electron in $In_xGa_{1-x}N$ can be determined by the following equation [5] taking into account the approximation $m_n^*{}_{GaN} = 0.2m_0$ and $m_n^*{}_{InN} = 0.05m_0$:

$$m_n^*\left(In_xGa_{1-x}N\right) = \left(x0.05 + (1-x)0.2\right)\times m_0\,. \tag{5-3}$$

For $In_{0.09}Ga_{0.91}N$, I determined the electron effective mass as $m_n^*(In_{0.09}Ga_{0.91}N) = 0.19m_0$. Because both dielectric constants of w-GaN (9.5) and w-InN (9.3) are quite similar, the value 9.5 was used for low InN mole fraction like in $In_{0.09}Ga_{0.91}N$. I summarized the parameters at 295 K depending on the InN mole fraction in *Table 5-1*.

Table 5-1: Dielectric constant and Effective mass of electron for wurtzite GaN, InN and $In_{0.09}Ga_{0.91}N$ at 295 K

	GaN	InN	$In_{0.09}Ga_{0.91}N$
Effective mass of electron (m_n^*)	*0.22 m_0*	*0.05 m_0*	*0.19 m_0*
Dielectric constant (ε_s)	*9.5*	*9.3*	*9.5*

In *Fig. 5-8* the J-V measurement under dark condition is presented. I extracted the Schottky properties by fitting the J-V curve to the thermionic equation in the linear part (in red):

$$J = A^*T^2\exp\left(-\frac{q\phi_B}{kT}\right)\left[\exp\left(\frac{qV}{nkT}\right)-1\right], \tag{5-4}$$

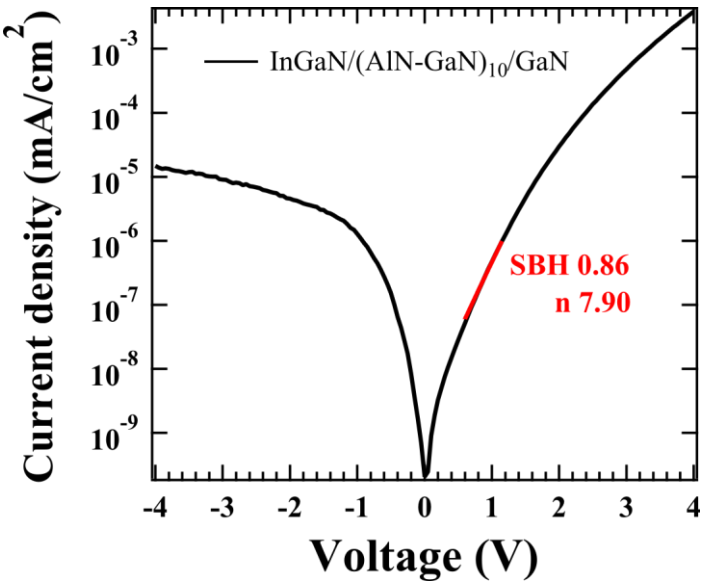

Fig. 5-8: Current-voltage measurement under dark condition for the Schottky properties on thick $In_{0.09}Ga_{0.91}N$ film

where ϕ_B is the Schottky barrier height (SBH), n the ideality factor of the diode, q the charge of electron, and A^* the effective Richardson constant, which is a function of the effective mass of electron m_e^* for the n-type material:

$$A^* = \frac{4\pi q m_e^* k^2}{h^3}, \tag{5-5}$$

where k is the Boltzmann constant and h is the Planck constant. m_e^* depends on the n-type material GaN or InGaN used. As I showed previously in *Table 5-1*, I used $m_e^* = 0.22 m_0$ for GaN and $m_e^* = 0.19 m_0$ for $In_{0.09}Ga_{0.91}N$. The calculated effective Richardson constant is $A^* = 26.4\ A\ cm^{-2}\ K^{-2}$ for n-type GaN and $A^* = 22.8\ A\ cm^{-2}\ K^{-2}$ for n-type $In_{0.09}Ga_{0.91}N$.

By numerical analysis, I used the following equation to fit the linear part of the J-V curve to extract the Schottky properties ϕ_B and n at 293 K depending on the effective Richardson constant A^* previously estimated:

$$J = A^* \times 293^2 \times \exp\left(-39.62 \times \phi_B\right) \times \left[\exp\left(\frac{39.62}{nV}\right) - 1\right] \tag{5-6}$$

The Schottky barrier height and the ideality factor obtained are summarized in the following table depending on the effective Richardson constant used:

Table 5-2: Schottky barrier height and ideality factor extracted from J-V analysis of $In_{0.09}Ga_{0.91}N$ at 293 K depending on the effective mass of electron and on the effective Richardson constant used.

	GaN	$In_{0.09}Ga_{0.91}N$
Effective mass of electron m_n^*	*0.22 m_0*	*0.19 m_0*
Effective Richardson constant A^* (A cm^{-2} K^{-2})	*26.4*	*22.8*

Parameters extracted from J-V analysis for $In_{0.09}Ga_{0.91}N$	Using GaN parameters	Using $In_{0.09}Ga_{0.91}N$ parameters
Schottky barrier height (eV)	*0.863*	*0.860*
Ideality factor	*7.907*	*7.907*

As *Table 5-2* clarifies, the difference between the Schottky barrier heights extracted for $In_{0.09}Ga_{0.91}N$ using the effective Richardson calculated for GaN or $In_{0.09}Ga_{0.91}N$ is only about 0.003 eV. And there is no difference concerning the ideality factor extracted. Thus I can conclude that for indium content lower than 10%, the effective Richardson constant and the effective mass of electron from n-type w-GaN material can also be used for InGaN films to estimate the Schottky properties.

On the thick $In_{0.09}Ga_{0.91}N$, the Schottky barrier height was estimated at ϕ_B = 0.86 eV and the ideality factor much higher than 2 at n = 7.90. Furthermore, the reverse leakage current of the diode is quite high, about 10^{-5} mA/cm^2 at -4V bias. A possible reason to explain this high leakage current is the presence of defects inside the Schottky junction.

5-1.3 Capacitance-Frequency and capacitance-voltage measurements

Before the capacitance-voltage (C-V) measurement, it is necessary to analyze the capacitance-frequency (C-f) measurement to determine the range of frequencies where the C-V does not fluctuate. *Figure 5-9* presents the C-f analysis for the Schottky contact on the thick $In_{0.09}Ga_{0.91}N$ film, where the capacitance has a small variation from 100 Hz to 50 kHz. Thus, I employed a frequency of 10 kHz for the C-V measurement.

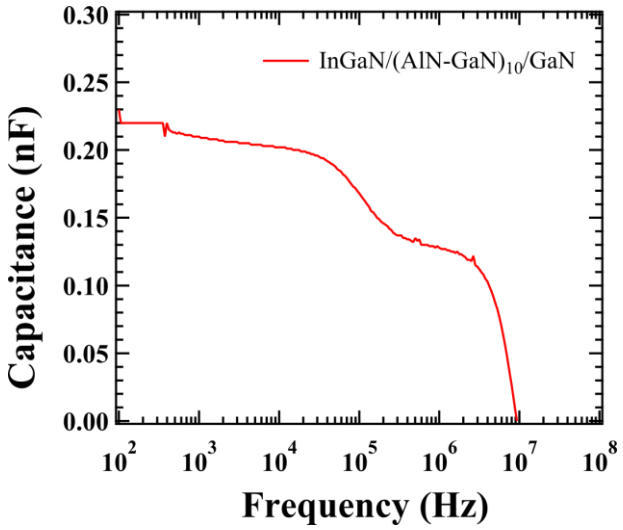

Fig. 5-9: Capacitance-frequency measurement under dark condition for the Schottky properties on thick $In_{0.09}Ga_{0.91}N$ film

Figure 5-10 presents the variation of $1/C^2$ as a function of the applied voltage measured at 10 kHz in order to estimated the built-in potential (V_{bi}), the carrier concentration (N_d) and the depletion layer (W_d) of the Schottky junction.

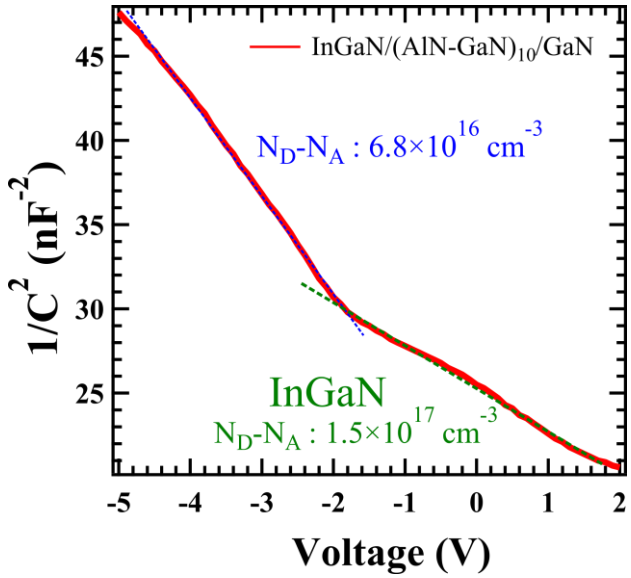

Fig. 5-10: Capacitance-voltage measurement under dark condition for the Schottky properties on thick $In_{0.09}Ga_{0.91}N$ film

The V_{bi} is obtained by extending the linear part of $1/C^2$ to zero and N_d depends on the slope and is determined by the following equation:

$$N_d = \frac{2}{A^2 q \varepsilon_s \varepsilon_0 \dfrac{\partial(1/C^2)}{\partial V}}, \tag{5-7}$$

where A is the Schottky area of the device, 6.2×10^{-3} cm^2. The depletion layer W_d is estimated as follow:

$$W_d = \sqrt{\frac{2\varepsilon_s \varepsilon_0 (V_{bi} + V)}{qN_d}}. \tag{5-8}$$

At V = 0V, the depletion layer depends only on the built-in potential V_{bi}, and the carrier concentration N_d.

In *Fig. 5-10*, two distinct slopes are clearly found with a transition at -1.75 V, reflecting that the sample structure consisted of two layers with different carrier concentrations. The estimated carrier concentrations from the two slopes were 1.5×10^{17} cm^{-3} and 6.8×10^{16} cm^{-3} corresponding to the $In_{0.09}Ga_{0.91}N$ layer and the under-layer, respectively. The depletion depth at -1.75 V was evaluated at 240-260 nm, in well accordance with the thickness of InGaN layer.

Because of the different under-layers below the thick $In_{0.09}Ga_{0.91}N$, V_{bi} could not be determined, but the SBH estimated at 0.86 eV which is lower than SBH obtained using GaN material, about 1.0~1.1 eV, clearly shows the presence of a defective layer at the interface between the metal and the film. This defective layer is also possibly related to the defects and defect levels present inside the InGaN film, which can be involved in the difference of carrier concentration estimated. It is possible to determine the concentration and the nature of these defect levels thanks to the Schottky junction and the depletion layer generated inside the thick $In_{0.09}Ga_{0.91}N$ film.

5-2 $In_{0.09}Ga_{0.91}N$ defect levels studied by deep level transient spectroscopy (DLTS)

5-2.1 Principle of the DLTS technique

The deep-level transient spectroscopy gives information by measuring how the non steady-state high-frequency capacitance changes with time. The DLTS invented by D.V. Lang [13] is now widely used to detect the defect levels in the bandgap. This method utilizes measurements of transient capacitance following the pulse-bias in a *p-n* junction or Schottky junction to monitor changes in the charge states of defects centers. The DLTS signal is the difference of capacitance at two different times after a filling pulse. It shows peaks for different trap levels in the sample at respective temperatures (T). If traps are filled by a filling pulse and the reverse bias is switched on again, the sample is in thermal non-equilibrium and relaxes into equilibrium by detrapping the charges back. This relaxation process is related with a capacitance transient. Its time constant is governed by the thermal emission rate ($e_{n,p}$) which depends on the trap energy level (E_t) at the temperature (T) :

$$e_{n,p} = \frac{1}{\tau_e} = \frac{\sigma_{n,p} \upsilon_{n,p} N_{C,V}}{g} \exp\left(-\frac{E_t}{kT}\right), \tag{5-9}$$

where $N_{C,V}$ is the effective density of states in the conduction or valence band, $\sigma_{n,p}$ is the capture cross section of the trap, $\upsilon_{n,p}$ is the thermal carrier velocity, and g is the degeneracy factor. This factor will be kept equal to 1. The

thermal carrier velocity and the effective density of states are both functions of the temperature as shown in the following equations:

Thermal carrier velocity:
$$\upsilon_{n,p} = \sqrt{\frac{3kT}{m^*_{n,p}}} \propto T^{1/2} \tag{5-10}$$

Effective density of state:
$$N_{C,V} = 2\left(\frac{2\pi m^*_{n,p} kT}{h^2}\right)^{3/2} \propto T^{3/2} \tag{5-11}$$

Equations (5-10) and *(5-11)* show the fact that the emission rate is correlated to the temperature T and exponentially dependent on $1/T$:

$$e_{n,p} \propto T^2 \exp\left(-\frac{E_t}{kT}\right) \tag{5-12}$$

$$\ln\left(\frac{T^2}{e_{n,p}}\right) \propto \frac{E_t}{kT} \propto \frac{1}{T} \tag{5-13}$$

So the thermal energy of the trap E_t (or activation energy) determined by the slope and the capture cross section σ determined by the intercept with horizontal axis, are the main features of the curve. Because in *Eq. (5-13)*, for each trap, the trap energy and the capture cross section are determined by its slope and intercept, respectively. From an Arrhenius plot, $ln(e_{n,p}) \sim 1/T$. The DLTS signal is scaled to capacitance because of the following equation:

$$DLTS = a\left(C(t_2) - C(t_1)\right) \tag{5-14}$$

The DLTS measurement was carried out in the wider temperature range from 10 to 450 K. During the raising of T, according to $exp(-E_t/kT)$ dependence of the thermal emission rate, as long as T is too low for significant thermal emission until t_2, the difference in *Eq. (5-14)* is equal to zero. If T is so high that the thermal emission is already over at t_1, the difference in *Eq. (5-14)* is also zero. Only if the emission time constant τ_e, or its inverse, the emission rate $e_{n,p}$, of one defect level falls into the so-called "rate-window" given by the definition of t_1 and t_2, a DLTS peak appears. We obtain the following condition for the DLTS peak to appear [14]:

$$e_{n,p} = \frac{\ln\frac{t_2}{t_1}}{t_2 - t_1} \tag{5-15}$$

The "rate-window" is the inverse of τ_e according to the formula of the relaxation time constant τ_e, and has the unit of s^{-1}.

The term "peaks" is often used in DLTS technique even if it is corresponding to "dips". In fact the presence of a negative peak (or a dip for convenience) indicates the presence of a majority trap level (electrons for n-type semiconductor).

From DLTS measurements, the traps concentration N_t (in cm^{-3}) can also be determined by using the carrier concentration at 300 K estimated by C-V ($n \sim N_D - N_A \equiv N_d$) measurement and the following equation:

$$N_t = 2N_d \frac{\Delta C}{C_0} \tag{5-16}$$

As far as we know, only one group has also used the DLTS technique to determine the defect level inside a thin InGaN layer [15]. And no group yet has studied these defect levels in a thick 200 nm InGaN layer. Concerning the GaN, many reports can be found. A summary of the capture cross section, defect levels and possible nature of those defects are presented in the following table for GaN and InGaN.

Table 5-3: Defects levels and their characteristics underlined by DLTS for w-GaN with their main related natures.

Material	**Defect level (eV) E_c-E_t=**	**Capture cross section (cm^{-2})**	**Defect concentration (cm^{-3})**	**Temperature of peak apparition (K)**	**Possible related nature of defects**	**Ref.**
InGaN	0.35-0.45 (DL1)	-	10^{13}	375	Origin still unknown, possibly related to vacancies	[15]
GaN	0.5-0.6 (E2)	4.94×10^{-17} ~1.6×10^{-15}	2.3×10^{13}~ 2.3×10^{14}	361	Nitrogen antisite (N_{Ga}), point-defect nature	[16]
GaN	0.23 (E1)	5.43×10^{-15}	9.5×10^{13}	162	Buffer growth condition	[16]
GaN	0.62	6×10^{-15}	4.1×10^{14}	335	Residual Mg in GaN	[17]
GaN	1.0 (A_1)	-	-	420	N interstitial	[18]
GaN	0.67 (A)	-	-	330	-	[18]
GaN	0.60 (B)	-	-	280	Foreign impurity, Carbon, C_{Ga} or more complex arrangements	[18]
GaN	0.35 (C)	-	-	180	V_N related complexes	[18]
GaN	0.25 (D)	-	-	135	V_N related complexes	[18]
GaN	0.16 (E)	-	-	110	Vacancy V_N	[18]
GaN	0.11	2.0×10^{-20}	4×10^{13}	140	C_{Ga}-related donors in GaN:C:Si	[19]
GaN	0.15	2.3×10^{-18}	5×10^{13}	110	C_{Ga}-related donors in GaN:C:Si	[19]

(continued to next page)

Material	Defect level (eV) E_c-E_t=	Capture cross section (cm^{+2})	Defect concentration (cm^{-3})	Temperature of peak apparition (K)	Possible related nature of defects	Ref.
GaN	0.20	2.5×10^{-17}	2.7×10^{14}	160	-	[19]
GaN	0.61	5×10^{-16}	2.9×10^{14}	310	Not related to C defect, intrinsic defect	[19]
GaN	E_v+0.9	2×10^{-13} ~7×10^{-15}	-	390	Hole trap when C co-doping, result of C incorporation	[19]
GaN	0.25 (E1)	1.6×10^{-15}	1.25×10^{14}	135	V_N related defect with threading dislocations	[14]
GaN	0.62 (E2)	2.4×10^{-15}	2.6×10^{15}	290	V_{Ga} related centers	[14]
GaN	0.602	8×10^{-16}	2.0×10^{14}	260-330	Neutral charge center	[20]
GaN	0.26 (E_1)	1.6×10^{-15}	2.6×10^{15}	175	-	[21]
GaN	0.58 (E_2)	2.9×10^{-15}	3.6×10^{14}	335	Nitrogen level	[21]
GaN	0.66 (E_3)	1.0×10^{-15}	3.8×10^{14}	390	Nitrogen level	[21]
GaN	0.45 (X)	3.0×10^{-19}	-	300~370	Defect arise from dislocation	[22]
GaN	0.58 (E_3)	2.0×10^{-15}	-	300~370	Isolated defect	[22]

D.C. Look et al. also found that the traps A_1, C, D, and E grow under plasma-ion irradiation, which shows their defect natures [18]. However the trap B at ~0.6 eV is unchanged after electron or plasma irradiation, which suggests that this trap is related to a pre-existing defects such as the Ga vacancy V_{Ga}.

5-2.2 Measurements using DLTS technique

The steady-state reverse bias and the filling pulse voltage in DLTS were 0 V and +10 V, respectively. The width of filling pulse was 100 μsec to ensure that all defects, even those with small electron capture cross sections were saturated. The DLTS measurements were carried out in the wider temperature range from 10 to 450 K. *Figure 5-11* shows the illustration of the measurement system:

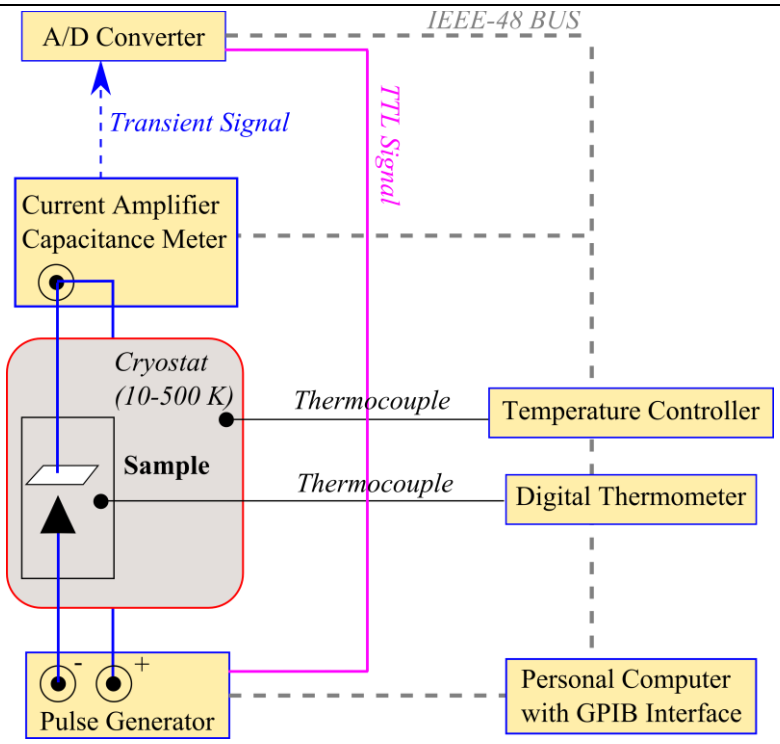

Fig. 5-11: DLTS measurement system

5-2.3 Analysis of DLTS measurements

I performed the DLTS analysis for the InGaN sample at various rate windows t_2/t_1 for a constant ratio 1/5 under 0 V bias as shown in *Fig. 5-12*. Two dips, denoted by E1 at 50 K and E2 at 325 K, are observed, which means traps for majority carrier are present. These dips are shifted with an increase in electron emission rate from 2×10^2 to 4×10^3 s^{-1}, previously defined as $e_n = 1/\tau_{max} = \ln(t_2/t_1)/(t_2-t_1)$.

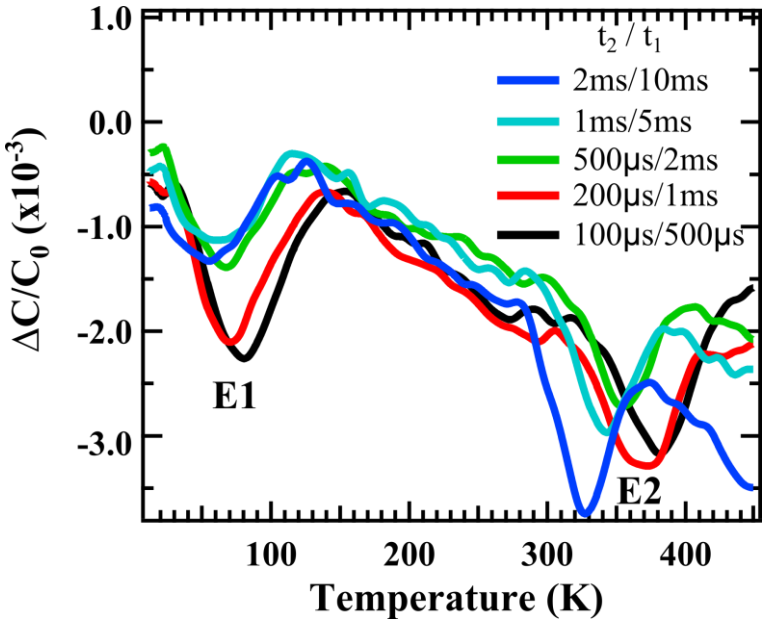

Fig. 5-12: DLTS spectra at various rate windows for the $In_{0.09}Ga_{0.91}N$ sample

The dip E1 is shifted to higher temperature when the electron emission rate increases with an enhancement of its amplitude. This reveals the fact that the defect level is located near the conduction band as shallow donors. Concerning the dip E2, it is shifted to lower temperature when the rate window increases with maximum amplitude for the lowest rate window. Thus the defect level E2 is located deeper under the conduction band.

Shallow impurities require a little energy, typically around the thermal energy or less, to ionize. Deep impurities require energies larger than the thermal energy to ionize so that only a fraction of the impurities present in the semiconductor contribute to free carriers. Deep impurities which are more than five times the thermal energy away from either band edge are very unlikely to ionize. Such impurities can be effective recombination centers in which electrons and holes fall and annihilate each other. Such deep impurities are also called traps.

The Arrhenius plot of the dip E2 is plotted with the previous DLTS data for GaN [15] in *Fig. 5-13* previously introduced in *Table 5-3*. And the one corresponding to the dip E1 is plotted in *Fig. 5-14* due to the large difference in scale.

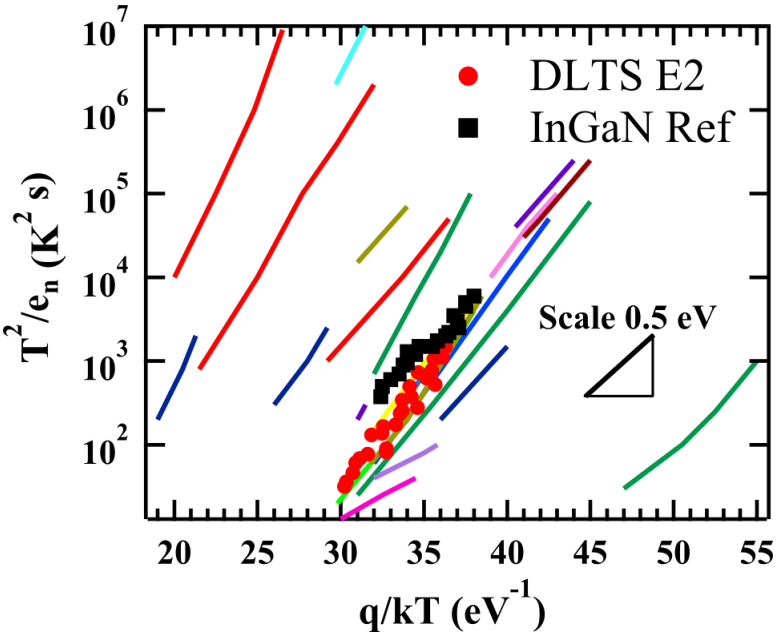

Fig. 5-13: Arrhenius plot of the dip E2 from DLTS analysis of the $In_{0.09}Ga_{0.91}N$ sample compared to defect levels of InGaN and GaN in Ref. [15].

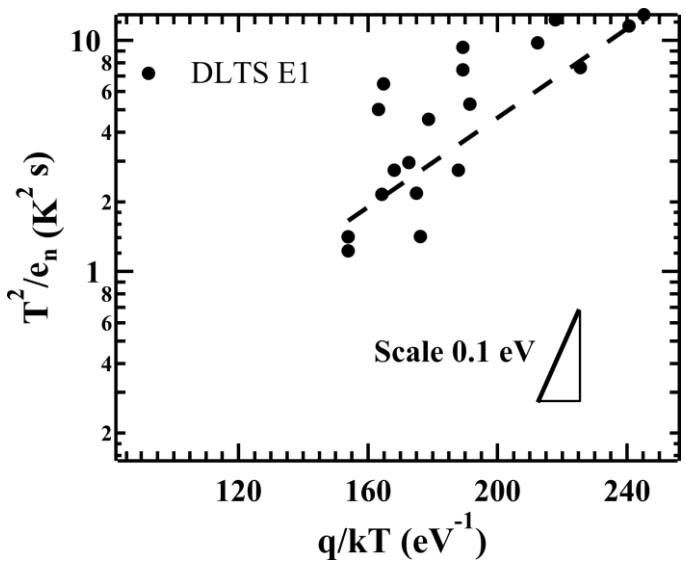

Fig. 5-14: DLTS Arrhenius plot of the dip E1 from DLTS analysis of the $In_{0.09}Ga_{0.91}N$ sample

The activation energy was evaluated 22 meV and 0.6 eV by the slope of the graphs for the defects E1 and E2, respectively. The defect level E1 with an activation energy of 22 meV is close to the one reported to be attributed to oxygen (23.3meV, [4]) or carbon (25.1meV, [4]) impurities in GaN material. Another candidate is the nitride vacancies V_N [4], [5]. However, the nature of this very shallow donor level is still not clear due to a dip present at a temperature range from 50 to 75 K, which is not commonly observed, and a small capture cross section about 2.3×10^{-20} cm^2. The concentration of defect level E1 was estimated at 4.5×10^{14} cm^{-3} from *Eq. (5-16)*.

The defect E2 located at 0.6 eV is commonly detected by DLTS, but there is still controversy to determine whether the origin comes from carbon impurity [18], the III-group element vacancy (V_{III}:Ga and/or In) point defects involving oxygen [15], and/or anti-site nitrogen (N_{Ga}) [16]. The concentration of defect level E2 is about 4.1×10^{14} cm^{-3}. Since both the concentration of defects E1 and E2 could not explain the carrier concentration obtained by C-V measurement of 1.5×10^{17} cm^{-3}, Thermal Admittance Spectroscopy (TAS) are also performed to examine the defects at shallow energy levels.

5-3 Shallow defect levels of $In_{0.09}Ga_{0.91}N$ analyzed by thermal admittance spectroscopy (TAS) technique

5-3.1 Principle of the TAS technique

The Thermal Admittance Spectroscopy (TAS) technique, also called Admittance Spectroscopy, is a very convenient tool for analyzing majority carrier traps. As shown by Sah et al. [23], one important feature of the capacitance of a diode (Schottky or diffused) in the presence of traps, or defect levels, is to be frequency and temperature dependent.

In principle, the presence of a deep level in the measured rectifying junction is determined by a flexion in the capacitance-frequency (C-*f*) curves and a peak in the conductance-frequency (*G*/*f*) curves which occurs at frequency f_0. This frequency is related to the emission rate of the deep level e_n (in the case of n-type semiconductor) as a function of temperature *T*:

$$w_0 = 2\pi f_0 \,, \qquad w_0(T) \propto e_n(T) \,, \qquad w_0(T) = \sigma_n \upsilon_n N_C \exp\left(\frac{-E_t}{kT}\right), \tag{5-17}$$

where σ_n is the capture cross section of the deep level, N_C is the density of states in the conduction band, υ_n the thermal velocity of electrons and E_t is the energy level of the donors bellow the conduction band edge.

However, the response of majority carriers at a measurement frequency is limited by the dielectric relaxation time (τ_{rel}). The majority carriers cannot respond to the measurement frequency (*f*) when the angular modulation frequency $\omega=2\pi f$ exceeds $1/\tau_{rel}$. The C-*f* and G/*f* curves should shift towards higher/lower frequencies by increasing/decreasing the measurement temperature, and hence it is possible to evaluate the dependence of the defect emission rate on temperature. The equivalent circuit of a Schottky diode or a *p-n* junction is a junction capacitance C in parallel with a junction conductance G (which governs the leakage current) and a series resistance R_s (which depends on bulk resistivity and on contact resistance), as shown in *Fig. 5-15*.

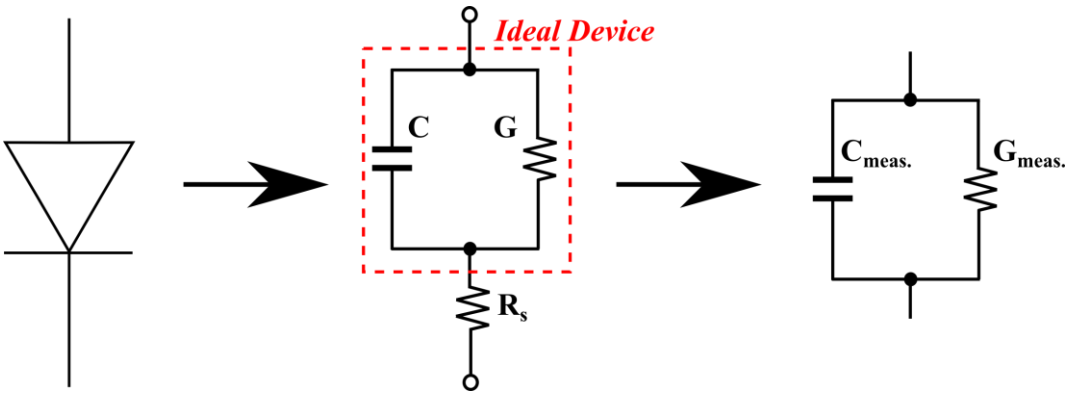

Fig. 5-15: Parallel equivalent circuit of a Schottky diode or p-n junction.

The energy diagram of the Schottky barrier with the presence of a defect level E_T is presented in Fig. 5-16 for n-type semiconductor under reverse-bias conditions. In the depletion region, the quasi-Fermi level for electrons is only drawn, which can be identified with the bulk Fermi level in the useful region.

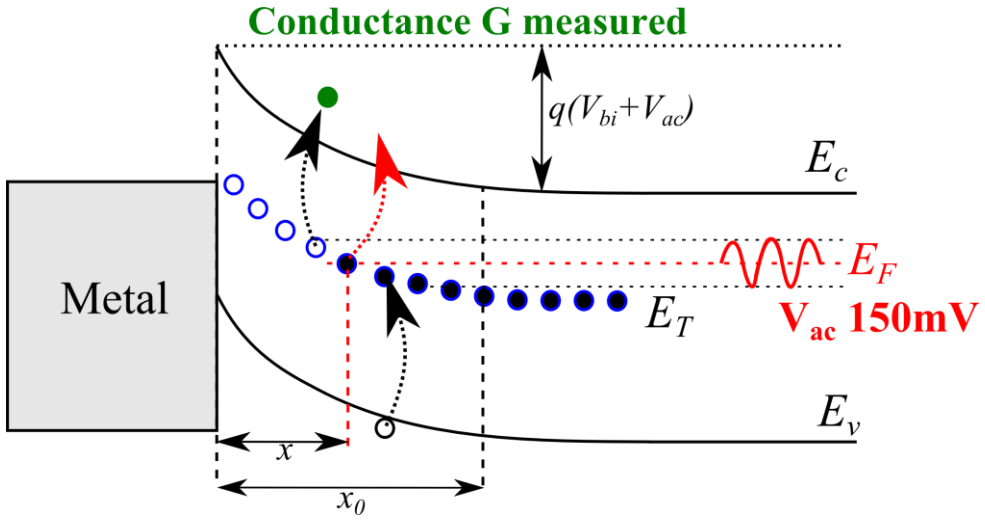

Fig. 5-16: Principle of TAS technique, energy diagram of a Schottky barrier (n-type semiconductor) with the presence of a defect level E_T.

If the applied voltage is changed from V_0 to $V_0+\delta V$ by a small fluctuation on the order of mV generally, the crossing point between E_F and E_T moves from x to $x+\delta x$. The traps which are thereby above the Fermi level emit their electron into the conduction band with an emission rate e_n. When the voltage is decreased again, the opposite occurs, thus leading to an additional current in the external circuit of the diode.

a) Expression of the conductance G_T and capacitance C_T

At low temperature, the total charge emitted (after an infinite time) is:

$$\delta Q = qN_T A\delta x\,, \tag{5-18}$$

where q is the electron charge, A is the diode area, and N_T is the concentration of traps. In homogeneous semiconductors, for traps near the conduction band the depletion width x_0 is given by [24]:

$$x_0 = \left(\frac{2\varepsilon V}{qN_+}\right)^{1/2}, \tag{5-19}$$

where ε is the dielectric constant for the material, N_+ is the concentration of fixed positive charge (in the case of a n-type semiconductor) in the depletion region, and V is the applied voltage changed from V_0 to $V_0+\delta V$. The variation of the depletion layer δx_0 is estimated by derivating the Eq. (5-19) according to x_0:

$$\delta x_0 = \frac{\partial x_0}{\partial V}\delta V = \frac{1}{2}\left(\frac{2\varepsilon}{qN_+}\right)^{1/2} V^{-1/2}\delta V \text{ , with } qN_+ = \rho(x_0) \tag{5-20}$$

which gives :

$$\delta x_0 = +\frac{\delta V}{x_0}\frac{\varepsilon}{\rho(x_0)}, \tag{5-21}$$

$\rho(x)$ is the local density of positive charges. In homogeneous semiconductors, it is equal to qN_+ in the whole depletion layer and $\rho(x_0)$ is equal to qn, where n is the number of free carriers in the bulk. The difference between N_+ and n arises because of the deep lying levels. Thus *Eq. (5-21)* can be rewritten:

$$\delta x_0 = \frac{1}{n}\left(\frac{\varepsilon N_+}{2qV}\right)^{1/2}\delta V . \tag{5-22}$$

From *Eqs. (5-18)* and *(5-22)* we obtain

$$\delta Q = q\frac{N_T A}{n}\left(\frac{\varepsilon N_+}{2qV}\right)^{1/2}\delta V . \tag{5-23}$$

If an ac signal, $\delta V = \delta V_0 \exp(j\omega t)$, is applied to the diode, the current in the circuit is given by:

$$i(t) = -\frac{dQ(t)}{dt} = e_n Q(t), \tag{5-24}$$

where e_n is the electron emission rate of the traps.

$$Q(t) = \delta Q(t) - \int_0^t i(t)dt . \tag{5-25}$$

By substituting *Eq. (5-25)* into *Eq. (5-24)* with the expression of $\delta Q(t)$ given by *Eq. (5-23)*, the current can be written:

$$i(t) = e_n\left(q\frac{N_T A}{n}\left(\frac{\varepsilon N_+}{2qV}\right)^{1/2}\delta V - \int_0^t i(t)dt\right). \tag{5-26}$$

The solution may be written:

$$i = \chi e_n \cos(\psi)\delta V_0 \ \exp\left[j(\omega t + \psi)\right], \tag{5-27}$$

with $\chi = q\frac{N_T A}{n}\left(\frac{\varepsilon N_+}{2qV}\right)^{1/2}$ and $\tan(\psi) = \frac{e_n}{\omega}$.

This current has two components one in phase, denoted i_{phase}, and the other in quadrature, i_{quad}, dependent on δV:

$$i_{phase} = \frac{e_n^2 \omega}{e_n^2 + \omega^2} \frac{\omega}{e_n} \chi \delta V_0 \ \exp(j\omega t), \tag{5-28}$$

and

$$i_{quad.} = \frac{e_n^2 \omega}{e_n^2 + \omega^2} \chi \delta V_0 \ \exp\left[j\left(\omega t + \frac{\pi}{2} \right) \right]. \tag{5-29}$$

Thus, the traps induce a conductance G_T given by [24]:

$$G_T = \frac{i_{phase}}{\delta V_0} = \frac{e_n \omega^2}{e_n^2 + \omega^2} \frac{N_T}{n} A \left(\frac{q\varepsilon N_+}{2V} \right)^{1/2}. \tag{5-30}$$

The exchange of electrons between the traps and the conduction band also leads to an additional capacitance C_T:

$$C_T = \frac{1}{\omega} \frac{i_{quad.}}{\delta V_0} = \frac{e_n^2}{e_n^2 + \omega^2} \frac{N_T}{n} A \left(\frac{q\varepsilon N_+}{2V} \right)^{1/2}. \tag{5-31}$$

b) Variation of G_T and C_T with temperature and frequency

I plotted the theoretical variation of C_T and G_T depending on the frequency in *Fig. 5-17* [24]. At high frequency, the additional capacitance disappears while the conductance remains constant. The admittance $C_T\omega$ has a maximum for $\omega = e_n$. The conductive to capacitive current ratio in the diode is $G_T/C_T\omega = \omega/e_n$. Consequently, the effect of the additional conductance increases with frequency. However, if the total capacitance of the barrier is $C=C_0+C_T$, with C_0 independent of the frequency, the ratio $G_T/C_0\omega$ vanishes at high frequency. Thus, the study of G_T or C_T can be made at a moderate frequency from 1 kHz to 200 kHz.

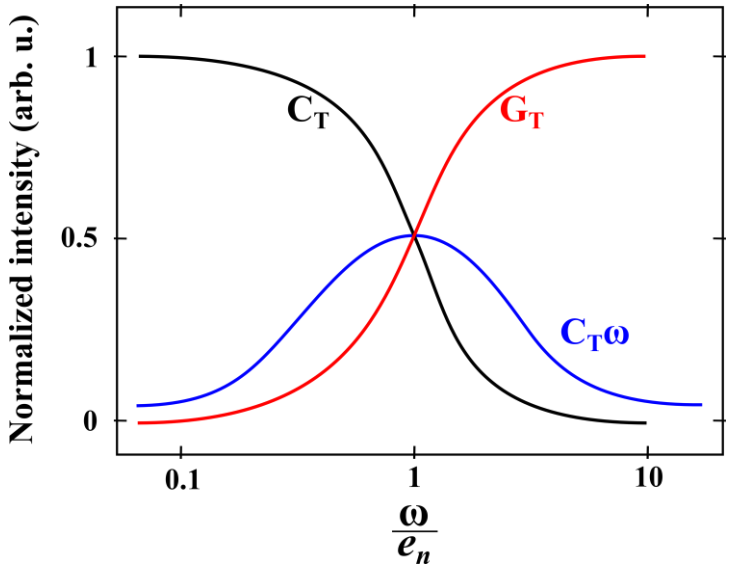

Fig. 5-17: Calculated variation of the capacitance C_T, the admittance $C_T\omega$, and the conductance G_T associated with one trap depending on the frequency ω.

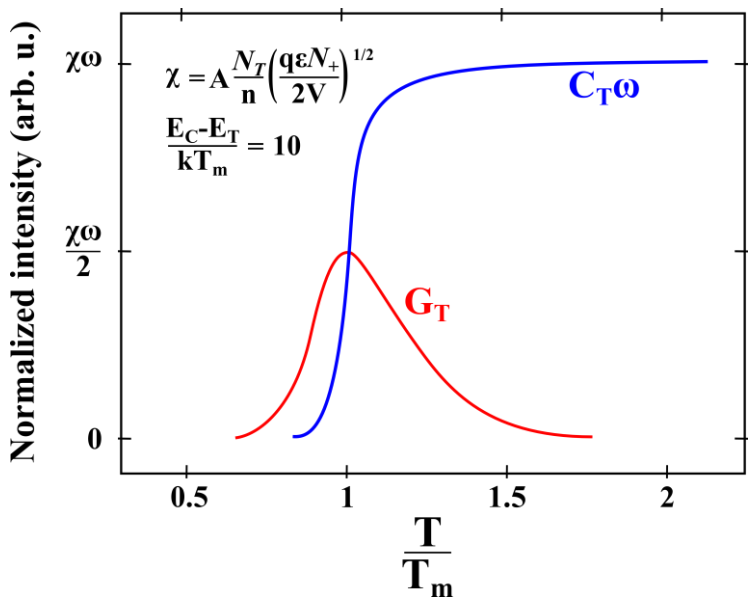

Fig. 5-18: Calculated variation of C_T and G_T as functions of temperature.

The electron emission rate en is related to the temperature through:

$$e_n = e_{n0} \exp\left[\frac{(E_T - E_C)}{kT}\right]. \tag{5-32}$$

The variation of e_n with the temperature is preponderant. Then the conductance has a maximum $e_n = \omega$ at a specific temperature:

$$T_m = \left[\frac{(E_T - E_C)}{k}\right]\left[\ln\left(\frac{\omega}{e_{n0}}\right)\right]^{-1}. \tag{5-33}$$

The theoretical variation of G_T and $C_T\omega$ depending on T is shown in *Fig. 5-18* [24]. In the presence of a defect with a specific energy level, the conductance as a function of temperature shows a specific peak and the capacitance as a function of temperature presents a step.

Compared with the DLTS technique, the main physical difference is that in the DLTS method all the levels in the depletion layer are involved because direct pulses are applied to the diode; as for the conductance (or additional capacitance), only traps near the Fermi level are involved. Another difference is that for shallow levels, only the traps located near the zero-field region of the junction are involved, so electric field effects are avoided.

c) General expression of the capacitance

The general expression of the capacitance of the Schottky barrier is:

$$C_0 = A\left(\frac{q\varepsilon N_+}{2V}\right)^{1/2}. \tag{5-34}$$

Then the measured capacitance in the presence of traps is written as [24]

$$C = C_0 + C_T = A\left(\frac{q\varepsilon N_+}{2V}\right)^{1/2}\left(1+\frac{N_T}{n}\frac{e_n^2}{e_n^2+\omega^2}\right). \tag{5-35}$$

A more complicated situation arises when the traps are not completely filled. This can happen with donor levels at intermediate temperatures because of the ionization energy of these levels (≈100 meV). The donors may then act as traps. If the Boltzmann statistics is assumed, a complete calculation provides the following approximate formula [24]:

$$C = A\left(\frac{q\varepsilon N_+}{2V}\right)^{1/2}\left[1+\frac{N_D}{n}\exp\left(-\frac{E_D-E_F}{kT}\right)\frac{e_n^2}{e_n^2+\omega^2}\right], \tag{5-36}$$

where N_D is the total number of donors. It is generally different from either n (the carrier concentration in the bulk) or N_+ (the density of positive charges) because of the compensation of the material. The term exp[-(E_D-E_F)/kT] leads to a small shift of the conductance peak maximum (T_m).

5-3.2 Measurements using TAS technique

The TAS measurements were carried out in the wider temperature range from 10 K to 450 K.

An AC modulation level of 150 mV and frequencies ranging from 1 kHz to 200 kHz were conducted in TAS analysis with a bias voltage from 0 to -3 V. *Figure 5-19* presents the TAS measurement system.

For the TAS analysis, the sample was set in a cryostat, and the conductance and capacitance were measured at a fixed frequency then the temperature was increased slowly. The measurement was repeated at different frequencies from 1 kHz to 200 kHz.

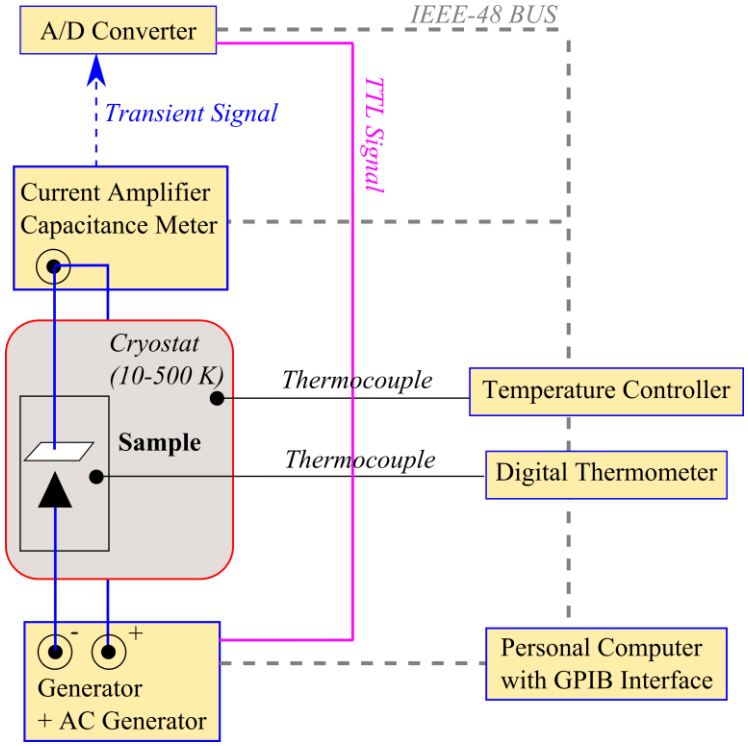

Fig. 5-19: TAS Measurement System

5-3.3 Analysis of TAS measurements

The conductance and capacitance for a thick $In_{0.09}Ga_{0.91}N$ are presented in the following figures. *Figure 5-20* corresponds to a measurement at a bias voltage of 0V, *Fig. 5-21* for -0.5V, *Fig. 5-22* for -1.0V, *Fig. 5-23* for -1.5V, and *Fig. 5-24* for -3.0V. The conductance depending on the temperature at different frequencies is presented on the left graphs *(a)* and the capacitance depending on the temperature at different frequencies is presented on the right graphs *(b)*.

For a bias voltage between 0 to -1.0 V (*Fig. 5-20*, *Fig. 5-21*, and *Fig. 5-22*), three peaks are present in the conductance curves, denoted by A1, A2 and A3, respectively.

The peaks A1 and A2 are shifted towards higher temperatures with increasing frequency as might be expected because of the increase of the emission rate e_n with increasing temperature. Moreover, the peaks A1 and A2 show a remarkable temperature-shift of capacitance dispersion toward higher temperature [red arrows for *Fig. 5-20(b)* to *Fig. 5-24(b)*]. So A1 and A2 correspond to bandgap states that are electronically active defects present inside the bandgap of the material.

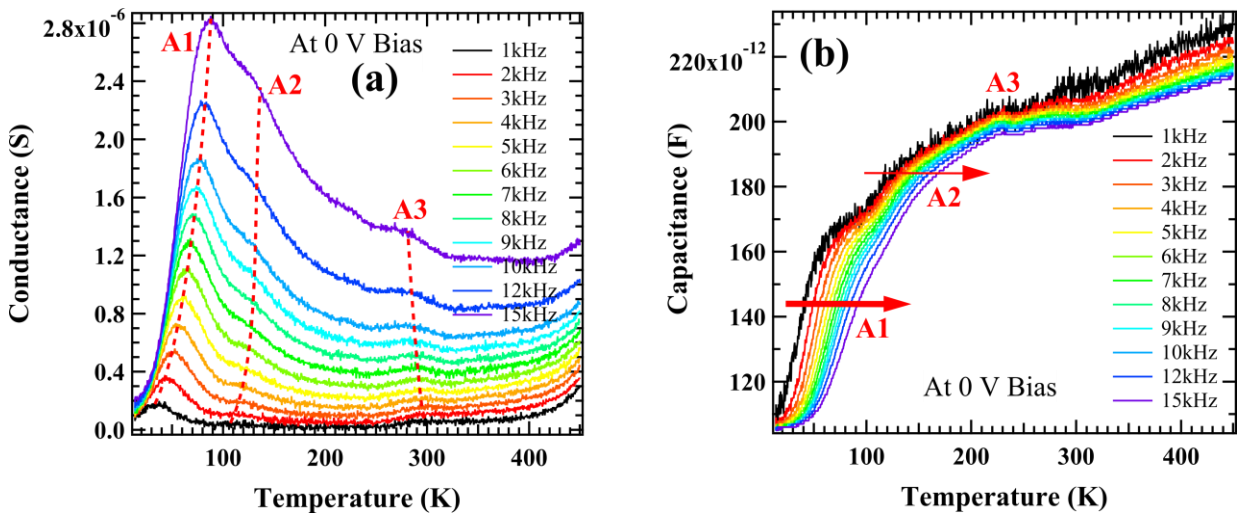

Fig. 5-20: Conductance and capacitance for $In_{0.09}Ga_{0.91}N$ depending on temperature and frequency at 0 V bias.

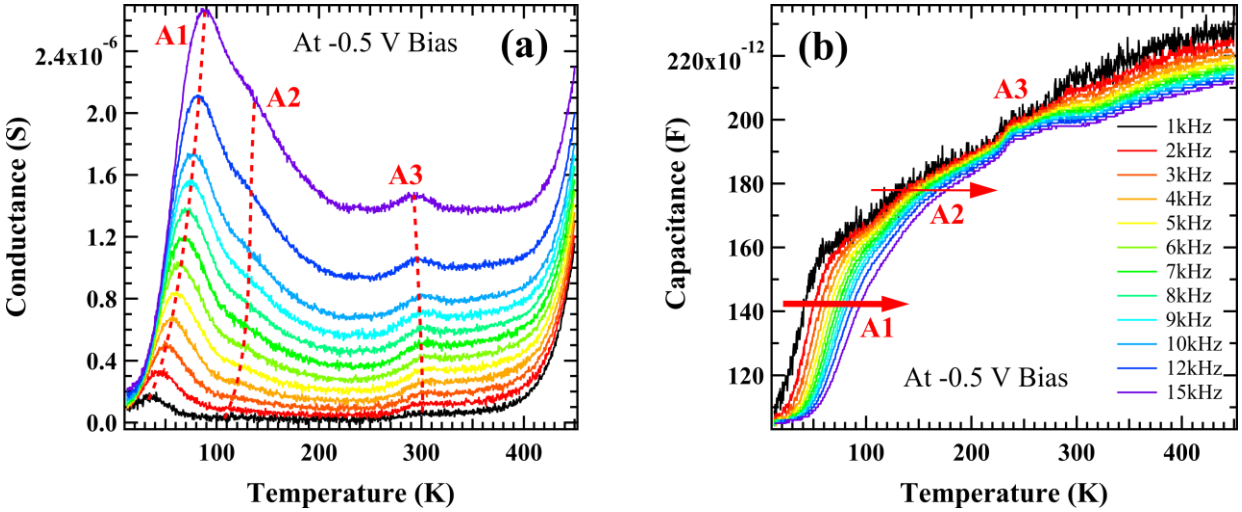

Fig. 5-21: Conductance (a) and capacitance (b) for $In_{0.09}Ga_{0.91}N$ depending on temperature and frequency at -0.5 V bias.

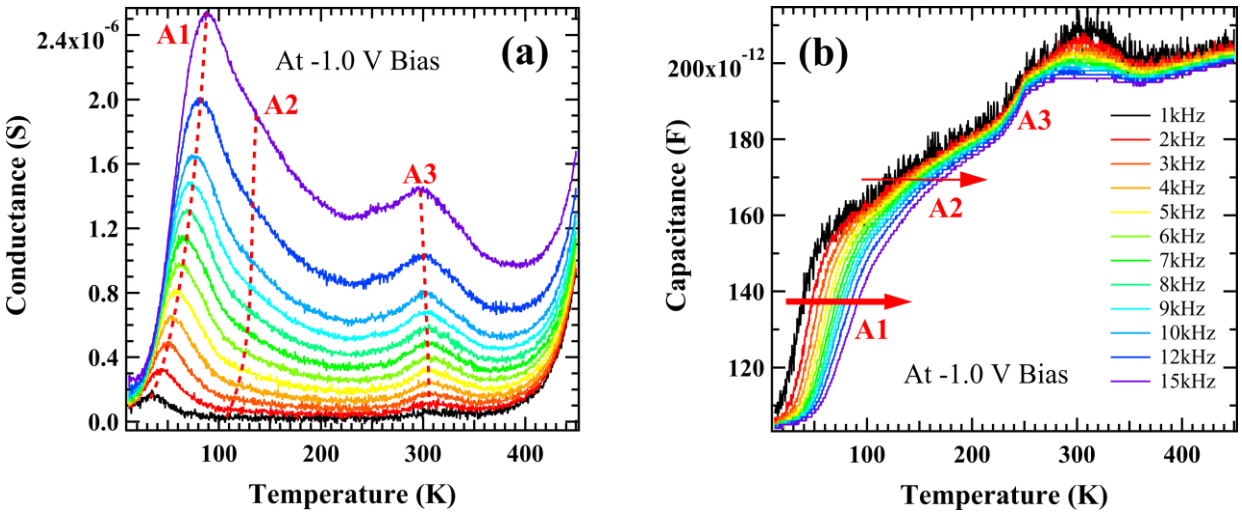

Fig. 5-22: Conductance (a) and capacitance (b) for $In_{0.09}Ga_{0.91}N$ depending on temperature and frequency at -1.0 V bias.

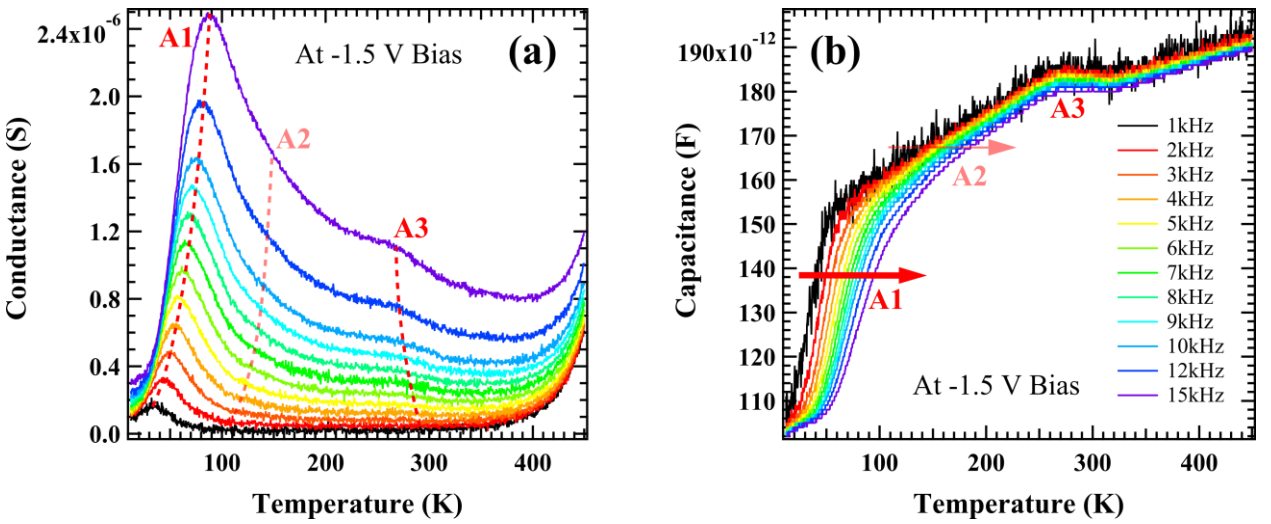

Fig. 5-23: Conductance (a) and capacitance (b) for $In_{0.09}Ga_{0.91}N$ depending on temperature and frequency at -1.5 V bias.

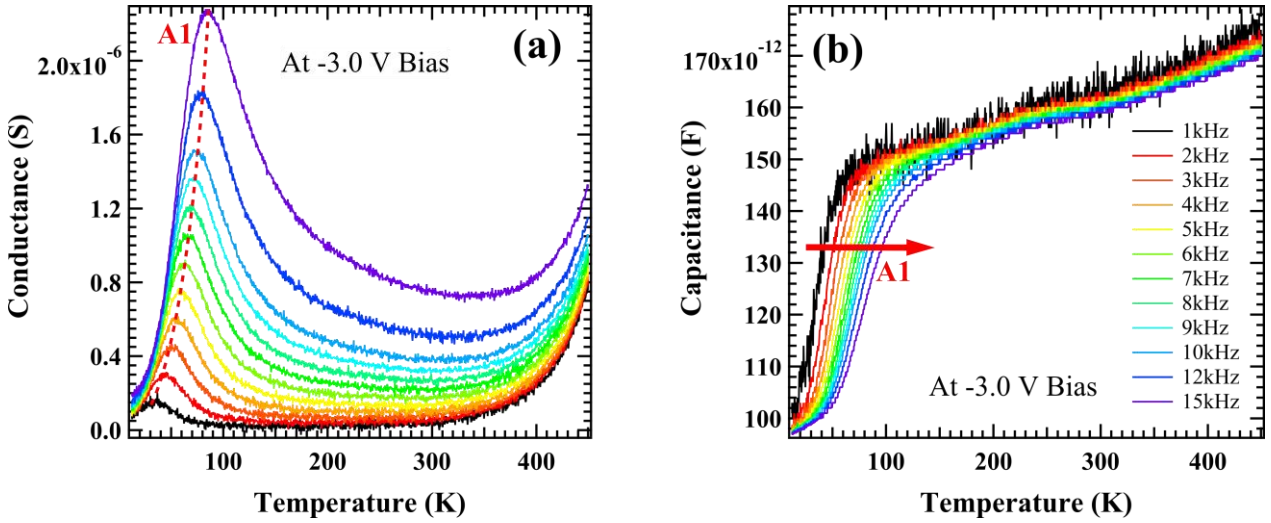

Fig. 5-24: Conductance (a) and capacitance (b) for $In_{0.09}Ga_{0.91}N$ depending on temperature and frequency at -1.5 V bias.

On the other hand, the peak A3 in the conductance curves from 0 to -1.5V, where this peak is observed, reveals a small shift toward lower temperatures with increasing frequency [*Fig. 5-20(a)*, *Fig. 5-21(a)*, and *Fig. 5-22(a)*]. On the capacitance-temperature graphs, there is no capacitance dispersion with temperature dependence but only a singularity. So the peak A3 seems to come from the structure without electronic response and can be related to a structural defect.

At higher bias voltage -1.5V and -3.0V (*Fig. 5-23*, and *Fig. 5-24*), the peak A2 becomes harder to evaluate even if the shape of the curve is still influenced by its presence. At -3.0V, the peak A3 also disappears. The depletion layer increases by the negative bias. I presented the maximum conductance signals at 15 kHz

frequency as a function of the bias voltage in *Fig. 5-25*. For the peaks A1 and A2, the conductance decreased with increasing negative bias voltage, and thus the thickness of the depletion layer. This means that the peaks A1 and A2 come from the top $In_{0.1}Ga_{0.9}N$ layer. The conductance signal for the peak A3 has a maximum between -0.5 and -1.0 V. So, the peak A3 is not related to the surface layer and could come from the interface GaN / InGaN where structural defects can occur due to the different growth conditions between GaN and InGaN films.

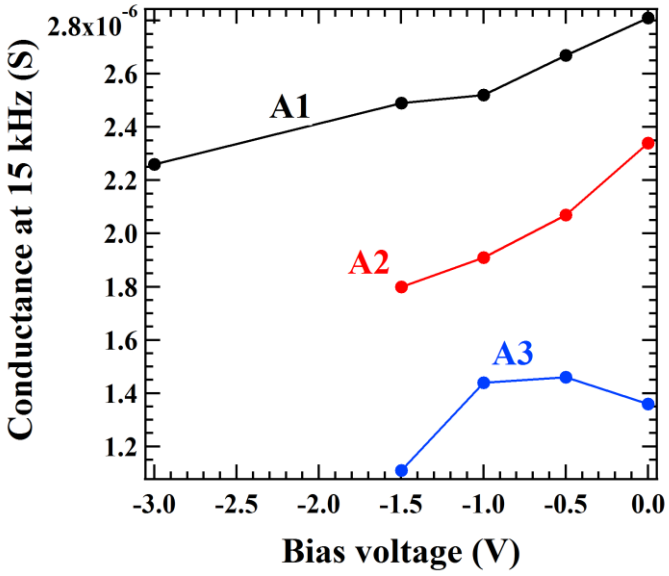

Fig. 5-25: Maximum conductance at 15kHz frequency in function of the bias voltage applied for each peak A1, A2, and A3 observed.

I used the conductance curve at 0 V bias in order to estimate the temperature where peaks A1 and A2 appeared depending on the frequency. I calculated the normalized conductance by the frequency ω using *G(n kHz)/ n kHz*, where n is the corresponding frequency ω of the measured conductance $G(\omega)$. *Figure 5-25* shows the temperature dependence of conductance normalized by the frequency $G(\omega)/\omega$ evaluated by the TAS measurement under 0 V bias condition. Three peaks A1~A3 are dominantly detected. Both peaks A1 at 40 K and A2 at 110 K in the 2 kHz measurement are shifted toward higher temperature with increasing frequency. The dependence of peak shift on the frequency indicates that the defects are regarded as electrically active [25].

With a similar method and *Eq. (5-9)* as for the DLTS technique, I plotted an Arrhenius graph to estimate the activation energy E_T of the defect level and its capture cross-section σ_n. Taking the degeneracy factor g equal to 1, the electron emission rate e_n from *Eq. (5-9)* can be written as follow:

$$e_n = \sigma_n \upsilon_n N_C \exp\left(-\frac{E_t}{kT}\right). \tag{5-37}$$

I calculated the thermal velocity of electron to be $\upsilon_n = 2.7\times10^7$ cm s^{-1} with an effective mass $m_e^* = 0.19\ m_0$ [4], and the effective density of states of conduction band ($N_c = 2.0\times10^{18}$ cm^{-3}). The activation energy of peak A1 and A2

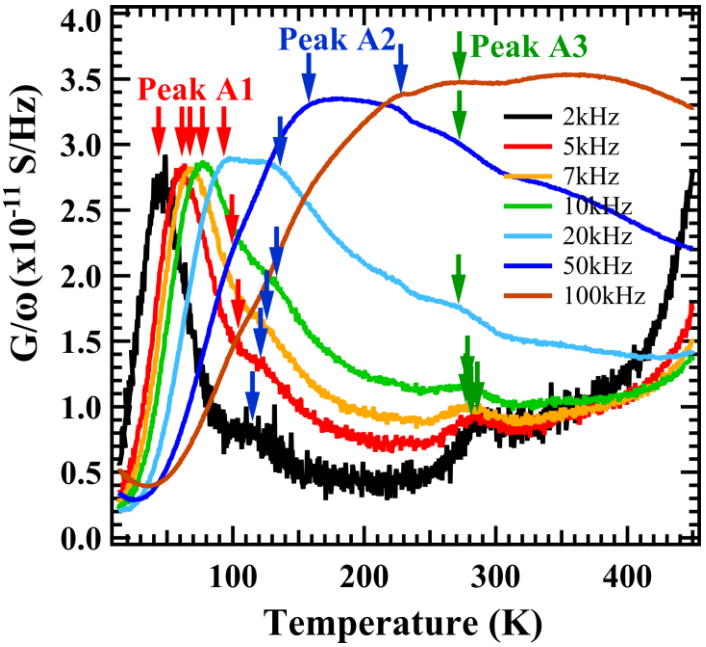

Fig. 5-26: Conductance normalized by the frequency from 2 to 100 kHz from TAS measurement.

was estimated at 7 meV and 108 meV, respectively, by the Arrhenius plot presented in *Fig. 5-27*. The cross section of A1 defect (E_t = 7 meV) was estimated at 2.4×10^{-20} cm^2.

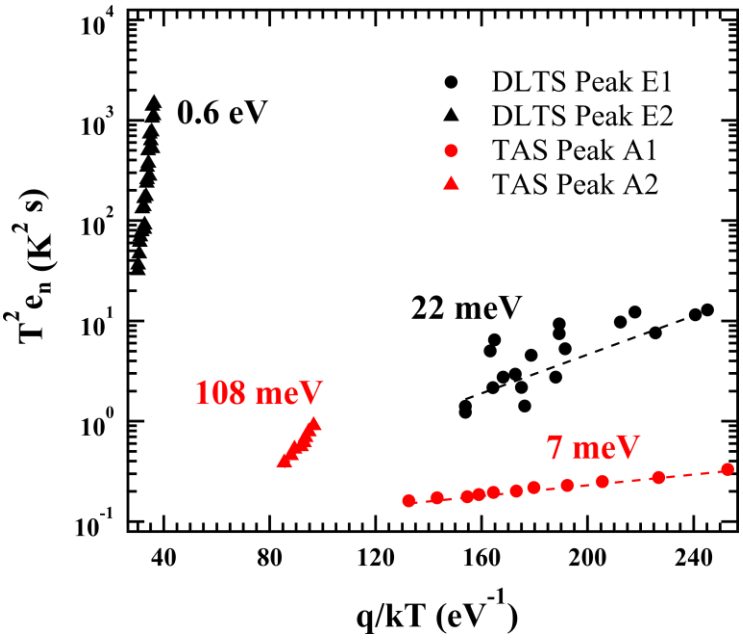

Fig. 5-27: Arrhenius plot of the defect levels underlined by TAS (A1, A2) and DLTS (E1, E2) analysis for $In_{0.09}Ga_{0.91}N$.

Taking both the small activation energy and the significantly small cross section into account, we have considered that the peak A1 would be attributed to higher carrier concentration of the InGaN. Since the defect corresponding to A1 with low energy level was not detected for GaN, we suggest that one of the possibilities would originate from indium-related defect like indium fluctuation. Also, Obata et al. reported that the formation energy of V_N decreased with increasing number of In adjacent to V_N [26], meaning that indium can gather easily around V_N in InGaN film. The V_N was theoretically predicted to act as a single donor of n-type residual carrier [27], though the concentration and energy level are still unknown.

The conductance measurement was also performed with applied bias voltage from -1V to 2V to analyze the distribution of the defects A1 and A2 inside the $In_{0.09}Ga_{0.09}N$ film. The thickness of the depletion layer was modified depending on the applied bias voltage. When the conductance measurement was performed at 10 kHz, the peak A1 was detected at the constant temperature of 75K while the temperature of peak A2 was shifted toward lower temperature from 140 K to 110 K as presented in *Fig. 5-28*. This result implies that the defect of peak A1 must be homogeneously distributed in the whole thickness of InGaN, while the defect of peak A2 should be localized near the surface. This confirms the hypothesis of the indium fluctuation for the origin of A1. The origin of A2 can be a defective surface and a reason for poor Schottky properties on $In_xGa_{1-x}N$ material such as lower barrier and higher ideal factor. Contrary to these defects, the peak A3, which is still unknown, shows no frequency dependence and could be related to a structural defect at the interface GaN / InGaN (*Fig. 5-26*).

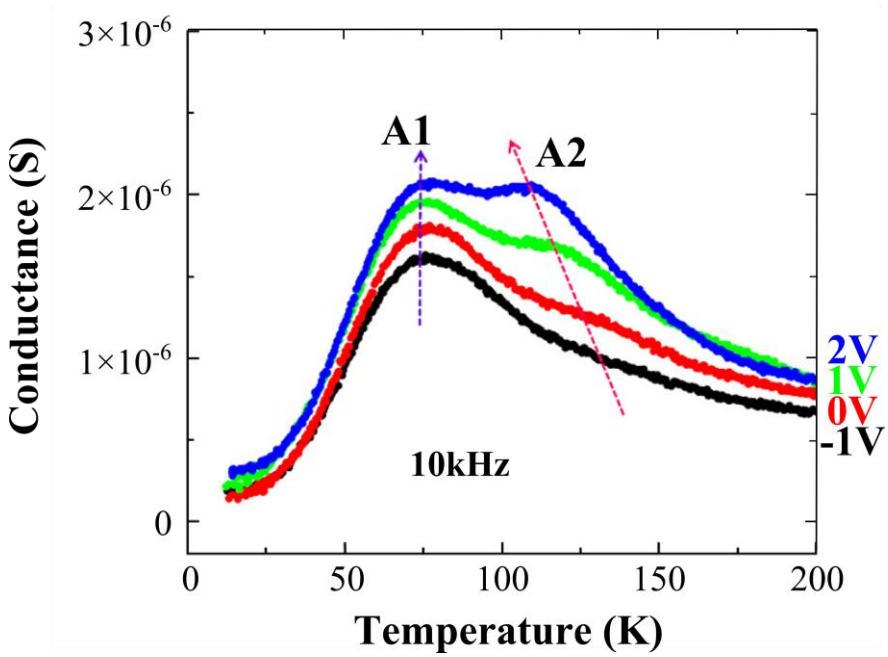

Fig. 5-28: Evolution of Peaks depending on bias voltage from -1V to 2V from the defect levels underlined by TAS analysis.

5-4 Low energy activation of defects related to dielectric relaxation

Three defect levels were found just below the conduction band at E_c-7meV (A1), E_c-108meV (A2) by TAS and E_c-22meV (E1) by DLTS. Furthermore, for TAS measurement, the capture cross-section measured was very small on the order of 10^{-17} to 10^{-20} cm^2. We need to clarify whether the characteristics of these defect levels are enough pertinent or they are due to a dielectric relaxation of the material.

A dielectric relaxation is the momentary delay in the dielectric of materials. This is usually caused by the delay in molecular polarization with respect to a changing electric field in a dielectric medium inside capacitors. The value ε_s may also be different from the semiconductor static permittivity. If during the emission process, the electron transit time from the metal-semiconductor interface to the barrier maximum x_m is shorter than the dielectric relaxation time, the semiconductor medium does not have enough time to be polarized, and smaller permittivity than the static value is expected.

TAS analysis was also performed on slightly Si doped GaN films. Three samples with different Si doping of 3×10^{16}, 5×10^{16} and 1×10^{17} cm^{-3} were employed. The defect levels observed were plotted on the Arrhenius plot beside the ones observed for $In_{0.09}Ga_{0.91}N$ as *Fig. 5-29* shows. The defect levels of GaN:Si were estimated at 19 to 25 meV for different samples, which was consistent with the shallow Si doping level. I calculated the corresponding capture cross section, which was about 1.64×10^{-16} cm^2 from the defect level of 25 meV, 4.14×10^{-19} cm^2 for the defect level of 24 meV and 2.39×10^{-18} cm^2 for the defect level of 19 meV, respectively. These low capture cross sections also found for other GaN material confirm that the defect levels revealed by TAS analysis

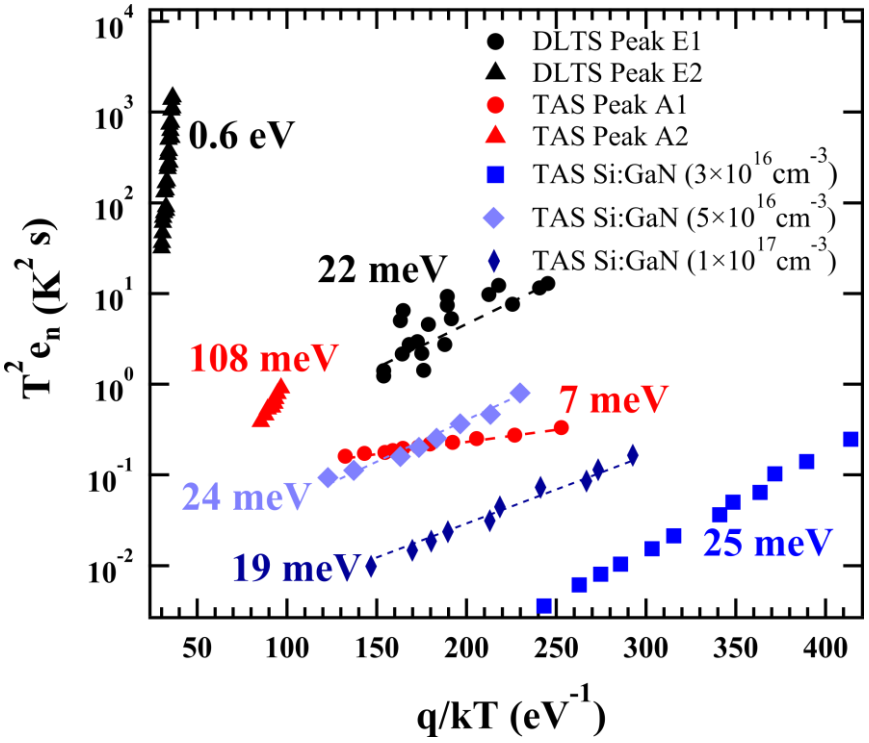

Fig. 5-29: Arrhenius plot of the defect levels underlined by TAS (A1, A2) and DLTS (E1, E2) analysis for $In_{0.09}Ga_{0.91}N$ compared with defect levels for Si doped GaN.

for our material $In_{0.09}Ga_{0.91}N$ are pertinent even if the capture cross section estimated has a small value of about 10^{-17} to 10^{-20} cm^2.

5-5 Deep level optical spectroscopy

In this section, I will describe the defect level revealed by the deep level optical spectroscopy for the $In_{0.09}Ga_{0.91}N$ sample. After the presentation of the principle of this analysis and the measurement system, the defect levels will be described in detail.

5-5.1 Principle of DLOS analysis

The principle of the DLOS measurement can be summarized as shown in *Fig. 5-30*. A defect level is depleted and charges are accumulated inside by modifying the applied voltage on the Schottky junction. These accumulated charges are released by the irradiation of a monochromatic light. A variation of capacitance occurs as a unique signature of a defect level when the radiation energy is enough to emit the charges to the conduction band. The position of the defect level corresponds to the energy necessary to excite the accumulated charges

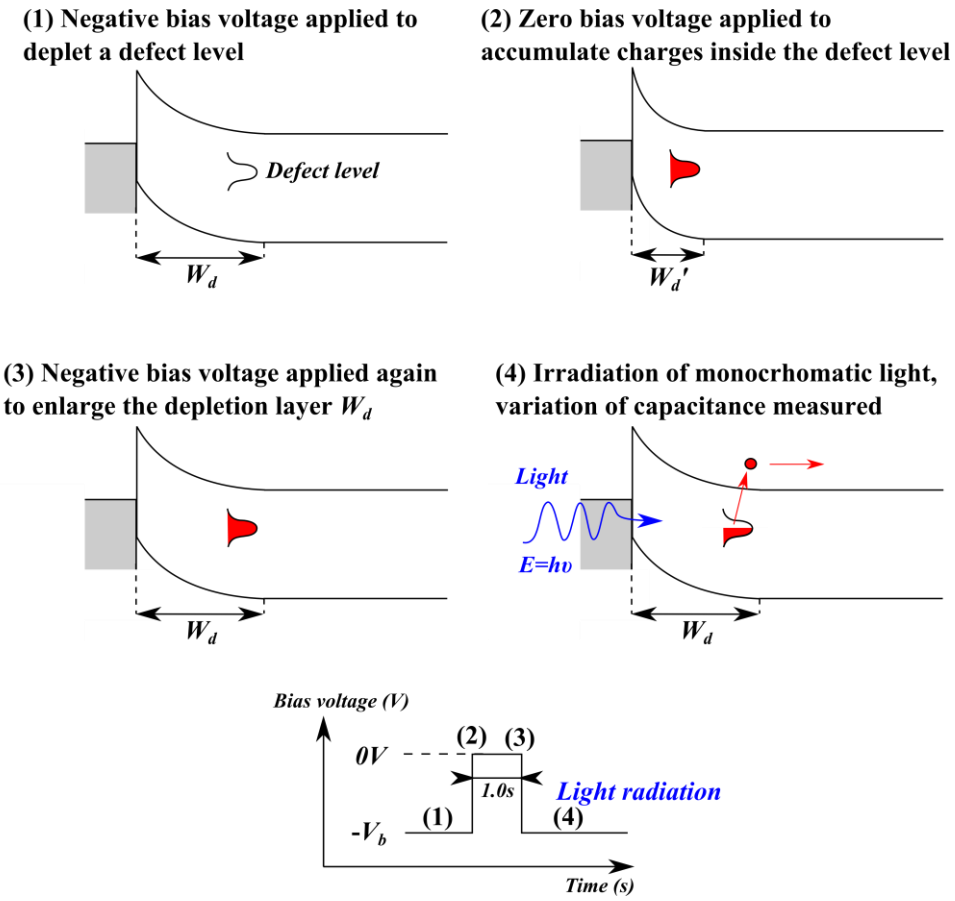

Fig. 5-30: Schematic principle of the DLOS measurement in four steps.

which corresponds to the energy of the monochromatic light. To detect the different defect levels inside the material, thus different photoemissions related to defects, the capacitance of the Schottky junction depending on the wavelength of the monochromatic light is performed [28].

5-5.2 Measurement using DLOS analysis

Deep-level optical spectroscopy (DLOS) analyses were performed, measuring photocapacitance transients as a function of incident photon energy from 0.78 eV up to 4.0 eV. The Schottky diode sample was maintained under different reverse bias voltage conditions. Prior to optical excitation, the deep levels were filled with electrons in the dark by applying a voltage pulse of +3 V with a pulse width of 3.0 sec.

Figure 5-31 presents the DLOS measurement system [28]:

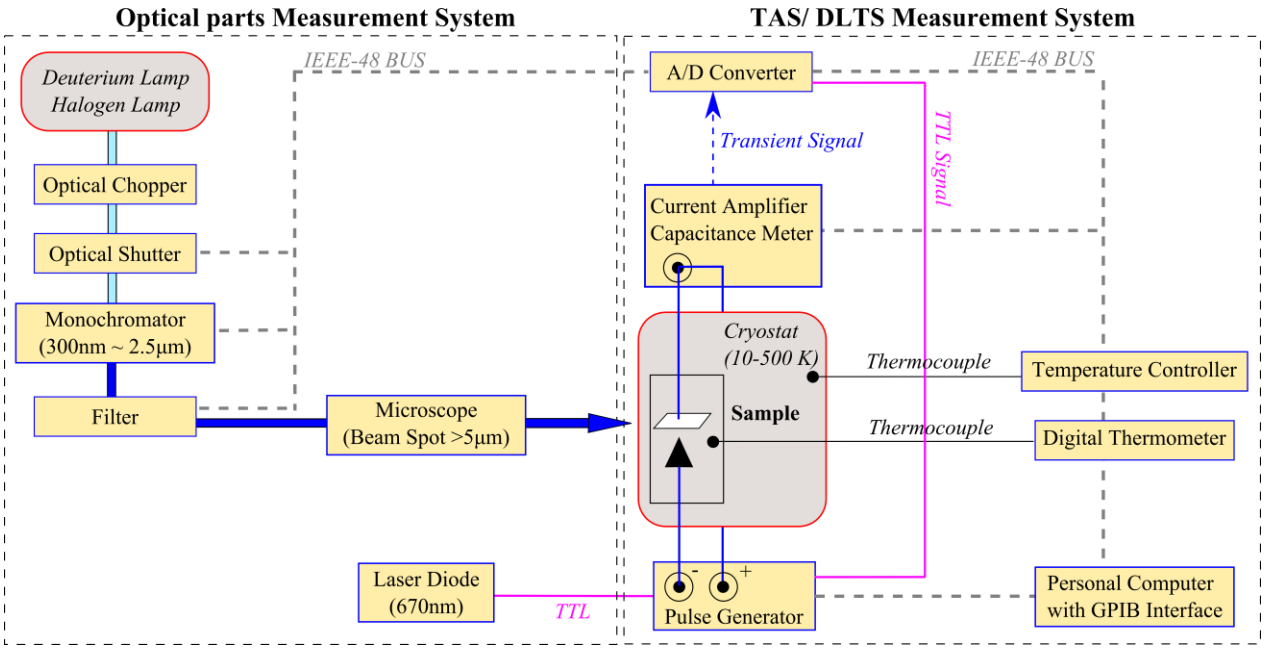

Fig. 5-31: DLOS Measurement System

5-5.3 Defect levels underlined by DLOS analysis

Figure 5-31 presents the DLOS spectra for the InGaN film under 0 V bias. Five photoemissions are detected at ~1.02 eV (S), ~ 1.70 eV (T2'), 2.07 eV (T3'), 2.70 eV (T4') and ~3.05 eV (T5') in addition to the near-band-edge (NBE) emission of $In_{0.09}Ga_{0.91}N$ and GaN at 3.2-3.5 eV. Compared to the five photoemissions identified at ~1.4 eV (T1), ~1.7 eV (T2: dislocation-related defect), ~2.1 eV (T3: Ga vacancies (V_{Ga}; the 2-/3- transition level [29], [30]) and/or V_{Ga}-O_N complex [31]), ~2.8 eV (T4: V_{Ga}-C complex) and ~3.15 eV (T5: shallow carbon (C_N) defects) from the GaN [32], the DLOS signal for the InGaN was one order of magnitude higher than those of the GaN. Each defect in the InGaN sample was located at energy between that of $In_{0.2}Ga_{0.8}N$ film grown

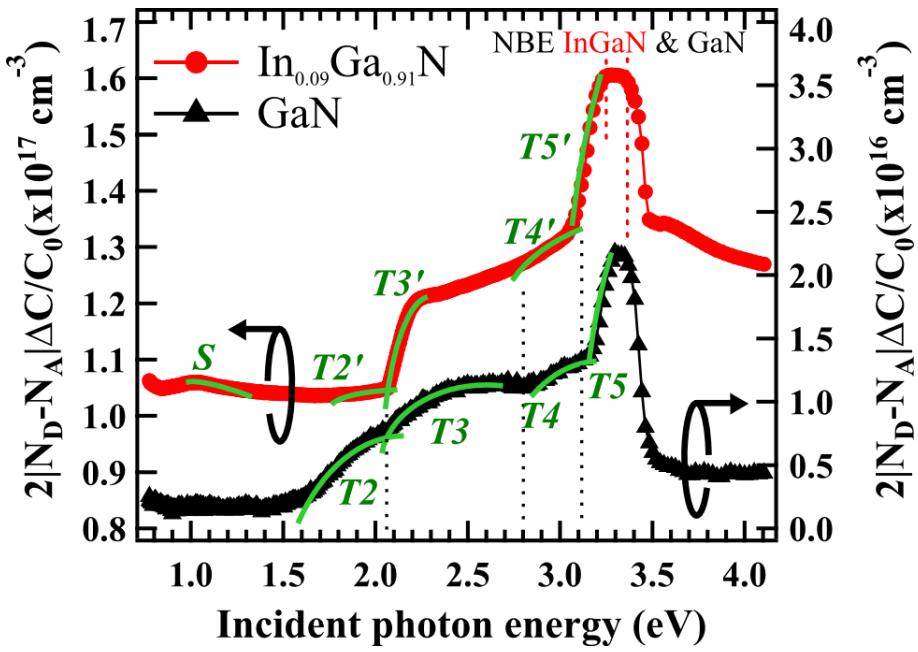

Fig. 5-32: DLOS Spectra measured at 0V bias condition for InGaN (left axis) and GaN (right axis). Five defect states denoted T1' – T5' are clearly observed in addition to the near-band-edge (NBE) emission of InGaN and GaN at 3.2 – 3.4eV.

by molecular beam epitaxy [33] and the GaN. Here, it is worth noting that T3' and T5' corresponding to vacancy and/or impurity – related defects are remarkably enhanced for the InGaN. Indeed the scale of the DLOS spectra is about 10^{17} cm^{-3} for $In_{0.09}Ga_{0.91}N$ in contrast with GaN for which it is about 10^{16} cm^{-3}.

The photoemission T3' and T5' of $In_{0.09}Ga_{0.91}N$ can be identified by analogy with GaN material: T3' (2.07 eV) is possibly related to cation vacancy (V_{III}) and complexes related with impurities such as oxygen (V_{III}-O_N). T5' can be related to the shallow carbon acceptor (C_N). For the $In_{0.09}Ga_{0.91}N$ material these two defects are much enhanced compared to GaN material. In addition to C_N at 3.15 eV, the V_N may be related to the increase of the defect of T5'. According to the increase of V_N, the cation vacancy complex with V_N was expected to be increased as well. Indeed, Uedono *et al.* concluded from the positron annihilation method that the cation vacancies coupled with multiple nitrogen vacancies (V_Ns) in InGaN was easily introduced [34]. In the *S*-*W* plot obtained from the positron annihilation, the cation vacancy coupled with oxygen is likely to have both lower *S*- and higher *W*-parameters than the theoretical values (defect free) for AlN [35] and InN [36]. The *S*- and *W*-parameters of the InGaN film from the positron annihilation indicated much lower V_{III}-O_N complex. From the DLTS analysis for GaN, the V_{Ga}-V_N complex defect was likely detected as continuously tailing peaks (negative slope with increasing temperature) in the range of 100 K – 300K in *Fig. 5-12*. This might support that the V_{Ga}-V_N complex was enhanced for InGaN sample [16]. However, since there is the report that the formation energy of V_{Ga}-O_N must be smaller than that of V_{Ga}-V_N in GaN [37], further experiments such as dependence of InN mole fraction is necessary to conclude the origin of both T3' and T5' detects.

In addition, by changing the bias voltage condition for the InGaN sample, the defect states of T3', T4' and T5' from the InGaN sample were dominantly observed near the interface InGaN / multi-layer structure. Since these defects were mainly generated at the initial InGaN growth, this might be related to difficulty of growth of thicker InGaN film without forming any defects such as V-pits on the surface.

5-6 Conclusion

$In_{0.09}Ga_{0.11}N$ films of 200 nm in thickness were grown on GaN templates on c-sapphire substrates by MOCVD. In order to detect deep-level defects which would give large influence on the carrier transport of photon-passive devices such as III-V nitride solar cells, TAS, DLTS and DLOS measurements were performed on the InGaN sample. TAS analysis revealed both two defect levels with different activation energies. The defect located at E_c-7 meV seems to be uniformly distributed in the InGaN layer, which should originate from an indium fluctuation and/or nitrogen vacancy. The defect energy level of E_c-108 meV was dominantly detected near the interface between the electrode and InGaN, probably due to an interface state with Ni-electrode and i-InGaN.

From the DLTS analysis, two other defect levels were found inside $In_{0.09}Ga_{0.91}N$, one located just under the conduction band at E_c-0.22 meV and one deep level located at E_c-0.6 eV. This deep level was commonly observed for GaN and was often reported as a cation vacancy such as V_{Ga}.

From the comparison of DLOS spectra of GaN and InGaN, it is suggested that the defects at E_c-2.07 eV and at E_c-3.05eV must be easily introduced by alloying InN with GaN for thicker $In_{0.09}Ga_{0.91}N$ films.

A summary of all the defect states found in this study is presented in *Fig. 5-33*.

Finally I can also discuss the extrinsic or intrinsic character of each defects observed for our $In_{0.09}Ga_{0.91}N$ material. I personally think that the defects observed by DLOS at E_c-2.07 eV, E_c-3.05 eV and the one observed by DLTS at E_c-0.6 eV are intrinsic defects of InGaN and GaN materials. Thus these three defects must be the cause of recombination center for free charges. Future studies are necessary to develop processes which can reduce the concentration of these level defects.

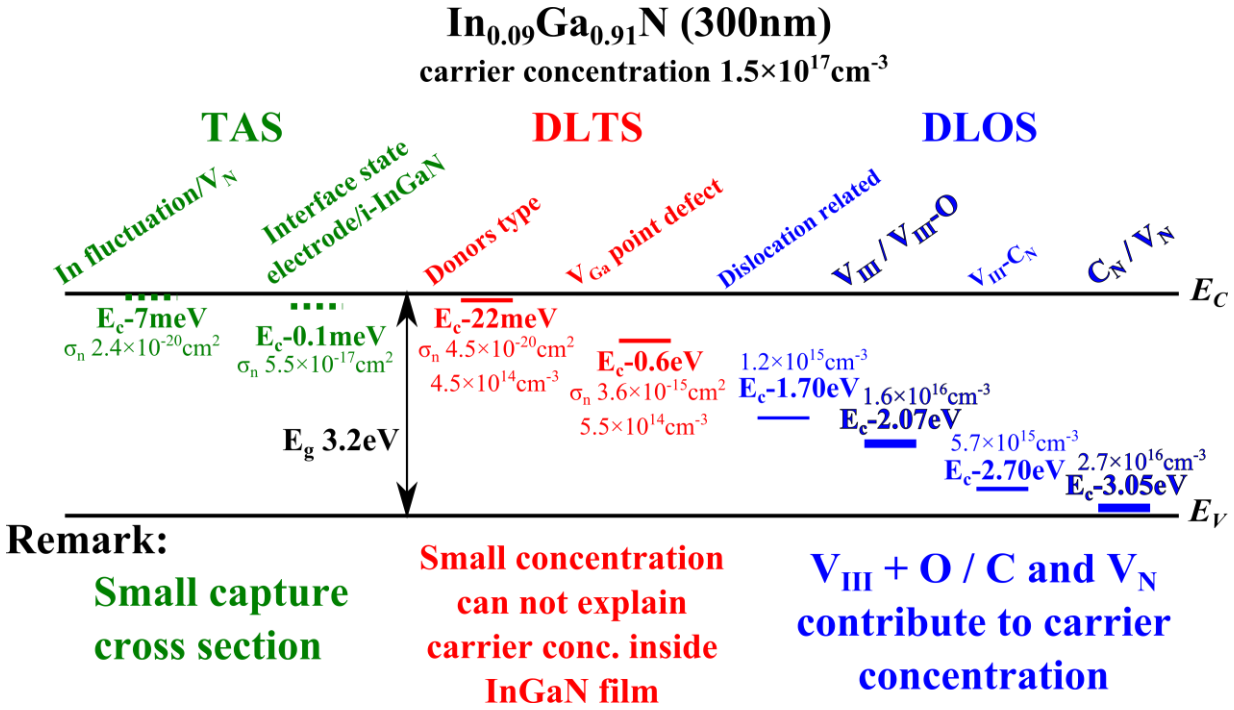

Fig. 5-33: Summary of the defect states found in $In_{0.09}Ga_{0.91}N$ films by using the TAS, DLTS and DLOS measurements.

References chapter 5

[1] F. A. Padovani and R. Stratton, "Field and Thermionic-field emission in Schottky barriers," *Solid-State Electronics*, vol. 9, pp. 695–707, 1966.

[2] Y. Park and K. Hyunsoo, "Substantial Pinning of the Fermi Level of Plasma-Treated n-Type GaN Surfaces," *Applied Physics Express*, vol. 4, p. 015702, 2011.

[3] S. Strite and H. Morkoç, "GaN, AlN, and InN: A review," *Journal of Vacuum Science & Technology B*, vol. 10, no. 4, p. 1237, Jul. 1992.

[4] F. Mireles and S. E. Ulloa, "Zeeman splitting of shallow donors in GaN," *Applied Physics Letters*, vol. 74, no. 2, pp. 248–250, 1999.

[5] S. Lin, S. Zeng, X. Cai, J. Zhang, S. Wu, L. Sun, and B. Zhang, "Simulation of doping levels and deep levels in InGaN-based single-junction solar cell," *Journal of Materials Science*, vol. 47, pp. 4595–4603, 2012.

[6] W. Moore, J. Freitas, and R. Molnar, "Zeeman spectroscopy of shallow donors in GaN," *Physical Review B*, vol. 56, no. 19, pp. 12073–12076, Nov. 1997.

[7] P. Perlin, E. Litwin-Staszewska, B. Suchanek, W. Knap, J. Camassel, T. Suski, R. Piotrzkowski, I. Grzegory, S. Porowski, E. Kaminska, and J. C. Chervin, "Determination of the effective mass of GaN from infrared reflectivity and Hall effect," *Applied Physics Letters*, vol. 68, no. 8, p. 1114, 1996.

[8] L. Piper, T. Veal, I. Mahboob, C. McConville, H. Lu, and W. Schaff, "Temperature invariance of InN electron accumulation," *Physical Review B*, vol. 70, no. 11, p. 115333, Sep. 2004.

[9] G. Martin, a. Botchkarev, a. Rockett, and H. Morkoç, "Valence-band discontinuities of wurtzite GaN, AlN, and InN heterojunctions measured by x-ray photoemission spectroscopy," *Applied Physics Letters*, vol. 68, no. 18, p. 2541, 1996.

[10] A. Kasic, M. Schubert, Y. Saito, and Y. Nanishi, "Effective electron mass and phonon modes in n-type hexagonal InN," *Physical Review B*, vol. 65, p. 115206, 2002.

[11] L. Hsu, R. E. Jones, S. X. Li, K. M. Yu, and W. Walukiewicz, "Electron mobility in InN and III-N alloys," *Journal of Applied Physics*, vol. 102, p. 073705, 2007.

[12] L. R. Bailey, T. D. Veal, P. D. C. King, C. F. McConville, J. Pereiro, J. Grandal, M. a. Sánchez-García, E. Muñoz, and E. Calleja, "Band bending at the surfaces of In-rich InGaN alloys," *Journal of Applied Physics*, vol. 104, no. 11, p. 113716, 2008.

[13] D. V. Lang, "Deep-level transient spectroscopy: A new method to characterize traps in semiconductors," *Journal of Applied Physics*, vol. 45, no. 7, pp. 3023–3032, 1974.

[14] H. K. Cho, F. A. Khan, I. Adesida, Z. Fang, and D. C. Look, "Deep level characteristics in n-GaN with inductively coupled plasma damage," *Journal of Physics D: Applied Physics*, vol. 41, p. 155314, 2008.

[15] M. Meneghini, C. de Santi, N. Trivellin, K. Orita, S. Takigawa, T. Tanaka, D. Ueda, G. Meneghesso, and E. Zanoni, "Investigation of the deep level involved in InGaN laser degradation by deep level transient spectroscopy," *Applied Physics Letters*, vol. 99, no. 9, p. 093506, 2011.

[16] H. K. Cho, C. S. Kim, and C. Hong, "Electron capture behaviors of deep level traps in unintentionally doped and intentionally doped n-type GaN," *Journal of Applied Physics*, vol. 94, p. 1485, 2003.

[17] A. Hierro, S. A. Ringel, M. Hansen, J. S. Speck, U. K. Mishra, and S. P. DenBaars, "Hydrogen passivation of deep levels in n – GaN," *Applied Physics Letters*, vol. 77, pp. 1499–1501, 2000.

[18] D. C. Look, Z.-Q. Fang, and B. Claflin, "Identification of donors, acceptors, and traps in bulk-like HVPE GaN," *Journal of Crystal Growth*, vol. 281, no. 1, pp. 143–150, Jul. 2005.

[19] A. Armstrong, A. R. Arehart, D. Green, U. K. Mishra, J. S. Speck, and S. a. Ringel, "Impact of deep levels on the electrical conductivity and luminescence of gallium nitride codoped with carbon and silicon," *Journal of Applied Physics*, vol. 98, no. 5, p. 053704, 2005.

[20] J. Pernot and P. Muret, "Electronic properties of the EC-0.6 eV electron trap in n-type GaN," *Journal of Applied Physics*, vol. 103, no. 2, p. 023704, 2008.

[21] P. Hacke, T. Detchprohm, K. Hiramatsu, N. Sawaki, K. Tadatomo, and K. Miyake, "Analysis of deep levels in n-type GaN by transient capacitance methods," *Journal of Applied Physics*, vol. 76, no. 1, p. 304, 1994.

[22] Z. H. Mahmood, A. P. Shah, A. Kadir, M. R. Gokhale, A. Bhattacharya, and B. M. Arora, "Charge deep level transient spectroscopy of electron traps in MOVPE grown n-GaN on sapphire," *Physica Status Solidi (B)*, vol. 245, no. 11, pp. 2567–2571, 2008.

[23] C. T. Sah, L. Forbes, L. L. Rosier, and A. F. Tasch, "Thermal and optical emission and capture rates and cross sections of electrons and holes at imperfection centers in semiconductors from photo and dark juncttion current and capacitance experiments," *Solid State Electronics*, vol. 13, pp. 759–788, 1970.

[24] G. Vincent, D. Bois, and P. Pinard, "Conductance and capacitance studies in GaP Schottky barriers," *Journal of Applied Physics*, vol. 46, no. 12, p. 5173, 1975.

[25] D. L. Losee, "Admittance spectroscopy of impurity levels in Schottky barriers," *Journal of Applied Physics*, vol. 46, no. 5, p. 2204, 1975.

[26] T. Obata, J. Iwata, K. Shiraishi, and A. Oshiyama, "First principles studies on In-related nitride semiconductors," *Journal of Crystal Growth*, vol. 311, no. 10, pp. 2772–2775, May 2009.

[27] I. Gorczyca, A. Svane, and N. E. Christensen, "Calculated defect levels in GaN and AlN and their pressure coefficients," *Solid State Communications*, vol. 101, no. 10, pp. 747–752, 1997.

[28] Y. Nakano, K. Noda, H. Fujikawa, T. Morikawa, and T. Ohwaki, "Deep-Level Characterization of Tris (8-hydroxyquinoline) Aluminum with and without Quinacridone Doping," *Japanese Journal of Applied Physics*, vol. 46, no. 4, pp. 2636–2639, 2007.

[29] J. Neugebauer and C. G. Van de Walle, "Gallium vacancies and the yellow luminescence in GaN," *Applied Physics Letters*, vol. 69, no. 4, p. 503, 1996.

[30] S. Limpijumnong and C. G. Van de Walle, "Diffusivity of native defects in GaN," *Physical Review B*, vol. 69, p. 035207, 2004.

[31] N. Son, C. Hemmingsson, T. Paskova, K. Evans, A. Usui, N. Morishita, T. Ohshima, J. Isoya, B. Monemar, and E. Janzén, "Identification of the gallium vacancy–oxygen pair defect in GaN," *Physical Review B*, vol. 80, no. 15, p. 153202, Oct. 2009.

[32] Y. Nakano, M. Lozac'h, N. Matsuki, K. Sakoda, and M. Sumiya, "Photocapacitance spectroscopy study of deep-level defects in freestanding n-GaN substrates using transparent conductive polymer Schottky contacts," *Journal of Vacuum Science and Technology B*, vol. 29, no. 2, p. 023001, 2011.

[33] E. Gür, Z. Zhang, S. Krishnamoorthy, S. Rajan, and S. A. Ringel, "Detailed characterization of deep level defects in InGaN Schottky diodes by optical and thermal deep level spectroscopies," *Applied Physics Letters*, vol. 99, p. 092109, 2011.

[34] A. Uedono, S. Ishibashi, T. Watanabe, X. Q. Wang, S. T. Liu, G. Chen, L. W. Sang, M. Sumiya, and B. Shen, "Vacancy-type defects in InxGa1–xN alloys probed using a monoenergetic positron beam," *Journal of Applied Physics*, vol. 112, no. 1, p. 014507, 2012.

[35] A. Uedono, S. Ishibashi, S. Keller, C. Moe, P. Cantu, T. M. Katona, D. S. Kamber, Y. Wu, E. Letts, S. a. Newman, S. Nakamura, J. S. Speck, U. K. Mishra, S. P. DenBaars, T. Onuma, and S. F. Chichibu, "Vacancy-oxygen complexes and their optical properties in AlN epitaxial films studied by positron annihilation," *Journal of Applied Physics*, vol. 105, no. 5, p. 054501, 2009.

[36] C. Rauch, I. Makkonen, and F. Tuomisto, "Identifying vacancy complexes in compound semiconductors with positron annihilation spectroscopy: A case study of InN," *Physical Review B*, vol. 84, no. 12, pp. 1–9, Sep. 2011.

[37] T. Mattila and R. M. Nieminen, "Point-defect complexes and broadband luminescence in GaN and AlN," *Physical Review B*, vol. 55, no. 15, pp. 9571–9576, 1997.

Chapter 6

6- Fabrication of solar cell devices and photovoltaic properties of Schottky junction, *p-n* homojunction, and *p-i-n* junction using $In_xGa_{1-x}N$ films

In this chapter, I will describe the fabrication of Schottky junction on GaN and InGaN films focusing on the potential of these films for photovoltaic application. For this, the Schottky junction is realized by using two different transparent conducting polymers (TCO), polyaniline and PEDOT:PSS. PEDOT:PSS shows better Schottky properties and the junction properties have a better stability. This work also presents a new device using a thin metal layer deposited on the TCO in order to enhance the photovoltaic properties obtained and maintain these properties for long duration.

Then, the photovoltaic properties obtained using *p-n* homojunction InGaN devices will be compared with the *p-i-n* structure InGaN device. Even if the *p-n* homojunction InGaN shows poor photovoltaic properties, it is a suitable advancement for the future of the InGaN material applied for photovoltaic devices.

6-1 Fabrication of Schottky junction using Transparent Conducting Polymers

6-1.1 Choice of the Transparent Conducting Polymers

Since H. Shirakawa et al. discovered in 1977 that the polyacetylene can realize extremely high electrical conductivity [1], the field of conducting polymers has attracted a high interest for the development of materials which are stable in the conducting state, easily processable, and relatively simple to produce at low cost. The high conductivity of polyaniline (PANI) was firstly reported by R. De Surville et al. in 1980 [2]. The structure of PANI is presented in *Fig. 6-1*. Also in 1980, A. F. Diaz and J. A. Logan reported that polyaniline films could serve as electrodes [3]. Since 1980 to 2000, conducting polymers based on polyaniline, polypyrrole, polythiophene, polyphenylene and poly(p-phenylene vinylene) attracted the most attention. Among these, polyaniline stands out for its ability to provide processable and conductive forms in a bulk amount at relatively low cost. Unfortunately these products suffer from degradation due to the possible presence of benzidine moieties in the polymer [4]. Moreover the (hetero) aromatic polypyrrole, polythiophene and poly(p-phenylene vinylene) have the disadvantage of being insoluble and infusible.

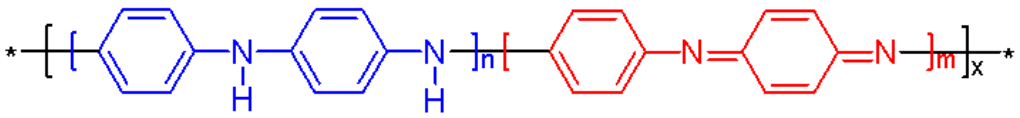

Fig. 6-1: Structure of polyaniline (PANI).(m, n) = (0.5, 0.5) with 50% of amine bonds C-NH-C and 50% of imine bonds C=N-C.

During the second half of 1980s, scientists at the Bayer AG research laboratories in Germany developed a new polythiophene derivate, poly(3,4-ethylenedioxythiophene), more commonly denoted by PEDOT or PEDT. PEDOT was initially developed to give a soluble conducting polymer.

At first, PEDOT was found to be an insoluble polymer, but with very interesting properties: a very high conductivity of 300 S/cm, almost transparent in thin, oxidized film and a very high stability in the oxidized state. *Figure 6-2* shows the chemical structure of PEDOT:PSS [5]. The solubility problem was subsequently circumvented by using a water soluble polyelectrolyte, poly(styrene sulfonic acid) (PSS), as the charge balancing dopant during polymerization to yield the PEDOT:PSS (or PEDT/PSS). This combination results in good properties: high conductivity (10 S/cm), high visible-light transmissibility and excellent stability [6]. Films of PEDOT:PSS can be heated in air at 100˚C for over 1000 h only with a minimal change in conductivity [6].

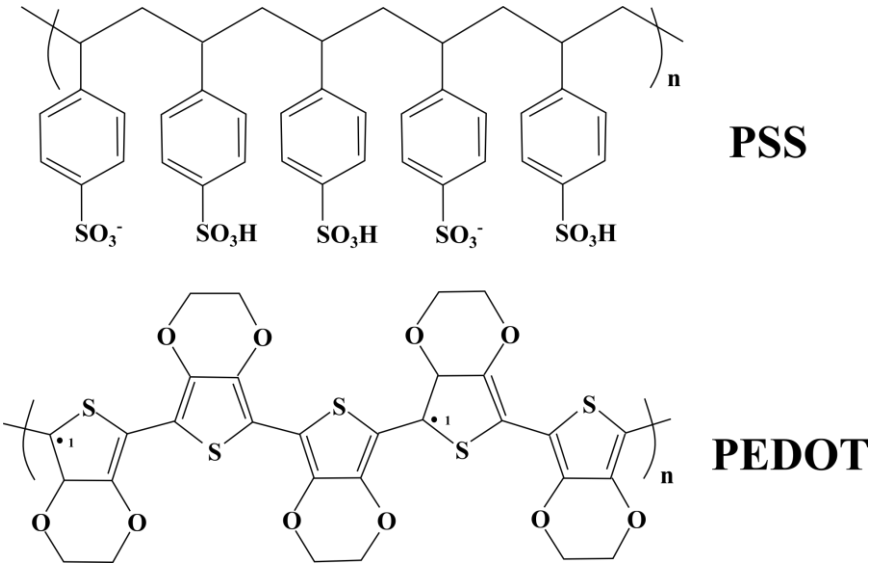

Fig. 6-2: Chemical structure of PEDOT:PSS

a) Properties of PEDOT:PSS and derivatives

PEDOT exhibits an electronic bandgap, defined as the onset of the π-π* absorption, of 1.6 – 1.7 eV and an absorption maximum wavelength of 610nm, making it deep blue in color. The band gap of PEDOT can be controlled by adjusting the highest occupied molecular orbital (HOMO) and lowest unoccupied orbital (LUMO) energy levels of the π-system [6]. Polymers with bandgaps ranging from 1.4 to 2.5 eV have been prepared. For example, vinylene (Eg = 1.4 eV), 2,5-dialkoxyphenylene (Eg = 1.75 to 2.0 eV), biphenyl (Eg = 2.3 eV), dialkylfluorene (Eg = 2.3 eV) and carbazole (Eg = 2.5 eV). Another derivate, the polymer PBEDT-CNV (where the B is stands for bis) with Eg = 1.1~1.2 eV [6].

The conductivity of these films was found to be a function of the nature of the dopant anion, which is 1-10^2 S/cm at room temperature. Use of PF_6^- as the dopant counterion has provided especially interesting materials with high room temperature conductivity (300 S/cm). Other studies focus on improving the PEDT conductivity. For example, PEDT films doped with sulfated poly(β-hydroxyether) (PEDT/S-PSE) can reach high conductivity in the range of 150-180 S/cm. Also conductivity as high as 400 S/cm was reported when using bis-trifluoromethyl-functionalized sulfated poly(β-hydroxyether) [6].

b) Recent researches using PEDOT:PSS for Schottky junction

N. Matsuki et al. used PANI [7], [8], and PEDOT:PSS [8] as transparent conductive polymer (TCP) on n-type GaN for photovoltaic devices.

Recently, the UV-ozone irradiation effect on electrical property of PEDOT:PSS film was investigated [9]. Two points were clarified. Firstly, the direct UV irradiation decomposes the chemical bonding of PEDOT:PSS and secondly, the ozone and atomic oxygen oxidize the polymer surface, which forms a dipole and increases the PEDOT:PSS work function.

Other works were to study layers of PEDOT:PSS, ITO, or PEDOT:PSS+ITO on P3HT:PCBM and MDMO-PPV:PCBM bulk heterojunction (organic) solar cells [10]. V_{oc} of solar cells could be kept constant with ageing if ITO electrode was avoided. However, due to the higher series resistance, low values of photocurrent were observed using only PEDOT:PSS for the realization of solar cells. But, this indicates that more conductive films of PEDOT:PSS could lead to ITO-free solar cells and consequently to lower-cost, longer-lifetime, all organic solar cells.

On the other hand, the insertion of a thin layer of PEDOT:PSS between copper phthalocyanine (CuPc, this is a organic semiconductor) nanowires and the ITO electrode for solar cell devices improved the contact and reduced the series resistance by an order of magnitude [11].

J.W. Jung et al. worked on fabrication of high efficiency polymer solar cells [12]. They synthesized a new transparent conductive polymer by using polyaniline. The device with PSSa-g-PANI exhibited a photo conversion efficiency 20 % higher than that of the device with PEDOT:PSS due to unique high transparency in the UV-vis region (especially 450-650 nm) and high conductivity of PSSa-g-PANI. For 40nm of PSSa-g-PANI, the conductivity is 0.10 S/cm compared to only 0.007 S/cm for PEDOT:PSS with the same thickness.

Because of PEDOT:PSS and derivates are a few years old, the research to enhance the properties of transparent conductive polymers remains intensive.

6-1.2 Fabrication process of transparent conducting polymer on GaN and InGaN films

After the deposition of GaN or InGaN film on the sapphire substrate by MOCVD, the transparent conducting polymer was deposited by spin-coating under air ambient. A rapid thermal annealing step was necessary just after the spin-coating in order to evaporate the solvent inside the film. These processes were optimized and described in the following.

a) Deposition program of the spin-coating

The most important point of the spin-coating is to spread a homogeneous layer of the transparent conductive polymer without edge effect. The edge effect originates from a wrong optimization of the spin coating program where the edge of the sample has a higher thickness of deposited film. The different programs used are presented in *Fig. 6-3*.

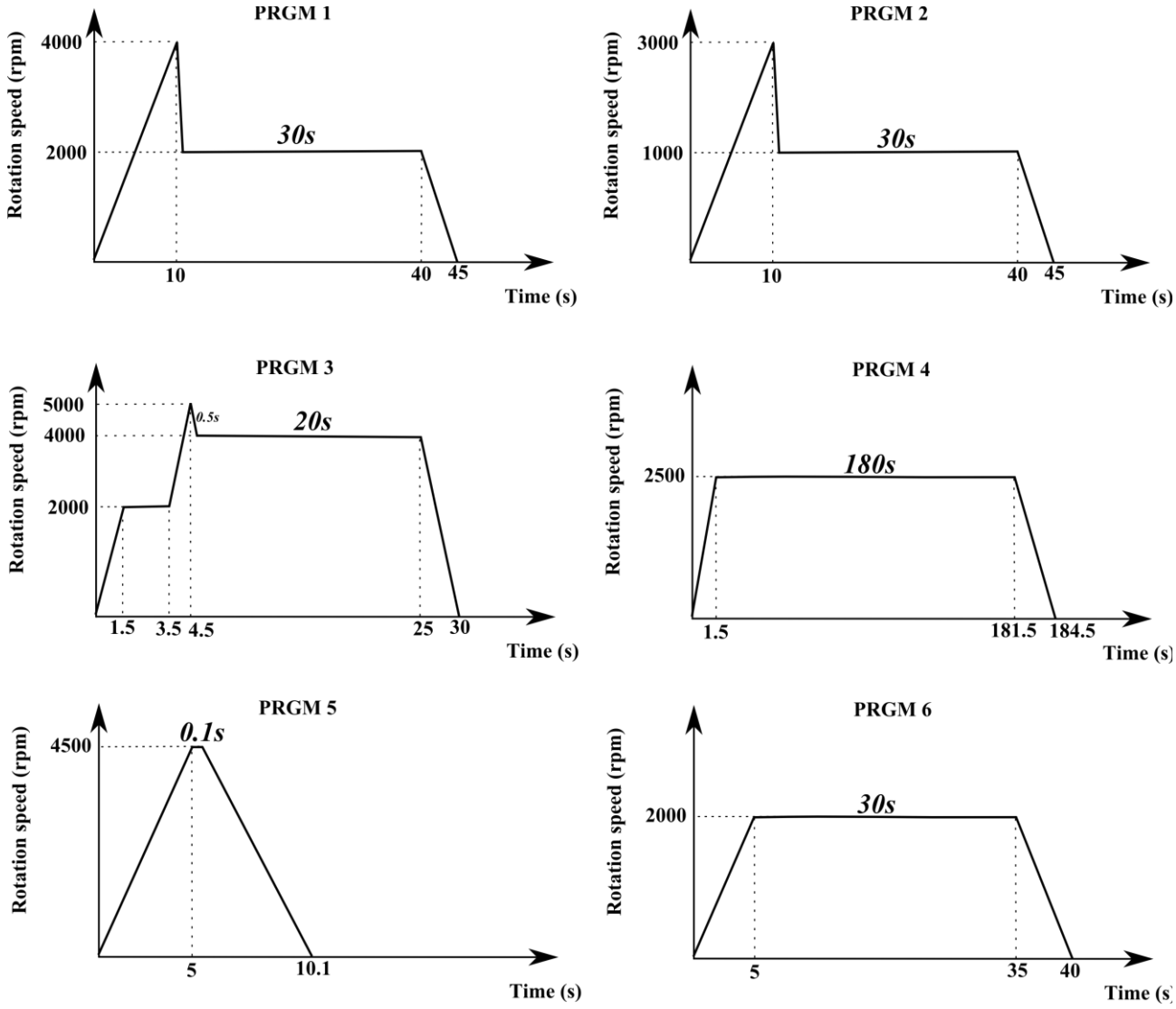

Fig. 6-3: Presentation of the different spin-coating programs used to deposit PANI and PEDOT:PSS on GaN and InGaN films.

Program 1 of the spin-coating achieved the best result in terms of homogeneity for both the PANI and the PEDOT:PSS films. After the spin-coating, the samples were put on a hot plate under ambient air at 250ºC for 10 min in order to evaporate the solvent. I repeated this process four times in order to obtain a thicker transparent conducting polymer. I estimated the thickness by a surface profilometer. After the four-depositions process, the thickness of the PEDOT:PSS film was estimated at 0.58µm on sapphire and 0.66µm on GaN film. I estimated the

thickness of about 0.20 µm for one PANI layer by surface profilometer. The thickness of one PEDOT:PSS layer was much larger and was about 0.42µm because of a higher viscosity compared to PANI.

b) Transparency of conducting polymer

I used the transmittance equipment to verify the transparency of the two conducting polymers, PANI and PEDOT:PSS. The transmittance spectra obtained are presented in *Fig. 6-4* for one layer of each polymer corresponding to 0.20 µm and 0.42 µm in thickness for PANI and PEDOT:PSS, respectively. As the spectra

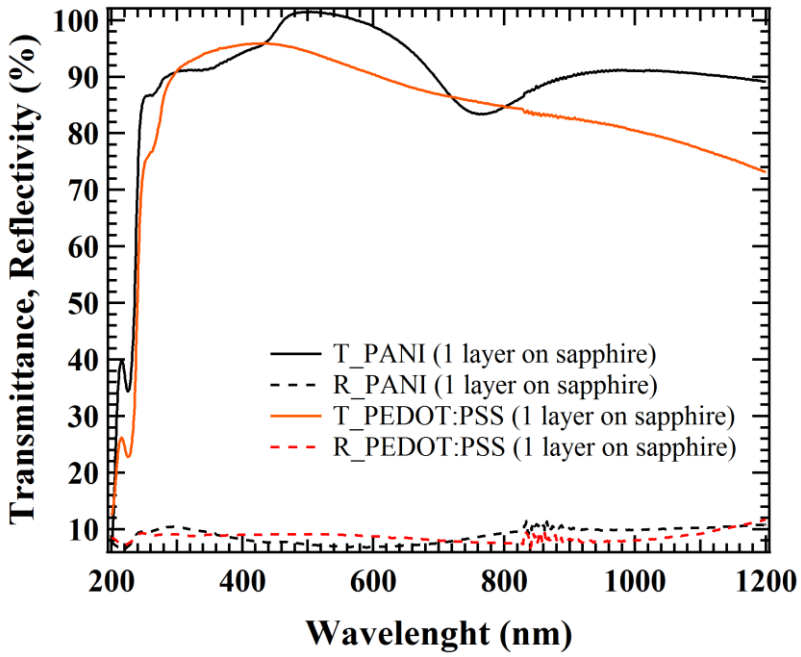

Fig. 6-4: Transmittance and reflectivity of a single layer of PANI and PEDOT:PSS deposited on sapphire substrate.

clarified, both PANI and PEDOT:PSS have a transmittance higher than 80% for the solar spectrum (300 – 1000 nm) with a reflectivity lower than 10%, which made these polymer suitable for the transparent front Schottky contact.

c) Optimization of solvent evaporation on hot plate

In order to enhance the conductivity of the transparent conducting polymers PEDOT:PSS and PANI, I optimized the annealing temperature on the hot plate under ambient air. I measured the resistivity of the film after 10 min at different temperature from 0 to 350ºC. *Figure 6-5* presents the conductivity on the left axis and the resistivity on the right axis for one layer of PEDOT:PSS. *Figure 6-6* presents the conductivity and the resistivity for one layer of PANI.

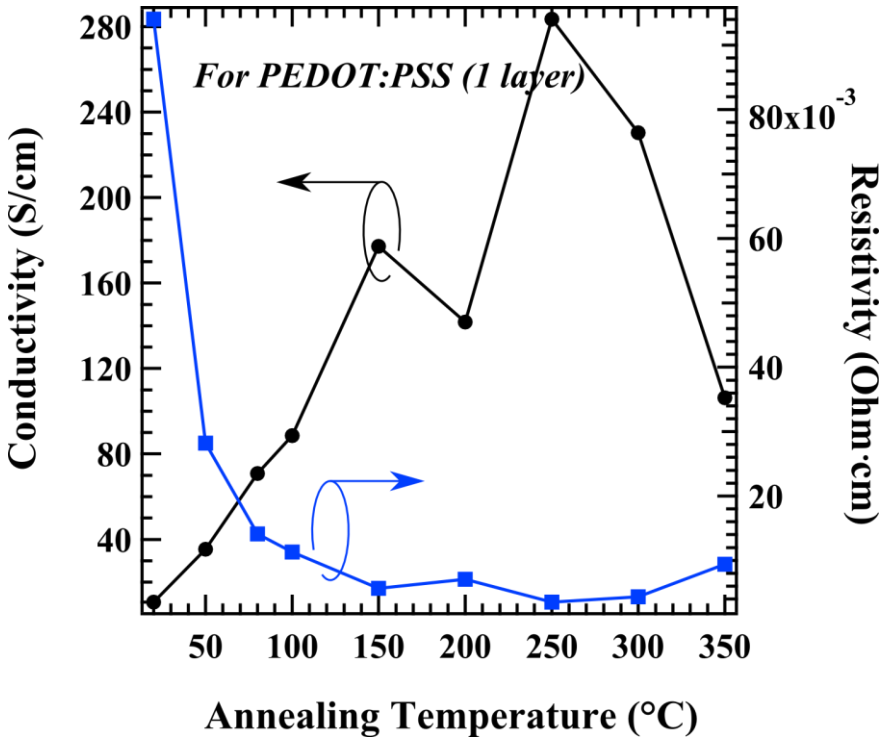

Fig. 6-6: Evolution of the conductivity of a PEDOT:PSS layer depending on the annealing temperature by using the hot plate under ambient air

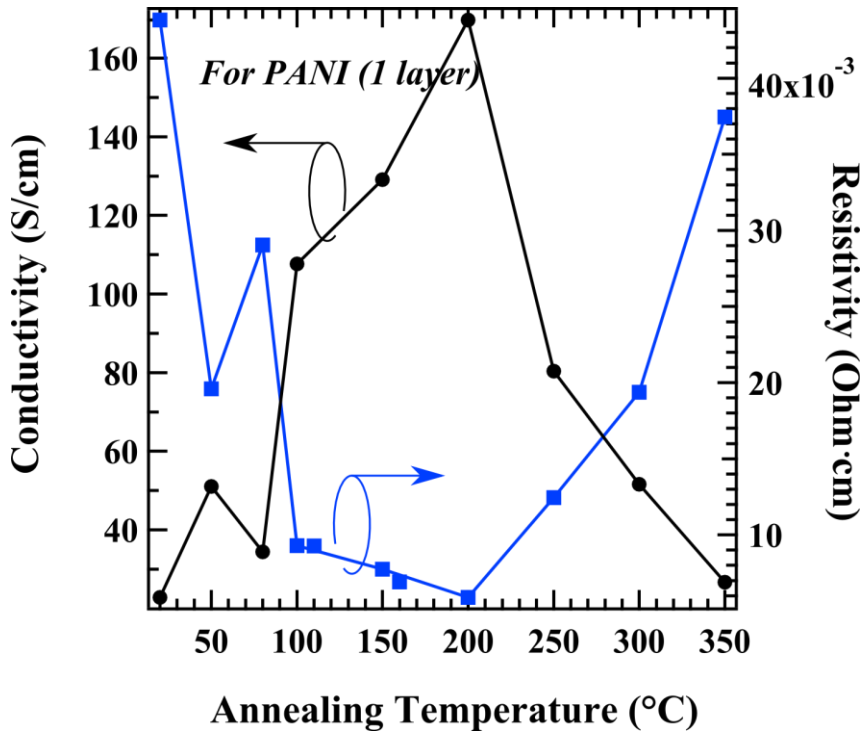

Fig. 6-5: Evolution of the conductivity of a PANI layer depending on the annealing temperature by using the hot plate under ambient air

As *Fig. 6-6* and *Fig. 6-5* show, the annealing of PEDOT:PSS achieved a maximum of conductivity at 250ºC for 10 min. For the case of PANI this maximum was about 200ºC. Thus for the design of the Schottky junction using these polymer different annealing temperatures were applied depending on PEDOT:PSS or PANI.

6-2 Fabrication of Schottky junction and investigation of photovoltaic properties of the GaN and InGaN films

To demonstrate the photovoltaic effect of n-GaN and n-$In_xGa_{1-x}N$ semiconductors, I fabricated Schottky junction devices using transparent conducting polymers (TCP). I employed two TCPs: PEDOT:PSS and polyaniline (PANI), because of their high electron affinity (about 5.2eV, which is the same as gold), their good conductivity and their high transmittance for the solar spectrum of about 80% from 300 to 1500 nm as I previously confirmed. These TCPs are known as p-type organic materials and are electrochemically stable conjugated polymers [8]. I elaborated a new contact structure on GaN or $In_xGa_{1-x}N$ semiconductor, composed of the TCP and a thin Ti/Au front grid (20/20nm) deposited by an e-beam evaporator. With such a structure, I realized the Schottky junction with excellent properties as summarized in *Table 6-1*:

Table 6-1: Schottky and photovoltaic properties of GaN and $In_xGa_{1-x}N$ (x~0.10) films by using PANI and PEDOT:PSS for the Schottky junction.

		Schottky properties		**Photovoltaic properties**		
		SBH (eV)	Ideality factor	V_{oc} (V)	J_{sc} (mA/cm$_2$)	Fill factor
PANI	GaN	0.99	1.7	0.60	0.14	0.56
	$In_{0.11}Ga_{0.89}N$	0.71	2.8	0.11	0.25	0.28
PEDOT:PSS	GaN	0.90	1.05	0.67	0.33	0.69
	$In_{0.09}Ga_{0.91}N$	0.72	3.0	0.30	0.39	0.29

The Schottky properties displayed in *Table 6-1* are presented in *Fig. 6-7*. Because of a larger amount of defects inside InGaN material, the reverse leakage current under negative bias voltage is two orders of magnitude higher than the GaN material. Furthermore the Schottky barrier height was reduced in the case of InGaN with a large ideality factor of the diode. We should note that the Schottky properties using the PEDOT:PSS on both films, GaN or InGaN, had better properties. Photovoltaic properties could be obtained by using these devices. The photovoltaic properties are summarized in *Table 6-1*, and presented in *Fig. 6-8*. For the photovoltaic properties, the devices using the PEDOT:PSS display better properties with larger V_{oc} and J_{sc} compared to the device using the PANI film. The V_{oc} for InGaN material was poor compared to the GaN film because of a higher amount of defects inside this material resulting in a lower-quality Schottky junction.

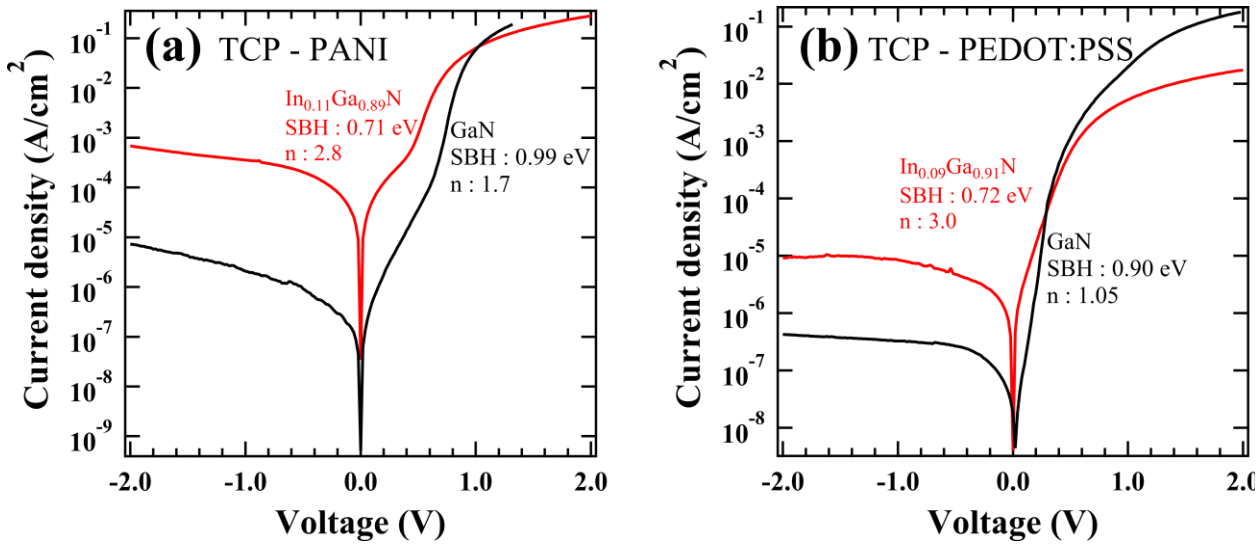

Fig. 6-7: (a) Schottky properties of the Schottky junction realized by PANI on n-GaN and n-$In_{0.11}Ga_{0.89}N$. (b) Schottky properties of the Schottky junction realized by PEDOT:PSS on n-GaN and n-$In_{0.09}Ga_{0.91}N$.

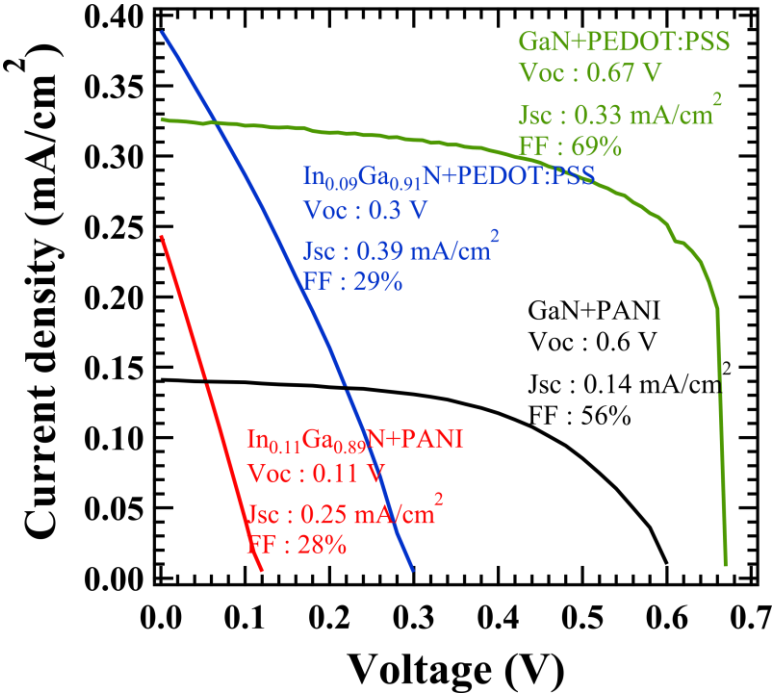

Fig. 6-8: Photovoltaic properties of Schottky solar devices using PANI and PEDOT:PSS on n-GaN, n-$In_{0.09}Ga_{0.91}N$ and n-$In_{0.11}Ga_{0.89}N$ films.

Unfortunately, these photovoltaic properties decreased after few days. I contacted the transparent conducting polymer by using silver paste which also contained some solvent. After annealing the device in order to evaporate the solvent of the silver paste, I believe that a few amount of solvent was kept inside the contact formed. This could contribute to the degradation of the Schottky and photovoltaic properties.

To overcome this difficulty, I fabricated a new device consisting of a thin metallic deposition Ti/Au (20/20 nm) as a front grid on the PEDOT:PSS, because this transparent conducting polymer had higher Schottky and photovoltaic properties. This new device is presented in *Fig. 6-9 (a)*. As the picture in *Fig. 6-9 (b)* displays, the active area of such a device can reach about 0.41cm^2, which is larger than most of solar cells using small surface of GaN or InGaN films.

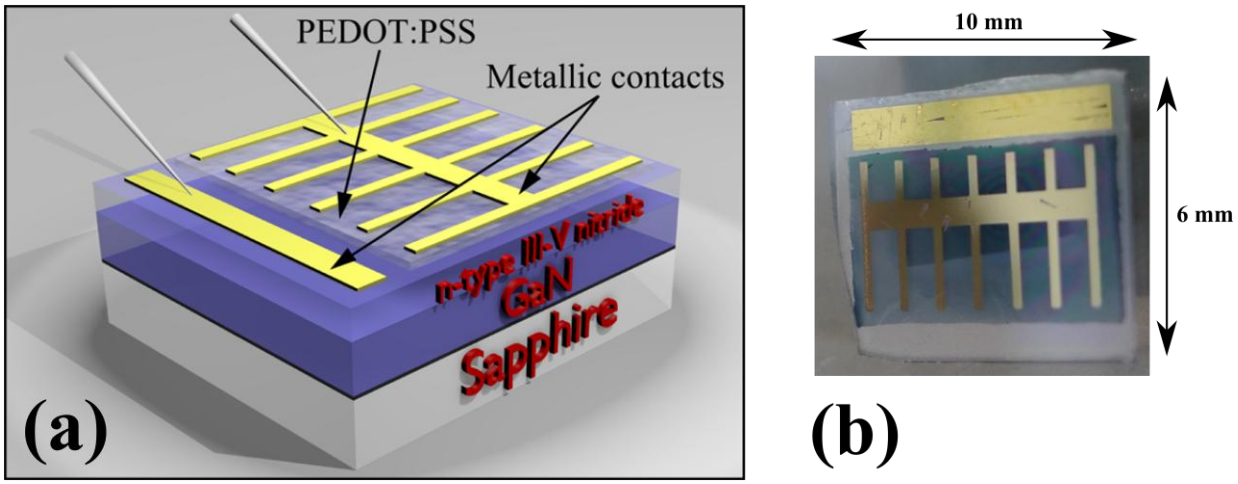

Fig. 6-9: (a) Schematic illustration of the new Schottky solar cell device using metallic contacts on PEDOT:PSS deposited on GaN or InGaN films. (b) Picture of one device, the active area is about 0.41cm^2.

By using such a device, for the n-GaN semiconductor, I obtained the best Schottky barrier height (SBH) of 1.15eV with a low ideality factor of 1.3 using PEDOT:PSS and compared to a Schottky junction that I fabricated using a thin gold layer of 70Å instead (*Fig. 6-10*) . I confirmed that the Schottky properties of n-GaN by using the PEDOT:PSS can reach the Schottky properties of thick metallic deposition Ni/Au with a Schottky barrier height of 0.88 and an ideality factor of 1.18 [13]. By using the front contact structure, I also obtained good photovoltaic properties with an improved fill factor of about 0.70 (*Fig. 6-11*) [14].

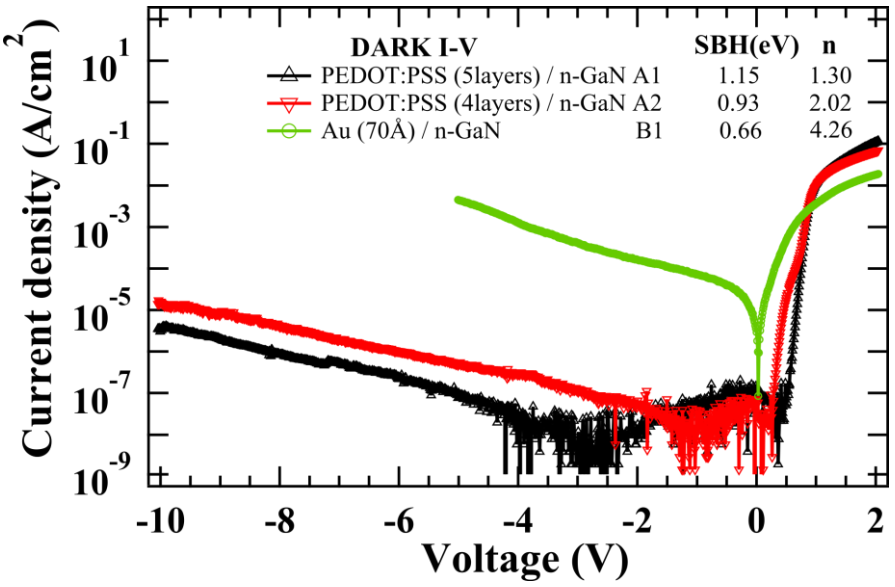

Fig. 6-10: Comparison of Schottky properties using PEDOT:PSS and a thin gold layer of 70Å on n-GaN

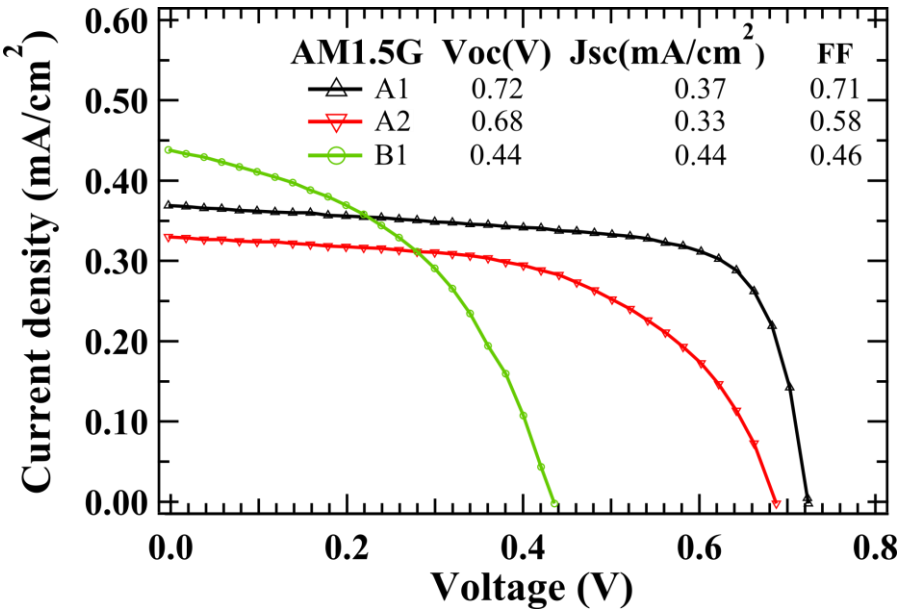

Fig. 6-11: Comparison of Photovoltaic properties using PEDOT:PSS and a thin gold layer of 70Å on n-GaN

Furthermore, by using this new device the Schottky properties could be kept and revealed almost no degradation with time. The evolution of the open-circuit voltage and the Schottky barrier height of the device A1 (presented in *Fig. 6-10* and *Fig. 6-11* for the dark and AM1.5G light conditions) are displayed in *Fig. 6-12*. To check the stability of these photovoltaic properties, J-V measurement under AM1.5G and dark conditions were carried out on PEDOT:PSS/n-GaN A1 device. The device was kept in a box under ambient air. *Figure 6-12* shows the evolution of SBH and V_{oc} during two months, we should note that the variation of SBH and V_{oc} are correlated.

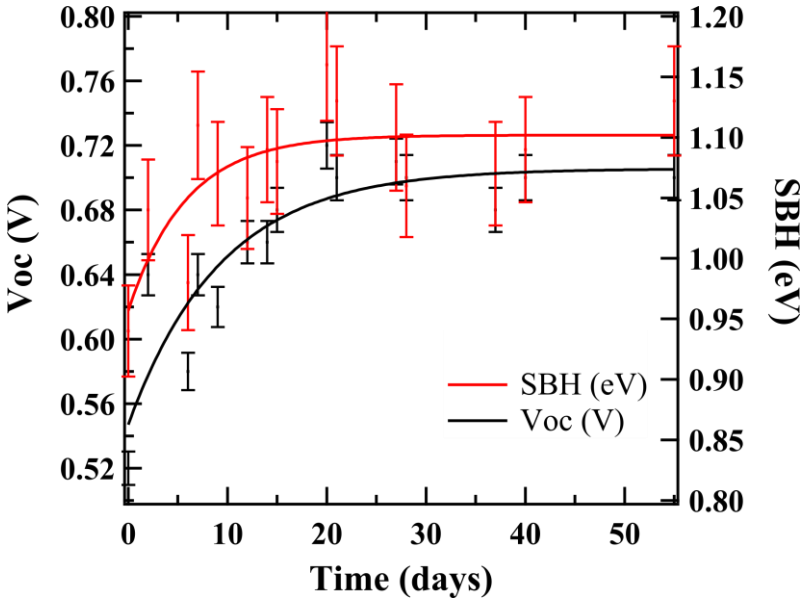

Fig. 6-12: Evolution of the open-circuit voltage (V_{oc}) and the Schottky barrier height (SBH) of the device A1 in function of time

During the first 10 days, SBH increased from 0.95 to 1.10eV and then remained constant at 1.10±0.05eV corresponding to a V_{oc} of 0.70±0.02V. The other parameters fluctuated inside their measurement uncertainties: Jsc at 0.30±0.05mA/cm^2, FF at 0.70±0.04 and the ideality factor n at 1.35±0.10. This observation could be described by an oxidation at the surface of PEDOT:PSS layer. T. Nagata et al. [9] have already observed an enhancement of PEDO:PSS work function after an ozone exposure. This enhancement can be due to the formation of dipoles on surface, which lift the HOMO level of PEDOT:PSS (π-conjugate polymer) towards higher binding energy as a result of oxidation. Even after 9 months, the devices exhibited a high Schottky barrier height (SBH) of about 1.17 eV, a high open-circuit voltage (V_{oc}) of about 0.71 V, and a fill factor of about 0.71 as presented in *Table 6-2*. However, only the short-circuit current (J_{sc}) decreased, which could be attributed to a possible degradation of the optical properties of the PEDOT:PSS layer.

Table 6-2: Schottky and photovoltaic properties of the devices A1 and A2 observed initially and after 9 months.

Devices	Photovoltaic properties (AM1.5G)			Schottky properties	
	V_{oc} (V)	J_{sc} (mA/cm^2)	FF	SBH (eV)	n
A1 (initial)	0.52	0.34	0.69	0.94	1.45
A1 (after 9 months)	0.71	0.15	0.71	1.18	1.24
A2 (initial)	0.66	0.34	0.73	0.92	1.83
A2 (after 9 months)	0.72	0.17	0.72	1.17	1.26

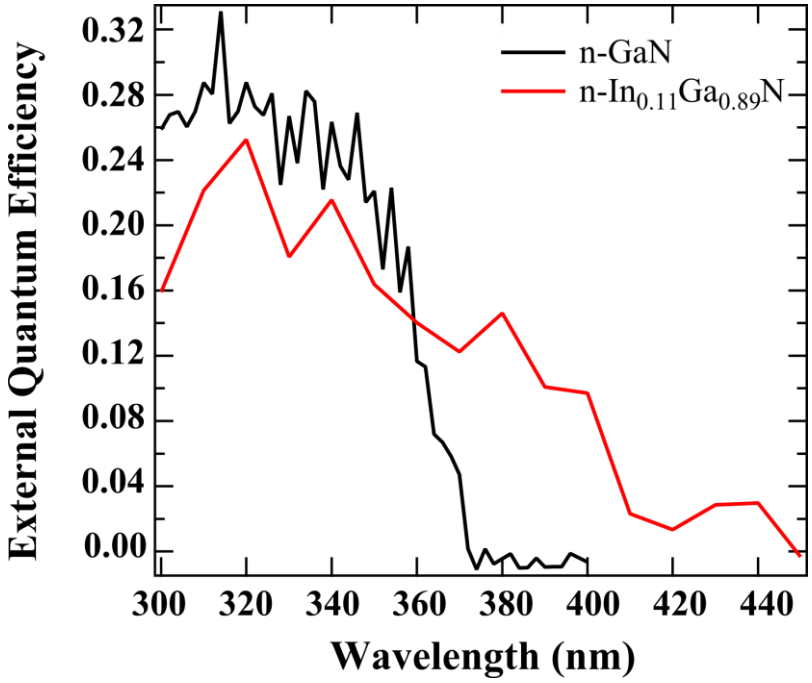

Fig. 6-13: External quantum efficiency of Schottky solar cells using a Schottky junction realized by PEDOT:PSS on n-GaN and n-$In_{0.11}Ga_{0.89}N$ films.

In *Fig. 6-13*, I observed an enhancement of the external quantum efficiency for larger spectra from 300 to 420nm for $In_{0.11}Ga_{0.89}N$ compared to GaN material (300 - 375nm), underlining the potential of $In_xGa_{1-x}N$ as an active layer in photovoltaic applications. This larger absorption of the solar spectrum explains the higher J_{sc} observed for the InGaN film over the GaN (*Fig. 6-8*).

Deep level optical spectroscopy (DLOS) analyses were also performed on my best Schottky devices using n-GaN to confirm if the new Schottky solar cell device could be used to study the deep level defects. The DLOS spectra of the devices A1, A2, A3 and B1 are presented in *Fig. 6-14*. Five photoemission states are identified for the device B1 at ~1.4eV (T1 with a concentration of $3\times10^{15}cm^{-3}$), ~1.7eV (T2: dislocation-related defect at $8\times10^{15}cm^{-3}$), ~2.1eV (T3: Ga vacancies at $11\times10^{15}cm^{-3}$, V_{Ga} $2^-/3^-$ transition level) and/or the V_{Ga}-O_N complex, ~2.8eV (T4: V_{Ga}-C_N complex at $13.5\times10^{15}cm^{-3}$) and ~3.2eV (T5: shallow acceptor carbon (C_N) at $18\times10^{15}cm^{-3}$) under the near band (NBE) edge photoemission from GaN [15]. Three photoemission states are observable of the device using PEDOT:PSS at lower concentration denoted by T3', T4' and T5'. Unfortunately the signal obtained was weak and could also contain defects inside the polymer itself. Two explanations are possible: first, due to free charge inside the polymer, some defects inside n-GaN could be passivate electronically.

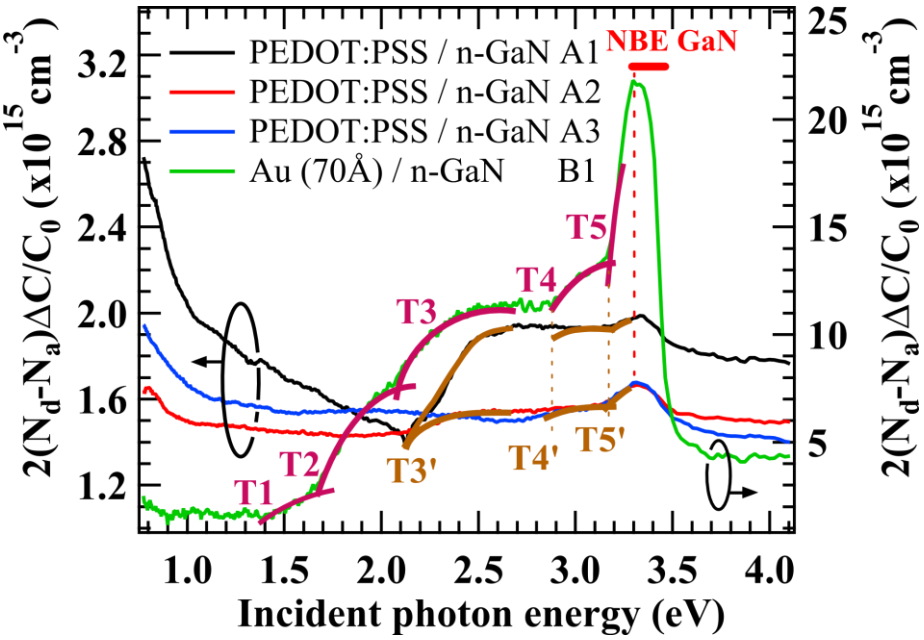

Fig. 6-14: DLOS spectra of Schottky solar cell using PEDOT:PSS/ n-GaN on left axis, and using Au (70Å) /n-GaN on right axis.

A second explanation can be from the signal attenuation due to the thickness of PEDOT:PSS on n-GaN. Other photoemission states below 2.3 eV seem to be generated from the polymer itself which could be attributed to the lowest π-π* transition of conjugate polymer [16]. For this matter, to analyze in detail the deep level defects inside n-$In_xGa_{1-x}N$ as I presented in Chapter 5, I fabricated thick metallic contacts using Ti/Au layers (50/100 nm) and ohmic contacts using Ni/Au (50/100nm).

6-3 Photovoltaic properties of *p-n* homojunction $In_xGa_{1-x}N$ compared to *p-i-n* junction

In this section, I fabricated a *p-n* homojunction $In_{0.1}Ga_{0.9}N$ film. The doping of the n-type material was realized by Si doping and the doping of the p-type material was realized by Mg doping. The dark and photovoltaic properties of this homojunction were compared to a *p-i-n* structure using InGaN film. The devices of both structures are presented in *Fig. 6-16*.

The XRD (0002)- and $(10\bar{1}1)$-planes 2θ-ω scans for both structure are shown in *Fig. 6-15*. The InN mole fraction was estimated at about 10% for both structures. From (0002)-plane 2θ-ω scan, both structures show fringes beside InGaN peaks, which reveal the smooth interface between GaN and $In_{0.1}Ga_{0.9}N$ layers. The full width at half maximum (FWHM) of $In_{0.1}Ga_{0.9}N$ (0002)-plane rocking curves was about 0.089° for p-n homojunction and about 0.088° for p-i-n junction structure. Concerning the FWHM of $In_{0.1}Ga_{0.9}N$ $(10\bar{1}1)$-planes

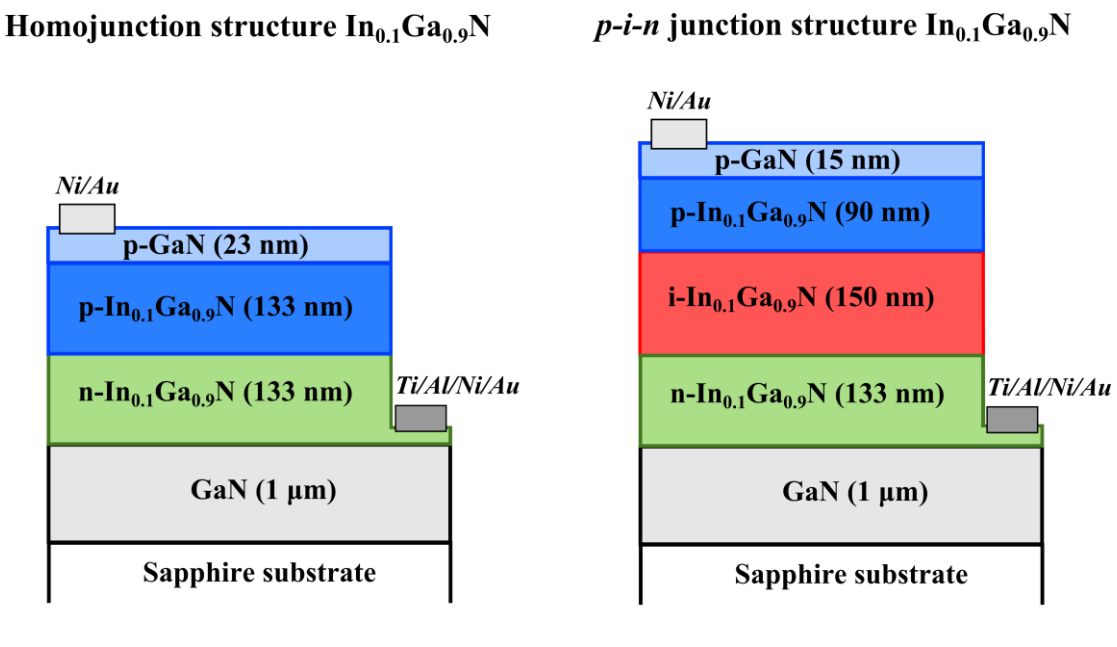

Fig. 6-16: Schematic structure of the p-n homojunction and p-i-n junction using $In_{0.1}Ga_{0.9}N$ films.

rocking curves, it was about 0.164º for p-n homojunction and about 0.172º for p-i-n junction structure. The XRD analysis reveals high crystal quality for both structures.

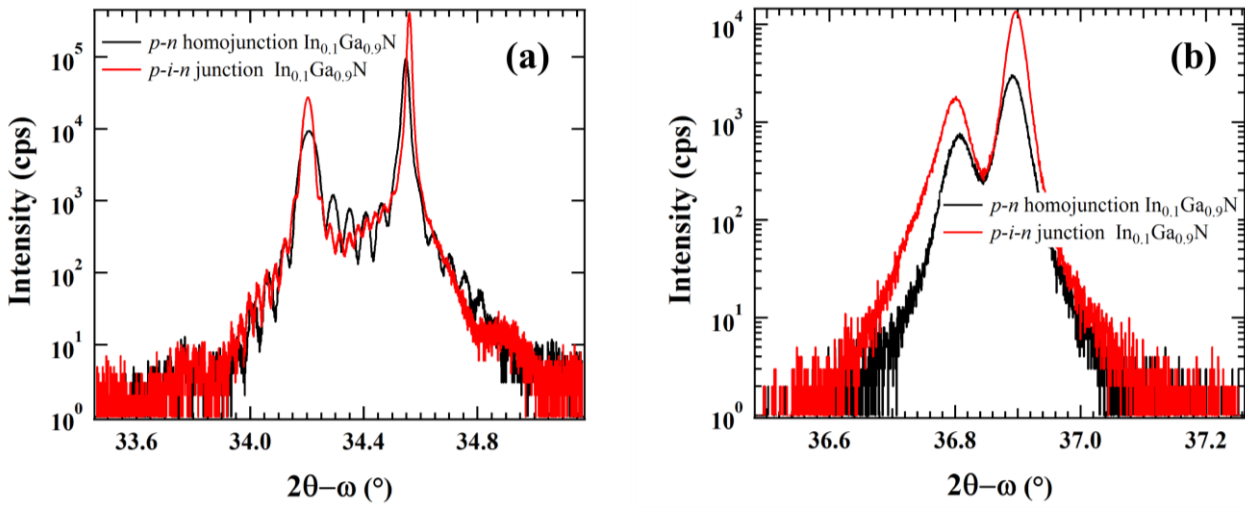

Fig. 6-15: XRD analysis of the p-n $In_{0.1}Ga_{0.9}N$ homojunction and the p-i-n $In_{0.1}Ga_{0.9}N$ junction for (a) (0002)*-plane 2θ-ω scan, and (b) (**10$\bar{1}$1**)-plane scan.*

Photovoltaic properties of the homojunction $In_{0.1}Ga_{0.9}N$ film could be observable, which is a proof for the enhancement of the crystal growth quality as I presented in Chapter 3. In *Fig. 6-17*, the photovoltaic properties of the homojunction $In_{0.1}Ga_{0.9}N$ and the *p-i-n* junction $In_{0.1}Ga_{0.9}N$ are compared. The photovoltaic properties of the homojunction are weaker than the ones of the *p-i-n* structures. The largest difference is the V_{oc} of the two devices: 1.1 V for the homojunction compared to 2.0 V for the *p-i-n* structure. Furthermore an enhancement of the Jsc from

0.6 to 0.9 mA/cm^2 is also observed. This indicates that an intrinsic layer between the p-type and n-type InGaN material is necessary to increase the solar spectrum absorption, which leads to a higher Jsc, but also to extend the depletion layer resulting in a better junction quality, which brings about a better V_{oc}.

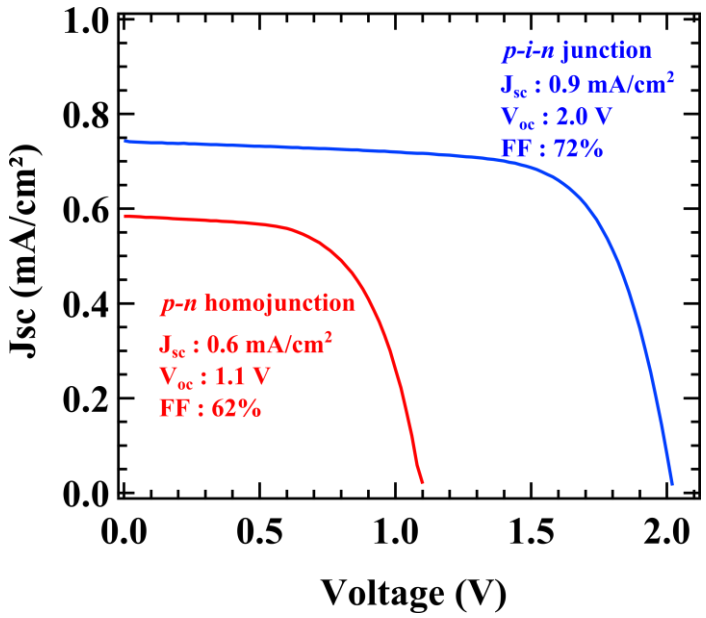

Fig. 6-17: Photovoltaic properties of the homojunction $In_{0.1}Ga_{0.9}N$ (in red) compared to p-i-n junction $In_{0.1}Ga_{0.9}N$ (in blue).

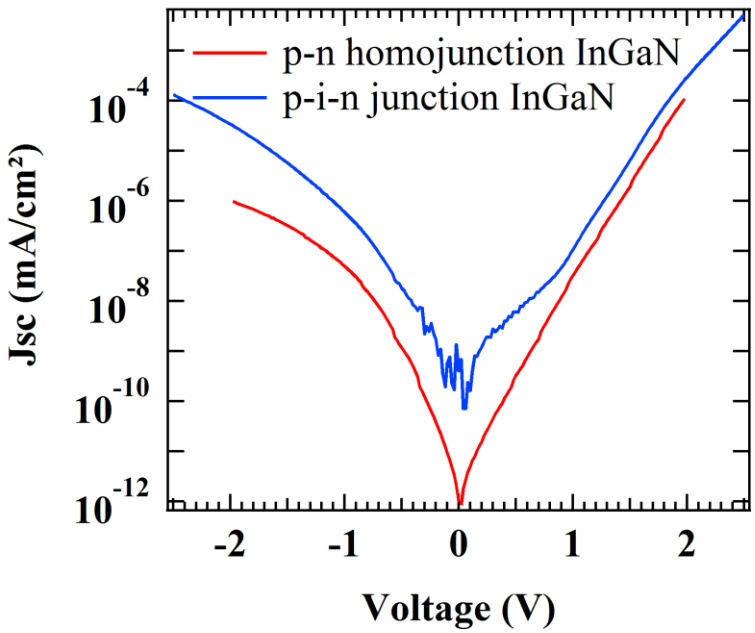

Fig. 6-18: Junction properties under dark condition for the p-n homojunction and p-i-n junction using $In_{0.1}Ga_{0.9}N$ films.

The junction properties under dark condition are presented in *Fig. 6-18*. The characteristic of both devices are unfortunately bad due to a large leakage current under reverse bias voltage. This leakage current is two orders of magnitude lower for the p-n homojunction certainly because the total thickness of InGaN material is smaller for this device compared to the *p-i-n* junction. Another possibility is the reduced amount of interface in the case of the homojunction device. An important point to notice is the low reverse voltage necessary to break the characteristic of the homojunction around – 3 V.

Improvement of the InGaN material is still necessary to reach better photovoltaic properties by reducing the reverse leakage current. This reduction is certainly related to the unintended doping level of the n-type material and intrinsic layer.

Although the *p-n* $In_{0.1}Ga_{0.9}N$ homojunction solar cell does not reach the photovoltaic properties of *p-i-n* $In_{0.1}Ga_{0.9}N$ junction, its properties are high compared to literature. B. R. Jampana et al. reported p- $In_{0.15}Ga_{0.85}N$ / n-$In_{0.17}Ga_{0.83}N$ *p-n* junction solar cells with a V_{oc} of 1.11 V, a J_{sc} of 0.022 mA/cm^2, and a FF of 42 % under AM 1.5 with UV filter [17]. C. Yang et al. reported p-$In_{0.18}Ga_{0.82}N$ / n-$In_{0.15}Ga_{0.85}N$ *p-n* junction solar cells with a V_{oc} of 0.43 V, a J_{sc} of 3.4×10^{-2} mA/cm^2 and a FF of 57% [18] under 360 nm illumination. M. Islam et al. reported $In_{0.25}Ga_{0.75}N$ p_+-*n* junction solar cell with a V_{oc} of 1.5 V, a J_{sc} of 0.5 mA/cm^2, and a FF of about 50 % [19] under AM 1.5 illumination. Although the InN mole fraction of these solar cell devices is higher than 10 %, the short-circuit current obtained was lower than the *p-n* $In_{0.1}Ga_{0.9}N$ that I fabricated, which can be related to the recombination of photogenerated carrier with poor InGaN material quality. The XRD spectra of these devices revealed large full width at hall maximum (FWHM) for InGaN (0002) rocking curves, which is generally the case of $In_xGa_{1-x}N$ at higher InN mole fraction.

6-4 Conclusion

Schottky solar cell devices using transparent conducting polymers such as PANI and PEDOT:PSS on n-GaN and n-InGaN were realized. Good Schottky properties under dark conditions and photovoltaic properties could be achieved with the PEDOT:PSS. I improved the Schottky solar cell devices by depositing a thin metallic front grid directly on the PEDOT:PSS. Thanks to this device the active area of the solar cell could be increase to about 0.41cm^2, which is larger than laboratory solar cells using InGaN.

The *p-n* homojunction $In_{0.1}Ga_{0.9}N$ shows some photovoltaic properties, which is a good advancement to employ InGaN as an active layer for photovoltaic devices. This homojunction had lower photovoltaic properties than *p-i-n* junction, which implies the necessity of an intrinsic layer in order to enhance the absorption and the depletion layer formed between the p-type and n-type InGaN layer. But, compared to literature, the photovoltaic properties of the *p-n* homojunction $In_{0.1}Ga_{0.9}N$ fabricated are better with a V_{oc} of 1.1 V, a J_{sc} of 0.6 mA/cm^2 and a FF of 62 %.

To reach good p-n junction properties, it is essential to know the diffusion profile of dopants inside the material. Secondary ion mass spectroscopy analysis revealed a high diffusion of Mg elements inside InGaN. For the realization of p-n junction InGaN, a key point will be the precise control of the junction depth where the hole and electron concentrations are compensated.

I fabricated Schottky junctions that were greatly improved by Mg compensation on n-type $In_{0.07}Ga_{0.93}N$ films. The Schottky junction formed had a high Schottky barrier height of 1.18 eV, a low ideality factor of 1.07 and a very low leakage current about 10^{-8} mA/cm^2 at reverse bias voltage of -4 V. Thus it is worth trying to use the Mg compensation technique during n-InGaN and i-InGaN growth layer in order to reduce the unintended n-type doping. For future studies, the Mg compensated InGaN process can be used instead of the intrinsic InGaN to reduce the large reverse leakage voltage observed for both homojunction and *p-i-n* junction using InGaN films. I hope it would enhance the photovoltaic properties observed in this study.

References chapter 6

[1] H. Shirakawa, E. J. Louis, A. G. MacDiarmid, C. K. Chiang, and A. J. Heeger, "Synthesis of electrically conducting organic polymers: halogen derivatives of polyacetylene, (CH) x," *Journal of the Chemical Society, Chemical Communications*, no. 16, p. 578, 1977.

[2] R. De Surville, M. Jozefowicz, L. T. Yu, J. Pepichon, and R. Buvet, "Electrochemical chains using protolytic organic semiconductors," *Electrochimica Acta*, vol. 13, no. 6, pp. 1451–1458, 1968.

[3] A. F. Diaz and J. A. Logan, "Electroactive polyaniline films," *Journal of Electroanalytical Chemistry and Interfacial Electrochemistry*, vol. 111, no. 1, pp. 111–114, 1980.

[4] A. V. Murugan, C.-W. Kwon, G. Campet, B. . Kale, T. Maddanimath, and K. Vijayamohanan, "Electrochemical lithium insertion into a poly(3,4-ethylenedioxythiophene)PEDOT/V_2O_5 nanocomposite," *Journal of Power Sources*, vol. 105, no. 1, pp. 1–5, Mar. 2002.

[5] Y. Xia and J. Ouyang, "Anion effect on salt-induced conductivity enhancement of poly(3,4-ethylenedioxythiophene):poly(styrenesulfonate) films," *Organic Electronics*, vol. 11, no. 6, pp. 1129–1135, Jun. 2010.

[6] L. B. Groenendaal, F. Jonas, D. Freitag, H. Pielartzik, and J. R. Reynolds, "Poly (3,4-ethylenedioxythiophene) and Its Derivatives : Past , Present , and Future," *Advanced Materials*, vol. 12, pp. 481–494, 2000.

[7] N. Matsuki, Y. Irokawa, T. Matsui, M. Kondo, and M. Sumiya, "Photovoltaic Action in Polyaniline/n-GaN Schottky Diodes," *Applied Physics Express*, vol. 2, p. 092201, 2009.

[8] N. Matsuki, Y. Irokawa, Y. Nakano, and M. Sumiya, "Pi-Conjugated polymer/GaN Schottky solar cells," *Solar Energy Materials and Solar Cells*, vol. 95, no. 1, pp. 284–287, 2011.

[9] T. Nagata, S. Oh, T. Chikyow, and Y. Wakayama, "Effect of UV – ozone treatment on electrical properties of PEDOT : PSS film," *Organic Electronics*, vol. 12, no. 2, pp. 279–284, 2011.

[10] M. Girtan and M. Rusu, "Role of ITO and PEDOT : PSS in stability / degradation of polymer : fullerene bulk heterojunctions solar cells," *Solar Energy Materials & Solar Cells*, vol. 94, pp. 446–450, 2010.

[11] G. Chintakula, S. Rajaputra, and V. P. Singh, "Schottky diodes on nanowires of copper phthalocyanine," *Solar Energy Materials and Solar Cells*, vol. 94, no. 1, pp. 34–39, 2010.

[12] J. W. Jung, J. U. Lee, and W. H. Jo, "High-Efficiency Polymer Solar Cells with Water-Soluble and Self-Doped Conducting Polyaniline Graft Copolymer as Hole Transport Layer," *Journal of Physical Chemistry C*, vol. 114, pp. 633–637, 2010.

[13] K. Wang, R. X. Wang, S. Fung, C. D. Beling, X. D. Chen, Y. Huang, S. Li, S. J. Xu, and M. Gong, "Film thickness degradation of Au / GaN Schottky contact characteristics," *Materials Science and Engineering B*, vol. 117, pp. 21–25, 2005.

[14] M. Lozac'h, Y. Nakano, L. Sang, K. Sakoda, and M. Sumiya, "Fabrication of transparent conducting polymer/GaN Schottky junction for deep level defect evaluation under light irradiation," *Physica Status Solidi (a)*, vol. 210, no. 3, pp. 470–473, Mar. 2013.

[15] M. Lozac'h, Y. Nakano, L. Sang, K. Sakoda, and M. Sumiya, "Study of Defect Levels in the Band Gap for a Thick InGaN Film," *Japanese Journal of Applied Physics*, vol. 51, p. 121001, Nov. 2012.

[16] N. G. Semaltianos, C. Koidis, C. Pitsalidis, P. Karagiannidis, S. Logothetidis, W. Perrie, D. Liu, S. P. Edwardson, E. Fearon, R. J. Potter, G. Dearden, and K. G. Watkins, "Picosecond laser patterning of PEDOT : PSS thin films," *Synthetic Metals*, vol. 161, no. 5–6, pp. 431–439, 2011.

[17] B. R. Jampana, A. G. Melton, M. Jamil, N. N. Faleev, R. L. Opila, I. T. Ferguson, and C. B. Honsberg, "Design and Realization of Wide-Band-Gap (~2.67 eV) InGaN p-n Junction Solar Cell," *IEEE Electron Device Letters*, vol. 31, no. 1, pp. 32–34, 2010.

[18] C. Yang, X. Wang, H. Xiao, J. Ran, C. Wang, G. Hu, X. Wang, X. Zhang, J. Li, and J. Li, "Photovoltaic effects in InGaN structures with p – n junctions," *Physica Status Solidi (a)*, vol. 204, no. 12, pp. 4288–4291, 2007.

[19] M. R. Islam, M. R. Kaysir, M. J. Islam, A. Hashimoto, and A. Yamamoto, "MOVPE Growth of InxGa1−xN (x ~ 0.4) and Fabrication of Homo-junction Solar Cells," *Journal of Materials Science & Technology*, vol. 29, no. 2, pp. 128–136, Feb. 2013.

Chapter 7

7- Conclusions and perspectives

The principal purpose of this work was to study the potential of InGaN films for photovoltaic application. To successfully complete this project, I focused on four main tasks. First, I had to clarify the key parameters for the growth condition of InGaN films to control the material bandgap. Secondly, I had to analyze the band alignments of the device structure and especially between the p-GaN and InGaN layers where a band offset occurs. Thirdly, I needed to analyze the defects and deep levels associated to identify some possible recombination centers and understand their nature. Then finally, I fabricated Schottky junction and homojunction *p-n* devices to examine the photovoltaic properties of InGaN films.

After the first and second chapter concerning the introduction of the purpose of research and the fundamental physics with the presentation of characterization techniques, the third chapter treated the optimization of the InGaN films in terms of crystal quality, electronic and optical properties, and the control of the material bandgap. The N_2 ambient gas as carrier gas to grow InGaN was necessary. The ammonium flow, the ratio of metalorganic sources and the temperature are the key parameters to control the growth speed and thus the high crystal quality with a reduced unintended n-type material. With an ammonium flow of 10 sLm and a growth temperature of 1000ºC, the GaN layer could reach a lower free-carrier concentration of about 2×10^{18} cm^{-3} and a higher electron mobility of about 260 cm^2/Vs. For the InGaN, the optimized growth conditions were an ammonium flow of 7sLm, a ratio of metalorganic sources of about 0.74 and a temperature range from 850 to 750ºC to obtain $In_xGa_{1-x}N$ films with the indium content of $6 < x < 15$ %. Using these conditions, the global carrier concentration could be reduced down to $1\sim2\times10^{17}cm^{-3}$ keeping a higher electron mobility up to 180 cm^2/Vs for an InN mole fraction of 14%. The InN mole fraction is used to control the bandgap of the InGaN film, and I realized a strain growth of InGaN above the GaN epilayer until an InN mole fraction of 10%. Above 10%, the film starts to have a more relaxed growth mode and defects were greatly increased. Thus the modulation of the bandgap from 3.4 to 3.0 eV corresponds to an InN mole fraction from 0 to 10%. In the present status, this bandgap is still too large to be usable in a single *p-n* homojunction solar cell. Nevertheless it is possible to use its photovoltaic properties for the realization of a 4^{th}-terminal solar cell structure using $In_{0.1}Ga_{0.9}N$ on the top of the tandem structure.

The fourth chapter treated the band alignment analysis. The samples were analyzed by HX-PES at Spring 8 to estimate the valence band maximum. I have found that the valence band maximum was shifted to lower binding energy when the InN mole fraction increased. The band offset between the valence band maximum of p-GaN and i-$In_{0.07}Ga_{0.93}N$ was estimated at 0.2 eV. Furthermore the GaN was found to have an upward band bending on surface instead of a downward band bending for InN films. I estimated for the first time that the Fermi level of InN material with a low carrier concentration of about 5×10^{17} cm^{-3} is located inside the bandgap of InN. Regarding the presence of the band offset between p-GaN and i-InGaN, it seems better to develop an InGaN *p-n* homojunction to avoid any barrier for the photogenerated carrier and especially for the hole transport.

The fifth chapter developed the deep-level defect analysis. Three techniques were employed in order to extract the maximum information of these different deep levels: the thermal admittance spectroscopy (TAS), the deep level transient spectroscopy (DLTS), and the deep level optical spectroscopy (DLOS). The TAS measurement revealed two shallow donor defects at Ec-7 meV and Ec-108 meV. Judging from the bias dependency, the defect at Ec-7 meV was located homogeneously inside the film, which could be attributed to In fluctuation or V_N vacancies. The defect at Ec-108 meV was found to be located near the surface, which could be attributed to some interface states. The DLTS analysis also revealed two defect levels located at Ec-22meV and Ec-0.6 eV. The first defect could be attributed to impurities like oxygen, carbon, residual silicon or V_N vacancies. The second defect at Ec-0.6eV had already been observed for GaN material and could be attributed to V_{Ga} vacancies or its complex associated with oxygen impurities. Finally, the DLOS technique clarified five photoemission states due to the presence of deep level defects. The main defects for InGaN film were the ones located below the conduction band at E_c-2.07 eV and E_c-3.05 eV corresponding to V_{Ga} vacancies and their complexes associated with oxygen or carbon impurities and the shallow carbon C_N or V_N vacancies, respectively. All the defects contributed to the unintended n-type material for GaN and InGaN film. The deepest defects were linked with the V_{Ga} vacancies, which must be most responsible for the capture of photogenerated carrier.

The sixth chapter developed the optimization of the Schottky junction devices using transparent conducting polymers on GaN and InGaN films. The photovoltaic properties were examined for both of these films, but because of more defects present inside the InGaN films, the photovoltaic properties obtained were poor. Nevertheless, the spectral response was extended down to 440 nm for the InGaN device, which implies the potential of these films for photovoltaic applications. The sixth chapter also presented the photovoltaic properties of a *p-n* homojunction $In_{0.1}Ga_{0.9}N$ compared to a *p-i-n* structure. First of all, thanks to the optimization of InGaN layer deposition, I could obtain some photovoltaic properties for a pure *p-n* homojunction InGaN. By inserting an intrinsic layer, the V_{oc} was greatly improved, which means that the depletion layer and the junction quality are also improved. Thus, the material quality is still low to be used for a *p-n* homojunction. In order to reduce the unintended n-type doping, Mg compensated doping layers were deposited on the surface of Schottky devices. The saturation current was considerably weaker than an conventional i-InGaN layer. A perspective of this finding is to use the Mg compensated layer as the n-type material for a *p-n* homojunction to confirm if the depletion layer is enhanced. Another utility of the Mg compensated layer is to help to assign more accurately the nature of the deep level defects present inside the InGaN layers.

However the photovoltaic properties of our devices are still limited bellow 1% of efficiency, after the determination of defects presented in this work, further studies need to be done in order to reduce the concentration of these defects or to passivate them electronically. For instance, the development of a rapid thermal annealing depending on the temperature and the ambient gas used, such as nitrogen or oxygen, related with the junction properties can open a path to post-fabrication processes for defects passivation. Another very interesting study could be to establish a correlation between the luminescent defects observed by cathodoluminescence and the rapid thermal annealing step used to clarify some defect behaviors depending on the ambient gas.

Research is still necessary to improve the InGaN material quality and the InN mole fraction to decrease the material bandgap in order to promote this material for photovoltaic devices applications. The present study was successful for the understanding of the nature of defects generated, the knowledge of the band structure of InGaN material, and its opens a path to future processes of defects passivation, which will enhance the InGaN material quality for photovoltaic applications.

List of Publications

First author publications:

1. M. Lozac'h, Y. Nakano, L. Sang, K. Sakoda, and M. Sumiya, "Study of defect levels in the band gap for a thick InGaN film", *Jpn. J. Appl. Phys.* **51** (2012) 121001.

2. M. Lozac'h, S. Ueda, S. Liu, H. Yoshikawa, S. Liwen, X. Wang, B. Shen, K. Sakoda, K. Kobayashi, and M. Sumiya, "Determination of surface band bending in $In_xGa_{1-x}N$ films by hard X-ray photoemission spectroscopy", *Sci. Technol. Adv. Mater.* ***14*** (2013) 015007.

3. M. Lozac'h, Y. Nakano, L. Sang, K. Sakoda, and M. Sumiya, "Fabrication of transparent conducting polymer/GaN Schottky junction for deep level defects evaluation under light irradiation", *Phys. Stat. Sol. (a)* **210** (2013) 470.

Co-author publications:

4. M. Sumiya, M. Lozac'h, N. Matsuki, S. Ito, N. Ohhashi, K. Sakoda, H. Yoshikawa, S. Ueda, and K. Kobayashi, "Valence band structure of III-V nitride films characterized by hard X-ray photon electron spectroscopy", *Phys. Stat. Sol. C* **7-8**, 1903-1905 (2010).

5. Y. Nakano, M. Lozac'h, N. Matsuki, K. Sakoda, and M. Sumiya, "Photocapacitance spectroscopy study of deep-level defects in freestanding n-GaN substrates using transparent conductive polymer Schottky contacts", *J. Vac. Sci. Technol. B* **29**, 023001 (2011).

6. L. Sang, M. Takeguchi, W. Lee, Y. Nakayama, M. Lozac'h, T. Sekiguchi, and M. Sumiya, "Phase separation resulting from Mg doping in p-InGaN film grown on GaN/Sapphire template", *Appl. Phys. Exp.* **3**, 111004 (2010).

7. Y. Nakano, M. Lozac'h, L. Sang, and M. Sumiya, "Electrical investigation of band-gap states in thicker InGaN films", submitted to *Jpn. J. Appl. Phys.*

List of Presentations

Oral presentations:

1. M. Lozac'h, K. Watanabe, S. Ueda, H. Yoshikawa, K. Kobayashi, K. Sakoda, and M. Sumiya (2010) "Growth and characterization of thick $In_xGa_{1-x}N$ films for photovoltaic device", *The Japan Society of Applied Physics – 57th Spring meeting (JSAP 57th)*, Tokai University, Kanagawa, Japan, March 2010.

2. M. Lozac'h, K. Nakano, K. Sakoda, and M. Sumiya (2011) "Schottky solar cells using transparent conductive polymer on III-V nitride thin films", *The Japan Society of Applied Physics – 58th Spring meeting (JSAP 58th)*, Atsugi, Kanagawa, Japan, March 2011.

Poster presentations:

3. M. Lozac'h, K. Sakoda, and M. Sumiya (2010) "Growth and characterization of $In_xGa_{1-x}N$ films for solar cell application", *Electronic Material Symposium (EMS 29th)*, Laforet Shuzenji, Izu, Japan, July 2010.

4. M. Lozac'h, Y. Nakano, K. Sakoda, and M. Sumiya (2011) "Properties of III-V nitride thin film Schottky solar cells using transparent conductive polymer", *5th Asian-Pacific Workshop on Widegap Semiconductors (APWS-2011)*, Toba, Mie, Japan.May 2011.

5. M. Lozac'h, Y. Nakano, L. Sang, K. Sakoda, and M. Sumiya (2012) "Schottky properties enhanced by using compensated Mg doped InGaN thin films material at interface metal-InGaN", *4th International Symposium on Advanced Plasma Science and its Applications for Nitrides and Nanomaterials (ISPlasma 2012)*, Chubu University, Aichi, Japan, March 2012.